Acoustic Noise Based Sensorless Control of Permanent Magnet Synchronous Machine

Amirhossein Malekipour

THÈSE

Pour obtenir le grade de

DOCTEUR DE L'UNIVERSITÉ GRENOBLE ALPES

École doctorale : EEATS - Electronique, Electrotechnique, Automatique, Traitement du Signal (EEATS)
Spécialité : Génie électrique
Unité de recherche : Laboratoire de Génie Electrique

Contrôle sans capteur basé sur le bruit acoustique d'une Machine Synchrone à Aimants Permanents

Acoustic Noise Based Sensorless Control of Permanent Magnet Synchronous Machine

Présentée par :

AMIRHOSSEIN MALEKIPOUR

Direction de thèse :

Laurent GERBAUD PROFESSEUR DES UNIVERSITES, Université Grenoble Alpes	Directeur de thèse
Lauric GARBUIO MAITRE DE CONFERENCES, Université Grenoble Alpes	Co-encadrant de thèse
Pierre GRANJON MAITRE DE CONFERENCES, GRENOBLE INP	Co-encadrant de thèse

Rapporteurs :

Babak NAHID-MOBARAKEH
PROFESSEUR, McMaster University
Gérard CHAMPENOIS
PROFESSEUR EMERITE, Université de Poitiers

Thèse soutenue publiquement le **18 décembre 2023**, devant le jury composé de :

Babak NAHID-MOBARAKEH PROFESSEUR, McMaster University	Rapporteur
Gérard CHAMPENOIS PROFESSEUR EMERITE, Université de Poitiers	Rapporteur
Jérôme ANTONI PROFESSEUR DES UNIVERSITES, INSA Lyon	President
Seddik BACHA PROFESSEUR DES UNIVERSITES, Grenoble INP	Examinateur
Sokha LY DOCTEUR EN SCIENCES, VALEO	Examinateur

Invités :

Adrien Corne
ASSISTANT PROFESSOR, G2ELab

Dedication

To the pillars of my world,

As I stand on the precipice of this academic achievement, I find it impossible to express in simple words the depth of my gratitude for your unwavering love, support, and encouragement. You have been the guiding stars of my life, illuminating the darkest of nights with your unshakeable faith in my dreams.

Mom, *your love has been an inexhaustible source of inspiration, and your sacrifices have sculpted my path. Your nurturing spirit and boundless optimisim have been a beacon of hope throughout my academic journey.*

Dad, *your wisdom and srength have always been my anchor. Your unalloyed belief in my potential has driven me to push my boundaries and fulfill my goals.*

To my beloved ones, *you are the pages of this thesis, the chapters of my life. This work is not simply a testament to my academic endeavours but a testament to the extraordinary support and love that have always been surrounding me. It is a culmination of your sacrifices, late nights, and our shared dreams.*

In dedicating this thesis to you, I hope to capture a fraction of the love and appreciation that fills my heart. My success is your success, and my gratitude is boundless.

Amirhossein
October 18, 2023

Acknowledgements

I extend my profound appreciation to my esteemed thesis supervisors, ***Prof. Laurent Gerbaud****,* ***Dr. Lauric Garbuio****, and* ***Dr. Pierre Granjon****, for their unwavering support, invaluable guidance, and unceasing commitment to excellence throughout the course of my research and the writing of this dissertation.*

Their extensive knowledge, academic acumen, and dedication have been pivotal in shaping the intellectual contours of this work. Their insightful feedback, meticulous scrutiny, and sage consel have illuminated my path, inspiring me to strive for the highest standards of scholarly achievement.

I am truly indebted to ***Lauric****, who sadly passed away and left us alone, yet his mentorship, patience, knowledge, and supportiveness are always engraved in my heart. Lauric always believed in my abilities and encouraged me to push harder, and I am thankful to him for all these driving forces.*

Dear ***Laurent*** *and* ***Pierre****, I am sincerely grateful for your guidance, professionalism, expert pieces of advice, and technical comments which resulted in the excellence of my research.*

My friend, ***Adrien****, I would like to extend you a special thanks for being a peer and working alongside me on the FAME project. Our collaboration was mutually-beneficial, as we grew, learnt, and excelled in our careers together.*

Last but not least, being surrounded by brilliant supervisors, friends, and colleagues at ***G2Elab*** *provided me with an unforgettable experience that helped me to grow both personally and professionally, delve into research, contribute to science, and develop my professional career.*

Amirhossein
October 18, 2023

Contents

List of Tables

List of Figures

Glossary

Nomenclature

Chapter 1

Symbol	Unit	Definition
T	-	Clarke Transformation
$\vec{V_s}$	V	Stator voltage space phasor
R_s	Ω	Stator resistance
$\vec{i_s}$	A	Stator voltage space phasor
$\vec{\psi_s}$	Wb	Stator flux space phasor
$V_{\alpha s}$,$V_{\beta s}$	V	α- and β-axis stator voltages
$i_{\alpha s}$,$i_{\beta s}$	A	α- and β-axis stator currents
$\psi_{\alpha s}$,$\psi_{\beta s}$	Wb	α- and β-axis stator fluxes
ψ_m	Wb	Permanent magnet flux
θ_e,θ_m	Rad	Electrical and mechanical angles
L_s,L_m	H	Stator self and mutual inductances
ω_e,ω_m	Rad/s	Electrical and mechanical fundamental frequencies
V_d,V_q	V	d- and q-axis stator voltages
ψ_d,ψ_q	Wb	d- and q-axis stator fluxes
i_d,i_q	A	d- and q-axis stator currents
L_d,L_q	H	d- and q-axis stator inductances
p	-	Stator pole pair number
T_e	N.m	Generated torque
ρ	-	Differential operator
V_γ,V_δ	V	Stator voltage in the estimated γ- and δ-axis

i_γ,i_δ	A	Stator current in the estimated γ- and δ-axis
e_γ,e_δ	V	Stator EEMF in the estimated γ- and δ-axis
$\hat{\omega_e}$	Rad/s	Estimated electrical fundamental frequency
$\hat{\theta_e}$	Rad	Estimated electrical angle
λ_α,λ_β	Wb	*alpha*- and β-axis total stator fluxes
x	-	State variable of the system state-space model
u	-	Input of the system state-space model
y	-	Output of the system state-space model
A,B,C,I,J,0	-	Constant matrix coefficient
P	-	Perturbation term
O	-	Observed disturbance
H	-	Feedback gain matrix
V_{dh},V_{qh}	V	High-frequency term in the d- and q-axis voltages
i_{dh},i_{qh}	A	High-frequency term in the d- and q-axis currents
V_h	V	Amplitude of the HFI voltage
ω_h	Rad/s	Frequency of the HFI voltage
I_{hp},I_{np}	A	Amplitudes of the positive- and negative-sequence of $i_{\alpha\beta h}$
$I_{d'h}$,$I_{q'h}$	A	High-frequency terms of the estimated dq-frame currents
V_N	V	Amplitude of the positive-sequence of $i_{\alpha h}$
V_1	V	Amplitude of the zero-sequence voltage
$i_{\alpha h-prc.}$,$i_{\beta h-prc.}$	A	Processed α- and β-axis currents
T_h	s	Period of the square-wave HFI voltage
k	-	Constant integer
t	s	Instance of time
$V_{\alpha\beta-pulse}$	V	Injected voltage in INFORM method
$i_{\alpha\beta-pulse}$	V	Induced current in INFORM method
I_i	A	Amplitude of the current i^{th} harmonic
ϕ_i	Rad	Phase of the current i^{th} harmonic
B_r^{PM},B_θ^{PM}	T	PM radial and tangential airgap fields
B_r^{Arm},B_θ^{Arm}	T	Armature radial and tangential airgap fields
b_r^{PM},b_θ^{PM},b_r^{Arm},b_θ^{Arm}	-	Constants depending on r and j
r	m	Radius of analysis in the airgap
j	-	The number of spatial harmonics
λ_α,λ_β	-	Real and imaginary components of the complex permeance

λ_{dc},$\lambda_{\alpha n}$,$\lambda_{\beta n}$	-	Constants depending on the stator slots dimensions
N_s	-	Number of stator slots
F_r,F_θ	N	Radial and tangential airgap forces
M_m	Kg	Global mass matrix
C_m	N.s/m	Global damping matrix
K_m	Pa	Global rigidity matrix
F_m	N	Nodal force vector matrix
X	m	Nodal displacement matrix
$\tilde{F_k}$	N	Amplitude of the force k^{th} harmonic
$\tilde{X_k}$	m	Amplitude of the displacement k^{th} harmonic
c_0	m/s	Sound wave speed in a given medium
γ	m^2/s	Kinematic viscosity
ρ	Kg/m^3	Medium mass density
P	Pa	Sound pressure
v	m/s	sound propagation velocity

Chapter 2

Symbol	**Unit**	**Definition**
f_e,f_m,f_{ei}	Hz	Electrical, mechanical, and current frequencies
F_r^{PM},F_r^{Arm}	N	PM radial airgap forces considering the PM and Arm impacts
K_T	-	Transformation matrix
$L_{\alpha\beta}$	H	Inductance matrix in $\alpha\beta$-frame
L_{dq}	H	Inductance matrix in dq-frame
$V_{\alpha\beta h}$,V_{dqh}	V	HFI voltages in the $\alpha\beta$- and dq-frame
$i_{\alpha\beta h}$,Vi_{dqh}	V	Resulting HFI currents in the $\alpha\beta$- and dq-frame
$i_{\alpha\beta}^{V_{\alpha\beta h}}$	A	HF current in the $\alpha\beta$-frame with HFI voltage in $\alpha\beta$-frame
$i_{\alpha\beta}^{V_{dqh}}$	A	HF current in the $\alpha\beta$-frame with HFI voltage in dq-frame
V_{phd}	V	Gate pulses in deadtime-included PWM
V_{phi}	V	Gate pulses in ideal PWM
V_{ref}	V	Reference PWM waveform, which is to be compared with the carrier
V_c	V	PWM carrier waveform
m_a	-	PWM modulation index
T	s	Period of the carrier signal

D	-	PWM duty cycle
V_{dc}	V	DC link voltage
K,k	-	Constant integers

Chapter 3

Symbol	**Unit**	**Definition**
h	-	Order of the chosen harmonic
i,k	-	Coefficients used in the design of BPFI and BPFII
C	-	Gain of the chosen BPF
f_b,f_c	Hz	Passing band and central frequency of the BPF
W,X	-	Gain and input of the ADALINE
d,μ	-	Error and learning rate of the ADALINE
e	Rad	Estimation error of PLL/QPLL
K_p,K_i	-	Proportional and integral coefficients of the PLL loop filter
G_{QPLL}^{frw}	-	Forward-path transfer function of the QPLL
G_{QPLL}	-	Closed-loop transfer function of the QPLL
ξ	-	Damping coefficient of the second-order system
ω_n	Rad/s	Undamped natural frequency of the second-order system
τ_{sd},τ_{sq}	s	Time constant of the d- and q-frame current loop
T_{sw}	s	Period of the switching
G_i^{frw}	-	Forward-path transfer function of the current loop
K_{p_i},K_{I_i}	-	Proportional and integral gain of the current loop PI regulator
τ_i	s	Current loop time constant
T_{s_i}	s	Accumulated time constant of the digital delays
τ_{elec}	s	Time constant of the PMSM electrical model
G_i	-	Closed-loop trabsfer function of the current loop
T_e,T_l	N.m	Electromagnetic and load torque
J	Kg.m^2	The rotor moment of inertia
B	N.m.s/rad	Frictional damping coefficient
ω_m	Rad/s	Rotor mechanical speed
G_ω^{frw}	-	Forward-path transfer function of the speed loop
K_{p_ω},K_{i_ω}	-	Proportional and integral coefficient of the speed loop PI
A_i,A_o	V	Amplitude of the PLL input and output

h_i,h_o	-	Harmonic order of the PLL input and output
ω_e,$\hat{\omega}_e$	Rad/s	Actual and estimated frequency
K_{RC}	-	Gain of RC
ξ_{RC}	-	Damping coefficient of RC
ω_{RC}	Rad/s	undamped natural frequency of RC
α,γ	-	Constant coefficients in RC design
G_{RC}	-	Closed-loop transfer function of the compensation block
G^{frw}_{RCPLL}	-	Open-loop transfer function of RCPLL
G^{cl}_{RCPLL}	-	Closed-loop transfer function of RCPLL
G^{frw}_{ω}	-	Open-loop transfer function of the speed loop with RCPLL

Abbreviation

PMSM	Permanent magnet synchronous motor
SM	Synchronous machine
IM	Induction machine
FOC	Field-oriented control
IPMSM	Interior PMSM
SPMSM	Surface PMSM
CA	Commutation angle
BEMF (EMF)	Back Electromotive Force
EEMF	Extended EMF
LDO	Linear disturbance observer
SMO	Sliding-mode observer
EKF	Extended Kalman filter
LPF	Low-pass filter
BPF	Band-pass filter
HPF	High-pass filter
PLL	Phase-locked loop
ANN	Artificial neural network
LESO	Linear extended state observer
SNR	Signa-to-noise ratio
HFI	High frequency injection
PWM	Pulse width modulation

INFORM	Indirect flux detection by online reactance measurement
PM	Permanent magnet
Arm	Armature
FEM	Finite-element method
RPWM	Random PWM
ADALINE	Adaptive linear neuron
QPLL	quadrature PLL
ADC	Analog-to-digital converter
FFT	Fast fourier transform
RC	Resonanr controller
RCPLL	RC-based PLL
ADALINE-PLL	ADALINE-based PLL
SOGI	Second-order generalized integrator
SRFPLL	Synchronous reference-frame PLL
EPLL	Enhanced PLL
PMSG	Permanent magnet synchronous generator

General Introduction

Electric motors have always had a pivotal role in industry. At first, DC motors were abundantly used, due to their simple control and satisfactory torque dynamics. Then, AC machines became more widespread, owing to their simpler structure and less mechanical sophistication. Prior to the era of modern power electronics, open-loop and constant V/f ratio control algorithms were the most utilised control methods of AC machines. Introduction of powerful processors and proliferation of efficient semiconductor switches have culminated in a tangible leap within the power electronic industry, directly influencing the electric motor drive technologies and related control algorithms.

Nowadays, cutting CO_2 emission is at the forefront of attention of the governments and global decision-makers. To this end, the topic of transportation electrification has garnered especial importance. Within this context, reliability, flexibility, and redundancy are vital keywords defining a successful technology. Having the characteristics like wide speed range, high torque density, robust structure, and low disseminated vibration and acoustic noise has made the permanent magnet synchronous motor (PMSM) an apt AC machine, especially within the electrified drivetrains.

Having a high-performing and reliable operation, field-oriented control (FOC) is an integral part of any AC motor control algorithm. The coordinate transformation is the heart of FOC, which entails having access to the instantaneous rotor position. The rotor position is usually captured through position sensors, in the form of encoder, resolver, or hall-effect sensor. However, these sensors need to be regularly tuned and are bulky, expensive, and susceptible to conductive noise and faulty operation; therefore, seeking more relible and cheaper acquisition techniques has become a trending research topic, resulted in the emergence of sensorless control algorithms.

Given the operating speed, different sensorless mehods exist; at zero and low-speed range, the saliency tracking-based methods are widely adopted. Besides, the model-based algorithms are utilised for the medium-high speed operation. Scanning the literature, a plethora

of research is found concerning these two methods.

On the other hand, this thesis proposes a novel method for PMSM sensorless control implementation which utilizes the machine output acoustic noise, instead of the current or electromotive force (EMF). While the acoustic noise has traditionally been viewed as a drawback in PMSM operation, this cross-coupled phenomenon is deeply investigated and actively leveraged for the extraction and estimation of rotor position information.

In contrast to the conventional methods, the proposed sensorless method can cover a wide speed range. As the result, the acoustic noise-based sensorless control is of great potential in being applied to many applications, at least as the back-up control method in case of the main method failure, accentuating all of the mentioned keywords, *i.e.*, reliability, flexibility, and redundancy.

Chapter 1 discusses the fundamental modelling and control methods of PMSM, associated sensorless algorithms state-of-the-art, and vibration and acoustic noise occurrence in electric machines. Regarding the sensorless algorithms, all of the aspects of the existing methods, including the model-based and saliency tracking-based, are extensively discussed.

Chapter 1 provides the necessary elements for the proposed methods and analyses provided in Chapter 2 and Chapter 3.

Chapter 2 deeply investigates the vibroacoustic behaviour of PMSM, in response to various high-frequency injection (HFI) and PWM voltages. Given each condition, the harmonics of current, electromagnetic fields, airgap radial forces, and resulting vibration and acoustic noise are investigated. Finally, it is proved that, if PMSM is excited by an HFI or PWM voltage, the radiated acoustic noise serves as a rich source for extraction of the rotor position information.

Chapter 3 implements an acoustic noise-based PMSM sensorless control. Regardless of the excitation type (HFI or PWM only), two novel signal processing algorithms, for extraction of the speed-dependent components, are proposed. In the following step, the system stability is investigated. Finally, two novel position observers, equipped with adaptive harmonic compensation blocks, are proposed which greatly improve the estimation performance.

Chapter 4 evaluates the performance of the proposed methods through experimental tests on an actual testbench. Reliability, robustness and stability of all the proposed methods are verified through various tests conducted in static and dynamic conditions. In addition, successful performance of the proposed methods is benchmarked against the conventional sensorless algorithms in similar working points.

Chapter 1

State of the Art - PMSM Fundamentals, Sensorless Control, and Vibration and Acoustic Noise

This dissertation is dedicated to development of a closed-loop sensorless control for permanent magnet synchronous motor (PMSM) using the machine output acoustic noise, as the source for extraction and estimation of the rotor position information. As the result, this chapter details the following aspects:

- **PMSM fundamentals, operation, and conventional control algorithms**: it is necessary to review the fundamentals of PMSM operation and conventional control algortithms at first.
- **Sensorless control of PMSM**: instead of using the bulky, expensive, and faulty position sensors for acquiring the rotor position, sensorless algorithms are developed which provide the estimated values of the rotor position.
- **Vibration and acoustic noise phenomenon in PMSM**: the nature of vibration and resulting acoutic noise are deeply invesrigated in order to provide a suitable background for using the PMSM acoustic noise (or vibration) for the rotor position estimation in the following chapter, which finds its application in acoustic noise-based sensorless control.

1.1 PMSM Fundamentals, Operation, and Conventional Control Algorithms

Introduction

In the past, DC motors were abundantly used for variable-speed applications due to the fact that their torque and flux could be controlled by changing the field and armature currents in a linear manner. On the contrary to the ease of control and rapidity of torque response, DC motors have complicated mechanical structure which is a big disadvantage. Due to the existence of commutators and brushes mounted on the rotor, performing periodic maintenence is required.

AC motors, on the other hand, due to their simpler structure and especially after the maturity of power electronic converters and digital processors proved themselves as reliable and cost-effective alternative to their DC counterparts. It is possible to apply the similar flux and torque control principles to AC drives, by which the generated flux and torque are directly controlled by the respective flux-producing and torque-producing components of the current. This method is called field-oriented control (FOC) or vector control of AC drives which is applicable to both synchronous machines (SM) and asynchronous machines (or induction machines abbreviated as IM) [1].

In both IM and SM, the salient stator is made of a laminated iron core. The stator has windings responsible for producing stator-side magnetic field.

On the other hand, SM and IM have fundamentally different rotor structures. The rotor of IM can either be of squirrel cage, with the minimal manufacturing cost, or wound type. For SM, different rotor structures exist which results in having different types of machines as follows [2]:

- **Wound rotor SM**: In this structure, the rotor flux is generated through a DC-excited winding which is mounted on the rotor by means of brushes and slip rings. In order to facilitate the process of torque generation, an auxiliary winding can also be added to the rotor. This machine structure is shown in Fig. (1.1a).

- **Synchronous reluctance machine (SynRM)**: In this machine structure, there is no magnet or winding within the rotor structure. The rotor is made of laminated core which has several voids to better orient the flux paths as shown in Fig. (1.1b); consequently, the rotor is deemed to be of salient type which results in the generation

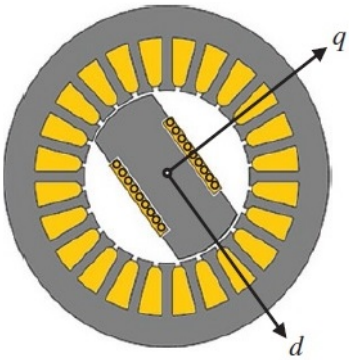

(a) Wound SM [2].

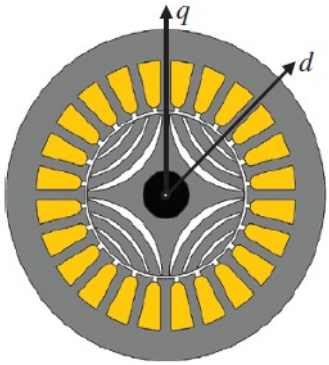

(b) SynRM [2].

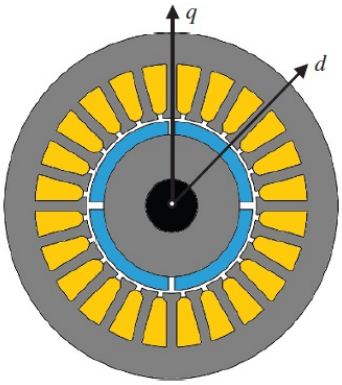

(c) SPMSM [2].

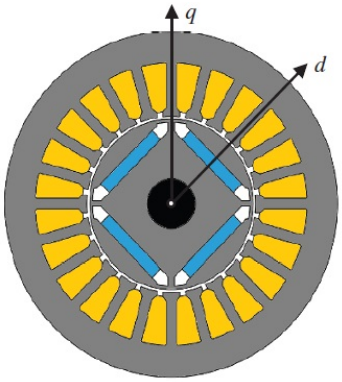

(d) IPMSM [2].

Figure 1.1: Different structures of SM.

of reluctance torque while operation. Compared to PMSM, this machine has lower efficiency, yet due to to absence of PM in the structure, the overall manufacturing cost is lower.

- **Permanent magnet SM (PMSM)**: In this structure, the rotor field is generated via using permanent magnets in the rotor structure. Depending on the position of the magnets, different types of PMSM can be obtained. Given the magnets mounted on the stator surface, the structure is called surface permanent magnet SM (SPMSM) shown in Fig. (1.1c). If the magnets are buried inside the rotor, the structure is interior permanent magnet SM (IPMSM) shown in Fig. (1.1d). The use of rare-earth magnets with high remnant flux yields machines with smaller size and higher efficiency. On the contrary, these high-performance magnets significantly increase the manufacturing cost and complexity of PMSM. **It is to be mentioned that all the analyses, simulations, and experimental results in this dissertation are provided for PMSM.**

In all SM topologies, the rotor always rotates in synchronism with the stator flux, meaning that the rotor always rotates at the synchronous frequency. By utilizing appropriate control strategy and power converter, the stator fundamental frequency could be altered which results in having variable speed operation. Also, the dq-frame is always aligned with the generated rotor flux as a convention.

1.1.1 Modeling of PMSM

In this subsection, the space phasor models of PMSM in the stationary ($\alpha\beta$) and synchronous rotating (dq) reference frames are reviewed. Modelling of PMSM in the $\alpha\beta$- and dq-frame is an important asset for the development of FOC and sensorless control algorithms.

1.1.1.1 PMSM Model in the Stationary Reference Frame Fixed to the Stator

Given an arbitrary vector $\vec{x}$ in the abc coordinate system (three-phase) as shown in Fig. (1.2), there always exist two orthogonal vectors representing the real and imaginary components, as mathematically provided in eq.(1.1). The x_0 component, known as the zero-sequence component, is introduced to the matrix to make it invertible. The transformation is made

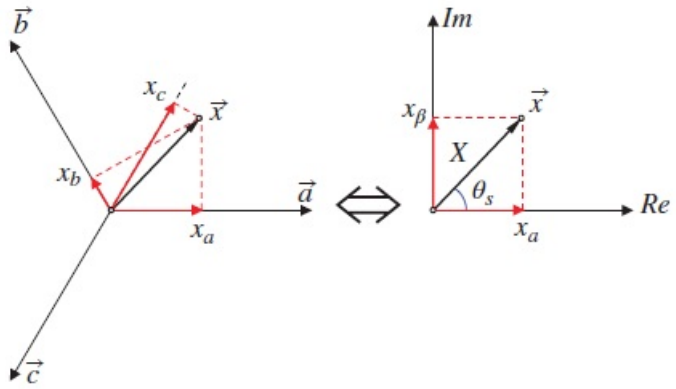

Figure 1.2: Transformation from the *abc*-frame to the stationary $\alpha\beta$-frame.

possible through using a constant matrix known as Clarke Transformation.

$$\begin{bmatrix} x_\alpha \\ x_\beta \\ x_0 \end{bmatrix} = T \begin{bmatrix} x_a \\ x_b \\ x_c \end{bmatrix} \tag{1.1}$$

$$T = \frac{2}{3} \begin{bmatrix} 1 & -\frac{1}{2} & -\frac{1}{2} \\ 0 & \frac{\sqrt{3}}{2} & -\frac{\sqrt{3}}{2} \\ \frac{1}{2} & \frac{1}{2} & \frac{1}{2} \end{bmatrix} \tag{1.2}$$

Using the same principle, the voltage equation in the three-phase system (Appendix A and eq. (A.1)) can be rewritten using the space phasor notation:

$$\vec{V}_s = R_s \cdot \vec{i}_s + \frac{d}{dt}\vec{\psi}_s \tag{1.3}$$

The above equation can be decomposed into its real and imaginary components as in eq. (1.4) and eq. (1.5).

$$V_{\alpha s} = R_s i_{\alpha s} + \frac{d\psi_{\alpha s}}{dt} \tag{1.4}$$

$$V_{\beta s} = R_s i_{\beta s} + \frac{d\psi_{\beta s}}{dt} \tag{1.5}$$

The stator flux components in the stationary reference frame are obtained as:

$$\psi_{\alpha s} = \psi_m \cdot \cos(\theta_e) + L_{ss} i_{\alpha s} \tag{1.6}$$

$$\psi_{\beta s} = \psi_m \cdot \sin(\theta_e) + L_{ss} i_{\beta s} \tag{1.7}$$

As the result, the voltage equations are obtained as:

$$V_{\alpha s} = R_s i_{\alpha s} + L_{ss} \frac{di_{\alpha s}}{dt} - \psi_m \omega_e \cdot \sin(\theta_e) \tag{1.8}$$

$$V_{\beta s} = R_s i_{\beta s} + L_{ss} \frac{di_{\beta s}}{dt} + \psi_m \omega_e \cdot \cos(\theta_e) \tag{1.9}$$

Within eq. (1.8) and eq. (1.9), the two terms containing the rotor speed (ω_e) are defined as the Back Electromotive Force (BEMF) which are induced rotational voltages.

1.1.1.2 PMSM Model in the Synchronous Rotating Reference Frame Fixed to the Rotor

Given the arbitrary vector $\vec{x}$ in the stationary reference frame shown in Fig.(1.2), it is possible to transform this vector to an arbitrary new reference frame which is rotating at a fixed speed (ω_s) as shown in Fig.(1.3). In this transformation, the original vector $\vec{x}$ is kept constant and only its real and imaginary components are changed with respect to the new coordinate system. The transformation from the stationary-frame to the synchronous-frame

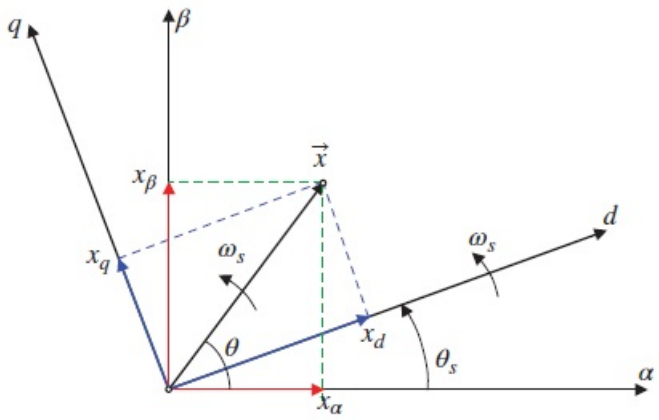

Figure 1.3: Transformation from the stationary frame to the synchronous frame.

is mathematically defined as:

$$\vec{x}_{dq} = \vec{x}_{\alpha\beta} \cdot e^{-j\theta_s} \tag{1.10}$$

$$\begin{bmatrix} x_d \\ x_q \end{bmatrix} = \begin{bmatrix} \cos(\theta_s) & \sin(\theta_s) \\ -\sin(\theta_s) & \cos(\theta_s) \end{bmatrix} \begin{bmatrix} x_\alpha \\ x_\beta \end{bmatrix} \tag{1.11}$$

where θ_s represents the arbitrary angle difference among the stationary and rotating frames. This transformation is completely invertible which makes it possible to transform the dq-frame components to their corresponding stationary frame version.

In SM, the rotor flux is aligned with the actual rotor angle; therefore, the chosen dq-frame rotates synchronously with the rotor speed and its actual angle corresponds to the instantaneous rotor position ($\theta_s = \theta_e$).

In order to obtain the SM model in the synchronous reference frame, eq. (1.3) is multiplied by $e^{-j\theta_e}$ and the components are decomposed which results in the following:

$$V_d = R_s i_d + \frac{d\psi_d}{dt} - \omega_e \psi_q = R_s i_d + L_d \frac{di_d}{dt} - \omega_e L_q i_q \tag{1.12}$$

$$V_q = R_s i_q + \frac{d\psi_q}{dt} + \omega_e \psi_d = R_s i_q + L_q \frac{di_q}{dt} + \omega_e \left(\psi_m + L_d i_d\right) \tag{1.13}$$

Applying the same transformation, the dq-frame flux equations are obtained as:

$$\psi_d = L_d i_d + \psi_m \tag{1.14}$$

$$\psi_q = L_q i_q \tag{1.15}$$

In eq. (1.12) and eq. (1.13), the terms containing ω_e are BEMF in the synchronous frame.

1.1.1.3 Torque Equation of PMSM

The general equation for the generated electromagnetic torque of an SM is provided in eq. (1.16) [3] ,[4].

$$T_e = \frac{3}{2} p \left(\psi_d i_q - \psi_q i_d\right) = \frac{3}{2} p \left(\psi_m i_q + \left(L_d - L_q\right) i_d i_q\right) \tag{1.16}$$

about which:

- The torque is composed of two terms, an electromagnetic torque generated as the result of interaction between the rotor flux and the stator current ($1.5p\psi_m i_q$), and a reluctance torque which is due to the difference of inductances in the d and q axes ($1.5p(L_d - L_q)i_d i_q$).
- For SPMSM, the values of direct- and quadrature-axis inductance are the same ($L_d = L_q = L_{ss}$), while for the IPMSM the q-axis inductnace is larger ($L_q > L_d$). Consequently, depending on the design and type of SM, the torque can be of electromagnetic origin only, reluctance origin only, or a combination of both.

1.1.2 Field-oriented Control of PMSM

In case of PMSM, the rotor flux (which is produced by the permanent magnets) is always aligned with the rotor position. Consequently, no flux observer or estimator is needed and the rotor flux angle is simply obtained by using a position sensor, which directly provides the position of the d-axis. This means that the available d-axis angle can be instantaneously used within the coordinate transformation for obtaining the dq-axis components of the current and voltage. Space phasor diagram of the SM is depicted in Fig. (1.4).

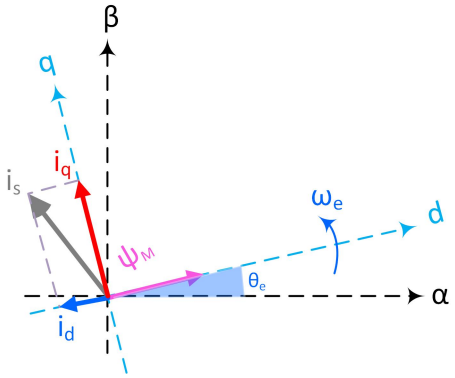

Figure 1.4: Space phasor illustration of the stator current and the rotor flux in the synchronous rotating reference frame (dq-axis).

As the result of this inherent feature and given eq. (1.14) and eq. (1.16), the magnetic flux can be controlled by the d-axis current and the electromagnetic torque is controlled by the q-axis current. It is to be mentioned that, in most of the conditions, the d-axis current is set to zero and only the q-axis current is controlled. The FOC comprises the instantaneous control of speed, torque, and currents as shown in Fig. (1.5). Both the speed and dq-frame currents are controlled through using PI regulators which have proved itself as an efficient control solution.

Looking at the dq-frame voltage equations in eq. (1.12) and eq. (1.13), the BEMF terms make the equations non-linear. If a PI regulator is to be used for the current regulation, the voltage equations must be linearized; therefore, the BEMF terms are fed forward to the control system (shown in Fig. (1.5) within the *Decoupling* box) which make [2]:

$$V_d = R_s i_d + L_d \frac{di_d}{dt} \tag{1.17}$$

$$V_q = R_s i_q + L_q \frac{di_q}{dt} \tag{1.18}$$

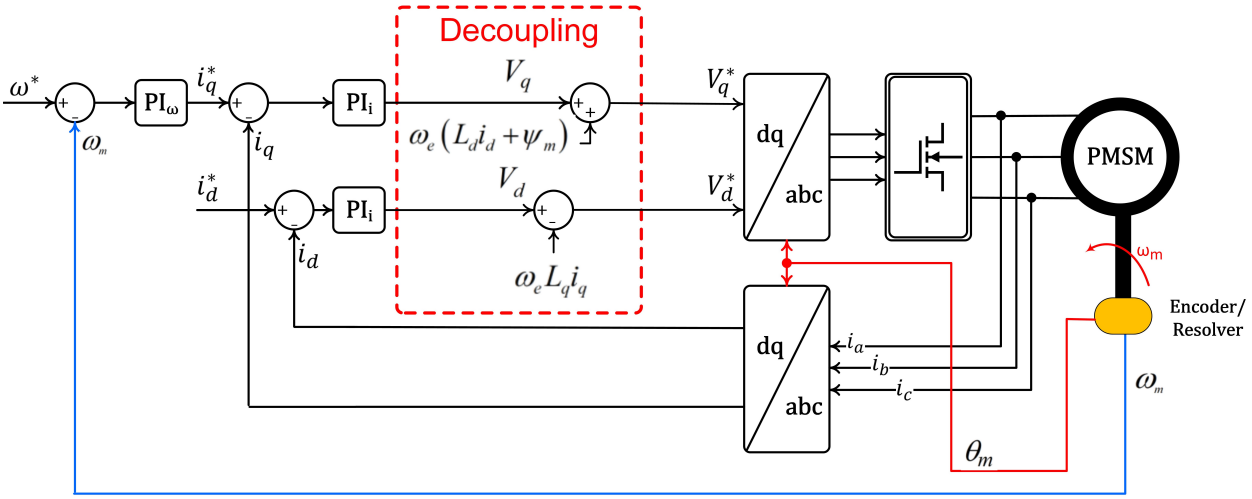

Figure 1.5: Block diagram of FOC.

1.1.2.1 Determination of the Angle Difference Among the Rotor and Stator Flux Vectors

In the FOC control of PMSM, the angle between the stator magnetic flux and rotor magnetic flux (created by the magnets) is crucial since it is directly used within the coordinate transformation blocks. At the first-time start-up, these two vectors are randomly placed and their respective angle (called commutation angle, CA) is unknown. Therefore, determination of the CA is of paramount importance. Determination of the CA can be done in two ways [5]:

- **Using DC Excitation**: in this method, the phase A is connected to the positive DC-link voltage and both the B and C phases are connected to the negative DC-link. As the result, a DC current is flowed within the windings and the stator current vector is aligned with the α-axis direction. Consequently, the rotor magnetic flux vector is forced to follow the stator current vector and the rotor moves and locks in a position which is the alignment position (the CA is equal to zero in this condition).

- **Using Current Controllers**: in this method, the coordinate transformation angle is kept constant at zero and the d-axis reference current is set to the machine nominal current and the q-axis reference current is set to zero. After reaching the steady-state, the stator curent vector is aligned with the α-axis and the rotor is forced to move until

it locks in a position which is alignment with the α-axis. Similar to the previous DC excitation method, the offset angle is equal to the CA.

Within the context of FOC, it is possible to apply two other auxiliary control strategies called 'maximum torque-per-ampere' and 'field-weakening', which are respectively reviewed within the Appendix A and Appendix B, at the end of this dissertation.

In this section, the fundamentals, models, and conventional control algorithms applicable to PMSM were detailed. In all of the control algorithms, and especially for the coordinate transformation, having an accurate knowledge about the rotor position was necessary. In the following section, the sensorless control of PMSM (in which the rotor position is estimated) is deeply investigated and the conventional and most recent algorithms are reviewed.

1.2 Sensorless Control of PMSM

PMSM has received extensive attention, as compared to its main competitor the induction machine, over the years in both industry and academic sectors, which is solely due to its reliability, efficient operation, wide speed range, and high torque density. In order to exhaust the maximum efficiency out of the PMSM, countless closed-loop algorithms are proposed, all of which are directly dependent upon the rotor position information which is usually obtained through using encoder or resolver.

However, these position sensors are bulky, expensive, and susceptible to conductive noise. Eliminating the position sensor, sensorless algorithms have garnered special attention [6], [7]. In all sensorless algorithms, the position information is estimated and fed to the coordinate transformation afterward. There are two methods of rotor position estimation, which depend on the speed range:

- **At medium to high speed**, the flux or BEMF models are used and the position information is estimated. This category of sensorless control is known as model-based method [8].
- **At standstill and low speed**, a high-frequency voltage/current signal is injected and the current/voltage response is used as a basis for the rotor position estimation. This category of sensorless control is known as saliency tracking-based method [9].

In the following part of this section, firstly the model-based sensorless control is reviewed. Afterward, the saliency tracking-based sensorless algorithms are reviewed. **As the proposed sensorless methods in this dissertation are fundamentally different from**

the conventional methods, a through review of the previous methods are provided in this section so as to provide the reader with a deep insight into the PMSM sensorless control.

1.2.1 Model-based Sensorless Control

As mentioned earlier, the model-based sensorless algorithms are suitable for medium to high speed regions. The first studies focused on the high-speed sensorless control, used open-loop strategies, which were highly sensitive to machine parameter mismatch and measurement errors [10–13]. In order to improve the poor dynamic performance of the open-loop methods, non-linear observer algorithms within a feedback loop were utilised [14–18]. These solutions were proposed to expand the system overall robustness and accelerating the estimation performance.

Two of the most utilised methods are the extended BEMF (EEMF) and flux models which contain the rotor position information and can be used for the purpose of estimation (replacing the position sensor). The EEMF model is firstly reviewd, then the flux model is provided. Additionally, the overall diagram of the model-based sensorless FOC algorithm is depicted in Fig. (1.6).

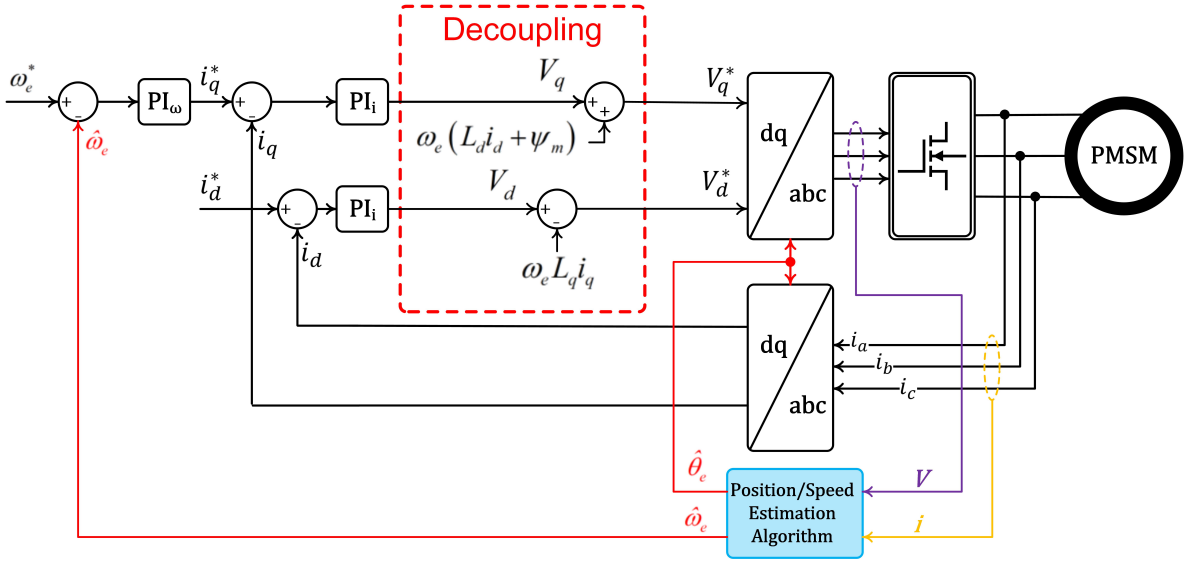

Figure 1.6: Block diagram of the model-based sensorless control of PMSM.

1.2.1.1 EEMF Model

The voltage equations in the synchronous dq-frame are given below, in the matrix form, for convenience.

$$\begin{bmatrix} V_d \\ V_q \end{bmatrix} = \begin{bmatrix} R_s + \rho L_d & -\omega_e L_q \\ \omega_e L_d & R_s + \rho L_q \end{bmatrix} \begin{bmatrix} i_d \\ i_q \end{bmatrix} + \begin{bmatrix} 0 \\ \omega_e \psi_m \end{bmatrix} \tag{1.19}$$

where ρ is the differential operator. This equation can be written with a new notation as follows [19–21]:

$$\begin{bmatrix} V_d \\ V_q \end{bmatrix} = \begin{bmatrix} R_s + \rho L_d & -\omega_e L_q \\ \omega_e L_q & R_s + \rho L_q \end{bmatrix} \begin{bmatrix} i_d \\ i_q \end{bmatrix} + \begin{bmatrix} 0 \\ E \end{bmatrix} \tag{1.20}$$

where

$$E = \omega_e \left(\left(L_d - L_q \right) i_d + \psi_m \right) + \left(L_q - L_d \right) \rho i_q \tag{1.21}$$

As can be seen, this model does not contain rotor position information and therefore cannot be used for the purpose of estimation. To approach this problem, eq. (1.20) is transformed to a new estimated rotating reference frame ($\gamma\delta$-frame), which is lagging the synchronous reference frame by the angle of $\theta_{diff} = \theta_e - \hat{\theta}_e$, in which the estimated position is denoted by $\hat{\theta}_e$.

$$\begin{bmatrix} V_\gamma \\ V_\delta \end{bmatrix} = \begin{bmatrix} R_s + \rho L_d & -\omega_e L_q \\ \omega_e L_q & R_s + \rho L_d \end{bmatrix} \begin{bmatrix} i_\gamma \\ i_\delta \end{bmatrix} + \begin{bmatrix} e_\gamma \\ e_\delta \end{bmatrix} \tag{1.22}$$

and

$$\begin{bmatrix} e_\gamma \\ e_\delta \end{bmatrix} = E \begin{bmatrix} -\sin\left(\theta_{diff}\right) \\ \cos\left(\theta_{diff}\right) \end{bmatrix} + \left(\hat{\omega}_e - \omega_e \right) L_d \begin{bmatrix} -i_\gamma \\ i_\delta \end{bmatrix} \tag{1.23}$$

Equation (1.23) is the EEMF model within which $\hat{\omega}_e$ represents the estimated angular frequency.

1.2.1.2 Linear Flux Model

Considering the transformation of dq-frame voltages (shown in eq. (1.19)) into the stationary $\alpha\beta$-frame as [22]:

$$\begin{bmatrix} V_\alpha \\ V_\beta \end{bmatrix} = \begin{bmatrix} R_s + \rho L_q & 0 \\ 0 & R_s + \rho L_q \end{bmatrix} \begin{bmatrix} i_\alpha \\ i_\beta \end{bmatrix} + \rho \begin{bmatrix} \lambda_\alpha \\ \lambda_\beta \end{bmatrix} \tag{1.24}$$

$$\begin{bmatrix} \lambda_\alpha \\ \lambda_\beta \end{bmatrix} = \left(\left(L_d - L_q \right) i_d + \psi_m \right) \begin{bmatrix} \cos\left(\theta_{diff}\right) \\ \sin\left(\theta_{diff}\right) \end{bmatrix} \tag{1.25}$$

Equation (1.25) represents the linear flux model of PMSM in the stationary reference frame which can be used for the estimation of rotor position information.

In order for the EEMF and/or flux models to be used for the sensorless algorithm, their actual values must be estimated through using observers, which is discussed in the following part.

In eq. (1.23) and eq. (1.25), a pair of orthogonal position-dependent components is appeared which is directly used for the estimation of rotor position information. The same notion is applicable to the proposed acoustic noise-based sensorless methods in this dissertation, detailed in Chapter 3.

1.2.1.3 Observer Design for the Model-based Sensorless Control

In order for the EEMF (or linear flux) models to be estimated, it is necessary to rewrite the associated models in state-space notation, as linear observable equations, as follows [23].

$$\begin{cases} \frac{d}{dt}\mathbf{x} = \mathbf{A}\mathbf{x} + \mathbf{B}\mathbf{u} \\ \mathbf{y} = \mathbf{C}\mathbf{x} \end{cases} \tag{1.26}$$

where

- $\mathbf{x}$ denotes the system state variable
- $\mathbf{u}$ is the voltage vector acting as the system input
- $\mathbf{y}$ is the system output
- $\mathbf{A}$, $\mathbf{B}$, and $\mathbf{C}$ are respectively constant coefficients.

Given each of the models, the variables accept different forms as follows [8].

- **EEMF Model**

$$\mathbf{x} = \begin{bmatrix} \mathbf{i} \\ \mathbf{e} \end{bmatrix} \quad \mathbf{A} = \begin{bmatrix} -\mathbf{I}\frac{R_s}{L_d} + \mathbf{J}\omega_e\frac{L_d - L_q}{L_d} & -\frac{\mathbf{I}}{L_d} \\ \mathbf{0} & \mathbf{J}\omega_e \end{bmatrix}$$
$$\mathbf{B} = \begin{bmatrix} \frac{\mathbf{I}}{L_d} \\ \mathbf{0} \end{bmatrix} \qquad \mathbf{C} = \begin{bmatrix} \mathbf{I} & \mathbf{0} \end{bmatrix} \tag{1.27}$$

where $\mathbf{i}$ and $\mathbf{e}$ are respectively the current and EEMF vectors and also:

$$\mathbf{I} = \begin{bmatrix} 1 & 0 \\ 0 & 1 \end{bmatrix} \quad \mathbf{J} = \begin{bmatrix} 0 & -1 \\ 1 & 0 \end{bmatrix} \quad \mathbf{0} = \begin{bmatrix} 0 & 0 \\ 0 & 0 \end{bmatrix} \tag{1.28}$$

- **Linear Flux Model** [24]

$$\begin{aligned} \mathbf{x} &= \begin{bmatrix} \mathbf{i} \\ \lambda \end{bmatrix} \quad \mathbf{A} = \begin{bmatrix} -\mathbf{I}\frac{R_s}{L_q} & -\frac{\mathbf{J}}{L_q} \\ \mathbf{0} & \mathbf{J}\omega_e \end{bmatrix} \\ \mathbf{B} &= \begin{bmatrix} \frac{\mathbf{I}}{L_q} \\ \mathbf{0} \end{bmatrix} \qquad \mathbf{C} = \begin{bmatrix} \mathbf{I} & \mathbf{0} \end{bmatrix} \end{aligned} \tag{1.29}$$

where λ is the vector of magnetic flux.

The linear observable PMSM model provided in eq. (1.26) can be approached by the well-known classical control approaches. In order to estimate the EEMF/linear flux, appropriate observer design should be adopted. Given the available methods and excluding the open-loop ones which are severely unreliable, two powerful observer designs stand out. The first one is to use an observer with the same order as the system, known as the '*full-order observer*', which has a complex parameter design procedure [25]. In order to eliminate such design sophistication, the *disturbance observer-based* techniques are the alternative solution [26].

1.2.1.3.1 Disturbance Observer-based Estimation Method

Using the stator current equations of PMSM, the disturbance observer can be developed as [8]:

$$\frac{d}{dt}\hat{\mathbf{i}} = \mathbf{P}\left(\mathbf{u}, \mathbf{x}, t\right) + \mathbf{O} \tag{1.30}$$

where $\mathbf{P}\left(\mathbf{u}, \mathbf{x}, t\right)$ represents the perturbation term depending on the model of PMSM, and $\mathbf{O}$ is the observed disturbance by which the EEMF vector is estimated. The condition for the accurate estimation of EEMF is that the observed current converges to its actual value. The simplest form of the disturbance-based observer is linear diturbance observer (LDO), in which the observed disturbance is designed in a linear feedback manner to facilitate the analysis procedure [27–29] shown in Fig. (1.7).

One of the biggest disadvantages of LDO is that its operation alters in high operating speeds. Therefore and to approach this shortcoming, sliding mode observer (SMO) has been used altenrnatively, which can cover almost the entire speed range [30–35]. The easy-to-

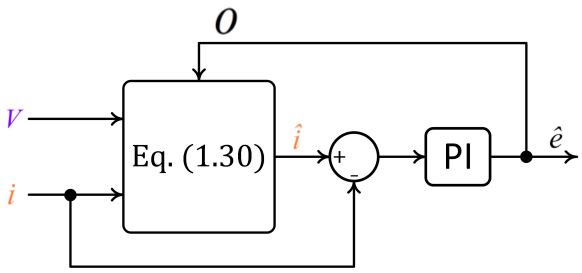

Figure 1.7: Block diagram of the linear disturbance observer.

implement structure of the SMO has made it one of the most widespread observers in the model-based PMSM sensorless control. On the other end of the scale, the observed EEMF contains excessive noise, known as the chattering phenomenon, which makes the use of an output low-pass filter essential [8]. In order to alleviate the chattering phenomenon and improve the EEMF estimation, an alternative SMO structure known as the super-twisting SMO is proposed and applied in [36–41].

1.2.1.3.2 Full-order Observer-based Estimation Method

As mentioned earlier, the complete PMSM model can be used with the addition of a feedback path to implement a full-order observer shown in Fig. (1.8). Within this observer structure, the EEMF acts as a state (not a disturbance), which eliminates the need for a high bandwidth design [8],[42]. The structure of a full-order observer, using the full model of PMSM, is given below

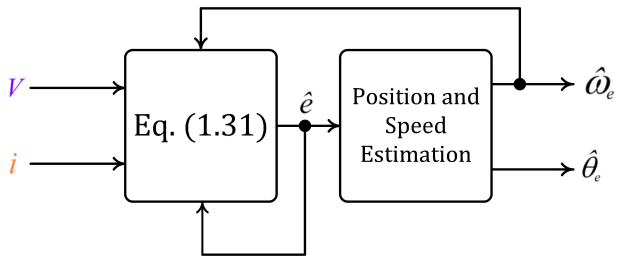

Figure 1.8: Block diagram of the full-order observer.

$$\begin{cases} \frac{d}{dt}\hat{\mathbf{x}} = \mathbf{A}\hat{\mathbf{x}} + \mathbf{B}\mathbf{u} + \mathbf{H}\left(\hat{\mathbf{y}} - \mathbf{y}\right) \\ \hat{\mathbf{y}} = \mathbf{C}\hat{\mathbf{x}} \end{cases} \tag{1.31}$$

where $\mathbf{H}$ is the feedback gain matrix. The full-order EEMF observer can be obtained in both the stationary and rotating reference frames, which are equivalent [43–47].

The full-order observer methodology requires designing of the gains, which is subject to

predefined conditions. On the contrary, the extended Kalman filter (EKF) is deemed as an optimum method by which the feedback gains are automatically calculated. As the result of this inherent characteristic, the EKF has become the estimation touchstone for nonlinear systems. Its application in model-based PMSM sensorless control is widely investigated in [48–54].

1.2.1.3.3 Position and Speed Estimation Algorithm

After estimation of the EEMF, through the disturbance observer or full-order observer, the position and speed of the rotor must be extracted (estimated) as they are key to the FOC algorithm. Given the fact that the estimated EEMF (or linear flux) is composed of two orthogonal waveforms, there are usually three main position estimation algorithms available within the literature, described in the following.

- **Trigonometric Function**

  In the first algorithm, a trigonometric function (usually an inverse tangent function) is used to directly estimate the position. The speed is obtained as the derivative of the estimated position therefore. Since the speed is obtained through a derivative procedure, the use of a low-pass filter (LPF) is indispensable which strengthen the estimation against unwanted noise [37],[38],[40].

- **Phase-Locked Loop (PLL)**

  The second position estimation method is the use of phase-locked loop (PLL) [30], [31], [55], [56]. PLL is a nonlinear feedback-based observer, in which the estimated speed and position are internal variables. Due to its simple design, PLL is one the widely-used estimation methods not only in PMSM sensorless control, but also in power system studies. The conventional PLL is a general second-order system, yet this second-order position observer outputs either a steady-state value or a cumulative value in the estimation error, when the input frequency is linearly changing. A revised version of the conventional PLL, taking into account the applied torque and real rotor dynamics, can also used, known as the Luenberger observer [57, 58].

  In order to make the estimation robuster against the input signal frequency variations, it is possible to use a type-III observer, which enables the user to have a greater control over the loop filter design and its frequency-domain behaviour [59]. The type-III observer can repress the estimation error, however, it is still susceptible to nonlinear

variations of the input signals frequency (nonlinear profile of the acceleration). As the result, an improved PLL observer with a compensation module is proposed in [60]. This observer utilizes a dynamic compensation block, which transforms the observer to a type-IV system, and enables it to better cope with the high-order input accelerations.

It is to be mentioned that the higher the PLL order, the more difficult the tuning will be. Moreover, the pole placement becomes increasingly important, since it can directly impact the overall speed-loop stability.

- **Adaptive Observer**

  Adaptive approach is an alternative solution for estimation of the rotor speed and position [32],[61]. In such observer structure, an adjustable model coupled with a gradient descendent algorithm is used in order to track the phase and frequency of the estimated EEMF.

1.2.1.3.4 Estimation Using Artificial Neural Network

The use of artificial neural network (ANN) for implementation of sensorless control, especially for the purpose of EEMF estimation, has also been investigated in the literature. ANN is usually used for prediction, model recognition, and nonlinear function estimation [62].

The back propagation-based ANN usually suffer from long learning speed and sluggish convergence rate, which is not at all suitable for sensorless control. Therefore, a new method with weights as adjustable functions is proposed in [62], which enhances the estimation performance and reduce the system complexity. A PMSM sensorless control based on radial basis function (RBF) ANN is proposed in [63].

Considering the nonlinear mathematical model of PMSM in the stationary frame, Lyapanov theory is used to design an ANN-based nonlinear adpaptive observer [64]. Flux spatial harmonics and inverter nonlinearities induce the fifth and seventh harmonics within the EMF waveforms. To this end, an adaptive training control-based filter is combined with an SMO through which the EMF harmonics are eliminated and the estimation performance is enhanced [65]. The adaptive filter uses the steepest descent algorithm for automatic adjustment of its parameters.

Integration of EKF and artificial neural network learning models for the sake of sensorless control of SynRM is investigated in [66]. Using a custom radial basis neural network, a precise analytical model describing the nonlinear current-flux relationships is obtained. Instead of using the detailed dynamic model of SynRM, posing a computational burden to the digital

processor, a new hybrid model is proposed which well integrates with the EKF structure and can be used even for low-end applications.

1.2.1.3.5 Estimation Performance Improvement

- **DC Offset Elimination**

  Regarding the EEMF-based sensorless control, measured values of the *dq*-frame voltages are included within the observer model, which can contain DC offset in practice. This DC offset culminates in an offset or a distortion in the estimated rotor position, and the performance is therefore degraded. The impact of such DC offset on the PLL estimation is investigated in [67] and to eliminate this DC error, a dual synchronous coordinate conversion compensation method is proposed. In this method, the error DC offset is estimated and the compensation is realised bu using a proportional-integral controller.

- **Estimation Harmonics Elimination**

  The sensorless performance is highly dependent upon the quality of EEMF/linear flux waveforms. Therefore, if there is any harmonics within these waveforms, the estimated rotor position would be negatively impacted. In order to tackle this problem, a hybrid filtering stage-based PLL is proposed by which the PLL estimation is improved [68]. In this method, the hybrid filtering stage is built by integration of band-pass filters and moving average windows tuned at each specific frequency.

  Sensorless performance of switched-flux PMSM (SFPM), having double-layer and single-layer windings, is investigated in [69]. It is shown that, depending on the winding type, the EMF can be of asymmetrical shape, nonsinusoidal shape, or sinusoidal shape. For asymmetric and nonsinusoidal EMF waveforms, due to the existance of extra harmonics ,the sensorless performance is directly influenced. In order to minimize this negative impact, an EMF harmonic compensation algorithm is proposed, which is not dependent on the machine parameters. In IPMSM, nonsinusoidal distribution of the rotor flux or the slot harmonics can be problematic in linear flux-based sensorless controls. In this case, the conventional observer in the *dq*-frame is unstable for low rotor speeds. In order to improve the performance, the rotor flux in the stationary-frame is considered and the flux harmonics are considered as the disturbances to the control system [70].

- **Improved Observers**

  The traditional linear extended state observer (LESO) cannot provide precise estimation in times of fast-paced EEMF dynamics, like in high speeds or big step changes within the reference speed, which has limited its application. An enhanced LESO, comprising a pure integral and high-frequency sinusoidal disturbance estimator, is proposed so as to extend the application scope of LESO [71]. The high-frequency changes of EEMF is estimated by adding the high-frequency sinusoidal disturbance observer to overall disturbance observer loop. In order to improve the dynamic performance of the conventional EEMF-based sensorless methods, an extended state observer is designed which is based on the differential term of the position estimation error [72]. As the result, rapid and precise estimation of the rotor position and load disturbance is made possible.

  A model-based PMSM sensorless control, based on a new estimation method for the position and speed error is proposed in [73]. The actual speed within the voltage equations is decomposed into the estimated and error terms, by which the error within the estimated position and speed are extracted. Using this estimation methodology has resulted in elimination of the speed error in steady-state operating points.

The model-based sensorless algorithms are now mature enough and extensively applied to industrial drives. However, they fail to operate at standstill and low speed regions which is solely ascribed to the poor signal-to-noise ratio (SNR) of EEMF/linear flux, caused by model uncertainty, inverter nonlinearity, etc. To solve this issue and extend the operating region of the sensorless algorithms, to standstill and low-speed regions, the saliency (tracking)-based methods are introduced, which are extensively discussed upon within the following part.

1.2.2 Saliency Tracking-based Sensorless Control

The saliency tracking-based methods are categorized into two subcategories [9]:

- **Signal injection-based methods**, in which a high-frequency injected (HFI) signal is superimposed (upon the fundamental excitation) and the machine response (containing the rotor position information) is investigated. The HFI can be placed within either the estimated dq-frame or the $\alpha\beta$-frame as shown in Fig. (1.9).

- **Fundamental pulsewidth modulation (PWM) excitation (FPE)-based methods**, in which the HFI is eliminated and the rotor position information is obtained from

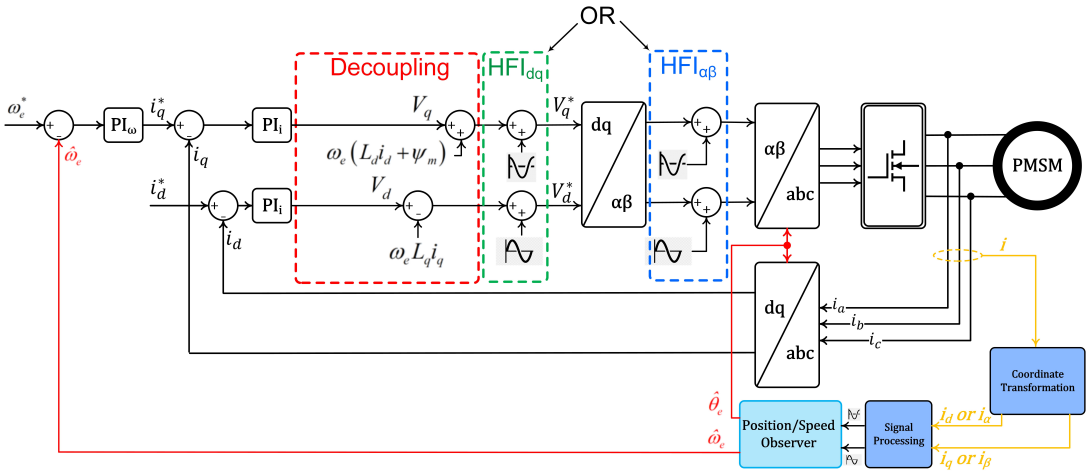

Figure 1.9: Block diagram of the saliency tracking-based sensorless control of PMSM.

the PWM signals.

1.2.2.1 Signal Injection-based Methods

This method is adopted for obtaining the rotor position through tracking the saliency of the machine [74]. Furthermore, the torque can be estimated by means of using HFI [75].

The HFI can be placed within either the rotating reference frame or stationary frame. As the result, the HFI can be of rotating or pulsating types. Moreover, the pulsating type can also be of sinusoidal or square-wave shapes.

Given all sinusoidal HFI types, the injected signal frequency must be at least hundreds of times greater than the electrical fundamental frequency, while tens of times lower than the switching frequency (in order for the HFI signal to be generated with satisfactory resolution). Adhering to this important design guideline and within the low-speed region, the resistive voltage drop and EMF terms within the voltage equations can be safely neglected. As the result, the voltage equations, in both the stationary and synchronous reference frames, are obtained as follows.

$$\begin{bmatrix} V_{dh} \\ V_{qh} \end{bmatrix} = \begin{bmatrix} L_d & 0 \\ 0 & L_q \end{bmatrix} \cdot \frac{d}{dt} \begin{bmatrix} i_{dh} \\ i_{qh} \end{bmatrix} \tag{1.32}$$

$$\begin{bmatrix} V_{\alpha h} \\ V_{\beta h} \end{bmatrix} = \begin{bmatrix} \Sigma L + \Delta L \cos(2\theta_e) & \Delta L \sin(2\theta_e) \\ \Delta L \sin(2\theta_e) & \Sigma L - \Delta L \cos(2\theta_e) \end{bmatrix} \cdot \frac{d}{dt} \begin{bmatrix} i_{\alpha h} \\ i_{\beta h} \end{bmatrix} \tag{1.33}$$

where $\Delta L = 0.5(L_d - L_q)$, $\Sigma L = 0.5(L_d + L_q)$, and the subscript "$h$" denotes the HFI component.

1.2.2.1.1 Rotating Signal injection

In this method, a complex voltage vector is injected within the $\alpha\beta$-frame as:

$$V_{\alpha\beta h} = \begin{bmatrix} V_{\alpha h} \\ V_{\beta h} \end{bmatrix} = V_h \begin{bmatrix} \cos(\omega_h t) \\ \sin(\omega_h t) \end{bmatrix} \tag{1.34}$$

where V_h represents the magnitude and ω_h denotes the frequency of the injected voltage vector. Given the injected voltage, the rotor position can be extracted using the following methods.

- **Current Response Processing**

  Applying the rotating voltage vector, the $\alpha\beta$-frame current vector is obtained as:

$$\begin{bmatrix} i_{\alpha h} \\ i_{\beta h} \end{bmatrix} = \begin{bmatrix} I_{hp}\sin(\omega_h t) + I_{hn}\sin(-\omega_h t + 2\theta_e) \\ -I_{hp}\cos(\omega_h t) - I_{hn}\cos(-\omega_h t + 2\theta_e) \end{bmatrix} \tag{1.35}$$

  where I_{hp} and I_{hn} are respectively the current magnitudes of the positive and negative sequences. As can be noticed, the rotor position information is only included within the negative-sequence current components. Therefore, a synchronous-frame filter (or demodulation or coordinate transformation) is used and the currents are transformed to the HF rotating frame to be:

$$\begin{bmatrix} i_{d'h} \\ i_{q'h} \end{bmatrix} = \begin{bmatrix} I_{hp}\sin(2\omega_h t) + I_{hn}\sin(2\theta_e) \\ -I_{hp}\cos(2\omega_h t) - I_{hn}\cos(2\theta_e) \end{bmatrix} \tag{1.36}$$

  in which the subscripts d' and q' represent the HF rotating frame. In the following step, eq. (1.36) is passed through a low-pass filter in order to isolate the position-carrying components. Finally, a PLL or trigonometric function can be used to extract the position. These two steps are mathematically shown in eq. (1.37). This method, known as the negative-sequence current method, is extensively used in the literature [57, 76–83]. The block diagram of the signal processing is also illustrated in Fig. (1.10).

  Omitting the conventional LPF form the signal processing, the HF current ellipse is traced by curve fitting using least square (LS) algorithm [84]. By processing the

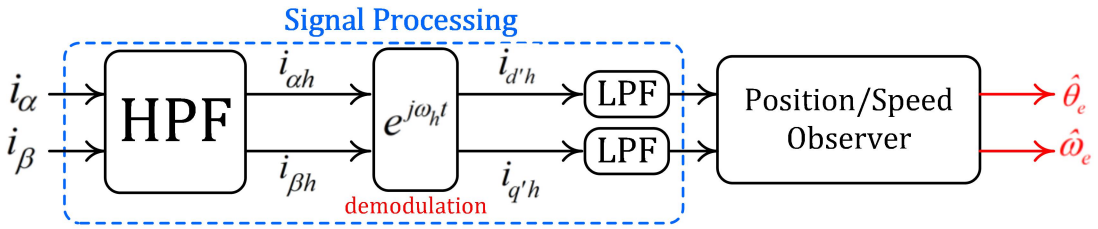

Figure 1.10: Overall block diagram of the signal processing for the rotating signal injection method.

coefficients of the fitted current ellipse equation, the rotor position is estimated.

$$\theta_e = 0.5 \cdot \tan^{-1}\left[-\frac{LPF\left\{i_{d'h}\right\}}{LPF\left\{i_{q'h}\right\}}\right] \tag{1.37}$$

- **Zero-sequence Voltage Processing**

  Additionally, the rotor position can be obtained through the zero-sequence voltage method [85–87]. Measuring the zero-sequence voltage entails having a balanced resitive load and access to the neutral point of the machine winding [9]. The value of the zero-sequence voltage is:

$$V_N \approx V_1 \cos\left(\omega_h t + 2\theta_e\right) \tag{1.38}$$

  with V_N being the zero-sequence voltage component and V_1 being its magnitude, which is a function of the machine inductance values and the magnitude of the HFI voltage. In order to extract the position information, the following signal processing is implemented.

$$\theta_e = 0.5 \cdot \tan^{-1}\left[\underbrace{LPF\left\{V_N \cdot \begin{bmatrix} 2\cos\left(\omega_h t\right) \\ 2\sin\left(\omega_h t\right) \end{bmatrix}\right\}}_{V_1 \begin{bmatrix} \cos\left(2\theta_e\right) \\ \sin\left(2\theta_e\right) \end{bmatrix}}\right] \tag{1.39}$$

1.2.2.1.2 Sinusoidal Pulsating Signal Injection

In this method, a pulsating HF voltage is injected in the estimated synchronous reference frame. Given the HFI voltage given in eq. (1.40), the HF current response within the

stationary reference frame is given in eq. (1.41).

$$V_{\hat{d}\hat{q}h} = \begin{bmatrix} V_{\hat{d}h} \\ V_{\hat{q}h} \end{bmatrix} = V_h \begin{bmatrix} \sin(\omega_h t) \\ 0 \end{bmatrix} \tag{1.40}$$

$$i_{\alpha\beta h} = \begin{bmatrix} i_{\alpha h} \\ i_{\beta h} \end{bmatrix} = \begin{bmatrix} \frac{\cos(\theta_e)\cos(\Delta\theta_e)}{L_d} + \frac{\sin(\theta_e)\sin(\Delta\theta_e)}{L_q} \\ \frac{\sin(\theta_e)\cos(\Delta\theta_e)}{L_d} - \frac{\cos(\theta_e)\sin(\Delta\theta_e)}{L_q} \end{bmatrix} \int V_{\hat{d}\hat{q}h} dt. \tag{1.41}$$

In the above equations, the subscript $\hat{d}\hat{q}$ represents the estimated synchronous reference frame and $\Delta\theta_e = \theta_e - \hat{\theta}_e$ is the difference among the actual and estimated position. In the steady-state condition, where $\Delta\theta_e \approx 0$, the current equation can be simplified as follows [9].

$$\begin{bmatrix} i_{\alpha h} \\ i_{\beta h} \end{bmatrix} = \frac{1}{L_d} \begin{bmatrix} \cos(\theta_e) \\ \sin(\theta_e) \end{bmatrix} \cdot \int V_{\hat{d}\hat{q}h} dt \tag{1.42}$$

As the result and in order to extract the rotor position information, as shown in Fig. (1.11), the following signal processign algorithm is adopted [9, 88–100].

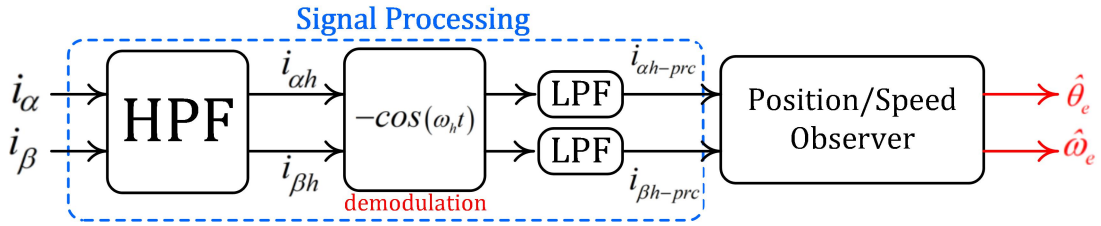

Figure 1.11: Overall block diagram of the signal processing for the sinusoidal-type pulsating signal injection method.

$$\begin{bmatrix} i_{\alpha h-prc.} \\ i_{\beta h-prc.} \end{bmatrix} = LPF \left\{ \frac{1}{L_d} \begin{bmatrix} \cos(\theta_e) \\ \sin(\theta_e) \end{bmatrix} \cdot \left(\underbrace{-\cos(\omega_h t)}_{demodulation} \cdot \int V_{\hat{d}\hat{q}h} dt \right) \right\} = I_{prc.} \begin{bmatrix} \cos(\theta_e) \\ \sin(\theta_e) \end{bmatrix} \tag{1.43}$$

$$\theta_e = \frac{1}{I_{prc.}} \tan^{-1} \left(\frac{\sin(\theta_e)}{\cos(\theta_e)} \right) \tag{1.44}$$

In the above equations, $i_{\alpha\beta h-prc.}$ denotes the processed current in the stationary reference frame and $I_{prc.}$ is a constant coefficient, which is a function of the machine inductances as well as the amplitude and frequency of the HFI voltage signal.

- **Signal Processing Improvement**

In the pulsating HFI methods, the control algorithm becomes unstable in high speeds and also a large error appears within the estimated position. Therefore, the impact of revolution speed and loading condition upon the estimation error need to be undergone a deep investigation. Given such consideration, a novel detection method for the amplitude of the HF current, which is independent of the revolution speed, is proposed [101]. Also, a position estimation error compensation method which considers the impact of speed and load is introduced.

There is an LPF in the signal processing algorithm of the conventional HF pulsating voltage injection methods, which can cause long convergence time and even limited system stability. To approach these shortcomings, a direct signal demodulation algorithm without any LPF is proposed, which enhances the system stability and dynamic performance [88]. Eliminating the LPF and band-pass filter from the signal processing, a new algorithm incorporating second-order generalized integrator (SOGI) serving as the harmonic extraction unit is proposed in [102]. This method improves the system dynamic performance and also the system parameters are more easily tuned, compared to the conventional LPF-based algorithms.

In addition to the conventional signal processing algorithm for the pulsating sinusoidal HFI method, it is possible to use both the positive and negative current sequences, which maximizes the salient inductance impact and inversely minimizes the impact of noise [103]. Using this method, the utilisation of the position-carrying current components in addition to the signal-to-noise ratio are accentuated.

1.2.2.1.3 Square-wave Pulsating Signal Injection

As mentioned earlier, the pulsating HFI signal can be a square-wave signal also. Since the waveform is a square-wave, the injection frequency can be mush higher than the sinusoidal case, which is advantageous to the separation of the HF signals and sideband harmonics. Moreover, it provides the drive with a quieter operation, since the frequency of the HFI signal can be placed high enough so as not be within the audible range [104–118].

Given a square-wave HFI voltage given in eq. (1.45), the HF current response in the estimated $\hat{d}\hat{q}$-frame is derived in eq. (1.46).

$$V_{\hat{d}\hat{q}h} = V_h \begin{cases} +1; kT_h \leqslant t < kT_h + {}^{T_h}\!/_2 \\ -1; kT_h + {}^{T_h}\!/_2 \leqslant t < k\left(T_h + 1\right) \end{cases} \tag{1.45}$$

$$\begin{bmatrix} i_{\hat{d}h} \\ i_{\hat{q}h} \end{bmatrix} = \frac{1}{L_d L_q} \begin{bmatrix} \Sigma L - \Delta L cos\left(2\Delta\theta_e\right) \\ -\Delta L sin\left(2\Delta\theta_e\right) \end{bmatrix} \cdot \int V_{\hat{d}\hat{q}h} dt \tag{1.46}$$

Looking at the $\hat{q}$-axis current, there is an alternating triangular waveform which contains the rotor position information. Through using a PI regulator, the term $\Delta\theta_e$ can be forced to zero, which is equivalent to the rotor position estimation. Alternatively, the rotor position estimation can be done by using a current axis with an offset angle of 45° [119].

- **Improved Methods**

  Given a square-wave HF signal injection method, the HF current magnitude is used for extraction of the rotor position information, but with a novel adaptive PLL updating its gain and badwidth with respect to the load changes [120, 121]. In order to enhance the dynamic performance of the conventional square-wave HFI methods, a method containing an adaptive complex-coefficient filter (ACCF) is proposed, which also eliminates the phase lag and therefore the need for compensation algorithms [122]. Also, the conventional PLL is replaced by a double PLL (DPLL), by which the estimation performance is improved and the position estimation error is reduced.

  Since the square-wave HFI implementation is done through the PWM modules, in practical conditions, the inverter deadtime, cross saturation, and secondary harmonics of the inductance should also be paid attention in order to improve the estimation performance [123–126]. The inverter nonlinearities, can be modeled by an HF resistance which is highly nonlinear, impacting the overall control performance [125].

  Applying HFI-based methods to non-salient PMSM is relatively difficult which is attributed to the low signal-to-noise ratio of the current response. In order to solve this problem, a square-wave HFI-based sensorless algorithm, using current oversampling, is proposed in [127].

  If a special HFI synchronized to the PWM carrier is used, the rotor position can be estimated [128]. The inverter output voltage error is highly affected by the amplitude and polarity of the sampled current, so a method for estimation of the instantaneous current value is proposed which paves the way for application of this method within the sensorless control.

  Dual three-phase PMSM has garnered increasing attention over the years, owing to the promising reliability characteristics. In order to further increase their potential, a sensorless control algorithm, utilizing square-wave HF signal injection, is proposed for

these machines [129]. The HFI is implemented within the harmonic subspace, which is decoupled from the torque subspace, resulting in torque ripple suppression and ease of signal separation.

- **Random Pulse Injection-based Methods**

  In order to lower the acoustic noise level of the HFI-based methods, a random pulse sequence (HFPVI-RPS) algorithm is proposed by which a random voltage pulse, with random width and amplitude, is used which spreads the spectral density of the current harmonics and pushes them to higher frequency zones [130, 131]. In order to have an HFI-based sensorless control with reduced acoustic noise level, the injection is done at the switching frequency while a special q-axis injection is utilised by which the torque ripple is also cancelled [132].

1.2.2.2 Fundamental PWM Excitation-based Methods

Although the HF signal injection-based methods are effective in the rotor position estimation at the standstill and low-speed operating conditions, existance of an extra injected signal coupled with observers are necessary for the method implementation. Consequently, the FPE-based methods, simplifying the overall algorithm, are proposed [9]. A rotor position extraction method which relies upon the carrier-frequency component signal and utilizes two reference frames is proposed [133]. The FPE-based methods, generally, can be categorized into three branches as follows.

1.2.2.2.1 Indirect Flux Detection by Online Reactance Measurement (INFORM) Method

This method was firstly proposed in [134]. Voltage vectors are applied in different directions and the induced current response is analysed, which makes this method a simple and easy-to-accomplish algorithm. Three cycles with a single current derivative measurement per cycle are enough to showcase the effectiveness of this method [9].

Given a set of injected voltage signals as:

$$V_{\alpha\beta-pulse} = V_h \cdot e^{jk.2\pi/3} \tag{1.47}$$

the induced current derivative is obtained as [9]:

$$\frac{d}{dt} i_{\alpha\beta-pulse} = \frac{V_{\alpha\beta-pulse}}{\Sigma L - \Delta L} \cdot \left[\Sigma L - \Delta L \cdot e^{j2\left(\theta_e - jk\frac{2\pi}{3}\right)}\right] \tag{1.48}$$

with $k = 0, 1, 2$ reflecting the injection in a, b, or c axes accordingly. The original INFORM algorithm suffers from current ripples, so modified versions are proposed to reduce the switching loss and extra harmonics [135, 136]. In order to further reduce the current distortion and required time for the algorithm execution, a new method is proposed in [137]. By interrupting the PWM pattern for a given time interval, it is possible to apply various voltage space phasors, which merely require the DC-link measurement [138].

1.2.2.2.2 Zero-sequence Current Derivatives (ZSCD) Measurements Method

In this method, the test voltage vectors are injected inside the machine, and induced zero-sequence current derivatives (dependent on the position-carrying dq-frame inductances) are obtained [139–145]. The derivative of the zero-sequence currents can be measured by using Rogowski coil and the rotor position is extracted [9]. Although the ZSCD method is simple and providing the sensorless operation with high efficiency, access to the neutral point of the machine windings is necessary, which makes this method not available for every industrial drive. Additionally, it is proved that the neutral-point voltage (if accessible) also carries the rotor position information even at standstill, without the need for any extra HF signal injection, which is also applicable to non-salient PM machines [146].

1.2.2.2.3 Zero-voltage Vector Injection Method

By comparing the acoustic noise and torque ripple of the HFI-based and FPE-based methods, the zero-voltage vector injection method is proposed [147–151]. The derivation calculations of current and zero voltage vectors are combined in this method, which is especially dedicated to standstill and low-speed operating zones. Comparing with the typical PWM switching patern, the amount of current ripple in this method is higher, yet the switching frequency is kept constant which can be helpful in terms of acoustic noise alleviation. Moreover, the acoustic noise associated with injecting the zero voltage vectors can be eliminated with the method proposed in [147].

1.2.2.3 Initial Position and Polarity Detection

The polariy of the stator flux and therefore the sign of the estimated position cannot be detected in the HF pulsating signal injection-based sensorless algorithms, which is a big issue with this family of sensorless algorithms. The HF model of PMSM shows that the saliency experiences two periods in each electrical cycle, so incorrect polarity leads to 180° error within the estimated electrical position.

1.2.2.3.1 Current-based Algorithm

The permanent magnets used within the structure of the PM machines, make the magnetization characteristics nonlinear. It is shown that the d-axis current value increases if the applied voltage vector is further aligned toward the north pole of the rotor (similarly, for the south pole alignment, the d-axis current possesses lower value) [152].

The cavities dedictaed to magnet placements in PM machines make a tangible difference in the values of the direct- and quadrature-axis inductances. By means of this spatial saliency, which is based on the rotor position, it is possible to identify the orientation of the direct- and quadrature-axis even at standstill condition, subject to the use of an HF rotating/pulsating voltage vector. The polarity of the magnets can be identified by using the impact of magnetic saturation on the saliency image [153].

Prior to the position estimation, a voltage pulse is injected within the arbitrary d-axis. Depending on the orientation of the d-axis toward the north or south pole, the current response would be different [154]. Given the hysteresis curve of the core, it is proved that the second-order harmonic of the d-axis current response carries rotor position information. If the d-axis is oriented toward the north pole, the current 2^{nd} harmonic has a positive average value, while there is a negative average value if the axis is oriented inversely [155].

In most of the magnet polarity detection algorithms, a train of short pulses are used, while the HF signal injection must be deactivated when the these pulses are being applied. To this end, a method relying on the amplitude variation of the d-axis current is proposed in [88]. This method detects the magnet polarity in three simple steps: first, the reference d-axis current is set to a tiny portion of the nominal value (with the reference q-axis current being always set to zero), and the HF current amplitude is obtained (through using a Recursive Discrete Fourier Transformation (RDFT) algorithm) and stored as the first value. Second, the reference d-axis current is made a couple of times higher and the new amplitude is stored as the second value. Finally, the two stored amplitudes are compared; if the first value is larger, the estimated rotor position is opposite to the actual value. Inversely, the estimated rotor position is in correct alignment only if the second stored current magnitude is larger.

1.2.2.3.2 Vibration-based Algorithm

Almost all of the conventional polarity detection algorithms are based on calculating the stator voltage equations. These methods have poor adaptability to PM machines having various saliency characteristics. Moreover, high sensitivity to the variations of electrical parameters is another stark weakpoint of these methods. Incorporating the dynamic electromechanical

equations of the PMSM, the surface vibration response of the machine, subject to dq-axis HF excitations, is used as an asset for detecting the initial magnetic polarity [156].

1.2.2.4 Performance Comparison of HFI-based Methods

In the rotating-vector injection method, a balanced three-phase HF voltage/current signal is injected within the stationary reference frame. On the other hand, an HF voltage/current signal (either a single or vector) is injected within the estimated synchronous reference frame in the pulsating signal injection method. The HF voltage injection is usually preferred, since the resulting current is processed and the rotor position is estimated straightforwardly [157].

The performance of pulsating and rotating HF signal injection methods are compared for an internal PM machine and an inset PM machine in [97]. The HFI methods are implemented in various working conditions for both PM machines, and it is observed that there is no conspicuous difference between their performance. As the result, both methods can be used interchangeably.

Moreover, at heavy loading conditions (requiring high q-axis current), the estimation error signal becomes dangerously small and therefore the estimation process is interrupted. However, the inset-type PMSM, compared to IPMSM, has higher threshold which means that it provides estimation for higher current level.

Given the nonlinearties of the whole system - including the motor, inverter, PWM, etc. - the performance of rotating and pulsating HFI methods are investigated in [124, 158]. Position estimation error expressions - taking into account the impacts of cross-saturation, multiple saliency, and finite resistance - are analytically obtained for both pulsating and rotational HFI methods. Additionally, it is proved that both methods showcase a similar tracking performance. Besides, the pulsating HFI method is shown to be less prone to dead-time effects. Finally, pulsating HFI generates more localized flux linkage distribution with lower intensity.

1.2.2.5 The Impact of System Nonlinearities on the Sensorless Performance

Magnetic saturation causes a cross-coupling effect between the d- and q-axis inductances when HFI methods are applied; therefore, a detailed investigation and modeling of the cross-saturation effect is conducted in [159]. Unless this phenomenon is taken into consideration in the machine model, the position estimation faces undesired error. An improved model of the brushless AC machine, taking into account the cross-coupling phenomenon on the dynamic

inductances is proposed in [160]. Moreover, by using a simple error correction method, this negative position estimation error is compensated. A detailed model with consideration of multiple saliencies enables us to not only estimate the rotor-related information, but also the magnet flux angle [161]. Invesigation of the operating points during which the sensorless control can be successfully commissioned, taking into account the saturation phenomenon and applicability to different machines, is presented in [162].

In HFI-based methods and by using two ancillary angles of the injected voltage and observed current (in addition to the classical rotor position), the dynamic performance of a highly saturated PMSM can be improved [163]. Given the sign of the derivative of the EMF absolute value within the stationary frame, it is possible to design an online tuning method for the angle of the injected HFI in order to reduce the position estimation error resulted from saturation and other nonlinear phenomena[164].

1.2.2.6 Other Studies

The majority of the saliency tracking-based sensorless algorithms are based on using an HFI signal, yet an HFI-independent method, without the need for a priori knowledge of the machine parameters and minimum tuning effort is proposed [165]. The machine parameters are identified in an online manner, owing to the last three sampled instances used within a finite control set model predictive current controller.

The sensorless performance for an electrically-excited synchronous machine fed by a load-commutated inverter, covering the entire speed range, is proposed in [166]. For the low-speed range, the rotor position estimation investigates the field current harmonics. On the other hand and for the high-speed region, an EMF-based position estimation method is proposed. In order to lower the stress while switching among the two estimation methods, a swift transition algorithm is also incorporated within the control algorithm. Moreover, a whole-speed-range sensorless control algorithm, using the voltage ripples obtained from an adaptive finite-control-set model predictive control (FCS-MPC), applicable to IPMSM is proposed in [167].

Stability of the overall sensorless control, which comprises the internal current loop, outer speed loop, and the position observer, is of paramount importance [168]. Appropriate placement of zeros and poles of each part of the system, i.e. proper design of the PI regulators with respect to the other system components, is a key criterion [169].

For a very special sensorless condition when the IPMSM machine is power-off and the speed and position are to be recorded, an ultra high-frequency (UHF) sinusoidal voltage is

injected and, given the RMS value of the injected signal with respect to the inherent machine saliency variation, the rotor position information is extracted [170].

1.2.3 Conclusion

In this section, the sensorless control of PMSM was extensively reviewed. First, the model-based methods, applicable to the medium-high speed range, were reviewed. Second, the saliency tracking-based methods, applicable to standstill and low-speed range, were extensively reviewed.

Almost all of the sensorless controls, were based on the electrical parameters of the machine. However, in this thesis, we want to show that it is well possible to use the output acoustic noise (or vibration) of the PMSM as a rich source for extraction of the rotor position information, alternatively.

As the result, in the following section, the fundamentals of the PMSM vibration/acoustic noise (especially that of electromagnetic origin) are extensively reviewed. Once the backgrounds had been established, the acoustic noise response of the machine, to specific HFI and PWM voltage methods, in addition to the proposed acoustic noise-based sensorless control will be respectively introduced in Chapter 2 and Chapter 3.

1.3 Acoustic Noise and Vibration Phenomena in PMSM

In this section, the fundamental concepts related to the vibration and resulting acoustic noise of PMSM are investigated, in a step-by-step manner. Among many reasons behind occurrence of vibration/acoustic noise, a special focus is placed upon the electromagnetic origin, since it is the base of our proposed methods in this thesis. The electromagnetic equations of the air-gap magnetic fields and radial forces are used as the ground for the calculations and methods provided in the next chapter; therefore, they are written in the most generalized format to be applicable to any PMSM.

As the electromagnetic origin of PMSM acoustic noise is the main focus of this section, the general format of the airgap magnetic fields is firstly reviewed. In the following step, the resulting generated forces within the airgap, which are applied to the mechanical structure of the stator, are provided since these are deemed the principal cause of the vibration occurrence [171]. Finally, the backgrounds related to the occurrence of vibration and resulting acoustic noise are deeply reviewed.

1.3.1 Air-gap Magnetic Field

Given the structure of a PMSM, the sum of the permanent magnet (PM) field and the armature-reaction (Arm) field constitutes the overall air-gap field, given a balanced three-phase current system defined below [172–175].

$$i_a = \sum_{i=1}^{\infty} I_i \cos\left(ip\omega_m t + \phi_i\right) \tag{1.49}$$

$$i_b = \sum_{i=1}^{\infty} I_i \cos\left(ip\omega_m t + \phi_i - {}^{2\pi}/_{3}\right) \tag{1.50}$$

$$i_c = \sum_{i=1}^{\infty} I_i \cos\left(ip\omega_m t + \phi_i + {}^{2\pi}/_{3}\right) \tag{1.51}$$

with

- I_i being the amplitude of the phase current i^{th} harmonic
- t being the instance of time
- ϕ_i being the phase of the current i^{th} harmonic.

For the sake of brevity, firstly the slotless model of PMSM is considered and the field equations are presented. In the following step, the field equations in the presence of stator slotting are presented.

1.3.1.1 Slotless Air-gap Field

Given a rounded slotless stator, magnets mounted on the rotor surface, and current sheets distributed around the inner surface of the stator, the radial and tangential components of the PM and Arm fields are obtained as follows [176]:

$$B_r^{PM}(r,\theta) = \sum_{j=1,3,5}^{\infty} b_r^{PM}(j,r).\cos\left(jp\left(\theta - \omega_m t\right)\right) \tag{1.52}$$

$$B_\theta^{PM}(r,\theta) = \sum_{j=1,3,5}^{\infty} b_\theta^{PM}(j,r).\sin\left(jp\left(\theta - \omega_m t\right)\right) \tag{1.53}$$

$$B_r^{Arm}(r,\theta) = \sum_{k=1}^{\infty}\sum_{i=1}^{\infty} b_r^{Arm}(r).\sin\left(k\theta \pm (ip\omega_m t + \phi_i)\right) \tag{1.54}$$

$$B_\theta^{Arm}(r,\theta) = \sum_{k=1}^{\infty}\sum_{i=1}^{\infty} b_\theta^{Arm}(r).\cos\left(k\theta \pm (ip\omega_m t + \phi_i)\right) \tag{1.55}$$

$$k \pm i = 3C, C \in \left\{\underbrace{0, \pm 1, \pm 2, \pm 4, \pm 5, \pm 7, \pm 8, ...}_{non-triplen}\right\} \tag{1.56}$$

with

- θ being the angular position around the stator periphery
- b_r^{PM}, b_θ^{PM}, b_r^{Arm}, and b_θ^{Arm} being constants depending upon the radius of analysis in the air-gap (r) and the number of spatial harmonics (j).

It is worth mentioning that in a PMSM, the phase current harmonics, (i), are of non-triplen order ($1, 5, 7, 11, 13, etc.$) [177].

1.3.1.2 Air-gap Field with Slotting Effect

Assuming a fictitious arc in the air-gap drawn within the polar coordinate system, the vector of magnetic field can be defined as follows.

$$\vec{B} = B_r + jB_\theta = \|B\| e^{j\varphi_B} \tag{1.57}$$

$$\|B\| = \sqrt{(B_r)^2 + (B_\theta)^2} \tag{1.58}$$

$$\varphi_B = \tan^{-1}\left({}^{B_\theta}/_{B_r}\right) \tag{1.59}$$

Applying a so-called conformal transformation to the magnetic field vector, the slotted stator model can be transformed into a slotless one through using a complex permeance model as defined below [176, 178]:

$$\vec{\lambda} = \lambda_\alpha - j\lambda_\beta \tag{1.60}$$

with

$$\lambda_\alpha = \lambda_{dc} + \sum_{n=1}^{\infty} \lambda_{\alpha n}.\cos(nN_s\theta) \tag{1.61}$$

$$\lambda_\beta = \sum_{n=1}^{\infty} \lambda_{\beta n}.\sin(nN_s\theta) \tag{1.62}$$

where

- λ_α and λ_β are real and imaginary components of the defined complex permeance
- λ_{dc}, $\lambda_{\alpha n}$, and $\lambda_{\beta n}$ are constant coefficients depending on the stator slots physical dimensions
- N_s denotes the number of slots.

Consequently, the magnetic field vector resulted from the stator slotted model is obtained as:

$$\vec{B}_s = (B_r + jB_\theta) \,.\, (\lambda_\alpha - j\lambda_\beta) = \underbrace{(B_r\lambda_\alpha + B_\theta\lambda_\beta)}_{B_{sr}} + j\,\underbrace{(B_\theta\lambda_\alpha - B_r\lambda_\beta)}_{B_{s\theta}} \tag{1.63}$$

in which B_{sr} and $B_{s\theta}$ respectively denote the radial and tangential field components. As the result, the radial and tangential components of the PM field can be obtained as follows.

$$B_{sr}^{PM}(r,\theta) = B_r^{PM}\lambda_\alpha + B_\theta^{PM}\lambda_B = \left[\sum_{j=1,3,5}^{\infty} b_r^{PM}(r,j) \,.\, \cos\left(jp\left(\theta - \omega_m t\right)\right)\right]$$
$$\left[\lambda_{dc} + \sum_{n=1}^{\infty} \lambda_{\alpha n} \,.\, \cos\left(nN_s\theta\right)\right] + \left[\sum_{j=1,3,5}^{\infty} b_\theta^{PM}(r,j) \,.\, \sin\left(jp\left(\theta - \omega_m t\right)\right)\right]\left[\sum_{n=1}^{\infty} \lambda_{\beta n} \,.\, \sin\left(nN_s\theta\right)\right]$$
$$\propto \sum_{j=1,3,5}^{\infty}\sum_{n=0}^{\infty} \cos\left(jp\left(\theta - \omega_m t\right)\right) \,.\, \cos\left(nN_s\theta\right) \tag{1.64}$$

$$B_{s\theta}^{PM}(r,\theta) = B_\theta^{PM}\lambda_\alpha - B_r^{PM}\lambda_\beta \propto \sum_{j=1,3,5}^{\infty}\sum_{n=0}^{\infty} \sin\left(jp\left(\theta - \omega_m t\right)\right) \,.\, \cos\left(nN_s\theta\right) \tag{1.65}$$

Similarly, the orthogonal components related to the armature reaction field are obtained as:

$$B_{sr}^{Arm}(r,\theta) = B_r^{Arm}\lambda_\alpha + B_\theta^{Arm}\lambda_\beta \propto \sum_{k=1}^{\infty}\sum_{i=1}^{\infty}\sum_{n=1}^{\infty} \sin\left(k\theta \pm \left(ip\omega_m t + \phi_i\right)\right) \,.\, \cos\left(nN_s\theta\right) \tag{1.66}$$

$$B_{s\theta}^{Arm}(r,\theta) = B_\theta^{Arm}\lambda_\alpha + B_r^{Arm}\lambda_\beta \propto \sum_{k=1}^{\infty}\sum_{i=1}^{\infty}\sum_{n=1}^{\infty} \cos\left(k\theta \pm \left(ip\omega_m t + \phi_i\right)\right) \,.\, \cos\left(nN_s\theta\right) \tag{1.67}$$

Consequently, the overall air-gap flux density, for either the slotless or slotted model, can be obtained as the separate sum of PM and armature-reaction fields. In addition, as shown in Fig. (1.12) and [176], the magnitude of the radial air-gap flux density is considerably greater than that of the tangential one (**simulation results are provided for a given PMSM in ALTAIR Flux software**). The figure compares the radial and tangential components of the flux density for two conditions of zero phase current (PM field only) and non-zero current (PM field + Arm field). Comparing the figures for zero and non-zero currents respectively shown by PM and PM+Arm, for either of the radial or tangential fluxes, the PM field possesses the highest contribution in the overall air-gap field. As the result, without losing the generality, the impact of the tangential fields can be conveniently disregarded. Given both

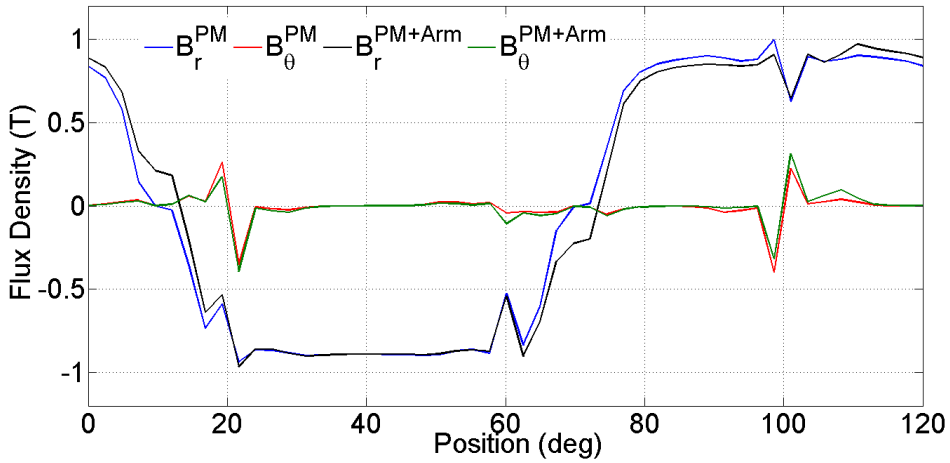

Figure 1.12: Radial and tangential air-gap flux density comparison.

the slotless and slotted stator models, the impact of rotor eccentricity, in which the rotor is not axially placed in the middle of the airgap resulting in a non-uniform airgap, is analytically investigated [179, 180]. The effect of eccentricity is modeled by using a perturbation method. It is shown that eccentricity makes a noticeable deviation within the field ditribution, and its impact is linearly related to the amount of eccentricity.

$$B_r^{PM+Arm} = B_r^{PM} + B_r^{Arm} \tag{1.68}$$

1.3.2 Air-gap Electromagnetic Force

Having obtained the air-gap fields, the radial and tangential components of the electromanetic force can be obtained using the Maxwell Stress Tensor as defined below, with the

vacuum permeability constant defined by μ_0, [181]:

$$F_r = \frac{B_r^2 + B_\theta^2}{2\mu_0} \approx \frac{B_r^2}{2\mu_0} \tag{1.69}$$

$$F_\theta = \frac{B_{sr}.B_{s\theta}}{\mu_0} \tag{1.70}$$

As the radial force, which is the principal reason for the occurrence of vibration and acoustic noise in electric machines, is orders of magnitude greater than the tangential force as shown in Fig. (1.13) and [181, 182], from this point onward, merely the radial force is taken into consideration.

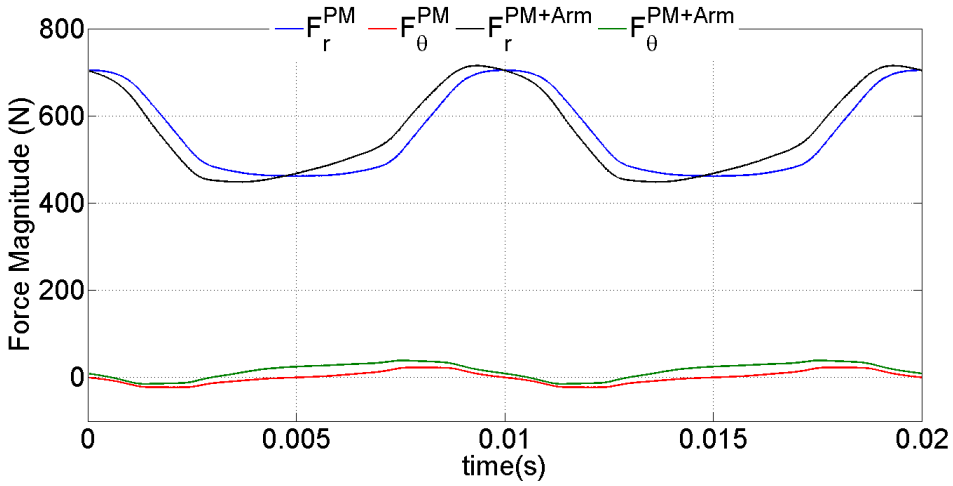

Figure 1.13: Radial and tangential air-gap force comparison.

It is proved that, in a condition with non-zero phase current, the impact of stator slotting on the radial forces is also negligible [176]. Consequently, the force equation can be simplified as shown in eq. (1.71). Since only the frequency components appeared in the radial forces are important in this study, the radial force equation can be approximated as eq. (1.72). Given that, the radial force comprises the self and mutual interactions between each PM and armature-reaction fields harmonic componets. To this end, the first, second, and third terms on the right side of eq. (1.72) respectively denote the PM self interaction, armature-reaction self interaction, and mutual interaction between the PM and armature-reaction. Therefore, knowing the exact frequency components appeared in the PM and armature-reaction fields

is enough for predicting the harmonics within the radial force.

$$F_r \approx \frac{\left(B_r^{PM}+B_r^{Arm}\right)^2}{2\mu_0} = \frac{\left(\sum\limits_{j=1,3,5}^{\infty} b_r^{PM}\cos\left(jp(\theta-\omega_m t)\right)+\sum\limits_{k=1}^{\infty}\sum\limits_{i=1}^{\infty} b_r^{Arm}\sin(k\theta\pm(ip\omega_m t+\phi_i))\right)^2}{2\mu_0} \quad (1.71)$$

$$\begin{aligned} F_r \propto & \sum_{j_1}^{\infty}\sum_{j_2}^{\infty} cos\left[\left(j_1 \pm j_2\right) p\left(\theta-\omega_m t\right)\right] + \\ & \sum_{k_1}^{\infty}\sum_{k_2}^{\infty}\sum_{i_1}^{\infty}\sum_{i_2}^{\infty} cos\left[\left(k_2 \mp k_1\right)\theta \pm \left(i_2 \mp i_1\right) p\omega_m t + \left(\phi_{i_1} \mp \phi_{i_2}\right)\right] + \\ & \sum_{j}^{\infty}\sum_{k}^{\infty}\sum_{i}^{\infty} sin\left[\left(k \pm jp\right)\theta \pm \left(i \mp j\right) p\omega_m t + \phi_i\right] \end{aligned} \quad (1.72)$$

Given different PMSM topologies with various pole/slot configurations, a comparative analysis regarding the frequency components in the fields and radial forces is carried out in [182]. In addition, in-depth study of the current harmonics impact upon the radial force, vibration, and acoustic noise frequency components is conducted in [183].

In conclusion, if the PM and armature-reaction fields are respectively with the arbitrary harmonic orders of i and j, the radial force harmonic orders are obtained as:

- $|i_1 \pm i_2|$ as the self contribution of PM field components.
- $|j_1 \pm j_2|$ as the self contribution of armature-reaction field components.
- $|i \pm j|$ as the mutual contribution of PM and armature-reaction fields components.

Having investigated the magnetic fields in frequency-domain, the specific harmonics within the radial forces are obtained. These forces are applied on the stator tooth tips, which are the initiator of the electromagnetic vibration. Therefore, the next part is dedicated to the vibration and acoustic noise of electic machines, including fundamentals, different origins, and methods of calculation.

1.3.3 Vibration and Acoustic Noise in Electric Machines

As far as technical definition concerns, *Vibration* is defined as a limited alternating movement of a particle (of an elastic structure or medium), when the equilibrium point is disturbed.

Sound is also technically defined as the transmitted vibration through an elastic structure, liquid, or gas when the frequency lies within the audible range of $20Hz$ to $20KHz$. A sound wave is generated as the result of energy transfer between the surface of a vibrating body and its surrounding medium. When the surrounding medium is air, the movement of each air particle is in a parallel direction with respect to the direction of the transfered energy (from the surface of the structure) [181].

The output vibration and acoustic noise of electric machines are always deemed a drawback and therefore having an acceptable level of vibration and acoustic noise, while operation, is an integral performance index. Vibration and acoustic noise in electric machines stem from three main origins namely electronic and electromagnetic, aerodynamic, and mechanical [184]. Figure (1.14) illustrates the various origins of acoustic noise and vibration in electric machines.

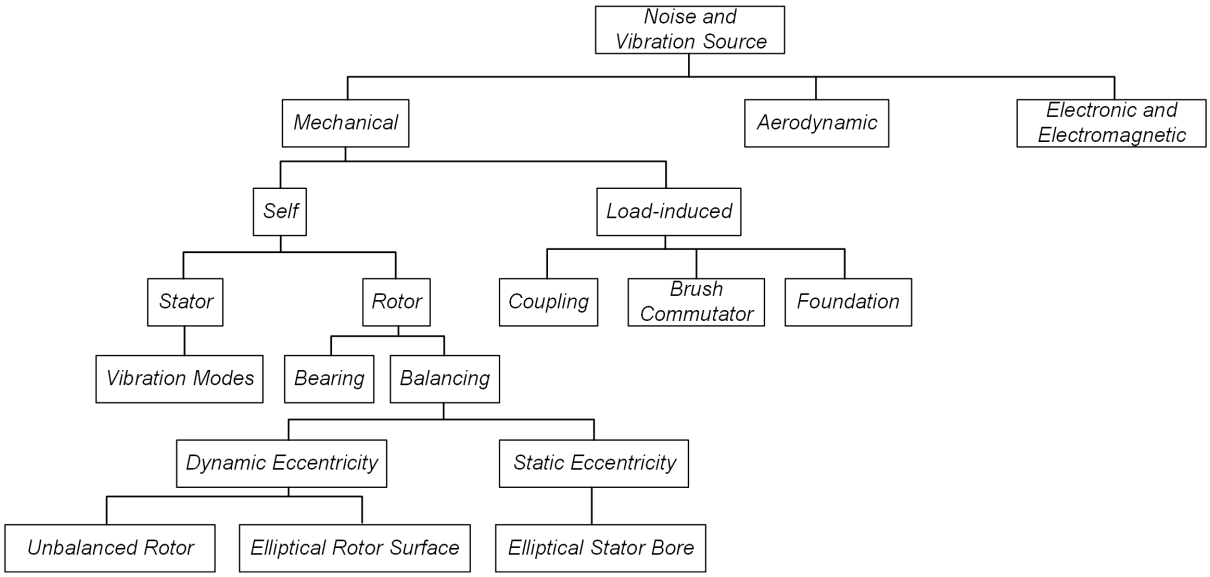

Figure 1.14: Origins of vibration and acoustic noise in electric machines.

- **Mechanical Origin**

  Compared to the other origins, the mechanical origin of the vibration and acoustic noise is eclectic and has the most diversity as shown in Fig. (1.14). Natural frequencies of stator and rotor are important since any harmonic excitation coinciding with those frequencies will lead to the resonance occurrence and therefore an abundant level of vibration and acoustic noise will be disseminated. Moreover, the bearing mounted at the end of rotor shaft adds up to the overall noise level. Balance of stator and rotor axes

is a key design parameter ensuring a homogenous air-gap; consequently, if there is any unbalance (i.e. eccentricity), the even field distribution is disturbed which culminates in uneven radial force distribution and extra vibration and acoustic noise.

In addition to the motor, the coupled load mechanical characteristics are of great importance, as any vibration on the load side is easily propagated to the motor through the coupling. Coupling, per se, is a complex mechanical structure comprising different moving components and connections; therefore, any imperfect connection or loose screw can lead to extra vibration and acoustic noise especially in high-speed revolutions [181].

The basement and foundation, on which the motor-load bench is mounted, must also be strictly fixed and signigicantly heavier than the whole test bench to make sure that there is no extra vibration induced to the system. In case of unappropriate weight ratio between the motor-load bench and the foundation, in specific speed ranges, the total structure experiences tremendous vibration, attributed to the resonance phenomenon.

- **Electronic and Electromagnetic Origin**

  Any parasitic effect related to high-order spatial and time harmonics in the current, magnetic fields, or MMF waveforms directly impacts the radial force harmonic content and results in additional vibration and noise; for instance high-order current harmonics, non-sinusoidal EMF, phase unbalance, and magnetic saturation. Additionally, any physical aspect influencing the magnetic fields, including eccentricity, stator or rotor skewing, slot openning, and electrical or mechanical faults, can also be considered as a source of vibration/acoustic noise [171, 181, 184].

- **Aerodynamic Origin**

  Considering integrated motor drives or electric vehicles having power-densed electric propulsion system, existence of an efficient thermal management system is essential; the coolant within the system can be liquid or natural air. In either case, a fan is placed responsible for maintaining a constant airflow which can produce high-pitch acoustic noise [181].

It is neccessary to mention that, in this thesis, we just focus on the **electromagnetic and electronic origins of the acoustic noise** in electric machines, since by a priori knowledge about the electromagnetic behaviour of the system and appropriate excitation, the electromagnetic fields and vibration/acoustic noise harmonics are directly predictable.

1.3.3.1 Vibration Fundamentals

The generated vibration and acoustic noise of the rotor/stator structure is the direct response to the applied excitations by the forces. As the result, if the frequency of the applied force is close to the natural frequencies of the structure and the order of the force harmonic component is the same as structure vibration mode, an abundant amount of vibration and acoustic noise, as the result of resonance, is generated [181].

Although it is possible to simply model the stator frame as a shell and derive analytical models for the low-order vibration modes prediction, the results will be erroneous for high-order modes and therefore utilization of more accurate models is indispensable. Due to the curvatures of the actual stator and rotor structures, the generated vibrations in the radial, tangential, and axial directions are coupled together meaning that excitation in only one of these directions might lead to the vibration in one or all of the directions. Consequently, accurate results can be obtained, provided that finite element modeling (FEM) is utilized [181].

In FEM, the stator and rotor geometries are devided into tiny segments called mesh; the higher the number of meshes, the higher the modelling fidelity and the more precise the results. Given a conveniently-precise meshed structure, the global equation of motion, given below, is solved and the natural frequencies and forced harmonic responses of the structures are obtained [171].

$$M_m \frac{\partial^2}{\partial t^2} X + C_m \frac{\partial}{\partial t} X + K_m X = F_m \tag{1.73}$$

Where the following parameters are defined as:

- M_m the global mass matrix
- C_m the global damping matrix
- K_m the global rigidity matrix
- F_m the nodal force vector matrix
- X the nodal displacement matrix.

Considering the availability of nodal force vectors and matrices of damping and rigidity, eq. (1.73) is solved, for each individual node, and the output nodal displacement vector matrix is obtained [171].

1.3.3.2 Natural Frequeny Calculation

Assuming that there is no excitation force applied to the system, which has no global damping, the general solution of eq. (1.73) provides us with the natural frequencies of the system under investigation.

$$M_m \frac{\partial^2}{\partial t^2} X + K_m X = 0 \tag{1.74}$$

Supposing that the output displacement matrix possesses a harmonic nature as follows:

$$X = X_0 e^{j\omega t} \tag{1.75}$$

with ω being the deformation angular frequency, eq. (1.74) can be rewritten as follows:

$$K_m X = \omega^2 M_m X \tag{1.76}$$

which is an eigenvalue problem with its responses providing the natural modes and frequencies of the structure [171].

1.3.3.3 Harmonic Response Analysis

Having obtained the radial forces and the natural frequencies, the nodal displacement and acceleration (vibration) matrices can be obtained. In a steady-state condition, the air-gap radial forces and nodal displacement vectors are considered to be in a harmonic regime defined as:

$$F_m = \sum_{k=1}^{\infty} \tilde{F}_k e^{jk\omega t} \tag{1.77}$$

$$X = \sum_{k=1}^{\infty} \tilde{X}_k e^{jk\omega t} \tag{1.78}$$

where $\tilde{F}_k$ represents a complex amplitude vector related to the k^{th}-order harmonic of the applied radial force and $\tilde{X}_k$ denotes the complex amplitude attributed to the k^{th} harmonic of the nodal displacement vector.

Considering each harmonic of the radial force, $\tilde{X}_k$ can be obtained as [171]:

$$\left[K_m - (k\omega)^2 M_m\right] \tilde{X}_k = \tilde{F}_k \tag{1.79}$$

In the following step, the nodal acceleration (vibration) is obtained given that the nodal

displacement is available.

$$\frac{\partial^2}{\partial t^2}\tilde{X}_k = (k\omega)^2 \tilde{X}_k \tag{1.80}$$

Equations (1.73-1.80) are solved for each mesh element, and the resulting displacement vector, in additions to its second-order derivatives giving the acceleration, are calculated in FEM-based environments.

1.3.3.4 Basics of Acoustic Noise

In acoustic science, the sound filed is typically identified through two important variables of the pressure (P) and velocity (v) of the medium particles. Two fundamental equations govern the dynamics of acoustic fields as follows [181].

$$\nabla^2 P\left(\vec{r},t\right) - \frac{1}{c_0^2}\frac{\partial^2 P\left(\vec{r},t\right)}{\partial t^2} = 0 \tag{1.81}$$

$$\frac{\partial \vec{v}\left(\vec{r},t\right)}{\partial t} + \left(\vec{v}\left(\vec{r},t\right).\nabla\right)\vec{v}\left(\vec{r},t\right) = \frac{1}{\rho}\nabla P\left(\vec{r},t\right) + \gamma \cdot \nabla^2 \vec{v}\left(\vec{r},t\right) \tag{1.82}$$

where

- ∇ is the divergence operator.
- $\vec{r}$ is the displacement vector in the Cartesian coordinate system.
- t represents the instance of time
- c_0 is the speed of sound wave in the corresponding medium
- γ denotes the kinematic viscosity
- ρ is the medium mass density.

Given the equations governing the vibration and acoustic noise, the frequency components within the radial forces are directly appeared within the vibration and acoustic noise waveforms, yet the amplitudes follow a highly non-linear nature. Therefore, FEM-based sofwares provide the highest accuracy in simulation of the vibration/acoustic noise of a complex body, like stator of an electric machine.

Given an approximate model of the stator geometry as a thin shell, the amplitude of the superficial vibration can be obtained by eq. (1.83) when a sinusoidal regime is considered

for the forces and vibro-acoustic waveforms [181, 185].

$$A_m = \frac{\frac{F_m}{M}}{\sqrt{\left(\omega_m^2 - \omega_r^2\right)^2 + 4\left(\xi_m \omega_r \omega_m\right)^2}} \tag{1.83}$$

where

- A_m denotes the vibration amplitude
- F_m represents the force magnitude
- M is the stator mass
- ω_m is the angular resonance frequency
- ω_r is the angular frequency of the applied force component
- ξ denotes the modal damping ratio.

Then, the sound power is calculated as:

$$\prod = \sum_{m,n=0}^{\infty} \sigma_{mn} \rho_0 c_0 S \left\langle \overline{v_{mn}^2} \right\rangle \tag{1.84}$$

with

- ρ_0 being the sound density
- σ_{mn} being the efficiency of the sound radiation
- S being the area of the radiating vibrating surface
- v_{mn} being the velocity of the vibrating stator surface

Considerig the electromagnetic origin of the vibration/acoustic noise in electric machines (including PMSM) and based on eq. (1.83) and eq. (1.84), the amplitudes of the vibration and acoustic noise are linearly dependent on the amplitude of the radial force. Moreover, the resonance phenomenon only intensifies the amplitude of the generated vibration/acoustic noise.

On the contrary to the affected amplitudes, the frequency components of the vibration/acoustic noise are not altered by the resonance phenomenon, and are exactly equal to the frequencies within the radial force [185].

1.3.3.5 Other Methods of Calculating Vibration and Acoustic Noise

Another method for rapid computation of electromagnetcally-induced vibration in electric machines is proposed in [186]. In this method, the radial force is calculated using field reconstruction method. The calculated forces, in parallel to the impulse vibration response, are used to compute the overall vibration of the stator.

A comprehensive and accurate analysis of the vibration/acoustic noise in PMSM is carried out in [187], which provides a systematic approach for vibroacoustic analysis of PMSM. It is shown that obtaining reliable results is bound to using a sufficiently-small mesh element for the vibrating surfaces. Moreover, the impact of tangential forces on the acoustic model derivation cannot be neglected.

Given an end-to-end coaxially-coupled PMSM, to its load generator, a lumped parametric model is developed which is used to predict the vibration/acoustic noise of such a system [188]. This method is based on using an effective modal mass and a modal participation factor accuracy enhancement technique.

1.3.3.6 Methods to Alleviate the Vibration and Acoustic Noise

Vibration/acosutic noise is inherent to PMSM operation, and finding ways to alleviate it has always been sought. Given the underlying nature of PMSM, successful vibration reduction is equal to finding methods to reduce the harmonics magnitude within the radial airgap forces. Such approaches can be opted in two ways: firstly, by optimizing the stator/rotor geometry in such a way that the concentration of the radial forces, on the tooth tips, is allayed. Secondly, through controlling the applied phase voltage/current, to indirectly impact the radial force magnitude. The former method falls outside of this thesis scope, so is not detailed any longer. However, the latter method can be done through various algorithms, among which the random excitation-based methods have shown superior performance.

Application of random or pseudo-random PWM (RPWM or PRPWM) methods, as a way to spread the harmonic noise power in a wide discrete frequency range, is reported in many papers in [189–192]. Not only is this method able to alleviate the vibration/acostic noise intensty but also reduces the torque ripple, resulting from the tangential component of the airgap field. In RPWM methods, the carrier signal, within the PWM generation algorithm, is built using a random pattern algorithm. As the result, the output PWM pulses are of random nature.

The current harmonic injection method is a proven solution for suppression of the radial

vibration in electric machines. Obtaining the relationship among the amplitude, frequency, and phase of the current harmonic and resulting vibration, a new current injection algorithm able to alter the radial force harmonics amplitude is proposed in [193].

1.3.3.7 Other Studies

The impact of rotor position error, for resolver-connected PMSM, on the harmonics of current, radial force, and resulting vibration/acoustic noise is deeply investigated in [185]. The study reveals that any position detection error, results in extra sideband harmonics within the phase currents, which in turn induces extra harmonics in the radial force. Therefore, excessive harmonics are generated in the vibration/acoustic noise waveform if there is a position tracking error.

Through proposing a multi-stage multiphysics method, the electromagnetic noise and sound quality of a PMSM, with a variable speed range, is realized [194]. Firstly, the radial forces are obtained for a 2D FEM model of PMSM with currents varying for a start-up scenario. In the following step, the mode superposition method is used and the resulting vibration is predicted. Finally, based on the structural mode data, a transfer function for predicting the output acoustic noise with given input radial force is established.

1.4 Conclusion

Throughout this chapter, three main topics were extensively investigated. First, the PMSM model in different coordinate systems in addition to the FOC algorithm. Second, PMSM sensorless algorithms, including both model-based and HFI-based methods. Third, the basics of vibration and acoustic noise in electric machines (i.e. formation mechanism, different origins, and analytical equations).

This thesis develops a novel PMSM sensorless control, which relies on the machine disseminated acoustic noise as the rotor position information source. As the result, the materials covered throughout this chapter served as the prerequisite for the upcoming proposed methods and analyses.

Given that, this thesis is organized as follows.

- **Chapter 2** investigates the PMSM vibroacoustic response in special excitation conditions, including the HFI and PWM voltage signals. As the result, the frequency-domain

response of the resulting current, magnetic fileds, radial force, vibration, and acoustic noise are investigated.

This chapter, also, answers the following questions:

- The raw output acoustic noise is fraught with countless harmonics, so how can it be used for the purpose of position estimation?
- Does the output acoustic noise follow an stochastic nature or can it be deterministically studied?

- **Chapter 3** is dedicated to the implementation of the acoustic noise-based sensorless control of PMSM. Two methods are proposed, one using an HFI voltage and the other using the PWM voltages.

  In order to implement the acoustic-based sensorless control, the signal processing algorithm, overall system modelling and stability analysis, and suitable position observer should be all considered.

  Additionally, this chapter provides answers to the following questions:

  - What is the structure of the proposed signal processing algorithm?
  - How to safeguard the signals from the environmental noise impact?
  - How does the proposed position observer affect the overall sensorless speed loop stability?
  - Which novel observer should be used to improve the estimation performance, in case there exist additional harmonics within the estimated values?

- **Chapter 4** experimentally evaluates the performance of the proposed acoustic noise-based sensorless algorithms. The proposed methods are benchmarked against various static and dynamic conditions.

  The answers to the following questions can also be found in this chapter.

  - Given the performance stability and robustness, are the proposed methods capable of keeping up with the existing, mature-enough sensorless algorithms?
  - Are the proposed methods able to satisfactorily perform under static and dynamic conditions?

  - As the estimation at standstill and low-speed are the most challenging aspects of every sensorless algorithm, how do the proposed methods perform in these conditions?

- **Conclusion** serves as the ending part of this dissertation, summarizing the key findings and insights obtained throughout the research on acoustic noise-based sensorless control. In addition, the **Conclusion** discusses potential future directions for research and improvement aspects that can be explored in the field of acoustic noise-based sensorless control, in order to further advance this new technology.

Chapter 2

Vibration and Acoustic Noise of PMSM in Special Conditions

Considering what have been provided in the previous chapter, in a PMSM, firstly the radial forces can be merely considered as the principal cause for the machine disseminated acoustic noise. Secondly, the impacts of stator slotting and air-gap tangential field components on the radial force formation is negligible. Although all the upcoming analyses are for a PMSM with the parameters given in Table. 2.1, similar method can be adopted for any PMSM, with arbitrary pole/slot configuration, without the loss of generality. Another point is that all the electromagnetic, mechanical, and electrical simulations are respectively conducted by *ALTAIR FLUX, ALTAIR PSIM*, and *ALTAIR Simlab*.

Table 2.1: Parameters of the studied PMSM.

Parameter	***Value***
No. of Slots/Poles	9/6
Rated Power	$1600W$
Rated Speed	$1500rpm$
d-/q-Axis Inductances	$140\mu H/178\mu H$
Phase Resistance	$97m\Omega$
PM Flux Linkage	$39.5mWb$

This chapter is organized as follows:

- Frequency-domain analysis of airgap fields and forces, under the fundamental excitation regime, is provided in **Section 2.1**.

- Given different HFI conditions, the harmonics of current and radial force are investigated in **Section 2.2**.
- Given the HFI conditions, the generated vibration and acoustic noise harmonics are investigated in **Section 2.3**.
- Removing the HFI, the PWM-induced acoustic noise is investigated in **Section 2.4**, named 'HFIless' condition.
- For the HFI and HFIless conditions (relying on PWM voltages only), the output acoustic noise is compared in **Section 2.5**.
- Conclusion is provided in **Section 2.6**.

2.1 Frequency-domain Composition of Air-gap Fields and Radial Forces

Given a PMSM with the general phase current format shown in eq. (2.1), the simplified model of the radial air-gap field - comprising the individual sum of PM and armature-reaction radial fields with using the super-position theorem - are provided in eq. (2.2)-(2.5) [182].

$$i_{ph} = \sum_{i=1}^{\infty} I_i . \cos\left(ip\omega_m t + \phi_i\right) \tag{2.1}$$

$$B_r^{Arm} = \sum_{k=1}^{\infty}\sum_{i=1}^{\infty} b_{arm}\left(r\right).I_i . \sin\left[k\theta \pm \left(ip\omega_m t + \phi_i\right)\right] \tag{2.2}$$

$$B_r^{PM} = \sum_{j=1,3,5}^{\infty} b_{PM}\left(r\right) . \cos\left[jp\left(\theta - \omega_m t\right)\right] \tag{2.3}$$

$$B_r^{Airgap} = B_r^{PM+Arm} = B_r^{PM} + B_r^{Arm} \tag{2.4}$$

$$k \pm i = 3C, C = \{0, \pm 1, \pm 2, \pm 4, \pm 5, \pm 7, \pm 8, ...\} \tag{2.5}$$

In the above equations, the parameters represent:

- i_{ph}, the phase current.
- I_i, amplitude of the i^{th} harmonic within the phase current.

- i, order of the harmonic within the phase current.
- p, the pole-pair count.
- ω_m, the rotor mechanical angular velocity.
- ϕ_i, phase of the i^{th} harmonic within the phase current.
- θ, the mechanical angle around the stator periphery.
- r, the calculation radius within the airgap, considering a spherical coordinate system.
- b_{PM} and b_{arm}, geometry-dependent variables.

Besides, in a PMSM, the current harmonics are always of specific nontriplen order (1, 5, 7, 11, etc.) [182].

For the PMSM used in this thesis, the harmonic components within the PM and armature-reaction radial fields are obtained as follows:

$$\mathbb{F}(B_r^{PM}) = jpf_m = f_e \times \left\{ \underbrace{1, 3, 5, 7, ...}_{j} \right\} \tag{2.6}$$

$$\mathbb{F}(B_r^{Arm}) = f_{ei} \times \{1, 2, 4, 5, 7, 8, ...\} \tag{2.7}$$

where:

- f_e denotes the fundamental electrical frequency.
- f_m corresponds to the fundamental mechanical frequency.
- f_{ei} represents the harmonics within the phase current (if the machine is only fed with the fundamental excitation, $f_e = f_{ei}$).

Given eq. (2.6), the PM-related field harmonics are merely dependent upon the number of pole pairs and the mechanical revolution speed, and resultantly directly related to the fundamental electrical frequency. The Armature-reaction field harmonics, however, are related to the harmonics appeared in the current, given eq. (2.7).

Given the pole/slot configuration of the considered PMSM and for the sake of brevity, 1/3 of the total stator and rotor peripheries, equal to 120° mechanical, can be used for the

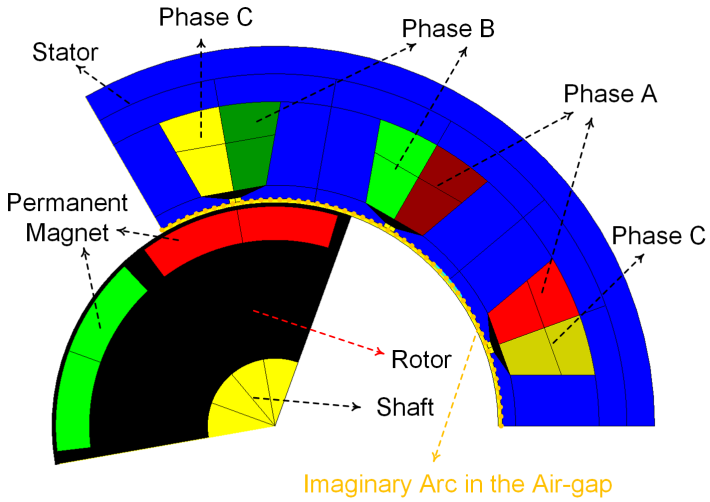

Figure 2.1: Symmetrical model of the PMSM with the arc drawn in the air-gap.

field analysis as shown in Fig. (2.1). A fictitious arc is drawn in the middle of the air-gap on which the magnetic fields are calculated.

Considering each radial and tangential field component, three different conditions are simulated (using transient analysis on a 2D model in ALTAIR Flux software):

- Firstly, the solo impact of permanent magnets - without any phase current.
- Secondly, the solo impact of armature-reaction - as the result of current injection within the machine and the PMs replaced by the stator lamination.
- Thirdly, the superposition of PM and armature-reaction fields.

Figure (2.2a) compares the radial air-gap fields for each of above-mentioned conditions. As can be noticed, B_r^{PM} is considerably greater that B_r^{Arm}. Moreover, waveforms of B_r^{PM} and B_r^{PM+Arm} are almost identical with a tiny difference existing. Consequently, in an actual condition where both the PM and armature-reaction fields exist, B_r^{PM} possesses the highest contribution and B_r^{Arm} can be safely disregarded. A similar behaviour exists for the tangential componets, as shown in Fig. (2.2b), where B_t^{PM} is almost equal to B_t^{PM+Arm}. Graphical representation of the magnetic flux density (B) distribution taking into account the permanent magnet field only, armature-reaction field only, and the overall field are respectively shown in Fig. (2.3-2.5). It is graphically evident that B^{PM} possesses the dominant portion in the overall flux density distribution, which certifies the aforementioned discussion.

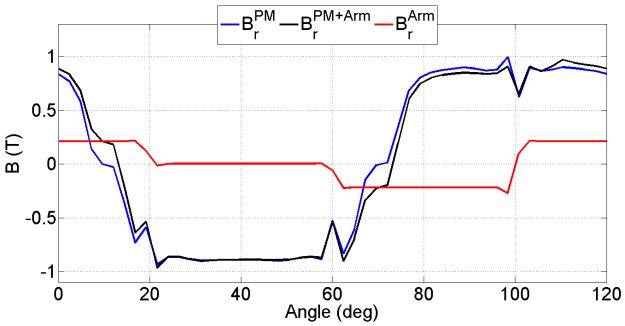

(a) Radial air-gap magnetic fields.

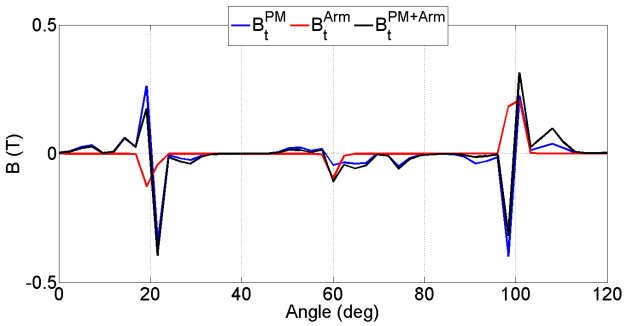

(b) Tangential air-gap magnetic fields.

Figure 2.2: Comparison of air-gap magnetic field components.

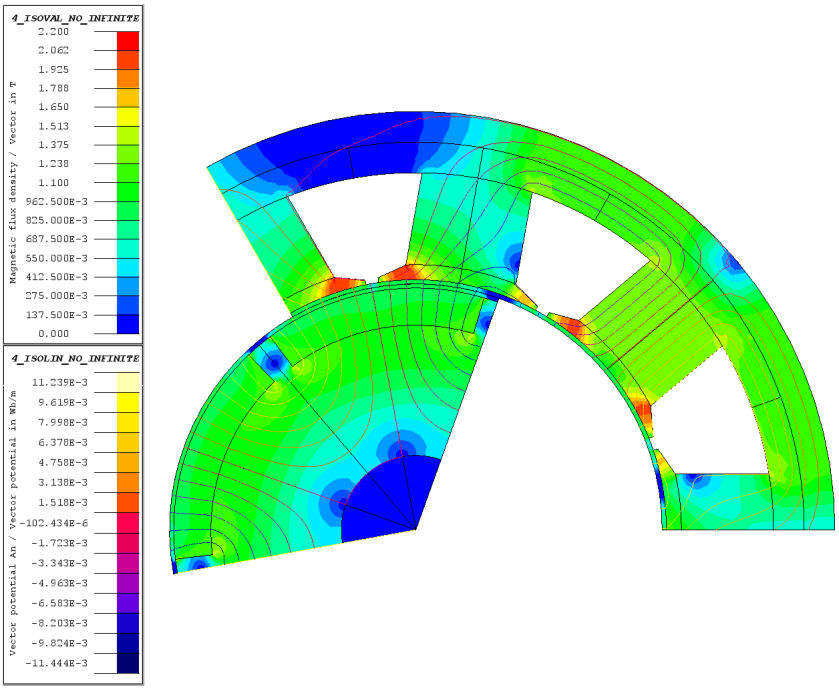

Figure 2.3: Flux density distribution showing B^{PM}.

Verifying eq. (2.6), (2.7), the frequency-domain analysis of the air-gap radial magnetic fields is shown in Fig. (2.6). It is observed that only the odd-order harmonics are dominant in the spectrum of B_r^{PM}, of which the 1^{st} and 3^{rd} possess the highest amplitudes. Looking at the harmonic spectrum of B_r^{Arm}, exactly non-triplen orders $(1, 2, 4, 5, 7, 8, ...)$ are appeared. Therefore and as the result of field superposition in actual case, the harmonic spectrum of B_r^{PM+Arm} hosts both even and odd orders, yet due to the dominance of B_r^{PM} over B_r^{Arm} validated in Fig. (2.2a and 2.2b), the magnitude of odd-order harmonics - especifically the

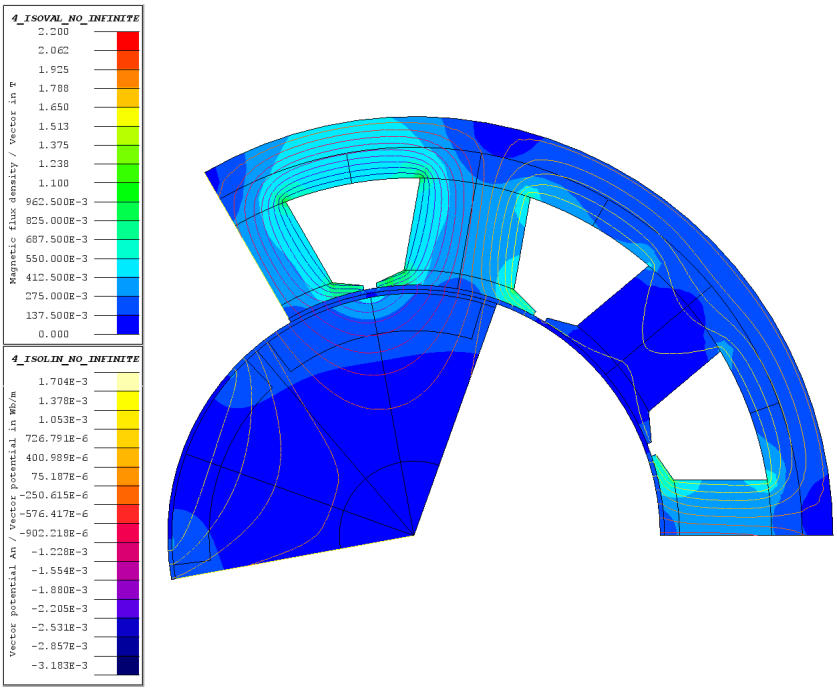

Figure 2.4: Flux density distribution showing B^{Arm}.

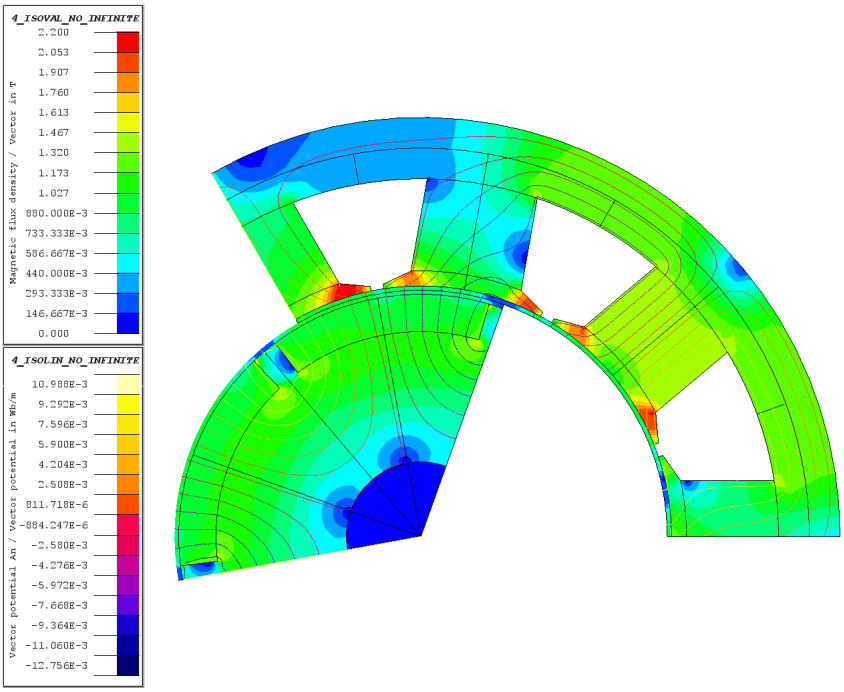

Figure 2.5: Flux density distribution showing B^{PM+Arm}.

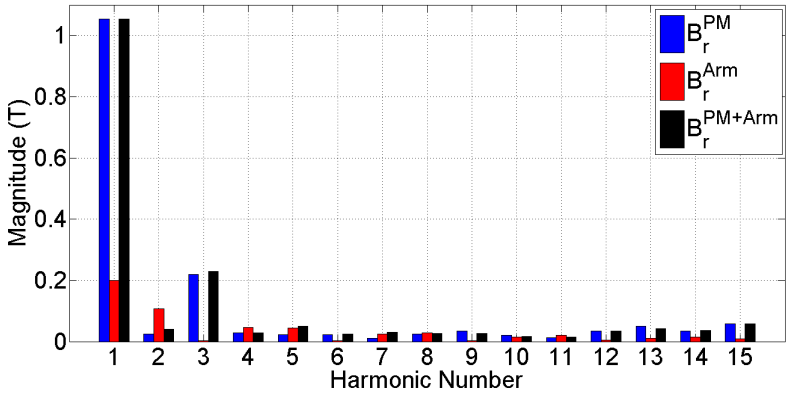

Figure 2.6: Frequency-domain analysis of radial air-gap magnetic fields.

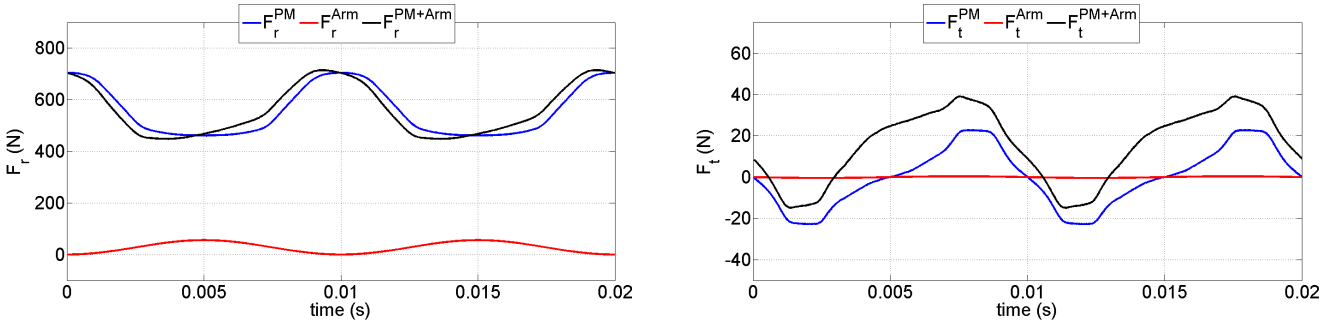

(a) Radial air-gap magnetic forces.

(b) Tangential air-gap magnetic forces.

Figure 2.7: Comparison of air-gap magnetic force components.

1^{st} and 3^{rd} - are more pronounced.

Having obtained the harmonics within the air-gap magnetic fields, radial forces can be analysed in the following step. An imaginary arc depicted in Fig. (2.1), covering only one of the tooth tips in the middle of the air-gap, is drawn and Maxwell Stress Tensor is applied and the applied forces to the given tooth tip are calculated as shown in Fig. (2.7). The total simulation time is chosen to be $0.02s$, representing the electrical period for a complete revolution at $1000rpm$, and the quadrature-axis current is chosen to be $30A$, which is equal to the nominal current.

Radial air-gap forces are compared in Fig. (2.7a) where F_r^{PM} is orders of magnitude greater than F_r^{Arm}; therefore, the total radial air-gap force (F_r^{PM+Arm}) is almost equal to F_r^{PM}. This is completely justifiable owing to the fact that the radial force is the fruit of magnetic fields interactions and it was verified that B_r^{PM} is in an undisputable dominance over B_r^{Arm}. For tangential forces, a similar behaviour is noticed where the impact of F_t^{Arm} is

almost negligible as compared to F_t^{PM}, as depicted in Fig. (2.7b). Additionally, it is worth mentioning that the overall amplitude of radial forces is meaningfully greater than that of tangential forces. Consequently, in analysis of air-gap forces, the radial ones are the only influential components.

Given the above-mentioned analysis and time-domain waveforms of the fields, the dominant harmonics within the radial forces are obtained as follows:

$$\mathbb{F}(F_r^{PM}) \approx \mathbb{F}(F_r^{PM+Arm}) = f_e \times \{2, 4, 6, 8, ...\} \tag{2.8}$$

$$\mathbb{F}(F_r^{Arm}) = f_e \times \{1, 2, 3, 4, ...\} \tag{2.9}$$

where the magnitudes of components related to the PM fields are times higher than those of armature-reaction. Consequently, in overall condition, it is feasible to only consider the impact of PM fields as shown in eq. (2.8). Frequency-domain analysis of radial air-gap forces is illustrated in Fig. (2.8). As expected, harmonics within the F_r^{PM} and F_r^{PM+Arm} are almost identical and are of even-order, while the amplitudes of the harmonics of F_r^{Arm} are almost negligible.

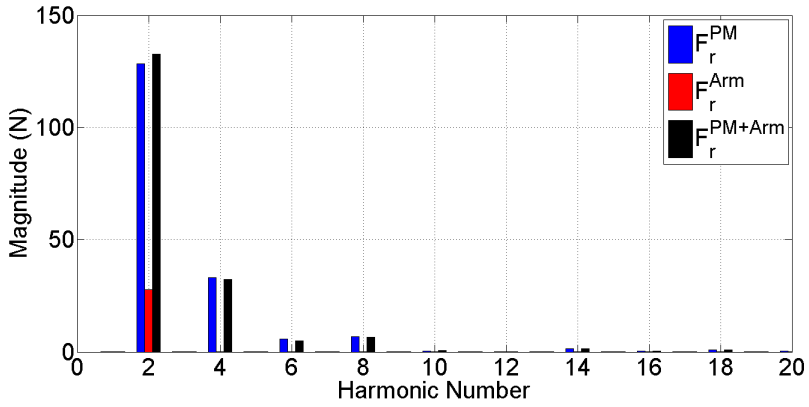

Figure 2.8: Frequency-domain analysis of radial air-gap magnetic forces.

In this section and given the fundamental excitation only, the overall airgap magnetic field - considering the impacts of permanent magnet and armature-reaction fields altogether - was investigated in the frequency domain. In the following step, the generated magnetic force harmonics were investigated. For both the airgap fields and forces, simulation results were provided in time- and frequency-domain to verify the analytical discussions.

In the next section, the impact of HFI on the harmonics of current, airgap fields, and radial forces is investigated.

2.2 Harmonics of Current and Radial Force in High-frequency Injection Condition

In this section, the motor is excited with a low-amplitude, high-frequency excitation and the impact of such excitation upon the radial force and disseminated acoustic noise is studied. The term $high - frequency$ is relative; actually, a voltage (or current) signal is superimposed on the fundamental machine excitation. The frequency of the injected signal must be conveniently higher than the fundamental frequency in order to make sure there is no interruption in the overall performance.

2.2.1 Inductance Matrix in an Estimated Coordinate System

Considering the voltage equations in the synchronous rotating reference frame (dq-frame) presented below in the matrix form,

$$\begin{bmatrix} V_d \\ V_q \end{bmatrix} = R_s \begin{bmatrix} i_d \\ i_q \end{bmatrix} + \omega_e \underbrace{\begin{bmatrix} 0 & -1 \\ +1 & 0 \end{bmatrix}}_{j} \begin{bmatrix} \lambda_d \\ \lambda_q \end{bmatrix} + \begin{bmatrix} \dot{\lambda_d} \\ \dot{\lambda_q} \end{bmatrix} \tag{2.10}$$

$$\begin{bmatrix} \lambda_d \\ \lambda_q \end{bmatrix} = \begin{bmatrix} L_d & 0 \\ 0 & L_q \end{bmatrix} \begin{bmatrix} i_d \\ i_q \end{bmatrix} + \begin{bmatrix} \psi_m \\ 0 \end{bmatrix} \tag{2.11}$$

where

- V_d and V_q represent the direct- and quadrature-axis voltages.
- i_d and i_q the quadrature-axis currents.
- ω_e the electrical fundamental frequency.
- λ_d and λ_q the quadrature flux linkages.
- L_d and L_q the qudrature inductances.
- ψ_m the PM flux.

The matrix of linkage fluxes can be reformatted as follows [195]:

$$\begin{bmatrix} \lambda_d \\ \lambda_q \end{bmatrix} = \begin{bmatrix} L_q & 0 \\ 0 & L_q \end{bmatrix} \begin{bmatrix} i_d \\ i_q \end{bmatrix} + \begin{bmatrix} \underbrace{\psi_m + (L_d - L_q)\, i_d}_{\lambda_{mmdq}} \\ 0 \end{bmatrix} = \mathbf{L_{qq}} \mathbf{i_{dq}} + \lambda_{\mathbf{mmdq}} \tag{2.12}$$

where λ_{mmdq} denotes the modified dq-frame flux linkage which, for most of the conditions where $i_d = 0$, is equal to ψ_m.

In the next step, the voltage equations are transformed to a new arbitrary rotating frame lagging the dq-frame by an angle defined as $\Delta\theta = \theta_e - \hat{\theta}_e$ with θ_e being the dq-frame position and $\hat{\theta}_e$ being the position of the estimated frame.

$$\boldsymbol{K_T}.\mathbf{V}_{dq} = \boldsymbol{K}_T.R_s \boldsymbol{i_{dq}} + \boldsymbol{K_T}.\omega_e.\boldsymbol{j}\lambda_{\boldsymbol{dq}} + \boldsymbol{K_T}.\dot{\lambda_{\boldsymbol{dq}}} \tag{2.13}$$

where K_T is the transformation matrix defined as:

$$\boldsymbol{K_T} = e^{j\Delta\theta} = \begin{bmatrix} \cos(\Delta\theta) & -\sin(\Delta\theta) \\ \sin(\Delta\theta) & \cos(\Delta\theta) \end{bmatrix} \tag{2.14}$$

Considering the transformation, the new flux linkage matrix is obtained as:

$$\hat{\lambda}_{\boldsymbol{dq}} = \boldsymbol{L_{qq}} \hat{\boldsymbol{i}}_{\boldsymbol{dq}} + \hat{\lambda}_{\boldsymbol{mmdq}} \tag{2.15}$$

$$\hat{\lambda}_{\boldsymbol{mmdq}} = \boldsymbol{K_T}.\lambda_{\boldsymbol{mmdq}} = \psi_m \begin{bmatrix} \cos(\Delta\theta) \\ \sin(\Delta\theta) \end{bmatrix} + \underbrace{(L_d - L_q)\, i_d \begin{bmatrix} \cos(\Delta\theta) \\ \sin(\Delta\theta) \end{bmatrix}}_{\lambda_1} \tag{2.16}$$

In the new coordinate system, the term λ_1 is equivalent to:

$$\lambda_1 = (L_d - L_q) \begin{bmatrix} \hat{i}_d \cos^2(\Delta\theta) + \hat{i}_q \sin(\Delta\theta)\cos(\Delta\theta) \\ \hat{i}_d \sin(\Delta\theta)\cos(\Delta\theta) + \hat{i}_q \sin^2(\Delta\theta) \end{bmatrix} = \Delta\hat{\boldsymbol{L}}_{\boldsymbol{dq}} \hat{\boldsymbol{i}}_{\boldsymbol{dq}} \tag{2.17}$$

where

$$\Delta\hat{\boldsymbol{L}}_{\boldsymbol{dq}} = \begin{bmatrix} 1 + \cos(2\Delta\theta) & \sin(2\Delta\theta) \\ \sin(2\Delta\theta) & 1 - \cos(2\Delta\theta) \end{bmatrix} \Delta L \tag{2.18}$$

$$\Delta L = \frac{L_d - L_q}{2} \tag{2.19}$$

Given eq. (2.15),(2.18), the inductance matrix in the new coordinate system is obtained as

follows:

$$\hat{\boldsymbol{L}}_{\boldsymbol{dq}} = \boldsymbol{L}_{\boldsymbol{qq}} + \Delta\hat{\boldsymbol{L}}_{\boldsymbol{dq}} = \begin{bmatrix} \Sigma L + \Delta L\cos(2\Delta\theta) & \Delta L\sin(2\Delta\theta) \\ \Delta L\sin(2\Delta\theta) & \Sigma L - \Delta L\cos(2\Delta\theta) \end{bmatrix} \tag{2.20}$$

where

$$\Sigma L = \frac{L_d + L_q}{2} \tag{2.21}$$

Consequently, if the arbitrary coordinate system is chosen to be fixed on the stator, the stationary coordinate system inductance matrix ($\alpha\beta$-axis) can be derived as in eq. (2.22). It is to be noted that, this format of displaying inductance profile is different from the classical notations since it is developed to incorporate the rotor position more effectively. Given the foregoing anlysis, vector diagram for a given d-axis voltage, transformed to different coordinate systems, is shown in Fig. (2.9).

$$\boldsymbol{L}_{\alpha\beta} = \begin{bmatrix} \Sigma L + \Delta L\cos(2\theta_e) & \Delta L\sin(2\theta_e) \\ \Delta L\sin(2\theta_e) & \Sigma L - \Delta L\cos(2\theta_e) \end{bmatrix} \tag{2.22}$$

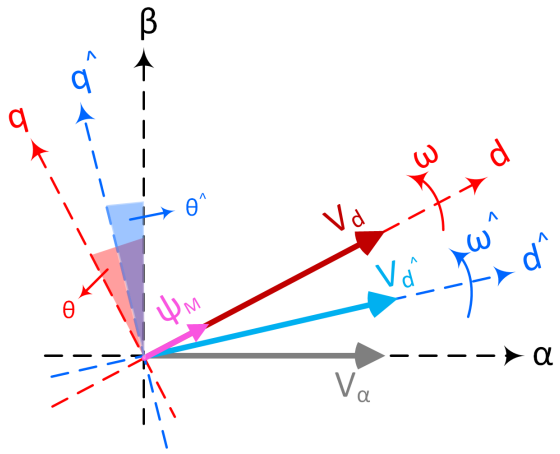

Figure 2.9: Projection of the d-axis voltage on the stationary and estimated reference frames.

2.2.2 High-frequency Injection and Current Harmonics

Given the classical notation of voltage equation in the stationary reference frame shown below:

$$\boldsymbol{V}_{\alpha\beta} = (R_s + \rho \boldsymbol{L}_{\alpha\beta})\, \boldsymbol{i}_{\alpha\beta} + \underbrace{\omega_e \psi_m \begin{bmatrix} -\sin(\theta_e) \\ \cos(\theta_e) \end{bmatrix}}_{EMF} \tag{2.23}$$

where ρ is the time-derivative operator. There is a frequency-dependent EMF term in the equation when the fundamental excitation is considered. If a periodic voltage signal having:

- the amplitude conveniently smaller than the fundamental component in order not to negatively impact the fundamental operation and torque production
- the frequency orders of magnitude larger than the fundamental electrical frequency

is superimposed on top of the fundamental voltage excitation, the EMF term is negligible and therefore eq. (2.23) gets a simple linear form shown in eq. (2.24). Additionally, if the HFI frequency is high enough, the resistive voltage drop can also be neglected.

$$\boldsymbol{V}_{\alpha\beta} \approx (\rho \boldsymbol{L}_{\alpha\beta})\, \boldsymbol{i}_{\alpha\beta} \Rightarrow \boldsymbol{i}_{\alpha\beta} \approx (\boldsymbol{L}_{\alpha\beta})^{-1} \int \boldsymbol{V}_{\alpha\beta}.dt \tag{2.24}$$

Although $\boldsymbol{L}_{\alpha\beta}$ is a function of electrical angle, since the HFI frequency is high enough, the differential operator is only applied to the current.

Having mentioned those, different combinations of HFI waveforms as a form of either voltage or current and in different coordinate systems can be used. Here in this thesis, only the voltage injection is considered, yet the anlysis is the same for the case of current injection. Figure (2.10) illustrates different voltage-type HFI methods.

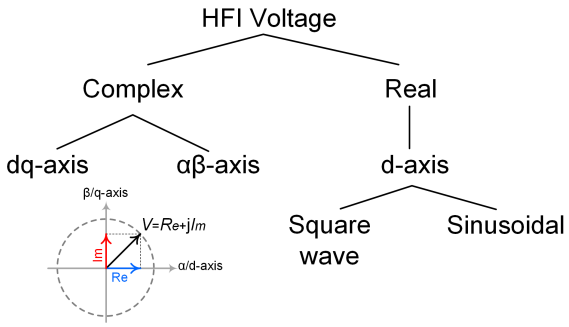

Figure 2.10: Different types of voltage-type HFI methods.

2.2.2.1 Complex HFI in $\alpha\beta$-frame

An arbitrary high-frequency complex voltage vector is injected in the $\alpha\beta$-frame shown below.

$$\boldsymbol{V}_{\alpha\beta h} = V_h e^{j\left(\omega_h t + \pi/2\right)} = V_h \begin{bmatrix} -\sin\left(\omega_h t\right) \\ \cos\left(\omega_h t\right) \end{bmatrix} \tag{2.25}$$

where V_h denotes the amplitude and ω_h represents the signal frequency. In such an excitation, the quadrature axes are being injectd with quadrature sinusoidal signals. Consequently, using eq. (2.24), the current in the stationary coordinate is obtained as follows.

$$\boldsymbol{i}_{\alpha\beta h} = \underbrace{\frac{1}{\omega_h\left(\Sigma L^2 - \Delta L^2\right)} \begin{bmatrix} \Sigma L - \Delta L\cos\left(2\theta_e\right) & -\Delta L\sin\left(2\theta_e\right) \\ -\Delta L\sin\left(2\theta_e\right) & \Sigma L + \Delta L\cos\left(2\theta_e\right) \end{bmatrix}}_{\left(L_{\alpha\beta}\right)^{-1}} \int \boldsymbol{V}_{\alpha\beta h}.dt \tag{2.26}$$

Using eq. (2.25), (2.26):

$$\boldsymbol{i}_{\alpha\beta}^{V_{\alpha\beta h}} = \underbrace{\frac{V_h}{\omega_h L_d L_q}}_{I_h} \begin{bmatrix} \Sigma L\cos\left(\omega_h t\right) - \Delta L\cos\left(\omega_h t - 2\theta_e\right) \\ \Sigma L\sin\left(\omega_h t\right) + \Delta L\sin\left(\omega_h t - 2\theta_e\right) \end{bmatrix} \tag{2.27}$$

Knowing the direct- and quadrature-axis inductances in addition to the constant amplitude and frequency of the injected signal, one can conclude that the coefficient $V_h/\omega_h L_d L_q$ is always available. It is worth mentioning that, L_d and L_q are directly influenced by the current amplitude and winding temperature; therefore, a look-up table can be used guarantee having the correct values in all conditions. Further simplifying eq. (2.27),

$$\boldsymbol{i}_{\alpha\beta}^{V_{\alpha\beta h}} = I_h\left(\Sigma L e^{j\omega_h t} - \Delta L e^{-j\left(\omega_h t - 2\theta_e\right)}\right) \tag{2.28}$$

there are two distinctive components appeared in the current spectrum at $\pm\left|\omega_h\right|$ and $\pm\left|\omega_h - 2\omega_e\right|$ of which the latter contains the rotor position information.

Verifying that through a simulation in PSIM software, a PMSM fed by a voltage-source inverter with a DC link voltage of $60V$, switching frequency of $10KHz$, and nominal current of $30A$ is considered. The motor is injected with an HFI in the stationary frame having an

amplitude of $10V$ and frequency of $1KHz$ as follows:

$$\boldsymbol{V}_{\alpha\beta h} = \begin{bmatrix} V_{\alpha h} \\ V_{\beta h} \end{bmatrix} = \begin{bmatrix} -10.\sin\left(2\pi \times 1000 \times t\right) \\ 10.\cos\left(2\pi \times 1000 \times t\right) \end{bmatrix} \tag{2.29}$$

In a three-second time duration, the reference speed is ramped up from standstill to $1000rpm$, shown in Fig. (2.11a), and the current waveform of i_α is depicted in Fig. (2.11b).

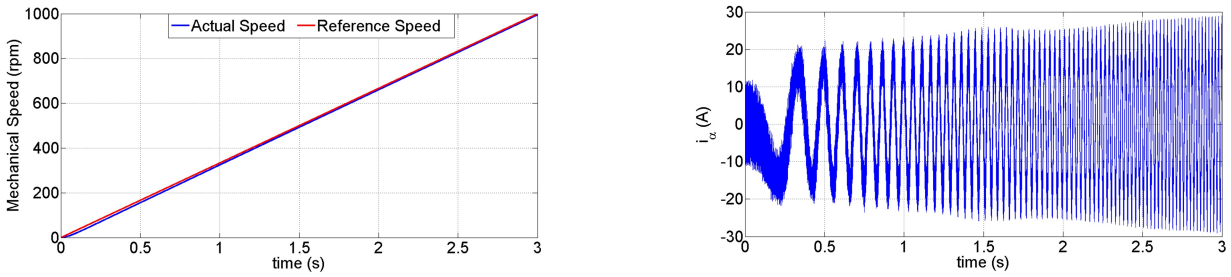

(a) Acceleration profile.

(b) α-axis current.

Figure 2.11: Speed and current profile during acceleration.

In order to perform a time-dependent harmonic analysis, a short-time Fourier transform algorithm is used and spectrogram of the current is obtained shown in Fig. (2.12). Con-

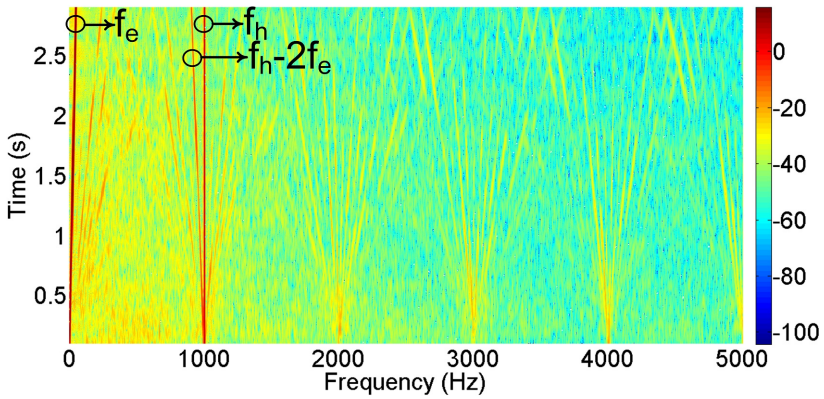

Figure 2.12: Spectrogram of the α-axis current when HFI is done in the $\alpha\beta$-frame (the colors are in dB unit).

sidering the linear relation of speed and time, the vertical axis of the spectrogram can also be linearly ascribed to the speed. There are three distinctive spectral rays appeared in the spectrogram:

- The first in the ultra low frequency zone representing the electrical fundamental frequency (f_e).
- The two others in the HFI frequency zone, exactly complying with what has been obtained in eq. (2.28) with a component at f_h and another one at $f_h - 2f_e$.

Needless to mention that, since the speed is varied in a linear relation to the time, spectral rays related to f_e, also behave the same.

2.2.2.2 Complex HFI in *dq*-frame

A complex high-frequency voltage vector is injected in the dq-frame as:

$$\boldsymbol{V}_{dqh} = V_h e^{j\left(\omega_h t + \pi/2\right)} = V_h \begin{bmatrix} -\sin\left(\omega_h t\right) \\ \cos\left(\omega_h t\right) \end{bmatrix} \tag{2.30}$$

the injected voltage is redefined in the $\alpha\beta$-frame as:

$$\boldsymbol{V}_{\alpha\beta h} = V_{dqh}.e^{j\theta} = jV_h.e^{j(\omega_h t + \theta_e)} \tag{2.31}$$

As the result, given eq. (2.26),the $\alpha\beta$-frame current vector is obtained as:

$$\begin{aligned} \boldsymbol{i}_{\alpha\beta}^{V_{dqh}} &= \underbrace{\frac{jV_h}{\omega_h L_d L_q}}_{I_H} \begin{bmatrix} \Sigma L - \Delta L\cos\left(2\theta_e\right) & -\Delta L\sin\left(2\theta_e\right) \\ -\Delta L\sin\left(2\theta_e\right) & \Sigma L + \Delta L\cos\left(2\theta_e\right) \end{bmatrix} \begin{bmatrix} \cos\left(\omega_h t + \theta_e\right) \\ \sin\left(\omega_h t + \theta_e\right) \end{bmatrix} \\ &= I_H \begin{bmatrix} \Sigma L\cos\left(\omega_h t + \theta_e\right) - \Delta L\cos\left(\omega_h t - \theta_e\right) \\ \Sigma L\sin\left(\omega_h t + \theta_e\right) + \Delta L\sin\left(\omega_h t - \theta_e\right) \end{bmatrix} \end{aligned} \tag{2.32}$$

The current spectrum hosts a pair of symmetrical components at $f_h \pm f_e$. On the contrary to the previous condition, although the HFI is implemented at f_h, there is no current component at this frequency. This phenomenon is also justifiable due to the fact that the injected voltage, which was originally in the dq-frame, is transformed to the stationary-frame in which a frequency shift, equal to $+f_e$, is introduced to the equations.

Maintaining the same acceleration profile, shown in Fig. (2.11a), the current spectrogram for the α-axis current is illustrated in Fig. (2.13), which completely verifies eq. (2.32).

Given Fig. (2.13) and except for the fundamental electrical frequency, there is a pair of distinctive sidebands around the injected frequency which are linearly widened with respect

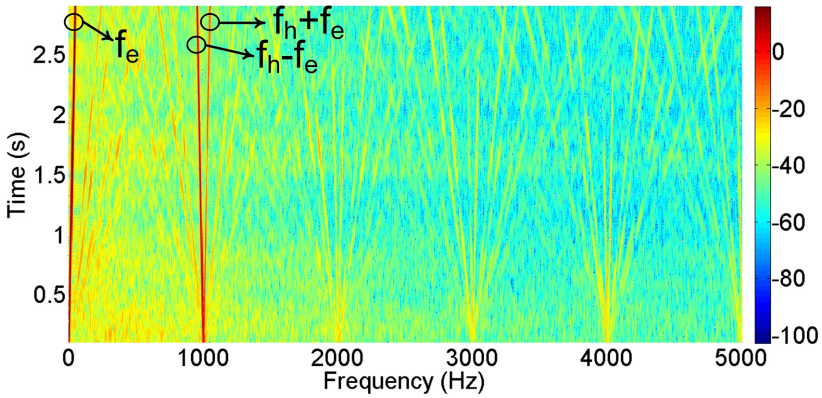

Figure 2.13: Spectrogram of the α-axis current when HFI is done in the dq-frame (the colors are in dB unit).

to the increasing-speed.

For complex injections in the $\alpha\beta$- and dq-axis and a specific condition of rotation at $500rpm$, providing the fundamental electrical frequency of $25Hz$, FFT of the α-axis currents are compared in Fig. (2.14). For the case of HFI in the $\alpha\beta$-axis, there are two current harmonics at $1KHz$ and $950Hz = f_h - 2f_e$. For the case of injection in the dq-axis, there are two symmetrical sidebands at $975Hz$ and $1025Hz$ representing components at $f_h \pm f_e$.

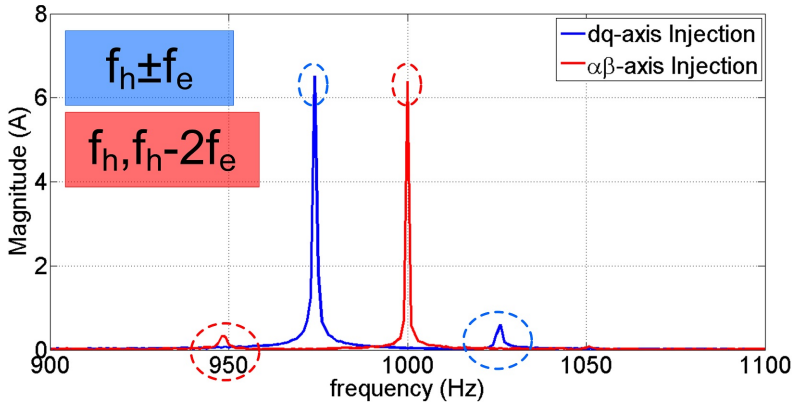

Figure 2.14: FFT of α-axis current for complex HFI in $\alpha\beta$- and dq-axis.

2.2.2.3 Sinusoidal Injection in *d*-axis

An arbitrary high-fequency signal is injected in the d-axis as:

$$V_{dh} = V_h . \cos(\omega_h t) \tag{2.33}$$

Similar to eq. (2.32), the α-axis current would contain symmetrical sidebands around the injected frequency; spectrogram of the current is depicted in Fig. (2.15). Comparing Fig.

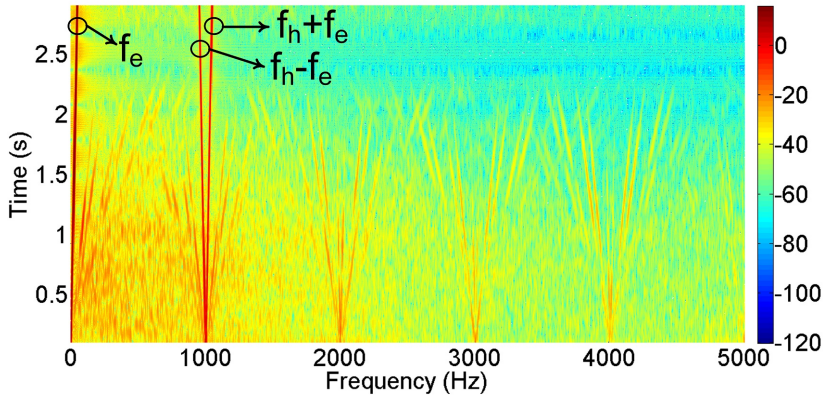

Figure 2.15: Spectrogram of the α-axis current when a sinusoidal HFI is done in the d-axis (the colors are in dB unit).

(2.13) and Fig. (2.15),there are more frequency components appeared in the zone below the injected frequency. This is due to the fact that the current would have asymmetrical components in its quadrature axes, as compared to the symmetrical components in eq. (2.32). Therefore, choosing a complex sinusoidal HFI results in a less-contaminated current profile.

2.2.2.4 Square-wave Injection in *d*-axis

Similar to the previous case, the HFI is implemented in the d-axis but with a square-wave signal. Since the square-wave signal is composed of multiple sinusoidal terms, the resultant current profile is more contaminated with extra harmonics which is clearly illustrated in Fig. (2.16). It is evident that, in addition to the components at $f_h \pm f_e$, there are two distinctive components at triple the injection frequency ($3f_h \pm f_e$).

FFT of the α-axis current for the sinusoidal and square-wave d-axis HFI implementation - for the fixed revolution speed of $500rpm$ and injection frequency of $1KHz$ - are compared in Fig. (2.17) in which, near the injection frequency, there are two dominant sidebands at $f_h \pm f_e$.

2.2.3 High-frequency Injection and Radial Force Harmonics

Given what have been discussed about, on the one hand, the PM-related fields are only dependent on the revolution speed and therefore not affected by the current harmonics.

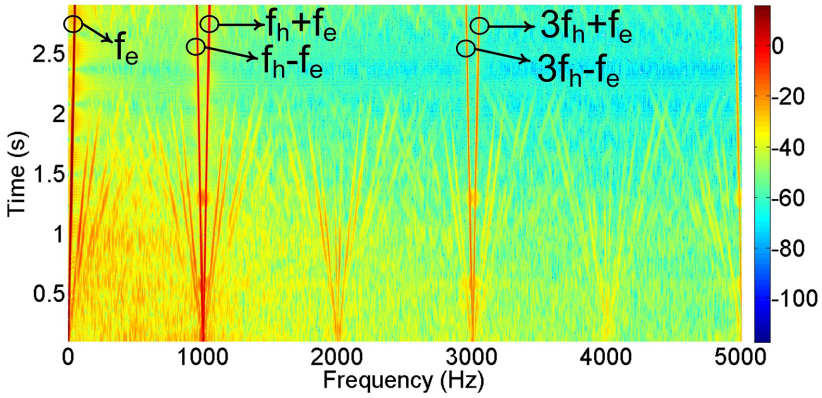

Figure 2.16: Spectrogram of α-axis current when a square-wave HFI is done in the d-axis (the colors are in dB unit).

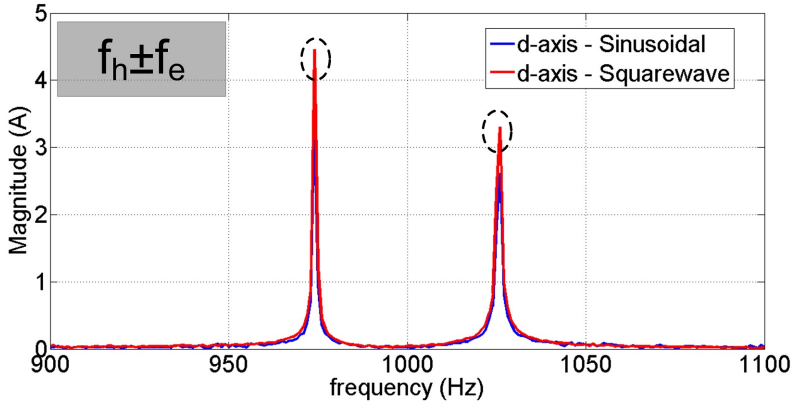

Figure 2.17: FFT of α-axis current for sinusoidal and square-wave d-axis HFI implementation.

On the other hand, the armature-reaction field is directly affected by the current harmonics. Additionally, all the previous analyses were conducted for the case of fundamental excitation where the current was mainly composed of one main component equal to the electrical fundamental frequency.

Consequently, considering the HFI condition in which a high-frequency component is superimposed on top of the fundamental excitation, there would be significant changes in the armature-reaction fields harmonics and therefore those of radial and tangential forces.

In the proximity of the injected frequency, the field harmonics are as follows:

$$\mathbb{F}\left(B_r^{PM}\right) = f_e \times \{1, 3, 5, 7, ...\} \tag{2.34}$$

$$\mathbb{F}\left(B_r^{Arm}\right) = f_{ei} \times 1 = \begin{cases} f_h \pm f_e, \ dq - frame\, HFI \\ f_h, f_h - 2f_e, \ \alpha\beta - frame\, HFI \end{cases} \tag{2.35}$$

Since the zone around f_h is the focal point of this section, higher multiples of the armature-reaction field harmonics ($i.e. f_{ei} \times \{2, 4, 5, 7, 8, ...\}$) are neglected.

2.2.3.1 *dq*-Frame HFI and Radial Force Harmonics

For a condition in which an HFI is implemented in the dq-frame, and based-on the interaction among PM and armature-reaction fields given in eq. (2.34) and eq. (2.35), the radial force harmonics are obtained as:

$$\mathbb{F}\left(F_r^{PM+Arm}\right) = f_h \pm f_e \times \{0, 2, 4, 6, ...\} \tag{2.36}$$

In HFI condition, the radial force frequency spectrum is composed of two main zones:

- **Low-frequency Zone**: mainly occupied by the even-order harmonics of the electrical frequency obtained in eq. (2.8).
- **High-frequncy Zone**: occupied by the frequencies obtained in eq. (2.36).

As the result, F_r^{PM+Arm} is no longer approximated by F_r^{PM}; therefore, the impact of F_r^{Arm} is more pronounced as its frequency spectrum encompasses high-frequency zone in which the PM-related harmonics have almost-negligible magnitudes. Figure (2.18) compares the radial

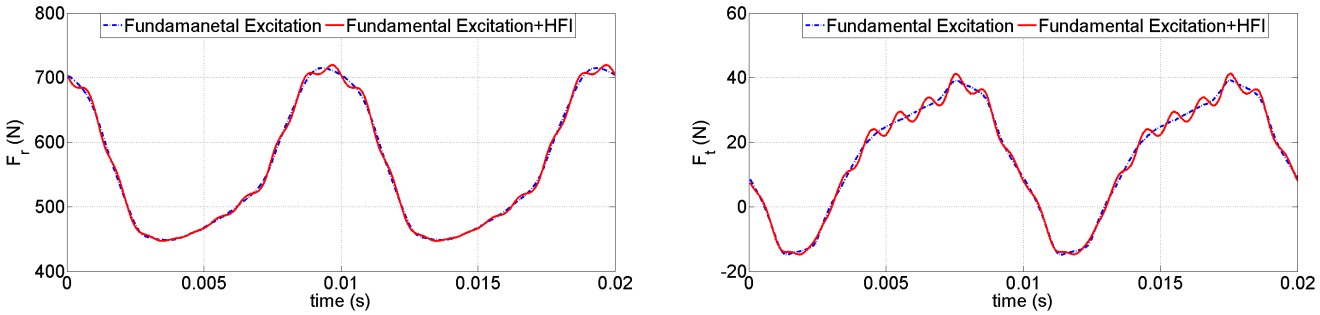

(a) Radial force.

(b) Tangential force.

Figure 2.18: Radial and tangential forces for the normal and dq-frame HFI conditions.

and tangential force profiles for the fundamental excitation and HFI conditions. For both cases, existence of high-order harmonics in the force waveforms are obvious which is directly

ascribed to the impact of HFI voltage on the armature-reaction fields. Besides, HFI implementation does not alter the average values of air-gap forces, while the magnitude of radial forces are orders of magnitude larger than the tangential forces, as expected. Therefore, even in HFI condition, the contribution of tangential forces is conveniently negligible.

2.2.3.2 $\alpha\beta$-frame HFI and Radial Force Harmonics

For an $\alpha\beta$-frame HFI and owing to the fields interactions, the harmonics within the radial forces are obtained as:

$$\mathbb{F}\left(F_r^{PM+Arm}\right) = f_h \pm f_e \times \{1, 3, 5, 7, ...\} \tag{2.37}$$

Similar to the previous case, Fig. (2.19) compares the radial and tangential forces for fundamental excitation and HFI conditions. All the observations in the previous condition hold true here except for the change in the HFI-related harmonics.

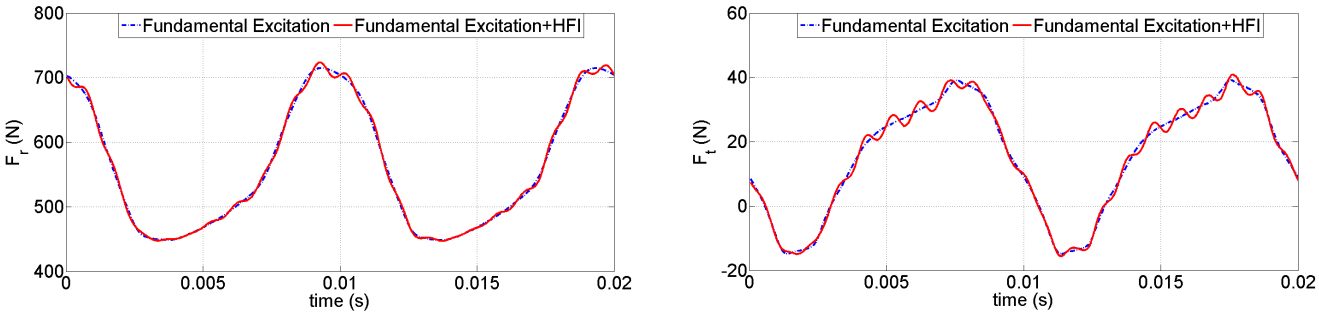

(a) Radial force.

(b) Tangential force.

Figure 2.19: Radial and tangential forces for the normal and $\alpha\beta$-frame HFI conditions.

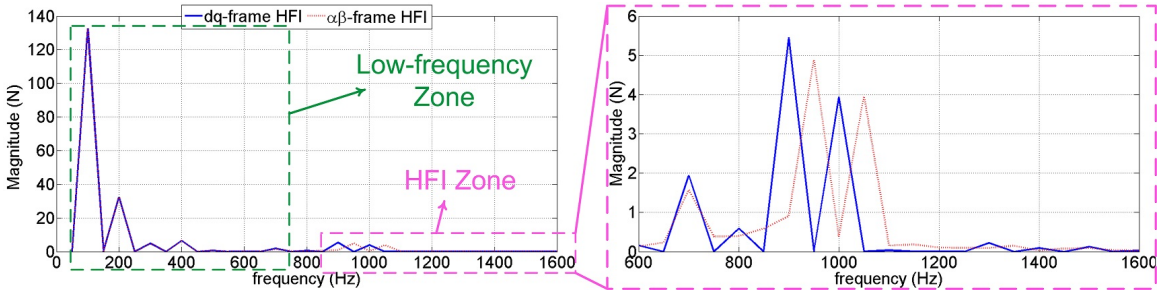

Figure 2.20: FFT of radial forces, considering dq- and $\alpha\beta$-frame HFI conditions.

Inspecting in the frequency domain for the revolution speed of $1000rpm$ and the electrical fundamental frequency of $50Hz$, Fig. (2.20) depicts the FFT of the dq-frame and $\alpha\beta$-frame

HFI conditions. The FFT can be devided into two sections; a low-frequency zone and an HFI-zone. The former corresponds to F_r^{PM} in which the even-order harmonics of the electrical frequency are appeared for both HFI scenarios. For the latter zone, there is a conspicuous difference existing in the harmonics which is directly related to the difference in the armature-reaction field harmonics. For the dq-frame HFI, there are even-order harmonics, while odd-order harmonics are generated in $\alpha\beta$-frame HFI. Additionally, Table. 2.2 details the harmonic contents of Fig. (2.20).

Table 2.2: Comparison of radial force harmonics for fundamental excitation and HFI methods shown in Fig. (2.20).

	Fnd. Exc. (Hz)	***dq*-frame HFI (Hz)**	**$\alpha\beta$-frame HFI (Hz)**
Low-freq. Zone	100, 200, 300, 400, 500, 700	100, 200, 300, 400, 500, 700	100, 200, 300, 400, 500, 700
HFI Zone	-	800, 900, 1000, 1100, 1300, 1400, 1500	950, 1050, 1150, 1250, 1350, 1450

In this section, the impact of HFI on the generated harmonics within the phase currents and resulting radial forces was investigated. In the following section, the HFI impact on the motor vibration and acoustic noise is investigated.

2.3 Harmonics of Vibration and Acoustic Noise in High-frequency Injection Condition

Due to the fields interactions, radial forces are generated with the concentrated impact points on the stator tooth tips. Following that, small displacements are occurred in the stator structure. Finally, some energy transfer takes place between the stator surface and the surrounding air molecules, which is perceived as the acoustic noise. Given the direct, linear energy transfer mechanism between the stator and the surrounding air, there would be almost identical harmonics generated in their waveforms (considering an ideal behaviour) which have different amplitudes (which is directly linked to the difference in their mechanical properties). Figure (2.21) illustrates the overal mechanism of vibration and acoustic noise generation in electric machines.

For the electromagnetic- and mechanical-domain analyses, ALTAIR Flux and ALTAIR Optistruct softwares are used respectively. Firstly, a 2D model of the machine is simulated

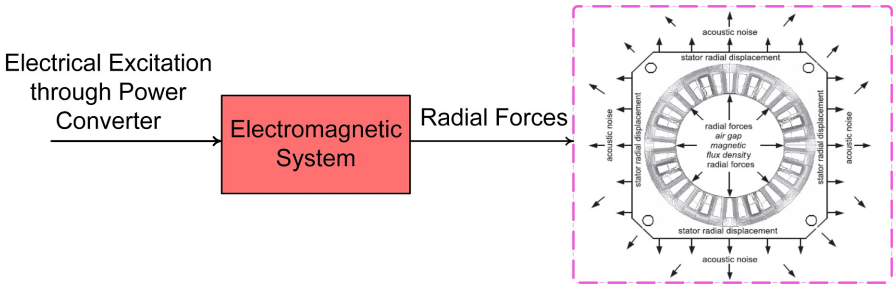

Figure 2.21: Mechanism of vibration and acoustic noise occurrence in electric machines.

and the radial forces are obtained. In the second step, a 3D model of the machine is created and the mesh on the stator tooth tips is exported to the ALTAIR Flux software. Given the exported mesh and the axial length of machine, calculated radial forces are homogenously distributed over each node in 3D domain. Finally, the 3D-mapped forces, serving as applied loads to the mechanical structure, are exported to ALTAIR Optistruct and the vibration on each node of the stator frame is obtained. The coupling workflow between the two software environments is graphically presented in Fig. (2.22).

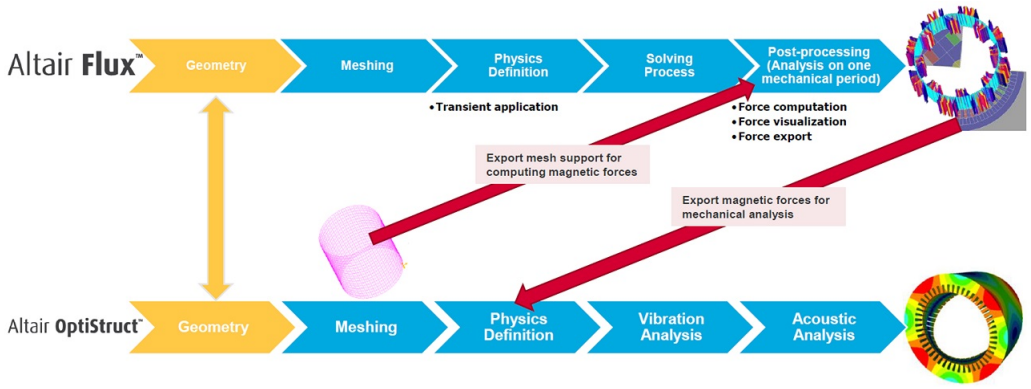

Figure 2.22: Coupling workflow between ALTAIR Flux and ALTAIR Optistruct (*ALTAIR Flux Official Example*).

2.3.1 Modal Analysis of Stator Structure

The first step in the process of vibration investigation of electric machines is to conduct a modal analysis through which the most-dominant low-order modes are identified. Therefore, the injected frequency must be chosen in such a way to be far from these resonance modes, in order to make sure that there would be no excessive vibrations.

For the sake of brevity, the impact of the end balls, cooling ribs, windings, and other stator attachments are neglected and the bare stator frame is considered for the simulation process. In the process of modal analysis, all the damping coefficients and fixed supports are neglected and the structure is impacted by an impulse of force, which contains almost infinite number of harmonics.

The dominant low-order mode shapes, also called the resonance modes or normal modes, of the stator frame are shown in Fig. (2.23). In addition and due to the inherent damping matrix of the structure, the impact of higher-order natural modes can be neglected in practice. The stator is made of steel with the mechanical properties given in Table. 2.3.

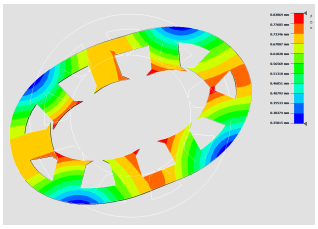

(a) Mode shape of $N = 2$ at $78Hz$.

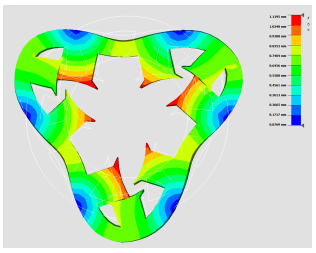

(b) Mode shape of $N = 3$ at $202Hz$.

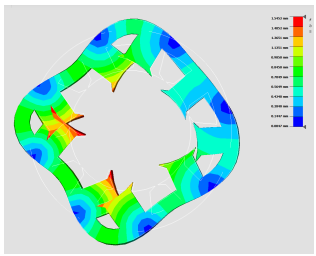

(c) Mode shape of $N = 4$ at $336Hz$.

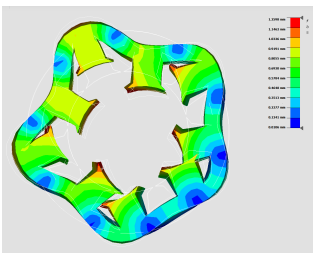

(d) Mode shape of $N = 5$ at $588Hz$.

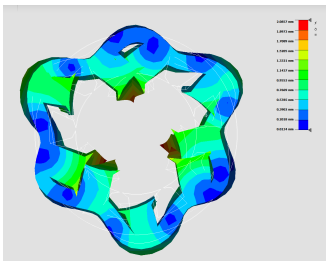

(e) Mode shape of $N = 6$ at $701Hz$.

Figure 2.23: Modal analysis of the dominant, low-order normal modes of the steel stator core.

Table 2.3: Mechanical Properties of Structural Steel

Structural Steel		
Property	**Symbol**	**Value**
Young's modulus (GPa)	E	207.0
Shear modulus (GPa)	G	80.0
Poisson's ratio	v	0.3
Density (Kg/m3)	ρ	7600.0
Yield strength (MPa)	S_y	370.0
Shear strength (MPa)	S_s	370.0

2.3.2 Simulation of Vibration Harmonics in HFI Condition

After calculation of radial forces, a 3D mechanical mesh is generated along the air-gap and the forces are equally mapped on each node. The meshed forces are then exported to the mechanical structure and applied to the corresponding impact points. Finally, the vibration, caused by the applied forces, is calculated. All the mentioned stages included in simulation of vibration, is illustrated in Fig. (2.24).

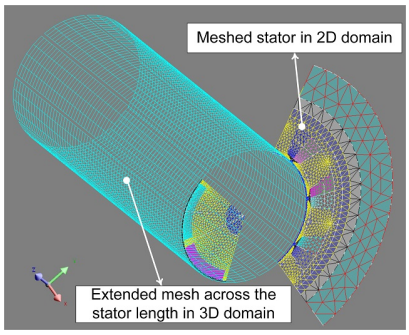

(a) 3D mesh along the stator axial length for force mapping.

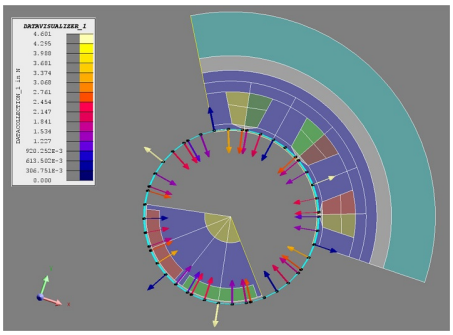

(b) Mapped forces in 2D view.

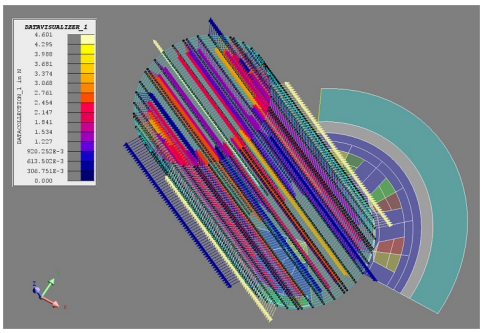

(c) Mapped forces in 3D view.

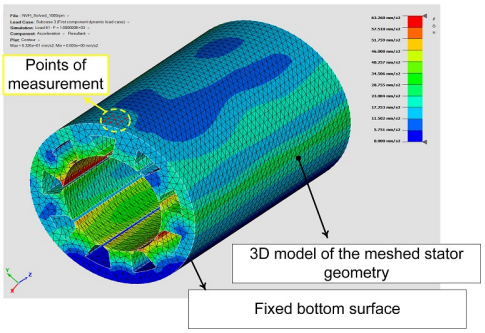

(d) Calculation of stator vibration.

Figure 2.24: Coupling of electromagnetic and mechanical domains for vibration simulation.

Similar to the actual case where the motors are screwed to the bench from the bottom, the lower surface of the stator core is also fixed in the simulation. In addition, the measurement points are chosen to be on the upper surface, which is similar to mounting an accelerometer on top of the stator.

For a normal condition with the revolution speed of $1000rpm$ with $f_e = 50Hz$ and without any HFI, the FFT of vibration is provided in Fig. (2.25). As discussed previously, the radial forces are dominantly occupied by the PM-related harmonics (even-order harmonics of the electrical fundamental frequency); therefore, the same harmonic orders are the dominant part in the vibration FFT. It is important to notice that, there is a noticeable gap between the magnitudes of even-order and odd-order harmonics in such a manner that the impact of odd-order harmonics is almost negligible. It is to be mentioned that, the calculated vibrations for all of the 9 measurement points (Fig. (2.24d)) are shown to make sure that the overall FFT contains similar harmonics regardless of the measurement place.

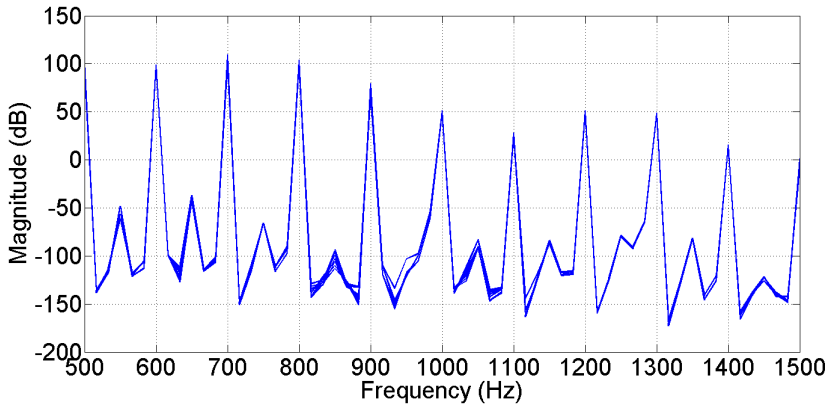

Figure 2.25: FFT of vibration for the injectionless operation.

2.3.2.1 Vibration Harmonics in *dq*-frame HFI Condition

Using the complex HFI voltage given in eq. (2.30), the vibration FFT is obtained as shown in Fig. (2.26). In line with the theoretical backgrounds, the FFT is only composed of even-order harmonics which has occurred due to the two following factors:

- Contribution of PM-related fields which was shown to have the most dominant share in the total radial force formation.
- The mutual impact of PM and armature-reaction fields, which contributes to the generation of even-order harmonics, especially for the components in the frequency range

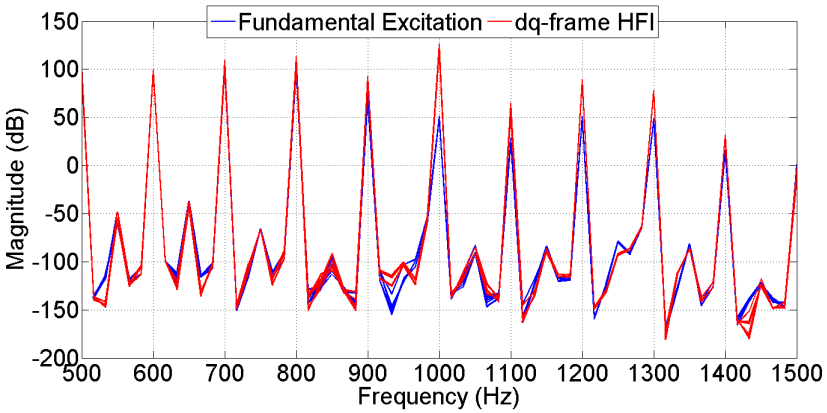

Figure 2.26: FFT of vibration for the dq-frame HFI condition.

above the injected frequency.

Given the harmonic magnitudes, introduction of dq-frame HFI has resulted in a magnitude increase for the even-order components compared to the normal condition (fundamental excitation only).

2.3.2.2 Vibration Harmonics in $\alpha\beta$-frame HFI Condition

Using the HFI voltage given in eq. (2.25), the FFT of simulated vibration is illustrated in Fig. (2.27).

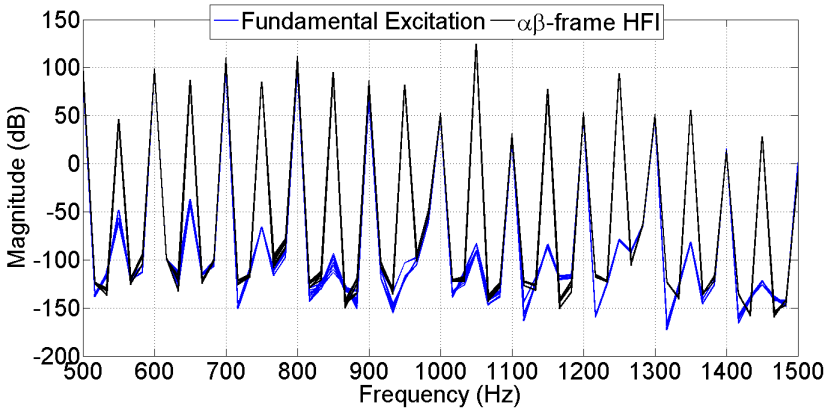

Figure 2.27: FFT of vibration for the $\alpha\beta$-frame HFI condition.

In this condition, there are:

- Even-order harmonics with exactly the same magnitudes as those of the normal condition, meaning that existence of these harmonics is merely attributed to the PM-related

forces.

- Large odd-order components, which are directly attributed to the mutual impact of PM and armature-reaction fields. It is important to note that, in the normal and *dq*-frame HFI conditions, there were no dominant odd-order harmonics in the vibration spectrum.

2.3.3 Experimental Analysis of Acoustic Noise Spectrum in HFI Conditions

In order to verify the aforementioned theoretical analyses and simulation results, the acoustic noise spectrum for the HFI conditions are experimentally inspected in this section. For each HFI condition, two types of plots are provided:

- **Spectrogram** for the speed ramp from zero to $1000rpm$, which verifies the generality of the provided analyses regarding the generated harmonics. In addition, spectrogram is a great illustrative asset for detecting the different zones in the acoustic spectrum, which helps the user to choose the frequency of the HFI voltage.

- **FFT** for the steady-state operating point at $500rpm$. In this plot, the zone around the injected frequency in enlarged and all the dominant components are identified.

2.3.3.1 Acoustic Noise Analysis in *dq*-frame HFI Condition

For this condition, the injection frequency is chosen to be $f_h = 1440Hz$ which is firstly, different from the previous value ($1000Hz$ in simulated conditions) and secondly, far enough from the low-order harmonics (related to the PM fields) and low-frequency stator natural modes. As the result, the applied HFI voltage is equal to:

$$\boldsymbol{V}_{\boldsymbol{dqh}} = 5.e^{j(2\pi*1440*t)} = 5 \begin{bmatrix} -\sin(2\pi * 1440 * t) \\ \cos(2\pi * 1440 * t) \end{bmatrix} \tag{2.38}$$

Spectrogram of the machine output acoustic noise is illustrated in Fig. (2.28). The spectrum hosts several different zones as follows:

- **PM-origined zone**, in which the low-frequency, even-order harmonics resulted from the impact of PM field are located. Although these harmonics contain speed-dependent

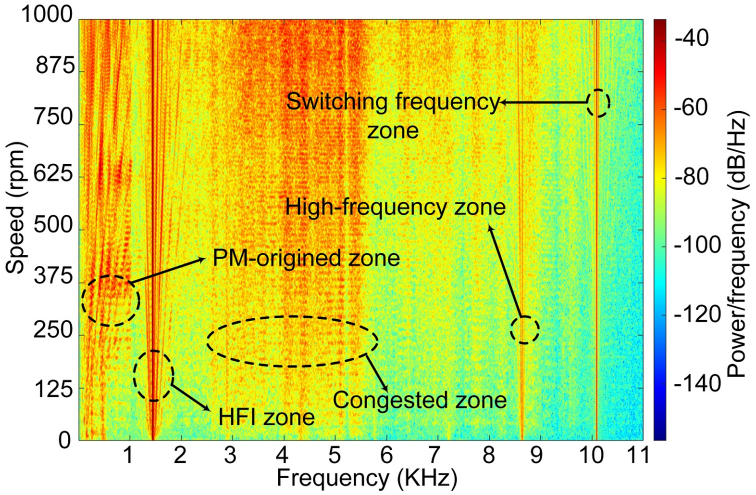

Figure 2.28: Acoustic noise spectrogram for the case of dq-frame HFI with $f_h = 1440Hz$.

information, there is no distinct separation among them (especially in the low speed range where they tend to be overlapping). Moreover, they are extended up to the frequency of $1000Hz$ in practice; therefore, it is better for the injected frequency to be located in higher frequencies.

- **HFI zone**, in which there are distinct speed-dependent components as defined in eq. (2.36). There are specific and clearly separated spectral rays in this zone without any interference from other unwanted frequencies.

- **Congested zone**, in which there are so many random resonant frequencies. In the low-speed region ($n_m < 375rpm$), the green background is dotted with orange spots. However, in the high-speed region ($n_m > 500rpm$), the background is contaminated with random orange spots. As the result, this is an unappropriate zone for the injection frequency to be located in.

- **High-frequency zone**, in which clear spectral rays are observed. The reason for occurrence of such high-frequency zone is the resonance between the high-order multiples of the injected frequency and high-order natural modes of the stator structure.

- **Switching frequency zone**, in which clear spectral rays related to the PWM switching frequency are generated.

Based on the experimental spectrogram of the available PMSM, the appropriate zone - which contains reliable rotor position information - is placed either

1200Hz < f_h < 2500Hz or at the proximity of the switching frequency (10KHz in our case). As the result, the HFI frequency is chosen at $f_h = 1440Hz$ in our experiments as an example.

Focusing on the HFI zone, the injected frequency proximity is enlarged and shown in Fig. (2.29). The highest peak has occurred at the injected frequency ($f_h = 1440Hz$) which is surrounded by the even-order multiples of the electrical fundamental frequency ($f_h \pm \{0, 2, 4, 6, 8, ...\}\, f_e$).

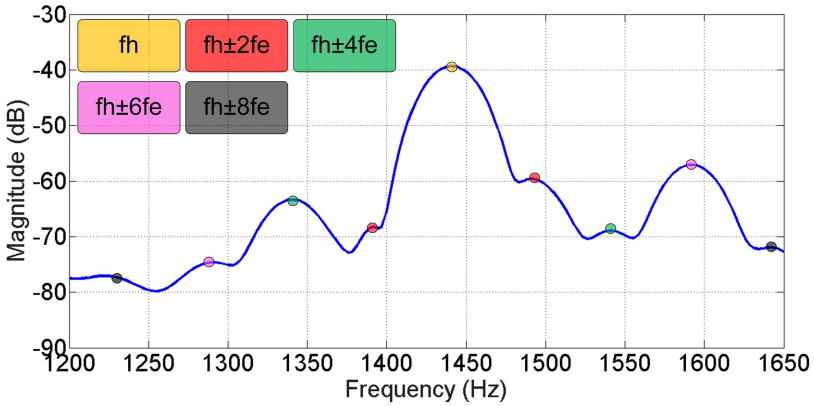

Figure 2.29: Acoustic noise FFT for the case of dq-frame HFI with $f_h = 1440Hz$ and $f_e = 25Hz$.

2.3.3.2 Acoustic Noise Analysis in $\alpha\beta$-frame HFI Condition

Having the same amplitude and frequency as the previous condition, an HFI voltage is injected in the stationary frame. The acoustic noise spectrogram is shown in Fig. (2.30). Exactly similar to the previous condition, there are five different zones appeared in the spectrum. Focusing on the zone around the injected frequency, the acoustic noise FFT is illustrated in Fig. (2.31), in which there are only odd-order dominant sidebands appeared ($f_h \pm \{1, 3, 5, 7, ...\}\, f_e$). Comparing the two HFI conditions, Table. 2.4 details the appeared sidebands frequencies. Given the provided FFT plots and this table, it is concluded that:

- For the case of dq-frame HFI, there are only symmetrical even-order sidebands appeared in the acoustic noise spectrum.
- For the case of $\alpha\beta$-frame HFI, there are only symmetrical odd-order sidebands appeared in the acoustic noise spectrum.

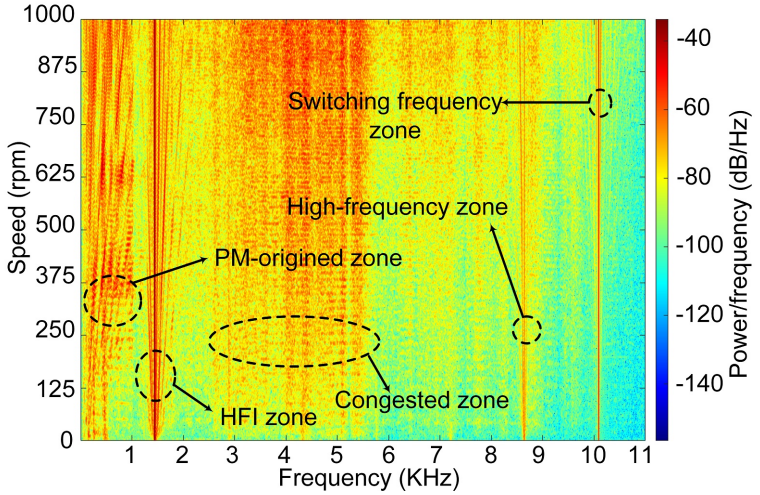

Figure 2.30: Acoustic noise spectrogram for the case of $\alpha\beta$-frame HFI with $f_h = 1440Hz$.

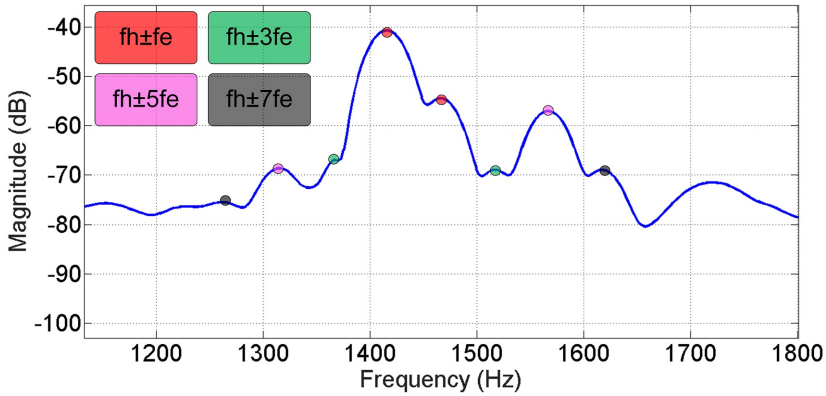

Figure 2.31: Acoustic noise FFT for the case of $\alpha\beta$-frame HFI with $f_h = 1440Hz$ and $f_e = 25Hz$.

Table 2.4: Speed-dependent sidebands in proximity of the injected frequency in different HFI conditions.

	Speed-dependent sideband (Hz)							
	fh	**fh±fe**	**fh±2fe**	**fh±3fe**	**fh±4fe**	**fh±5fe**	**fh±6fe**	**fh±7fe**
***dq*-frame HFI**	1440	-	1390 1490	-	1340 1540	-	1290 1590	-
$\alpha\beta$-frame HFI	-	1415 1465	-	1365 1515	-	1315 1565	-	1265 1615

It is worth mentioning that, the acoustic noise analysis for the other two HFI conditions (d-axis sinusoidal and square-wave signals) follow a similar trend and therefore are not

repeated here.

In addition to the HFI zone, which was extensively investigated in this section, the switching frequency zone (as shown in Fig. (2.28) and Fig. (2.30)) also hosts specific, speed-dependent spectral components. Therefore, the following section focuses on the analysis of this zone for exploitation of the rotor position information.

2.4 Harmonics of Current, Radial Force, and Acoustic Noise Considering the Impact of PWM Voltages

According to the provided spectrograms and focusing on the zone related to the switching frequency, there exist some distinct sidebands which are linearly dependent on the fundamental frequency. As the result, the impact of switching PWM on the current and radial force harmonics is investigated in this section.

2.4.1 PWM Process and Current Harmonics

In all inverter-fed PMSM drives, PWM voltage generation is an integral part which is known to be the fundamental reason behind the generation of high-frequency components within the current waveforms. Depending on the number of phases or the chosen strategy, one or multiple sinusoidal references are compared with a fixed high-frequency carrier, which can be of sawtooth or triangular waveform. The output of this binary comparison provides the gate pulses with variable duty cycles, in each narrow moving window considering the total period of the signal.

For a condition with a sawtooth carrier with the frequency of $1KHz$, three different DC inputs are used in order to provide three different duty cycles equal to 0.2, 0.5, and 0.95 for instance. The results are provided in Fig. (2.32); it is noticed that (given the different duty cycles), both the magnitude and frequency components of the FFT plots change. As the result, for a sinusoidal reference signal which is compared with a high-frequency carrier, having a generalized model providing the correct harmonics is indispensable.

Given only one of the phase legs of a three-phase inverter, the generated gate pulses with the resulting phase voltage are shown in Fig.(2.33). In ideal PWM, complementary gate pulses are applied to the switches in each leg. However, in practice and due to the delayed turning-off of each switch and avoiding the shoot-through occurrence, the rising edge of each gate pulse is delayed by a fixed amount (known as the deadtime). In deadtime-included

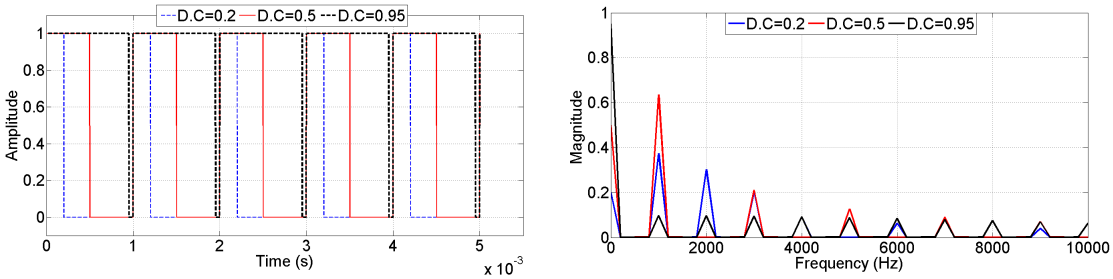

(a) Pulses with different duty cycles. (b) FFT of pulses with different duty cycles.

Figure 2.32: Comparison of pulses with different duty cycles.

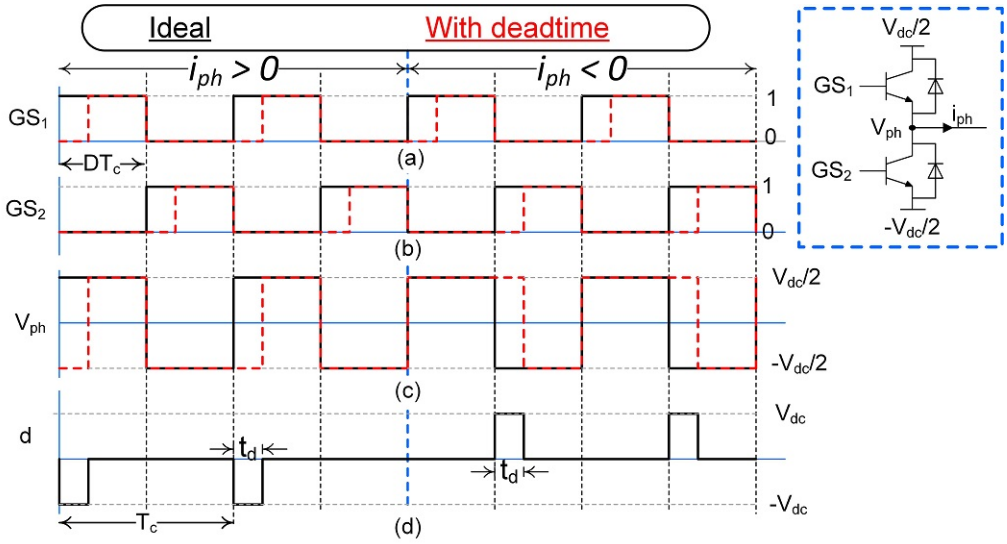

Figure 2.33: PWM voltage generation with and without the deadtime.

PWM, the switches in each leg are never conducting at the same time, meaning that there are small periods during which none of the switches are actually active which is known as the deadband.

Comparing the ideal and deadtime-included phase voltages, which are respectively shown by V_{phi} and V_{phd}, there is a current polarity-dependent periodic difference observed which is defined as [196]:

$$d = V_{phd} - V_{phi} \tag{2.39}$$

Given the fixed values of deadtime (t_d) and switching period (T_c), the waveform of d is only dependent on the current polarity, which has the frequency equal to the electrical fundamental component (f_e). Consequently, deadtime-included PWM can indirectly be investigated by separately analysing d and V_{phi} and superimposing their effect onto each

other.

2.4.1.1 Ideal PWM - Without the Deadtime

Considering a general format for the reference (v_{ref}) and triangular carrier (v_c) waveforms as shown below:

$$v_{ref}(t) = m_a.\cos(\omega_e t) \tag{2.40}$$

$$v_c(t) = \begin{cases} -1 + \frac{4}{T}(t - kT); & kT \leqslant t < (k+0.5)T \\ 3 - \frac{4}{T}(t - kT); & (k+0.5)T \leqslant t < (k+1)T \end{cases} \tag{2.41}$$

where:

- t denotes the time instance
- k a constant integer
- m_a the modulation index
- ω_e the frequency of the reference signal, which is equal to the electrical fundamental frequency in PMSM drive
- T period of the carrier signal

The output of the binary comparison - the applied gate pulse - given any arbitrary duty cycle, can be defined as:

$$GS(t) = \begin{cases} 0; & t_1 \leqslant t < t_2 \\ 1; & otherwise \end{cases} \tag{2.42}$$

where t_1 and t_2 are arbitrary time instances. Using the Poisson resummation method defined in, the gate pulse is re-established as [197]:

$$GS(t) = \sum_{mn} a_{mn}.e^{j\omega_{mn}t} \tag{2.43}$$

where

$$a_{mn} = \begin{cases} 0; & \omega_{mn} = 0 \\ \left[\frac{-2}{\omega_{mn}T} J_n\left(\frac{\omega_{mn}m_aT}{4}\right) j^{(m+n+1)}\right] . \left[e^{-j\frac{3\pi n\omega_e}{2\omega_c}} - (-1)^{m+n}.e^{-j\frac{n\pi\omega_e}{2\omega_e}}\right]; & \omega_{mn} \neq 0 \end{cases} \tag{2.44}$$

$$\omega_{mn} = m\omega_c + n\omega_e; \{m, n \in W | m \neq n\} \tag{2.45}$$

and J_n is the first-order spherical Bessel function.

Consequently, harmonic contents of the generated gate pulses are directly related to the interaction between the unequal values of m and n as defined below:

$$\mathbb{F}(GS) = \begin{cases} f_c \pm \{0, 2, 4, 6, ...\} \times f_e \\ 2f_c \pm \{1, 3, 5, 7, ...\} \times f_e \\ 3f_c \pm \{0, 2, 4, 6, ...\} \times f_e \\ etc. \end{cases} \tag{2.46}$$

For a simulated condition with $f_c = 1KHz$ and $f_e = 25Hz$, FFT of the applied phase voltage is illustrated in Fig. (2.34), which is in complete compliance with eq. (2.46).

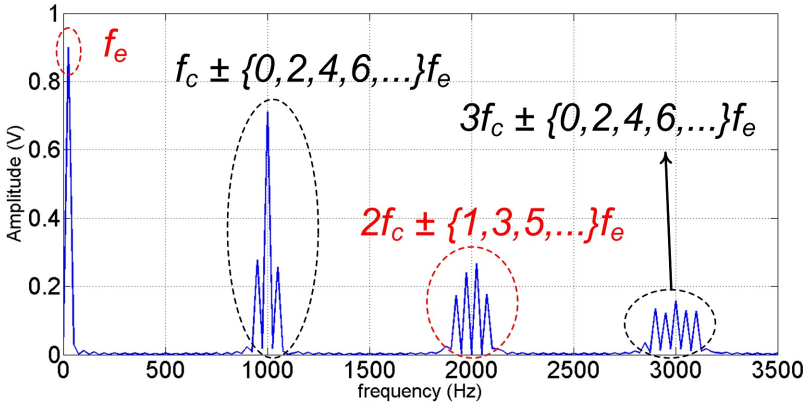

Figure 2.34: FFT of the phase voltage with ideal PWM.

2.4.1.2 Non-ideal PWM - Including the deadtime

Given Fig. (2.33), d is defined as follows:

$$d_{i_{ph}>0} = \begin{cases} -V_{dc};\ kT_c \leqslant t < kT_c + t_d \\ 0;\ otherwise \end{cases} \tag{2.47}$$

$$d_{i_{ph}<0} = \begin{cases} +V_{dc};\ DkT_c \leqslant t < DkT_c + t_d \\ 0;\ otherwise \end{cases} \tag{2.48}$$

Over each electrical fundamental period, d is completely periodic (also shown in Fig. (2.33)). As the result, the average value can be used instead:

$$\bar{d} = \frac{1}{T_e} \int_{KTe}^{(K+1)T_e} d.dt = \begin{cases} -V_{dc}.t_d/T_e; & i_{ph} > 0 \\ +V_{dc}.t_d/T_e; & i_{ph} < 0 \end{cases} \tag{2.49}$$

where:

- D denotes the switching duty cycle at each time instance.
- V_{dc} the DC-link voltage of inverter
- i_{ph} the phase current
- K a constant integer

Equation (2.49) is a square-wave signal with the period equal to T_e. Accordingly, the fourier series expansion is derived as:

$$\bar{d} = \frac{4V_{dc}.t_d}{\pi.T_e}.\sum_{n=1,3,5}^{\infty} \frac{1}{n}.\sin\left(n\omega_t t\right) = \frac{4V_{dc}.t_d}{\pi.T_e}.\sum_{n} \frac{1}{n}\left(\frac{e^{jn\omega_e t} - e^{-jn\omega_e t}}{j2}\right) \tag{2.50}$$

Given (2.50), introduction of deadtime to the PWM process, results in the generation of odd-order harmonics in the output phase voltage spectrum. The magnitude of these extra harmonics are in a reciprocal relation with the order of the harmonic; as the result, the lower the frequency, the higher the magnitude would be. Additionally, around the switching frequency, symmetrical odd-order sidebands would be generated.

The switching frequency is, usually, chosen in such a manner to be times higher than the fundamental frequency. Therefore, in the switching frequency proximity, one can conclude that:

$$\mathbb{F}\left(V_{phd}\right) = \mathbb{F}\left(V_{phi}\right) + \mathbb{F}\left(\bar{d}\right) \tag{2.51}$$

$$\mathbb{F}\left(V_{phi}\right) = f_c \pm \{0, 2, 4, 6, ...\} \times f_e \tag{2.52}$$

$$\mathbb{F}\left(\bar{d}\right) = f_c \pm \{1, 3, 5, 7, ...\} \times f_e \tag{2.53}$$

As the result, the phase voltage would contain frequency-dependent symmetrical sidebands of both even and odd orders around the switching frequency. Verifying the foregoing analysis, a simulation is carried out and the FFT of phase voltage for two conditions with $t_d = 0s$

(ideal PWM) and $t_d = 2\mu s$ (deadtime-included PWM) are compared as shown in Fig. (2.35). In this simulation, $f_c = 10KHz$ and $f_e = 50Hz$.

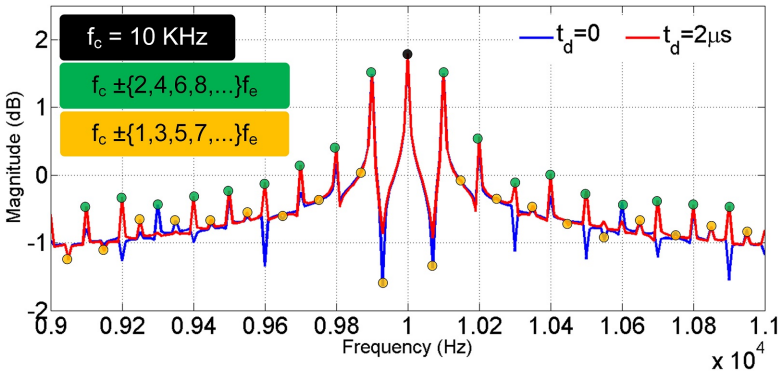

Figure 2.35: FFT of the phase voltage considering ideal and deadtime-included PWM models.

Although introduction of deadtime to the PWM culminates in the appearance of odd-order sideband harmonics, the even-order sidebands are, noticeably, the dominant components within the spectrum.

Given the 3-phase voltage equation of PMSM given in eq. (2.54) and the existing gap among the values of switching frequency and fundamental electrical frequency, the EMF term in addition to the resistive voltage drop are easily negligible. Therefore, the machine behaves like a 3-phase linear inductive circuit with the current equation as in eq. (2.55). The matrices of phase voltages and phase currents are also denoted by V_s and I_s. Based-on the linear circuit at the switching frequency, the current waveform would also host the exact same harmonics as the phase voltage.

$$\underbrace{\begin{bmatrix} V_{as} \\ V_{bs} \\ V_{cs} \end{bmatrix}}_{V_s} = \left(R_s + \frac{d}{dt}L_{ss}\right) \underbrace{\begin{bmatrix} i_{as} \\ i_{bs} \\ i_{cs} \end{bmatrix}}_{I_s} - \omega_e \psi_{PM} \begin{bmatrix} \sin(\theta_e) \\ \sin\left(\theta_e - 2\pi/3\right) \\ \sin\left(\theta_e + 2\pi/3\right) \end{bmatrix} \tag{2.54}$$

$$\boldsymbol{I}_s \approx L_{ss}^{-1} \int \boldsymbol{V}_s.dt \tag{2.55}$$

In order to scrutinize the current harmonics, the waveform is experimentally captured while the speed is fixed at $500rpm$, the peak amplitude is $10A$, and a constant deadtime of $1\mu s$ is applied.

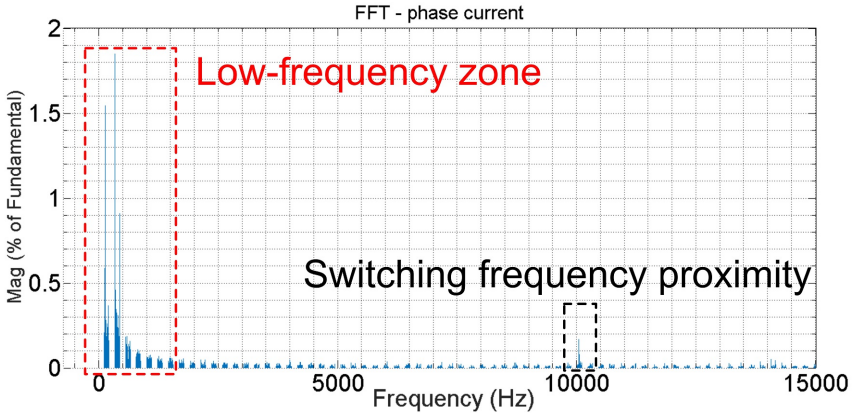

(a) FFT of phase current in the full frequency spectrum.

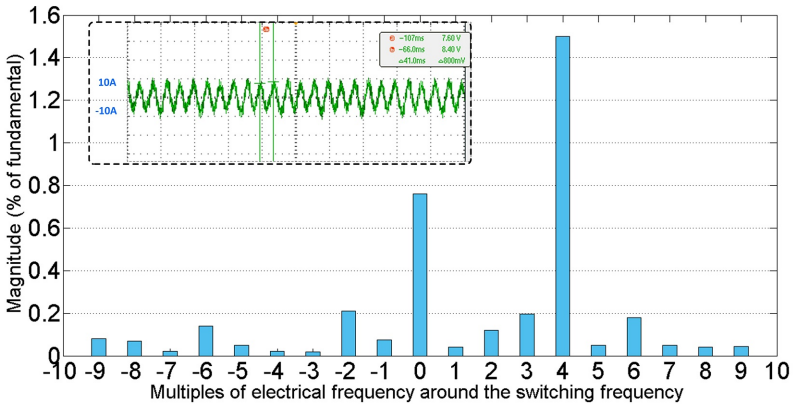

(b) FFT of the phase current in the switching frequency proximity.

Figure 2.36: Frequency-domain analysis of the phase current.

FFT of the captured phase current, considering the total spectral width, is shown in Fig. (2.36a) and the zoomed version focusing on the proximity of the switching frequency is illustrated in Fig. (2.36b). Although there are both even- and odd-order harmonics appeared around the switching frequency, the most dominant components are f_c, $f_c + 4f_e$, $f_c + 6f_e$, $f_c - 2f_e$, and $f_c - 6f_e$ which are all the even-order components (Fig. (2.36b)). Consequently, in practice, it is feasible to conclude that the most dominant harmonic components are the result of the ideal PWM.

2.4.2 PWM Process and Radial Force Harmonics

Following the same procedure as the previous sections and focusing on the switching frequency proximity, the radial force harmonic contents - with respect to the non-ideal PWM - can be obtained as:

$$\mathbb{F}\left(F_r^{Arm}\right) = f_{ei} \times 1 = f_c \pm \{1, 2, 3, 4, 5, ...\} \times f_e \tag{2.56}$$

$$\mathbb{F}\left(F_r^{PM}\right) = f_e \times \{2, 4, 6, 8, ...\} \tag{2.57}$$

$$\mathbb{F}\left(F_{ri}^{PM+Arm}\right) = f_c \pm \{0, 1, 3, 5, 7, 9, ...\} \times f_e \tag{2.58}$$

$$\mathbb{F}\left(F_{rd}^{PM+Arm}\right) = f_c \pm \{2, 4, 6, 8, ...\} \times f_e \tag{2.59}$$

- In eq. (2.56), as the result of armature-reaction and in congruence with eq. (2.51), both the even- and odd-order sidebands are appeared.
- For the PM-related components provided in eq. (2.57), there are even-order frequencies which are mostly dominant in the low-frequency zone.
- Equations (2.58) and (2.59) are respectively showing the radial force harmonics, as the result of PM and armature-reaction interactions, for ideal and deadtime-included PWM scenarios.

In terms of magnitude and as expressed in the previous sections, the harmonics generated from the interaction of PM and armature-reaction fields are dominant. Additionally, for the voltage harmonics, it was shown that the even-order components (related to the ideal PWM) have a dominant role compared to the odd-order ones (resulted from deadtime-included PWM). Consequently, it is expected that, harmonics in eq. (2.58) are more dominant than those in eq. (2.59).

2.4.3 PWM Process and Acoustic Noise Harmonics

The PMSM is operated at the constant speed of $500rpm$ with the switching frequency of $f_c = 10KHz$. In order to inspect the impact of acoustic noise sampling rate (f_{smp}), PWM deadtime (t_d), and other non-modelled nonlinearities of the inverter on the acoustic noise spectrum, three conditions are defined as follows:

- **Condition I** with $f_{smp} = 44.1KHz$ and $t_d = 1\mu s$ and the acoustic noise FFT shown in Fig. (2.37).

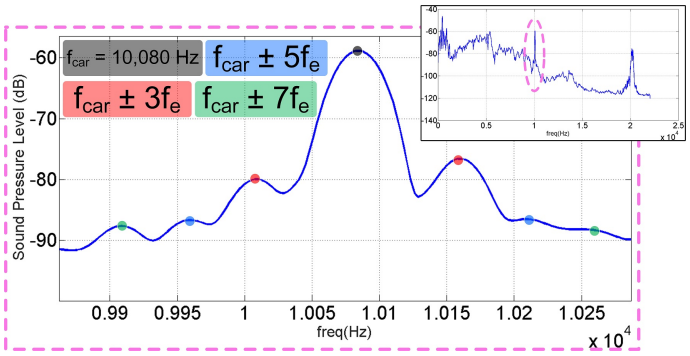

Figure 2.37: FFT of the acoustic noise in Condition I.

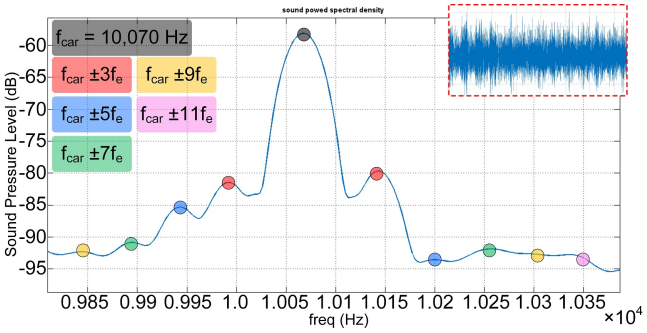

Figure 2.38: FFT of the acoustic noise in Condition II.

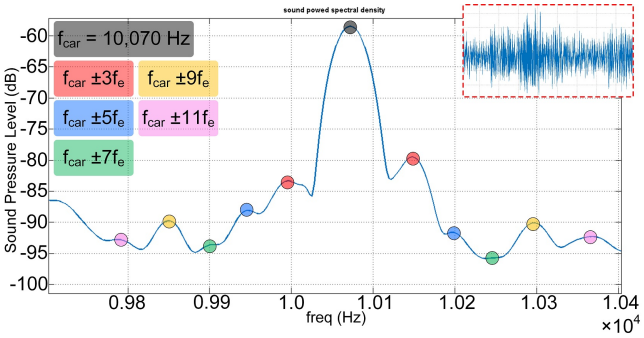

Figure 2.39: FFT of the acoustic noise in Condition III.

- **Condition II** with $f_{smp} = 44.1KHz$ and $t_d = 2\mu s$ and the acoustic noise FFT shown in Fig. (2.38).
- **Condition III** with $f_{smp} = 384KHz$ and $t_d = 1\mu s$ and the acoustic noise FFT shown in Fig. (2.39).

Figure (2.40) compares all the dominant components within the acoustic noise for the three mentioned conditions. Even though the inverter nonlinearities and PWM deadtime

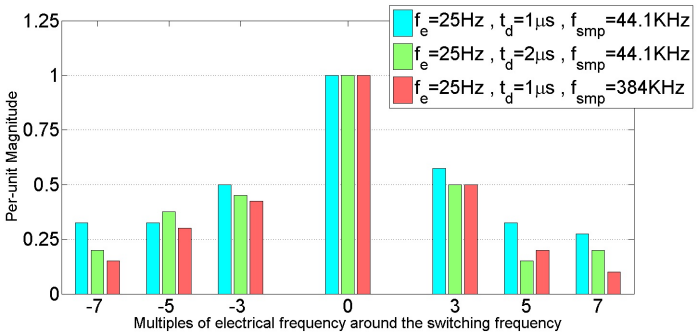

Figure 2.40: Comparison of Condition I, Condition II, and Condition III.

contaminate the current spectrum (verified in Fig. (2.36)), only the odd-order components - defined in eq. (2.58) - are appeared in the acoustic noise spectrum. The acoustic noise spectra do not contain any dominant components of even-order, which means that the odd-order components have been dominant within the radial force spectrum also. The magnitude of frequency components within the vibration and acoustic noise spectrum is highly dependent on the mechanical properties of the structure, including damping coefficients. Therefore, any radial force component with small magnitude is naturally damped and therefore is not appeared in the vibration and acoustic noise spectrum (an advantage for the signal processing and harmonic separation).

2.5 Comparison of Phase Current and Acoustic Noise Level in HFI and Injectionless Conditions

In this section, the phase current in addition to the disseminated acoustic noise level of the machine are compared, with and without HFI voltage. The terms "without HFI" or "HFIless" refer to the conditions where only the PWM voltage is applied. As the previous sections, the HFI and PWM frequencies are kept constant at respective values of $1440Hz$ and $10KHz$ while the machine is rotating at $500rpm$ with the maximum applied phase current of $22A$. Figure (2.41) illustrates the acoustic noise level of the PMSM in these two conditions. The following observation are made:

- There is a conspicuous gap between the generated peaks, which shows that the operation without HFI is naturally quieter.
- The peaks at the switching frequency have exactly the same magnitude for both con-

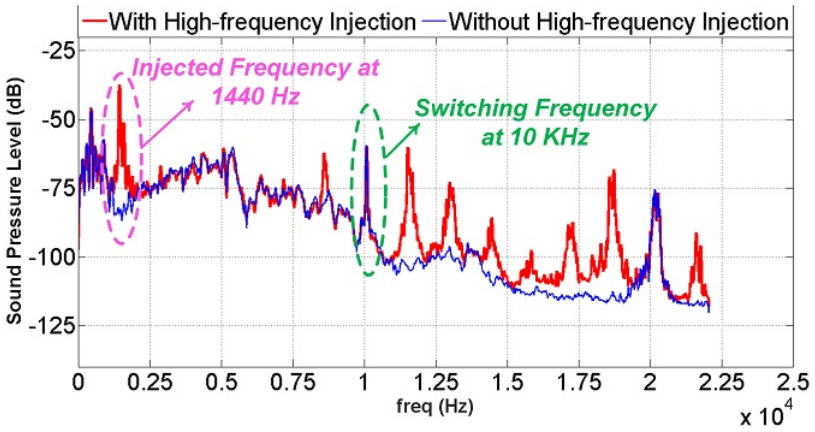

Figure 2.41: Acoustic noise level comparison in conditions with and without HFI voltage.

ditions, which means that addition of HFI voltage does not impact the components at the switching frequency.

- Applying an HFI voltage at a specific frequency not only generates the acoustic noise at that frequency but also induces additional components with relatively high magnitudes, which are all due to the resonance occurrence.

- Selection of the injection frequency in HFI condition must be done with the utmost care and with regards to the modal analysis of the stator, which ensures having components placement at appropriate zones.

The current profiles (phase current in addition to the dq-frame components) for the HFI and HFIless conditions are also compared in Fig. (2.42). For both conditions, the direct-axis current is set to zero, while the quadrature-axis current is regulated at $22A$. In the HFIless condition, the phase current has the maximum value of $22A$; however, it is increased to around $30A$ in the HFI condition. Threfore, introduction of HFI to the system has resulted in a 36% increase within the current amplitude. In addition, the impact is also tangible on the harmonics of the dq-frame current components, which are noticeably increased when HFI is applied.

2.6 Conclusion

This chapter analytically investigated the output acoustic noise of PMSM in frequency domain in special conditions. The impact of different HFI scenarios, with injection in either

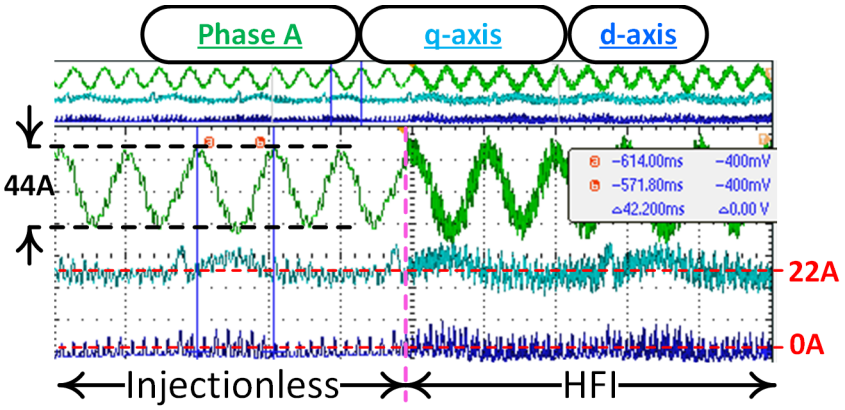

Figure 2.42: Current profile comparison in conditions with and without HFI voltage.

the $\alpha\beta$-frame or estimated dq-frame, on the harmonics of current, magnetic fields, radial force, and resulting acoustic noise was throughly investigated. Additionally, eliminating the extra HFI (HFIless), the impact of PWM voltage generation, in both ideal and non-ideal conditions, was investigated. Finally, It was shown that in both HFI and HFIless conditions, the acoustic noise spectrum hosts several specific speed dependent sidebands.

Therefore, the next chapter provides the necessary means by which the rotor position information could be extracted from the raw captured acoustic noise and be used in the control system in an active manner (for extraction of the rotor position information).

Chapter 3

Acoustic Noise-based Sensorless Control of PMSM

In the previous chapter, the acoustic noise of PMSM was deeply investigated in the frequency domain. It was shown that the acoustic noise spectrum contained several zones with speed-dependent componets. Two of the zones were given special attention:

- **HFI zone** in which, depending on the selected coordinate system for injection, there are either symmetrical even or odd multiples of the electrical fundamental frequency appeared around the injected frequency.
- **Switching frequency zone** in which there are distinctive odd-order multiples of the fundamental electrical frequency appeared around the carrier frequency, in a symmetrical manner.

Therefore, either of the zones could be used to obtain the rotor position information, which is the core of acoustic noise-based sensorless control with the overall schematic depicted in Fig. (3.1). This chapter is organized as follows:

- In order for the rotor position information to be extracted, the raw acoustic noise must be passed through a signal processing algorithm. This algorithm ensures the desired speed-dependant sidebands are properly extracted. Two different algorithms are proposed in **Section 3.1**.
- After extraction of the desired components, which carry rotor speed and position information, the observer topology (for estimation of rotor position and speed) is investigated in **Section 3.2**.

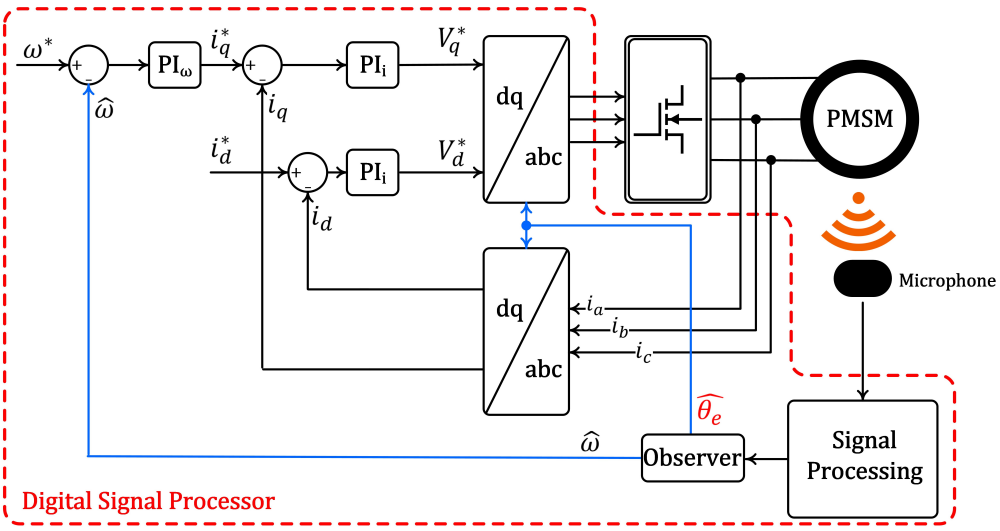

Figure 3.1: Overall schematic of a closed-loop PMSM sensorless control using the output acoustic noise.

- Modelling and stability analysis of the overall system - including the current, speed, and observer loops - are investigated in **Section 3.3**. This analysis is deemed important since the estimated values (rotor position and speed) are directly fed to the coordinate transformation blocks for the field-oriented control of PMSM.

- In **Section 3.4**, it is analytically shown that the estimated values contain specific-order harmonics. Therefore, two new observer topologies are proposed in **Section 3.5**. Compared to the conventional observer (PLL), these new observers are able to suppress the undesired estimation harmonics, which means an improved estimation performance.

- Conclusion of this chapter is provided in **Section 3.6**.

3.1 Signal Processing Algorithm

Being similar for both HFI-induced and PWM-induced acoustic noise, there are symmetrical sidebands of specific orders located around the goal frequency (which can be either HFI or the PWM carrier). In this section, two types of signal processing algorithms are presented by which a pair of orthogonal signals - which have the phase and frequency synchronized with the actual electrical frequency and position - are extracted. Successful extraction of these waveforms, with the lowest amount of extra harmonics, is an integral part of the signal

processing algorithm. In the following step, the extracted orthogonal signals are fed to an observer and the rotor speed and position are estimated.

Given each signal processing algorithm, the machine's output acoustic noise waveform is experimentally captured. Then, the signal is imported into MATLAB Simulink and the effectiveness of the proposed algorithms are verified through simulation.

3.1.1 Proposed Signal Processing - Type I

Being similar for the case of $\alpha\beta$-frame HFI and without the loss of generality, the overall diagram of the signal processing for the case of dq-frame HFI is illustrated in Fig. (3.2). The algorithm is composed of four stages:

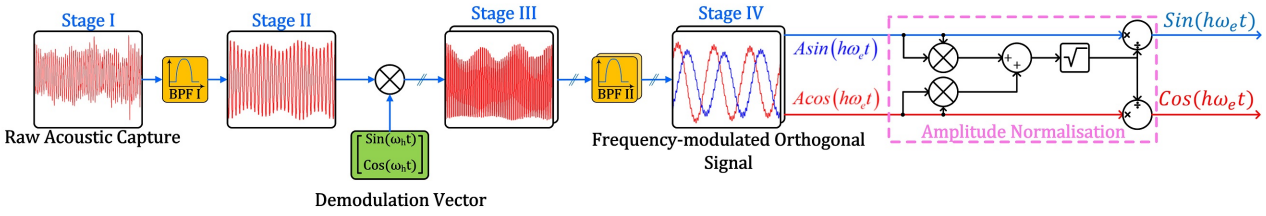

Figure 3.2: Proposed signal processing - Type I.

- **Stage I:** The raw acoustic noise is captured, which contains the full frequency spectrum. The waveform is composed of harmonics with the orders of $\sum_{n=1}^{\infty}(2n)\,f_e$, $\sum_{m=1}^{\infty} mf_{ei}$, and $\sum_{h=0,2,4,6}^{\infty} f_h \pm hf_e$ which are respectively ascribed to the fields generated by the individual impact of PM, individual impact of armature-reaction, and the mutual contribution of PM and armature-reaction. Given a condition with $f_e = 25Hz$ and $f_h = 1440Hz$, the waveforms in time and frequency domains are illustrated in Fig. (3.3).

- **Stage II:** In order to isolate the desired zone (proximity of the injected frequency at $f_h = 1440Hz$), the captured signal is passed through a band-pass filter (BPF I). Additionally, existence of this stage guarantees that any other undesired component within the acoustic spectrum is rejected; this is crucial in conditions where the environment is fraught with acoustic disturbance sources. At the end of this stage, the waveform is composed of components with the frequency of $f_h \pm h \times f_e$ where $h \in \{0, 2, 4, 6, 8, ...\}$. The width of this zone is directly dependent on the design of the BPF I.

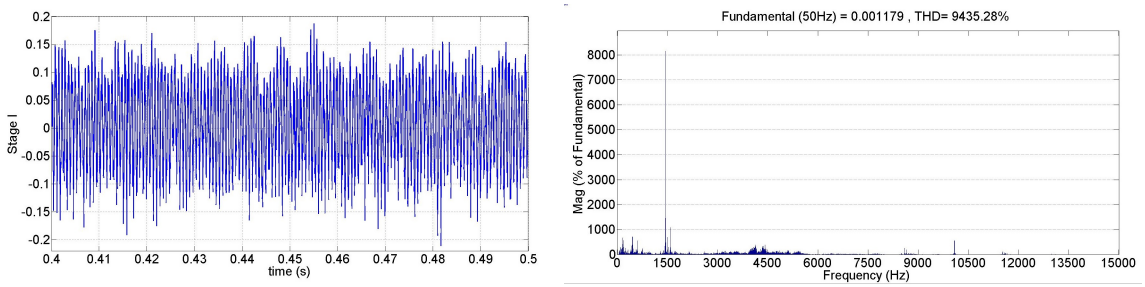

(a) Time-domain. (b) Frequency-domain.

Figure 3.3: Waveforms of Stage I.

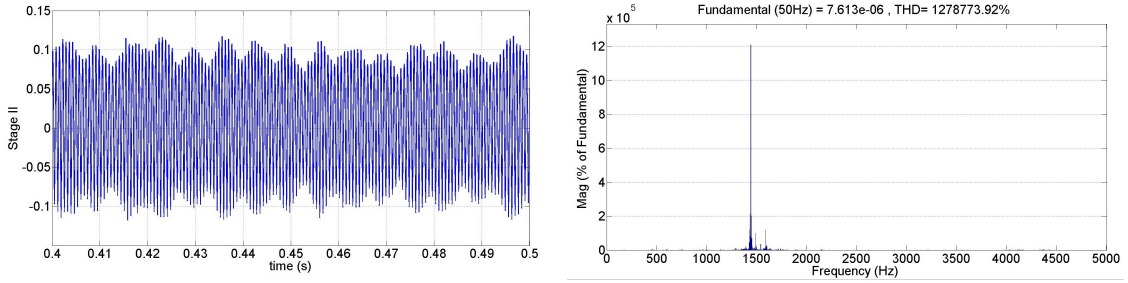

(a) Time-domain. (b) Frequency-domain.

Figure 3.4: Waveforms of Stage II.

The outputs of BPF I, in both time- and frequency-domain, are shown in Fig. (3.4). It is observed that the spectrum is just occupied by the HFI zone and all the other components are almost diminished (compared with Fig. (3.3b)).

- **Stage III:** In order to eliminate the specific component at the injected frequency, the signal is multiplied by a demodulating vector defined by $e^{\pm j\omega_h t}$. This demodulation can also be regarded as a coordinate transformation, from the stator frame to a new one rotating at the injected frequency. Therefore, all the spectral components are shifted by $\pm f_h$. The resulted waveform contains two spectral zones, one in the low-frequency at $\pm h \times f_e$ and the other around double the injected frequency at $2f_h \pm h \times f_e$.

  Also, a complex demodulation vector (instead of a single sinusoidal function) is used since a pair of orthogonal signals are to be generated from a single signal captured via the micophone. One of the two outputs of this stage, in both time- and frequency-domain, is shown in Fig. (3.5).

- **Stage IV:** The signal is again passed through another filter (BPF II) by which the

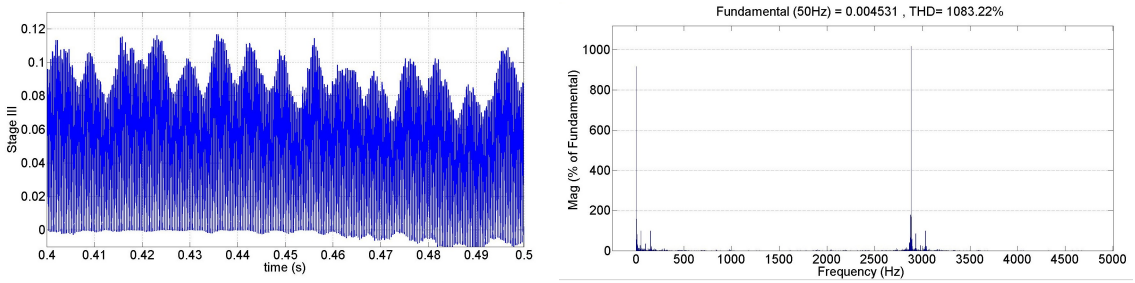

(a) Time-domain. (b) Frequency-domain.

Figure 3.5: Waveforms of Stage III.

desired component, at the low-frequency zone, is extracted. Moreover, a summary of the frequency components in each signal processing stage is provided in Table 3.1. The orthogonal waveforms have the specific frequency of $h \times f_e$, as graphically shown in Fig. (3.6). Choosing $h = 6$ (as an example), the waveforms of this stage are shown in Fig. (3.7). The output signal fundamental frequency is $150Hz$ which is equal to $6f_e^*$.

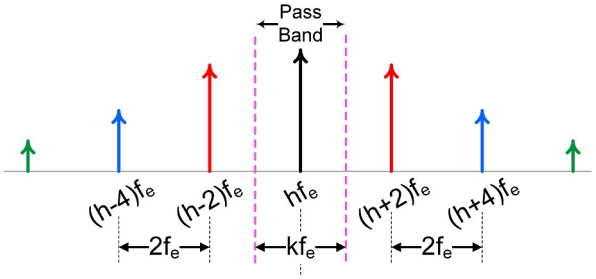

Figure 3.6: Graphical representation of extraction of the desired component through BPF II.

Table 3.1: Frequency contents in each signal processing stage.

Stage	***Frequency Components***
Stage I	$\sum_{n=1}^{\infty}(2n)\,f_e,\ \sum_{m=1}^{\infty} m f_{ei},\ \sum_{h=0,2,4,6}^{\infty} f_h \pm h f_e$
Stage II	$\sum_{h=0,2,4,6}^{\infty} f_h \pm h f_e$
Stage III	$\sum_{h=0,2,4,6}^{\infty} \pm h f_e,\ \sum_{h=0,2,4,6}^{\infty} (2f_h \pm h f_e)$
Stage IV	$\pm h f_e; h \in \{2,4,6,8,...\}$

$$A(t).e^{j(\omega_h \pm h\omega_e t)} \xrightarrow{\times e^{\pm j\omega_h t}} A(t)\left\{e^{j(2\omega_h \pm h\omega_e)t}, e^{\pm j(h\omega_e t)}\right\} \xrightarrow{BPFII} A(t).e^{\pm j(h\omega_e t)} \tag{3.1}$$

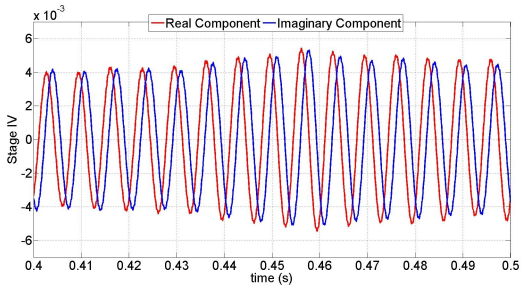

(a) Time-domain.

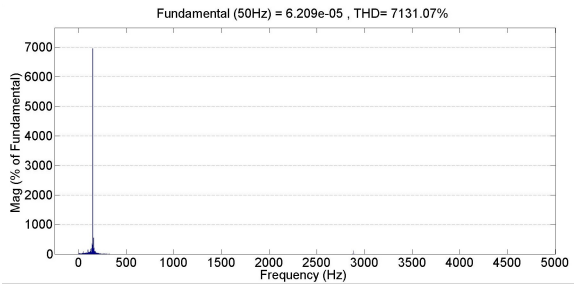

(b) Frequency-domain.

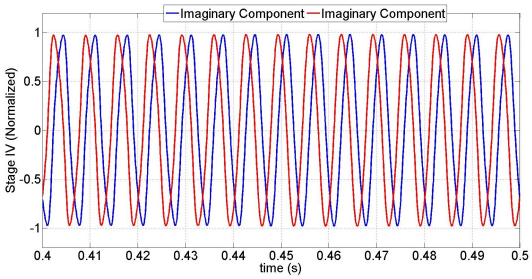

(c) Normalized.

Figure 3.7: Waveforms of Stage IV.

On the one hand, with proper design of the signal processing algorithm, accurate extraction of the desired components are guaranteed. On the other hand - due to the impacts of environmental noise, stator damping matrix at each frequency, amplitude of the injected voltage, saturation of the magnetic core, and parameter mismatch which alters the inductance values - there is no guarantee for the amplitude of the extracted signals to be always fixed. By using the orthogonality feature of the extracted waveforms, a normalization process is adopted, which provides the signals with unity amplitude in all conditions as given in eq. (3.2) where $A(t)$ denotes an arbitrary, time-varying amplitude. In the denominators, a tiny value, ϵ, is added to avoid 0/0 occurrence.

$$\begin{cases} \dfrac{A(t).\sin(h\omega_e t)}{\sqrt{(A(t).\sin(\omega_h t))^2+(A(t).\cos(\omega_h t))^2+\varepsilon}} \approx \sin(\omega_h t) \\ \dfrac{A(t).\cos(h\omega_e t)}{\sqrt{(A(t).\sin(\omega_h t))^2+(A(t).\cos(\omega_h t))^2+\varepsilon}} \approx \cos(\omega_h t) \end{cases} \tag{3.2}$$

Due to the nature of harmonics within the acoustic waveform, BPF is an integral part in the proposed algorithm. Therefore, successful tuning of the parameters is the key for the

Table 3.2: Design parameters of the band-pass filters.

Filter	***Central Frequency (fc)***	***Passing Band (fb)***
BPF I	f_h	$f_e^* \times h \times i$
BPF II	$h \times f_e^*$	$k \times f_e^*$

extraction of the desired components. The general transfer function of a BPF is defined as:

$$H_{BPF}(s) = C\frac{(2\pi f_b)\, s}{s^2 + (2\pi f_b)\, s + (2\pi f_c)^2} \tag{3.3}$$

where C, f_b, and f_c are respectively the gain, passing band, and central frequency of the filter. Given the different frequencies each BPF is designed to be working at, dissimilar parameters must be used as presented in Table. 3.2. For each filter, the central frequency and the passing band are made adaptive to the reference electrical frequeny (f_e^*). Two design parameters defined as $1 \leqslant i \leqslant 10$ and $0 \leqslant k \leqslant 2$ are defined which can be replaced by 1 in an ideal condition.

Tunable parameters are selected to improve the filtering robustness in face of stochastic environmental noise and non-modelled real-time conditions, which can cause small frequency drifts. Additionally, the bandwidth of BPF I has a noticeable impact on the overall transient response of the whole signal processing chain. At the same time, proper design of this filter plays a cardinal role in rejection of unwanted environmental distortions. Therefore, it is possible to choose different values for the parameter i in a trade-off manner while respecting $1 \leqslant i \leqslant 10$.

As the result, transfer functions of the two BPFs, included within the signal processing chain, are obtained as:

$$BPF\,I(s) = C_I\frac{(2\pi \times f_e^* \times h \times i)\, s}{s^2 + (2\pi \times f_e^* \times h \times i)\, s + (2\pi \times f_h)^2} \tag{3.4}$$

$$BPF\,II(s) = C_{II}\frac{(2\pi \times k \times f_e^*)\, s}{s^2 + (2\pi \times k \times f_e^*)\, s + (2\pi \times h \times f_e^*)^2} \tag{3.5}$$

In order to investigate the performane of BPF I and BPF II, i and k are iteratively changed while the other parameters are kept constant and bode diagrams are plotted as shown in Fig. (3.8). In this plot, $h = 6$, $f_e = 25Hz$, and $f_h = 1440Hz$; therefore, the central frequency of BPF II is located at $150Hz$.

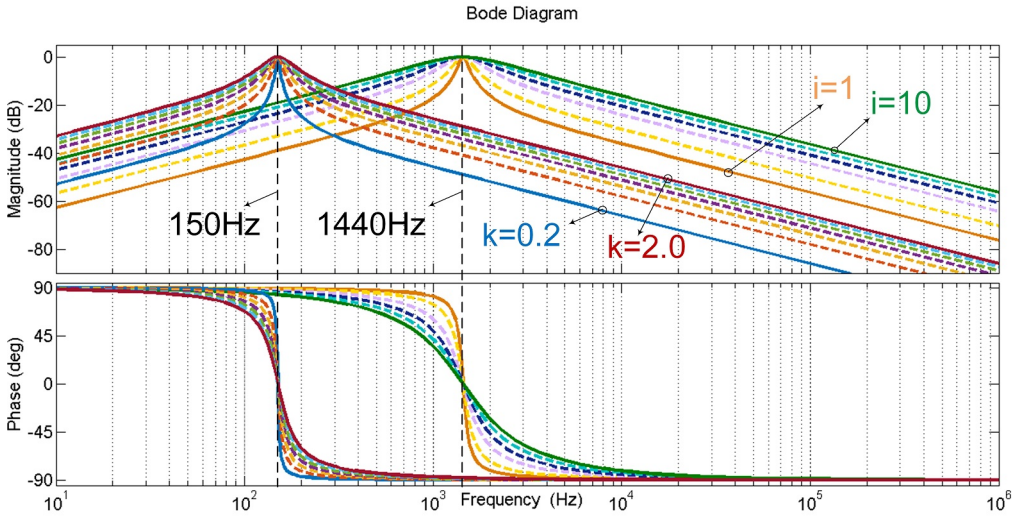

Figure 3.8: Bode diagram of BPF I and BPF II for different values of i and k.

3.1.2 Proposed Signal Processing - Type II

Application of adaptive neural networks, in the forms of Perceptron, ADALINE, and MADALINE, for pattern detection is introduced in [198]. The adaptive linear neuron or adaptive linear element (ADALINE) is a single-layer neural network which can serve as an efficient adaptive filter too [199].

Instead of using two stages of BPF in the signal processing chain, this algorithm extracts the desired component by incorporating a single-stage ADALINE-based filter. Similar to the previous case, the algorithm is explained for the dq-frame HFI condition although it is applicable to other scenarios.

3.1.2.1 ADALINE-based Filter

Assuming the input to be an arbitrary periodic signal, which can be broken into the sum of sinusoidal terms through the Fourier Series expansion, one can define it as:

$$f(t) = f_{dc} + \sum_{n=1}^{\infty} \left(a_n \sin(n\omega t) + b_n \cos(n\omega t)\right) \tag{3.6}$$

Moreover, considering the linear multiplication of matrix elements shown below,

$$F(t) = W^T.X \tag{3.7}$$

$$W = \begin{bmatrix} \alpha_0 \\ \alpha_1 \\ \beta_1 \\ \vdots \\ \alpha_n \\ \beta_n \end{bmatrix} \tag{3.8}$$

$$X = \begin{bmatrix} 1 \\ \sin(\omega t) \\ \cos(\omega t) \\ \vdots \\ \sin(n\omega t) \\ \cos(n\omega t) \end{bmatrix} \tag{3.9}$$

Equation (3.7) yields:

$$F(t) = \alpha_0 + \alpha_1 \sin(\omega t) + \beta_1 \cos(\omega t) + \cdots + \alpha_n \sin(n\omega t) + \beta_n \cos(n\omega t) \tag{3.10}$$

comparing eq. (3.10) and eq. (3.6), one could find a one-to-one correspondence; therefore, eq. (3.6) is linearly synthesized if and only if:

$$f(t) = F(t) \Leftrightarrow \begin{cases} \alpha_0 = f_{dc} \\ \alpha_1 = a_1 \\ \beta_1 = b_1 \\ \vdots \\ \alpha_n = a_n \\ \beta_n = b_n \end{cases} \tag{3.11}$$

This linear decomposition is realized by a multi-input, single-output neural network which has a single hidden layer. Adopting such a method, X and W respectively serve as the input and weight matrices of the neural network.

Assuming only knowing the input signal frequencies and if the input waveform is to be perfectly synthesized, the weight matrix must be made equal to the signal fourier series's coefficients. Therefore, a recursive algorithm - like the least-mean square (LMS) - is adopted and the weight matrix is continuously updated until the perfect match is reached (shown in eq. (3.13)). This algorithm serves as a non-linear feedback system, so the error between the

actual input and the ADALINE output

$$d(t) = f(t) - F(t) \tag{3.12}$$

is made zero (in this case, the ADALINE output is equal to the input signal). In order to provide control over the convergernce speed, an additional coefficient μ (called the learning rate) is introduced, which must always be $0 < \mu < 1$. Convergence speed is directly proportional to the learning rate, yet assigning high values to this parameter leads to unstability and divergence. Given the nature of the input signal and the non-linear structure of ADALINE, the value of μ is defined through trial and error. The overall structure of an ADALINE network is also illustrated in Fig. (3.9).

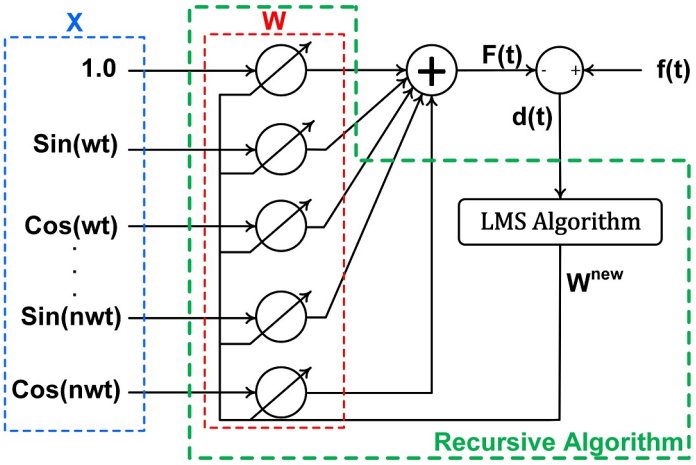

Figure 3.9: ADALINE network.

$$W^{new} = W^{old} + X^{old}.\mu.d \tag{3.13}$$

Following the same principle, ADALINE could be used as a filter (for extraction of a desired component from an arbitrary input):

- The desired components are used as the matrix X.
- The error term, in contrast to the usual scenario, is not zero. It is, in fact, the input waveform from which the desired components are subtracted.
- The values of matrix W are the actual amplitudes of the desired extracted signals. Therefore, ADALINE provides inherent normalization algorithm.

The adaptive filtering capability of ADALINE has led to its widespread use within the power system applications, including harmonic detection, active power filters, power conditioning mechanisms, online harmonic tracking, estimation of the power system frequency, and grid-synchronization [200–207].

ADALINE has also been used within the sensorless control of PMSM in order to improve the estimation performance. In order to suppress the undesired low-order harmonics within the EMF, the estimated EEMF is passed through an ADALINE, which results in an improved rotor position estimation [208]. In addition, ADALINE is also used for sensorless implementation of a five-phase PMSM, in which an ADALINE is put in series with the position observer [209]. Existence of non-sinusoidal EMF in PMSM results in currents with extra harmonic contaminations. Repressing these current harmonics, an ADALINE-based current harmonic suppression algorithm is proposed in [210]. The ADALINE is used to generate an adaptive feed-forward voltage, which is placed within the control loops.

3.1.2.2 Proposed ADALINE-based Signal Processing

Graphical representation of the proposed ADALINE-based signal processing is depicted in Fig. (3.10). The algorithm comprises three stages:

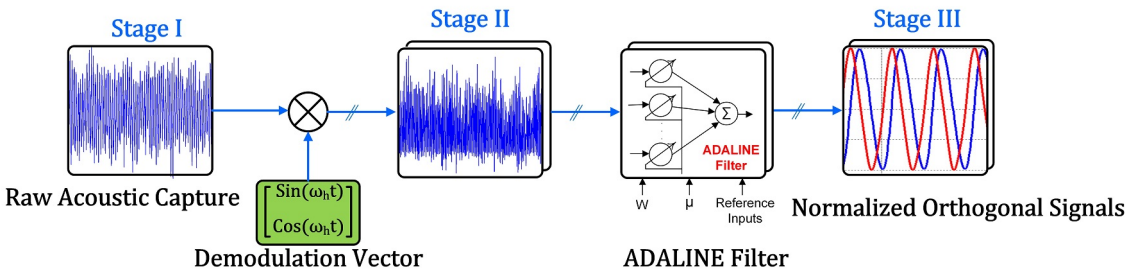

Figure 3.10: Signal processing - Type II.

- **Stage I**: the raw acoustic noise is captured via the microphone. This stage is exactly similar to the first stage of the previous signal processing algorithm.
- **Stage II**: the input acoustic waveform is directly demodulated by the vector $e^{\pm j\omega_h t}$, which results in the spectral displacement. Given a condition with $f_e = 25Hz$ and $f_h = 1440Hz$, the waveforms of this stage in both time- and frequency-domain are illustrated in Fig. (3.11).

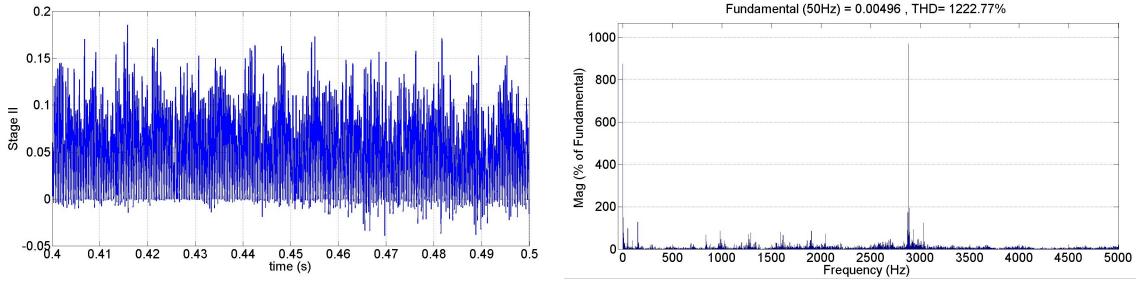

(a) Time-domain. (b) Frequency-domain.

Figure 3.11: Waveforms of Stage II.

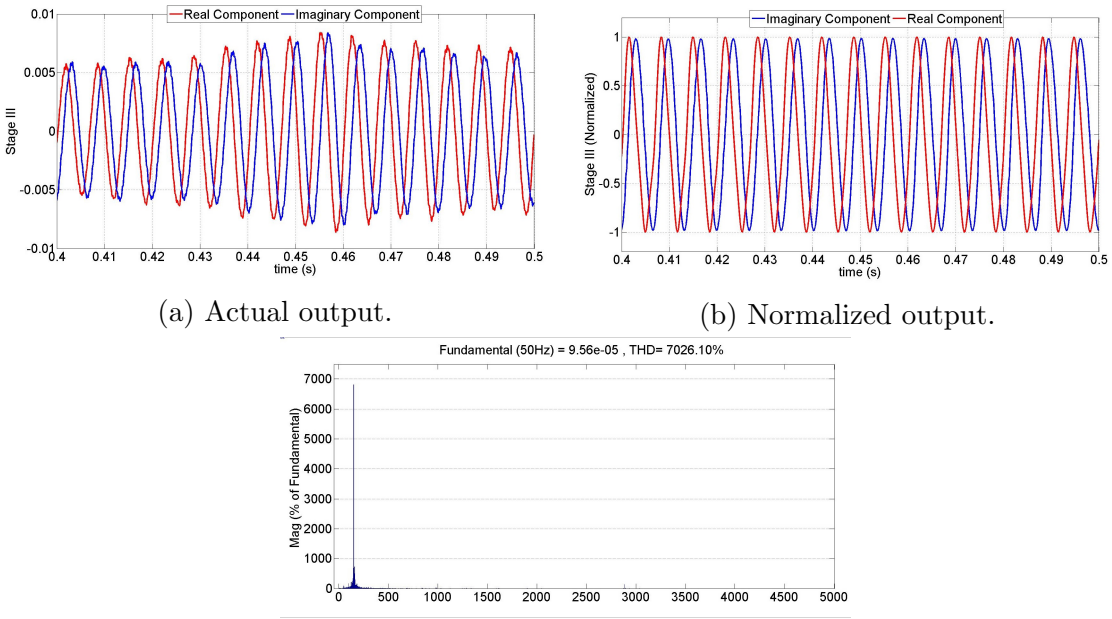

(a) Actual output. (b) Normalized output.

(c) Output FFT.

Figure 3.12: Waveforms of Stage III.

- **Stage III**: the desired component, located in the low-frequency zone, is extracted by using an ADALINE filter. For the operating point of $f_e = 25Hz$, $h = 6$, and $f_h = 1440Hz$, the extracted signals are illustrated in Fig. (3.12). It is clear that the ADALINE filter has been sucessful in precise extraction of the desired component at $150Hz$. As the ADALINE, inherently, estimates the desired harmonic amplitude, the normalization can also be embedded within the ADALINE.

3.2 Estimation of Rotor Speed and Position

At the output of the signal processing chain, a pair of speed-dependent orthogonal signals were obtained. Due to this inherent characteristic, the phase and frequency of these signals (which are linearly related to the electrical fundamental component) could be estimated through using an observer.

Assuming the normalized version of the two extracted signals to be respectively defined as:

$$\begin{cases} x_1 = \sin\left(h\omega_e t\right) \\ x_2 = x_1^{\perp} = \cos\left(h\omega_e t\right) \end{cases} \tag{3.14}$$

the instantaneous estimated phase ($\hat{\theta}_e$) and frequency ($\hat{\omega}_e$) are obtained as follows.

$$h\hat{\theta}_e = \tan^{-1}\left(\frac{x_1}{x_2}\right) = h\hat{\omega}_e t \;\; ; \;\; -\pi \leqslant h\hat{\theta}_e \leqslant +\pi \tag{3.15}$$

$$\dot{\hat{\theta}}_e = \hat{\omega}_e \tag{3.16}$$

Using the inverse-tangent function, the phase is instantaneously obtained as a sawtooth waveform ranging from $-\pi$ and π (shown in Fig. (3.13b)) and the frequency is the time derivation of the phase. Existence of a time-derivative element, boosts the system susceptibility to any sudden transition in the input or noise. Therefore, using this method for extraction of phase and frequency is not deemed suitable in this dissertation.

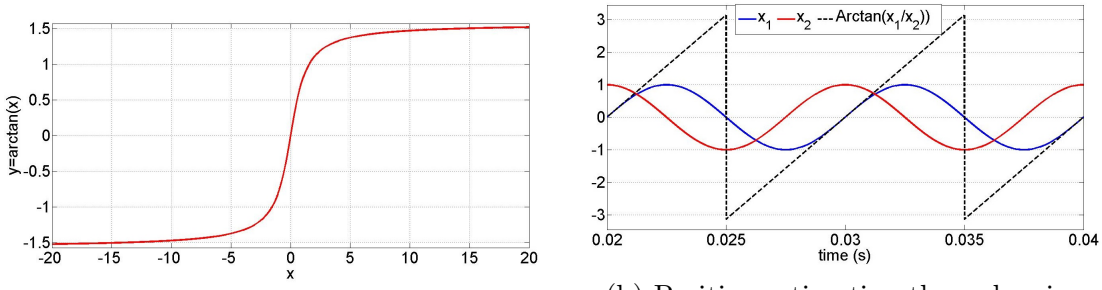

(a) Arctan curve.

(b) Position estimation through using Arctan function.

Figure 3.13: Estimation using Arctan function.

3.2.1 Quadrature Phase-Locked Loop (QPLL)

Figure (3.14) shows the observer used for the estimation of phase and frequency of the extracted signals. Since a pair of orthogonal signals (given in eq. (3.14)) are extracted, a PLL with heterodyning structure is used and the input phase and frequency are estimated. Dynamic equations of the QPLL can be written as:

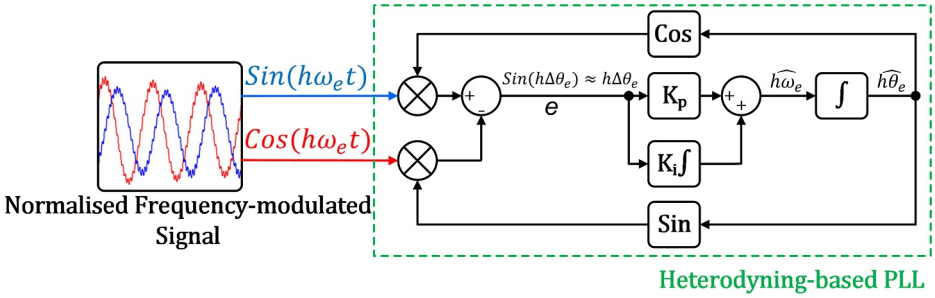

Figure 3.14: QPLL structure.

$$e = \left(x_1.\cos\left(h\hat{\theta}_e\right)\right) - \left(x_2.\sin\left(h\hat{\theta}_e\right)\right) = \sin\left(h\theta_e\right).\cos\left(h\hat{\theta}_e\right) - \sin\left(h\hat{\theta}_e\right).\cos\left(h\theta_e\right)$$
$$= \sin\left(h\underbrace{\left(\theta_e - \hat{\theta}_e\right)}_{\Delta\theta}\right) \tag{3.17}$$

$$h\dot{\hat{\theta}}_e = h\hat{\omega}_e \tag{3.18}$$

$$h\ddot{\hat{\theta}}_e = K_p.\dot{e} + K_i.e \tag{3.19}$$

where

- K_p denotes the proportional gain of the PI regulator.
- K_i denotes the integral gain of the PI regulator.
- e denotes the estimation error.

In the steady-state condition, due to the existence of the PI regulator within the QPLL structure, the estimation error would be zero. Therefore, in the Laplace domain, the forward-path transfer function of QPLL is obtained as:

$$G_{QPLL}^{frw} = L\left\{\frac{h\hat{\theta}_e}{e}\right\} = \frac{\hat{\Theta}}{E} = \frac{K_p s + K_i}{s^2} \tag{3.20}$$

In the steady-state condition, where $\sin(h\Delta\theta) \approx h\Delta\theta \approx 0$, the linearized version of QPLL could be used as shown in Fig. (3.15). Accordingly, the closed-loop transfer function of the QPLL could be defined as follows.

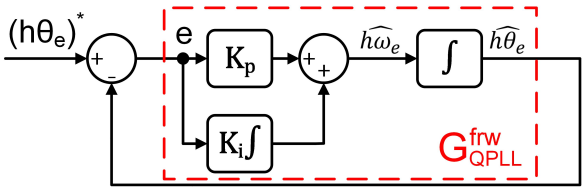

Figure 3.15: Linearized QPLL.

$$G_{QPLL} = \frac{G_{QPLL}^{frw}}{1 + G_{QPLL}^{frw}} = \frac{K_p s + K_i}{s^2 + K_p s + K_i} \tag{3.21}$$

The closed-loop transfer function of QPLL represents an ordinary second-order system with the characteristic equation defined as:

$$s^2 + k_p s + k_i \triangleq s^2 + 2\xi\omega_n s + \omega_n^2 \tag{3.22}$$

where ξ is the damping coefficient and $\omega_n = h\omega_e$ is the undamped natural frequency of the system. As the result, the PI regulator parameters are tuned as:

$$\begin{cases} K_p = 2\xi\omega_n \\ K_i = (\omega_n)^2 \end{cases} \tag{3.23}$$

Stability and dynamic response of QPLL is controlled by the roots of the charcteristic equation, which are in fact the poles of the closed-loop transfer function. The roots are:

$$s_{1,2} = \omega_n \left(-\xi \pm \sqrt{\xi^2 - 1} \right) \tag{3.24}$$

As ω_n is a positive number, ξ plays a cardinal role in the QPLL behaviour.

$$s_{1,2} = \omega_n \left(-\xi \pm \sqrt{\xi^2 - 1} \right) = \begin{cases} \omega_n \left(-\xi \pm \sqrt{\xi^2 - 1} \right) \ ; \ \xi > 1 (over - damped) \\ -\xi\omega_n \ ; \ \xi = 1 (critically - damped) \\ \omega_n \left(-\xi \pm j\sqrt{1 - \xi^2} \right) \ ; \ 0 < \xi < 1 (under - damped) \end{cases} \tag{3.25}$$

For a condition with $\omega_n = 2 * \pi * (6 * 25)$, the value of ξ is sweped from 0.6 to 1.5 and the

bode diagram and step response of the QPLL are respectively plotted in Fig. (3.16) and Fig. (3.17). Although change in the values of ξ has resulted in different transient responses, the QPLL has maintained its stability as the step reference value is perfectly followed and the phase margin, at the goal frequency of $150Hz$, is positive ($45 < P.M < 67.5$).

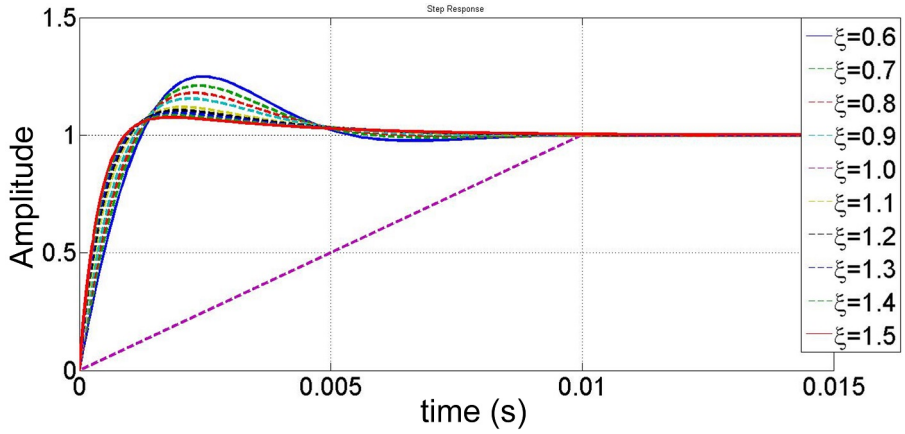

Figure 3.16: Step response of QPLL.

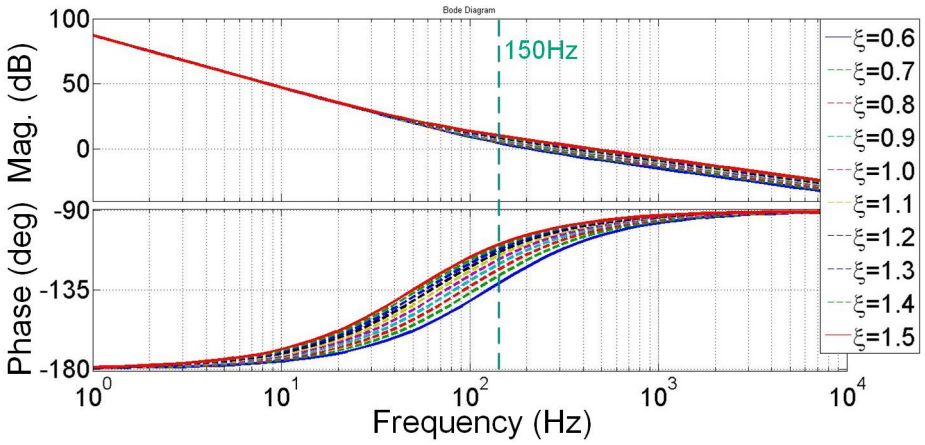

Figure 3.17: Bode diagram of QPLL.

Verifying the QPLL performance in estimation of the frequency and phase of the processed signals, a simulation is carried out for a condition where $h = 6$ and $f_e = 25Hz$. In this condition, the output of signal processing (for both Type I and Type II) are fed to a QPLL and the phase and frequency are estimated. The QPLL parameters are chosen as shown in eq. (3.23) and the results are illustrated in Fig. (3.18); regardless of the signal processing type, the QPLL is able to correctly estimate the phase and frequency with complete stability.

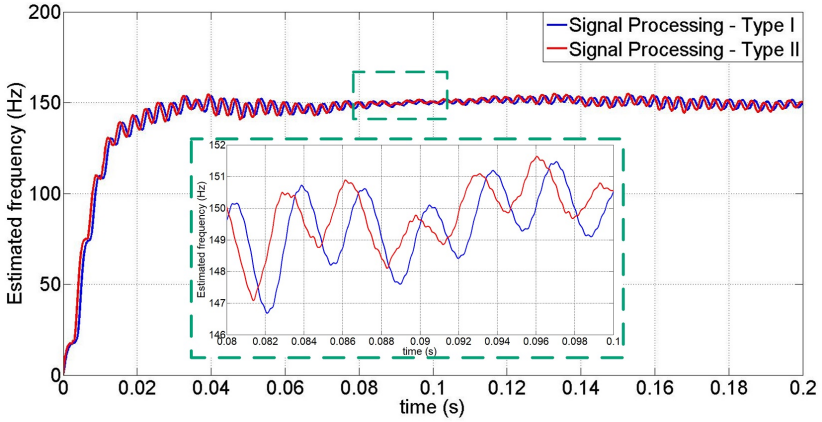

(a) Estimated frequency.

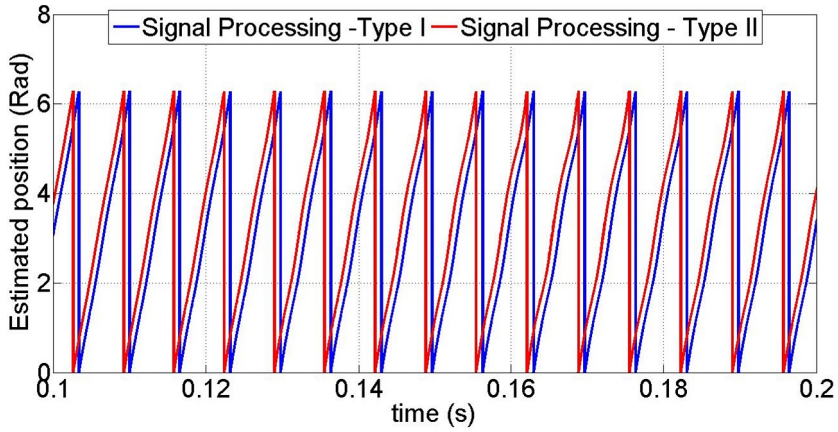

(b) Estimated position.

Figure 3.18: Estimation performance comparison between the proposed Type I and Type II signal processing algorithms.

As it is observed that there is a small shift between the estimated positions of the two methods, which is ascribed to the difference among the estimated frequencies. It is possible to make the performances similar, by fine-tuning the learning rate of the ADALINE (signal processing TypeII) and/or the parameters of the BPF II (signal processing TypeI).

3.3 Design of Control Loops and Stability Analysis

Field-oriented sensorless speed control of a PMSM follows a block diagram representation shown in Fig. (3.19). The system comprises three different loops:

- **Current loop** is the most internal loop by which the flux and electromagnetic torque

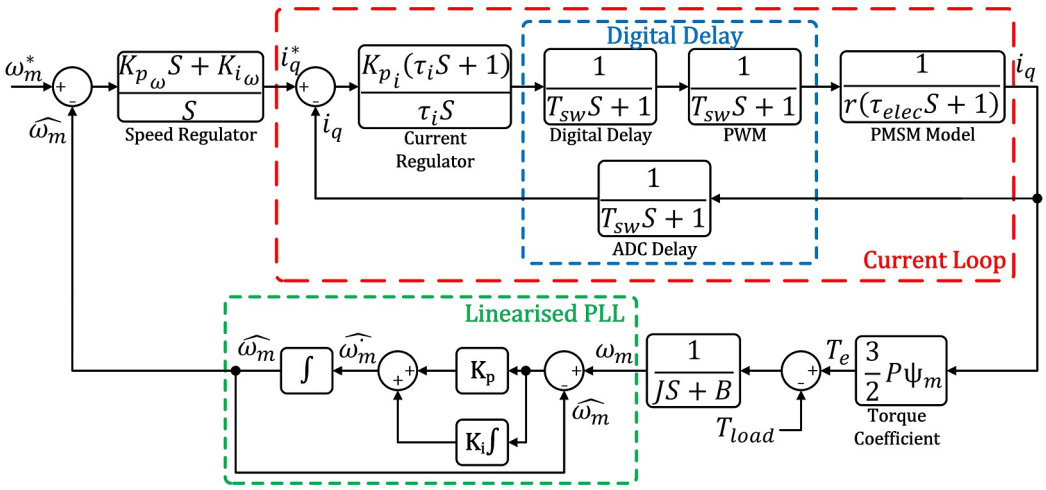

Figure 3.19: Overall block diagram representation of PMSM speed control.

are controlled, by directly regulating the d- and q-axis currents. The time constant of the current loop, as this loop is the most internal loop within the system, must be chosen to be the smallest, compared to other loops.

- **Speed loop** is the external loop through which the mechanical speed of the rotor is controlled. Compared to the current loop, this loop must have a time constant hundreds of time larger. This is also physically justifiable since the transient response of mechanical speed is considerably slower than the electrical current.

- **Linearized PLL** is another loop which is especially important in sensorless control. As the PLL has a closed-loop structure, with its own poles and zeros, its structure possesses an integral role in the overall stability of the system. Not only must the PLL be appropriately tuned, so as to provide an accurate and stable estimation, but also its interaction with the current and speed loops must be taken into cinsideration - as there exists an inextricable connection between all the loops within the system. It is to be mentioned that, in normal applications having position sensor, the linearized PLL transfer function can be easily replaced by a digital delay equal to the ADC sampling rate.

3.3.1 Current Loop

Structure of the current control loop is identical for both the d- and q-axis; therefore, only the tuning procedure for the q-axis is provided here. Given the synchronous-frame voltage

equations as below,

$$V_d = R_s i_d + \frac{d}{dt}\psi_d - \omega_e \psi_q \tag{3.26}$$

$$V_q = R_s i_q + \frac{d}{dt}\psi_q + \omega_e \psi_d \tag{3.27}$$

the two equations are coupled and therefore cannot be independently controlled. As the result, a decoupling term - exactly equal to the coupling terms - is added to each voltage making them linearly separable and feasible to be independently controlled. After the decoupling stage, a direct transfer function for the electrical part of the system could be defined as below:

$$\frac{I_d}{V_d} = \frac{1}{R_s\left(1 + \tau_{sd} s\right)} \;\; ; \;\; \tau_{sd} = \frac{L_d}{R_s} \tag{3.28}$$

$$\frac{I_q}{V_q} = \frac{1}{R_s\left(1 + \tau_{sq} s\right)} \;\; ; \;\; \tau_{sq} = \frac{L_q}{R_s} \tag{3.29}$$

Without the loss of generality, the rest of the analysis is merely dedicated to the q-axis current. Within the current loop, three digital delays are modelled to represent the actual scenario in digital signal processing. The delays related to the interrupt service routine (ISP) in each cycle, PWM of the inverter, and the unit-delay block essential for closing the feedback loop are all modelled by a first-order delay element shown in eq. (3.30). In digital implementation of PMSM control, a universal interrupt governs the whole system by which synchronous execution of code, PWM pulse generation, and ADC readings is ensured.

$$Delay\ \ Element = \frac{1}{T_{sw} s + 1} \tag{3.30}$$

Revised version of the current loop, with a unit feedback path, is depicted in Fig. (3.20). So, the forward-path transfer function is obtained as:

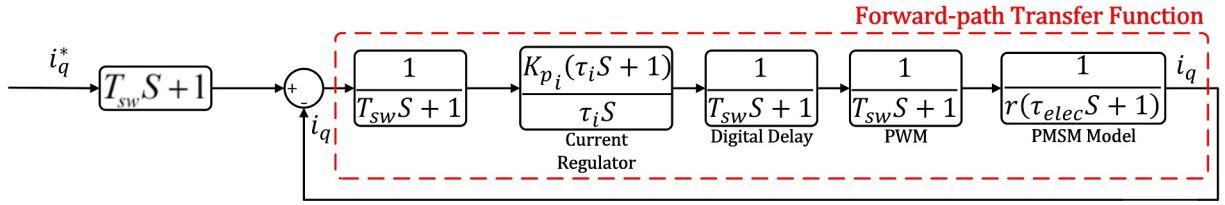

Figure 3.20: Current loop with a unit feedback path.

$$G_i^{frw} = \frac{K_{p_i}\left(\tau_i s + 1\right)}{\tau_i s} \cdot \frac{1}{T_{si} s + 1} \cdot \frac{1}{R_s\left(\tau_{elec} s + 1\right)} \tag{3.31}$$

where

- K_{p_i} denotes the proportional gain of the PI regulator within the current loop.
- K_{I_i} denotes the integral gain of the current loop PI regulator.
- τ_i represents the PI loop time constant.
- $T_{s_i} = 3T_{sw}$ is the accumulated time constant of the digital delay elements within the current loop.
- τ_{elec} is the electrical time constant of the PMSM model.

In order to cancel the impact of the slowest pole, close to the imaginary axis, the zero of the PI regulator must be equal to the pole of the PMSM model; therefore:

$$\tau_i = \tau_{elec} \rightarrow \frac{K_{p_i}}{K_{I_i}} = \frac{L_q}{R_s} \tag{3.32}$$

Based on the optimum-modulus (OM) criterion and eq. (3.32), the following relationship is obtained:

$$G_i^{frw} = \frac{K_{p_i}}{\tau_i s} \cdot \frac{1}{3T_{sw}s + 1} \cdot \frac{1}{r} \triangleq \frac{1}{2\xi s\left(\xi s + 1\right)} \rightarrow \frac{K_{p_i}}{r\tau_i} = \frac{1}{2T_{si}} \tag{3.33}$$

$$G_i^{frw} = \frac{1}{2T_{si}^2 s^2 + 2T_{si}s} \tag{3.34}$$

the overall closed-loop transfer function of the current loop is equal to:

$$G_i = (T_{sw}s + 1) \cdot \frac{G_i^{frw}}{1 + G_i^{frw}} \approx \frac{1}{1 - T_{sw}s} \cdot \frac{1}{2T_{si}^2 s^2 + 2T_{si}s + 1} \tag{3.35}$$

As $T_{si} = 3T_{sw}$, the term T_{si}^2 can be neglected and eq. (3.35) be simplified as a first-order delay element, to be used within the speed loop, shown by:

$$G_i \approx \frac{1}{1 - T_{sw}s} \cdot \frac{1}{6T_{sw}s + 1} \approx \frac{1}{5T_{sw}s + 1} \tag{3.36}$$

Given the available PMSM with $R_s = 97m\Omega$, $L_d = 140\mu H$, $L_q = 178\mu H$, and $T_{sw} = 1e^{-4}s$, the current loop's PI parameters are tuned as given in eq. (3.37).

$$\begin{cases} \tau_{iq} = \frac{L_q}{R_s} = \frac{178\mu H}{97m\Omega} = 1.83505 \times 10^{-3}s \\ K_{p_{iq}} = 0.297 \\ K_{I_{iq}} = 161.848451 \end{cases} \quad \begin{cases} \tau_{id} = \frac{140\mu H}{97m\Omega} = 1.44 \times 10^{-3}s \\ K_{p_{id}} = 0.2328 \\ K_{I_{id}} = 161.667 \end{cases} \tag{3.37}$$

Bode diagram of the forward-path transfer function of the q-axis current loop is illustrated in Fig. (3.21); the system is stable with a phase margin equal to 65.5°. Step responses of the system, considering the actual and approximated models respectively provided in eq. (3.35) and eq. (3.36), are compared in Fig. (3.22). Although the transient behaviour of the two models are different, the settling times are similar and both showcase a robust and stable performance.

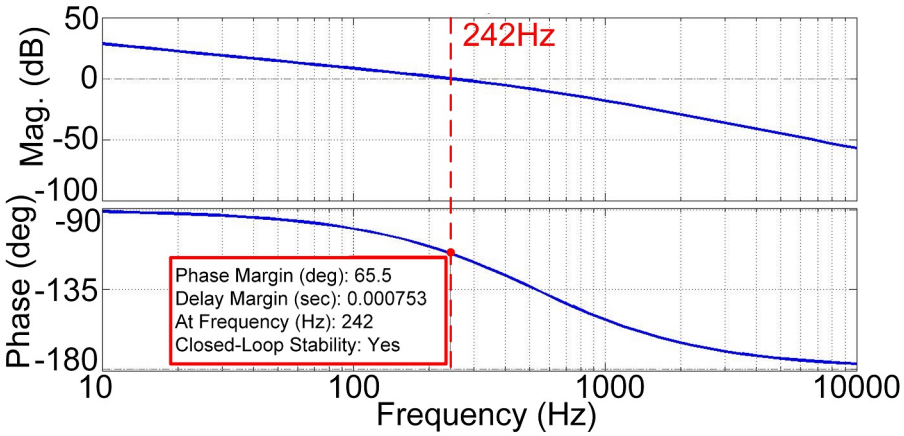

Figure 3.21: Bode diagram of the q-axis current loop.

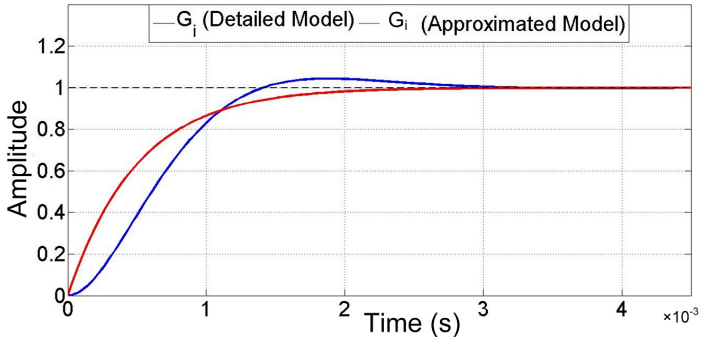

Figure 3.22: Step response of the closed-loop q-axis current loop.

3.3.2 Speed Loop

The speed loop dynamics is governed by the mechanical equation of motion:

$$T_e - T_\ell = J\frac{d\omega_m}{dt} + B\omega_m \tag{3.38}$$

in which

- T_e represents the generated electromagnetic torque.
- T_ℓ represents the applied load torque.
- J denotes the shaft moment of inertia.
- B denotes the frictional loss coefficient.
- ω_m is the rotor mechanical angular velocity.

In this equation, the load torque acts as an external disturbance to the system, against which the speed performance must be stable and robust. The overall block diagram of the speed loop is depicted in Fig. (3.23). The current loop is replaced by eq. (3.36), two first-order delays are addd to model the digital delays in the actual loop execution, and the speed observer - which can be the PLL or the position sensor - is added to the feedback path.

It is to be mentioned that, the linearized PLL model can also be regarded as a speed observer:

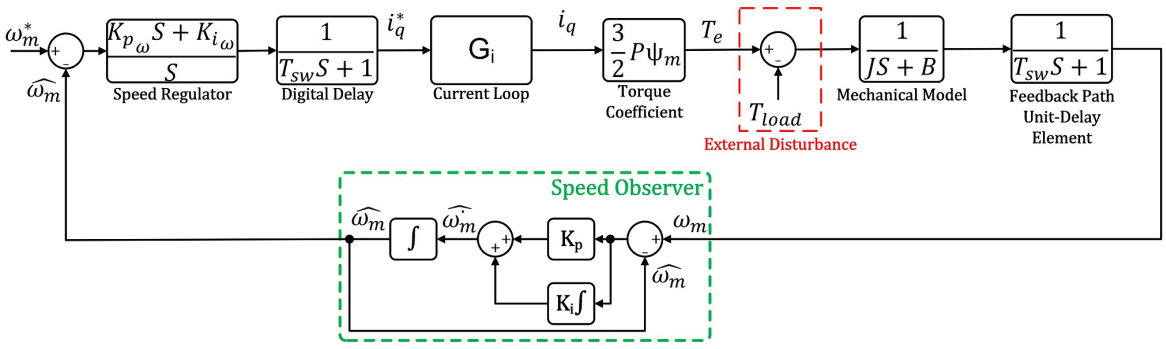

Figure 3.23: Simplified model of the speed loop, taking into acount the approximate model of the current loop in addition to the linearized PLL.

$$G_{QPLL} = \frac{\hat{\omega}_e}{\omega_e} = \frac{s.\hat{\theta}_e}{s.\theta_e} = \frac{K_p s + K_i}{s^2 + K_p s + K_i} \tag{3.39}$$

The forward-path transfer function of the speed loop is obtained accordingly as:

$$G_{\omega}^{frw} = \alpha.G_{QPLL}.\frac{K_{P_\omega}s + K_{i_\omega}}{s}.\frac{1}{T_{eq}s+1}.\frac{1}{Js+B} = \alpha.\frac{a_2s^2 + a_1s + a_0}{b_5s^5 + b_4s^4 + b_3s^3 + b_2s^2 + b_1s} \quad (3.40)$$

$$\begin{cases} a_2 = K_pK_{P_\omega} \\ a_1 = K_pK_{i_\omega} + K_iK_{P_\omega} \\ a_0 = K_iK_{i_\omega} \\ \alpha = 1.5p\psi_m \end{cases} \quad \begin{cases} b_5 = T_{eq}J \\ b_4 = T_{eq}B + J + T_{eq}JK_p \\ b_3 = B + T_{eq}BK_p + JK_p + T_{eq}JK_i \\ b_2 = BK_p + T_{eq}BK_i + JK_i \\ b_1 = BK_i \end{cases} \quad (3.41)$$

and the closed-loop transfer function of the speed loop is obtained as:

$$G_{\omega} = \frac{1}{G_{QPLL}}.\frac{G_{\omega}^{frw}}{1+G_{\omega}^{frw}} = \frac{c_2s^2 + c_1s + c_0}{d_5s^5 + d_4s^4 + d_3s^3 + d_2s^2 + d_1s + d_0} \quad (3.42)$$

$$\begin{cases} c_2 = \alpha K_pK_{P_\omega} \\ c_1 = K_pK_{i_\omega} + K_iK_{P_\omega} \\ c_0 = K_iK_{i_\omega} \end{cases} \quad \begin{cases} d_5 = T_{eq}J \\ d_4 = T_{eq}B + J + T_{eq}JK_p \\ d_3 = B + T_{eq}BK_p + JK_p + T_{eq}JK_i \\ d_2 = \alpha K_pK_{P_\omega} + BK_p + T_{eq}BK_i + JK_i \\ d_1 = \alpha\left(K_pK_{i_\omega} + K_iK_{P_\omega} + BK_i\right) \\ d_0 = \alpha K_iK_{i_\omega} \end{cases} \quad (3.43)$$

where

- K_{p_ω} represents the proportional gain of the speed loop PI regulator.
- K_{i_ω} represents the interal gain of the speed loop PI regulator.
- $T_{eq} = 5T_{sw} + 2T_{sw} = 7T_{sw}$.

The speed loop controller can be tuned in such a way that the controller time constant be at least 100 times greater than that of the current loop and the stability of performance is ensured; therefore, the following parameters are chosen:

$$\begin{cases} K_{p_\omega} = 0.75103 \\ K_{i_\omega} = 3.56848 \\ \tau_\omega = 21.046 \times 10^{-3}s \end{cases} \quad (3.44)$$

In order to inspect the intertwined mutual impacts of current, speed, and observer loops on the system stability and speed control dynamics, bode diagram and step response of the overall speed loop are shown in Fig. (3.24) and Fig. (3.25). The results are compared

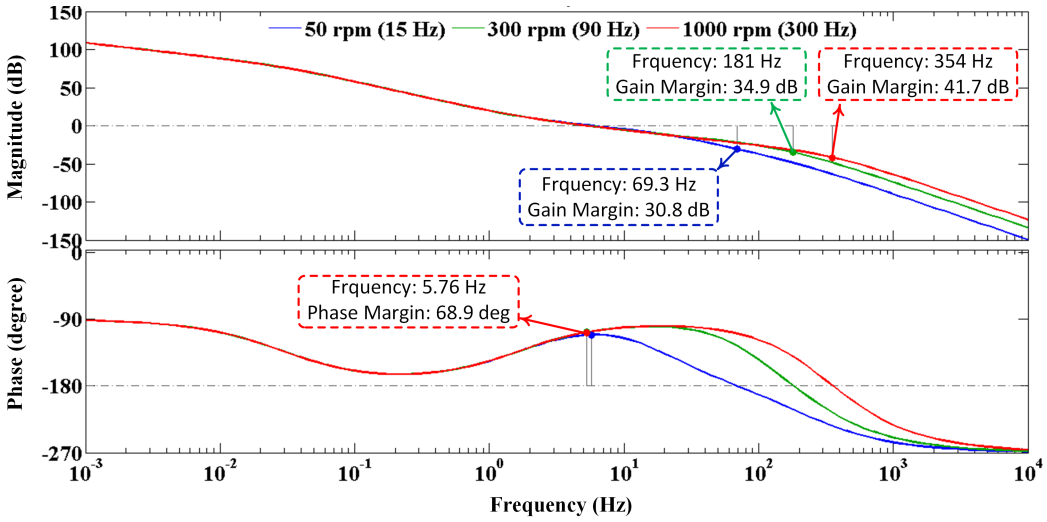

Figure 3.24: Bode diagram of the speed loop.

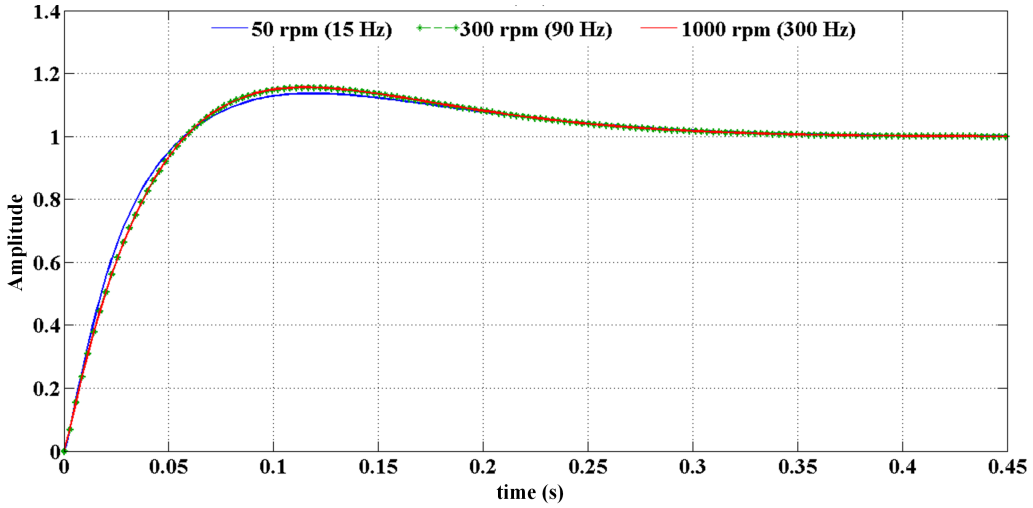

Figure 3.25: Speed loop step response.

for three different speeds of $50rpm$, $300rpm$, and $1000rpm$, which entails having different transfer functions for the QPLL (within the feedback path). Looking at the bode diagrams, the system showcases positive gain and phase margines, which is equivalent to the stability of the closed-loop system. In addition and as depicted in Fig. (3.25), for all of the three mentioned speeds, the system transient behaviours are stable and similar.

3.4 Harmonics Within the Estimated Values

Appearance of extra harmonics within the estimated outputs of the observer stems from both the input harmonics and the observer structure. Although a precise signal processing guarantees that the input waveform is of acceptible quality, there can be extra harmonics appeared within the observer estimated outputs which are solely ascribed to the observer structure. As the result, this section analytically investigates the different PLL topologies and derives the expected harmonics appeared within the estimated values. In the following step, the PLL structure is modified in order to eliminate the extra harmonics which results in the enhancement of the estimation performance.

3.4.1 Classic PLL

Considering the general structure of a PLL shown in Fig. (3.26) with a single input and single feedback path (with the input and output waveforms given in eq. (3.45) and eq. (3.46)), the error term is derived as:

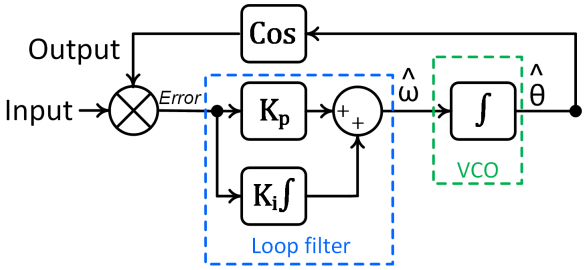

Figure 3.26: Structure of a general PLL.

$$v_{in} = A.\sin\left(\omega_{in}t + \varphi_{in}\right) \tag{3.45}$$

$$v_{out} = \cos\left(\hat{\omega}t + \hat{\varphi}\right) \tag{3.46}$$

$$Error = \frac{A}{2}\left(\underbrace{\sin\left[\left(\omega_{in}+\hat{\omega}\right)t + \left(\varphi_{in}+\hat{\varphi}\right)\right]}_{high-frequency} + \underbrace{\sin\left[\left(\omega_{in}-\hat{\omega}\right)t + \left(\varphi_{in}-\hat{\varphi}\right)\right]}_{low-frequency}\right) \tag{3.47}$$

with

- A the arbitrary input amplitude.
- ω_{in} arbitrary input frequency.

- $\hat{\omega}$ estimated frequency.
- φ_{in} arbitrary input phase.
- $\hat{\varphi}$ estimated phase.

In the steady-state condition, the PLL structure can be linearized which results in the following term for the Error.

$$Error = \frac{A}{2}\left(\underbrace{\sin\left[2\left(\omega_{in}t + \varphi_{in}\right)\right]}_{double-frequency} + \underbrace{\Delta\varphi}_{dc}\right) \tag{3.48}$$

Looking at eq. (3.47) and eq. (3.48), the Error is composed of two components; a high-frequency and a low-frequency term. In order to alleviate the magnitude of the double-frequency term, the loop filter is designed to act as a low-pass filter. Usually a simple PI regulator - equivalent to a first-order LPF - is used although it is possible to use higher-order loop filters. Since the loop filter is mainly responsible for outputting the estimated frequency (DC component), existence of the double-frequency term (even with a tiny magnitude) within the Error is unavoidable which is the most important issue in classical PLL.

For better inspection of the PLL behaviour, a sinusoidal input with the frequency of $100Hz$ is used and the loop-filter parameters (which are completely inline with what is provided in eq. (3.23)) are chosen as:

$$Input = \sin\left(200\pi t\right) \tag{3.49}$$

$$\begin{cases} K_p = 879.646 \\ K_i = 394784.176 \end{cases} \tag{3.50}$$

The waveforms of the PLL input, output, error, and estimated frequency are shown in Fig. (3.27). In addition, FFT of the input, output, and error are shown in Fig. (3.28). Looking at Fig. (3.27) and Fig. (3.28), even though the input is a single sinusoidal signal, the output and error signals contain more harmonics which are passed through the loop filter and appeared within the estimated frequency. The output contains odd multiples of the input frequency, which are $\{100, 300, 500, 700, ...\}Hz$. Given eq. (3.47) and due to the input-output interactions, the estmation error contains even-order multiples of the input frequency which are $\{200, 400, 600, 800, ...\}Hz$. As the harmonics within the estimated frequency and phase of the PLL are the result of the harmonics within the estimation error, the focus is placed

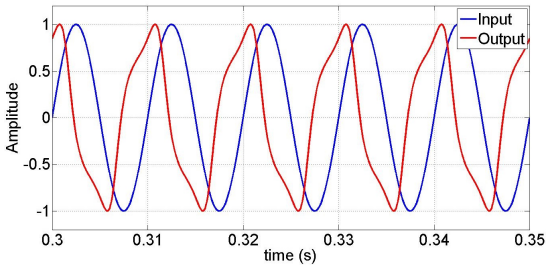

(a) PLL's input and output waveforms.

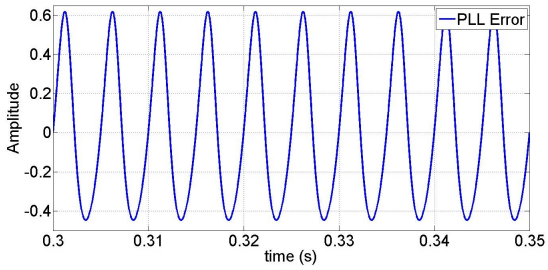

(b) PLL's estimation error.

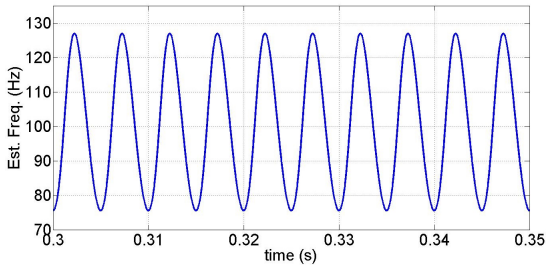

(c) PLL's estimated frequency.

Figure 3.27: PLL performance considering the waveforms of input, output, error, and estimated frequency.

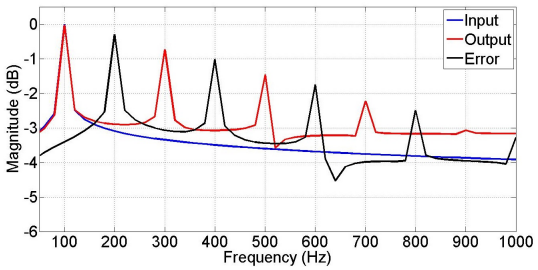

Figure 3.28: FFT analysis of PLL.

just on the estimation error.

In power system applications, where the input frequency fluctuations are limited, a feed-forward term equal to the input fundamental frequency is added to the output of the loop filter and this structure is called Synchronous Reference Frame PLL (SRFPLL). SRFPLL has rapid response, yet still suffers from the even-order harmonics in the error. An enhanced PLL version known as EPLL can be used instead by which the problem of even-order harmonics in the error is noticeably solved [211]. Although EPLL has inherited the rapid response from SRFPLL and, to a large extent, solved the double-frequency problem within the estimated error, it cannot be used in the context of sensorless control due to the following reasons:

- The fundamental frequency in sensorless applications is directly liked to the revolution

speed, so its fluctuations is beyond the lock-in range of EPLL or SRFPLL.

- The PLL must mimic the rotor dynamics through which the estimated position and speed are extracted and fed to the coordinate transformation blocks. Therefore, if a feed-forward term is used at the output of the loop filter, the estimated speed suddenly jumps to the reference speed, while the actual rotor dynamics are considerably slower and the system therefore cannot have a sustained stable operation.

Having mentioned those, quadrature PLL (QPLL), also known as heterodyning PLL, is widely used in sensorless applications and it is also used in our method. Throughout the following sub-section, the actual behaviour of QPLL is investigated.

3.4.2 QPLL

Given the QPLL toplogy illustrated in Fig. (3.14), the input and output pairs are considered to be of respective arbitrary amplitudes and frequencies of A_i, A_o, $h_i\omega_e$, and $h_o\hat{\omega}_o$. In the steady-state operating point, where $\omega_i \approx \hat{\omega}_o$, the error term is concluded as:

$$e = A_i \sin\left(h_i\omega_e t\right).A_o \cos\left(h_o\hat{\omega}_e t\right) - A_i \cos\left(h_i\omega_e t\right).A_o \sin\left(h_o\hat{\omega}_e t\right)$$
$$\approx \begin{cases} A_iA_o.\sin\left(\left|h_i - h_o\right|\omega_e t\right) \;\; ; \;\; h_i > h_o \\ 0 \;\; ; \;\; h_i = h_o \\ -A_iA_o.\sin\left(\left|h_i - h_o\right|\omega_e t\right) \;\; ; \;\; h_i < h_o \end{cases} \tag{3.51}$$

For a condition in which the input and output frequencies are of the same order ($h_i = h_o = h$), the error becomes a DC quantity which is diminished by the action of the PI (the loop filter). This DC error (defined in eq. (3.52)) is called the DC position offset in sensorless control applications.

$$e_{dc} = \sin\left(h\omega_e t\right).\cos\left(h\hat{\omega}_e t\right) - \cos\left(h\omega_e t\right).\sin\left(h\hat{\omega}_e t\right) = \sin\left[h\left(\omega_e - \hat{\omega}_e\right)t\right] =$$
$$\sin\left[h\left(\theta_e - \hat{\theta}_e\right)\right] \approx h\Delta\theta \approx 0 \tag{3.52}$$

Scenario I: Inputs with unequal amplitudes

Having the same frequency as the previous case, a pair of orthogonal inputs are fed to the QPLL:

$$\begin{cases} 1.\sin(200\pi t) \\ (1 \pm \varepsilon).\cos(200\pi t) \end{cases} \tag{3.53}$$

In order to model the non-ideal behaviour of the normalization block, the parameter $\varepsilon = 0.05$ is included within the inputs. The Input, output, error, and estimated frequency in both time- and frequency-domain are shown in Fig. (3.29) and Fig. (3.30).

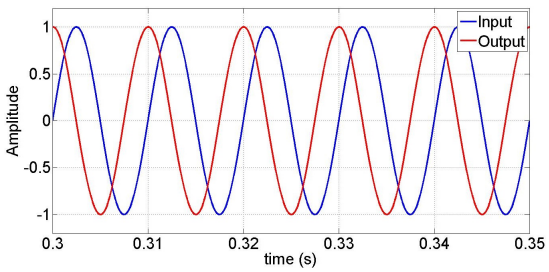

(a) QPLL's input and output waveforms.

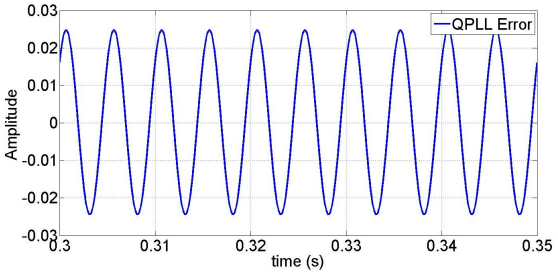

(b) QPLL's estimation error.

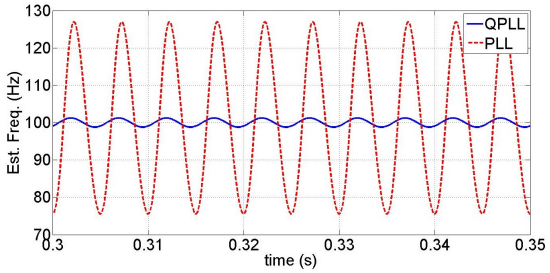

(c) QPLL's estimated frequency.

Figure 3.29: QPLL performance - Scenario I.

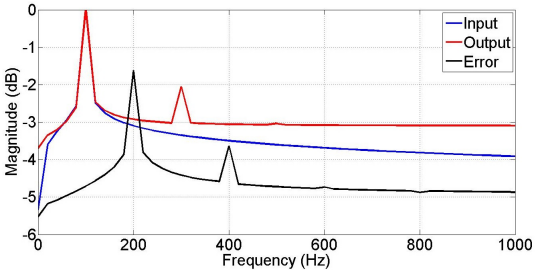

Figure 3.30: FFT analysis of QPLL - Scenario I.

Given the obtained simulation results, the following observations are made:

- In terms of frequency estimation, the performance of QPLL is unquestionably superior than PLL as compared in Fig. (3.29c). For the case of PLL, the estimated frequency has the ripple of around $50Hz$ while this value is less than $5Hz$ for QPLL.
- Similar to the PLL behavior, the output comtains odd multiples of the input harmonics, at $\{100, 300, 500, ...\}Hz$. As the result, the error contains even-order multiples of the input frequency at $\{200, 400, 600, ...\}Hz$.

Scenario II: Inputs with a fundamental frequency and harmonic contamination

Given a pair of orthogonal inputs containing the fundamental frequency at 100Hz in addition to harmonics at 200Hz and 400Hz as defined below:

$$\begin{cases} 1.\sin(200\pi t) + 0.1.\sin(400\pi t) + 0.05.\sin(800\pi t) \\ 1.\cos(200\pi t) + 0.1.\cos(400\pi t) + 0.05.\cos(800\pi t) \end{cases} \tag{3.54}$$

The simulation results in both time-domain and frequency-domain are provided in Fig. (3.31) and Fig. (3.32).

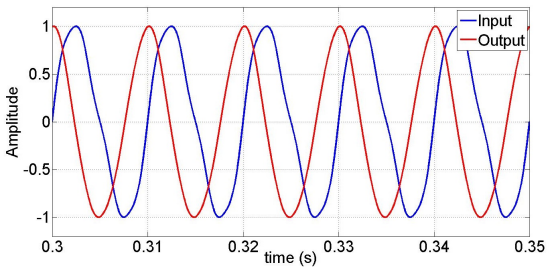

(a) QPLL's input and output waveforms.

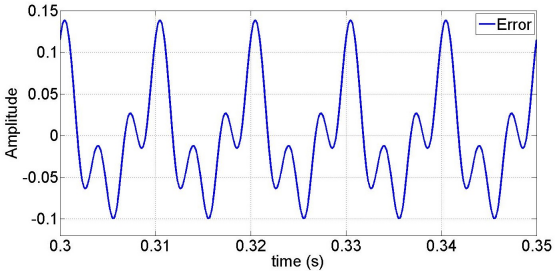

(b) QPLL's estimation error.

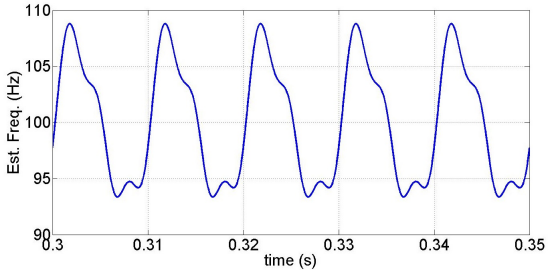

(c) QPLL's estimated frequency.

Figure 3.31: QPLL performance - Scenario II.

Even though the input only contains frequencies at $\{100, 200, 400\}Hz$, the output contains $\{100, 200, 300, 400, 500, 600, etc.\}Hz$. All the input frequencies in addition to the odd

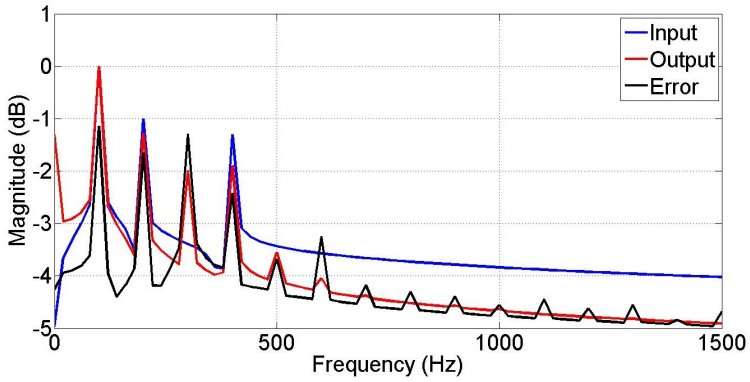

Figure 3.32: FFT analysis of QPLL - Scenario II.

harmonics of each input frequency are appeared in the output (for example: the components at 300Hz and 500Hz are respectively the 3^{rd} and 5^{th} harmonics of the input's 100Hz component and the 600Hz component is the 3^{rd} harmonic of the input's 200Hz component). Consequently (and as the result of input-output interactions), the error and estimated frequency contain components at $\{100, 200, 300, 400, 500, 600, 700, etc.\}Hz$.

In practice, for both HFI- and PWM-induced acoustic noise spectra, there exist a cluster of neighbouring, speed dependent sidebands around the central frequency of BPF II. Therefore, it is unfeasible for the signal processing to extract the desired sideband and reject the other ones. For instance and for the case of PWM-induced acoustic noise at the revolution speed of $500rpm$ with $f_e = 25Hz$ and $h = 7$, the FFT of QPLL input, output and estimation error are shown in Fig. (3.33).

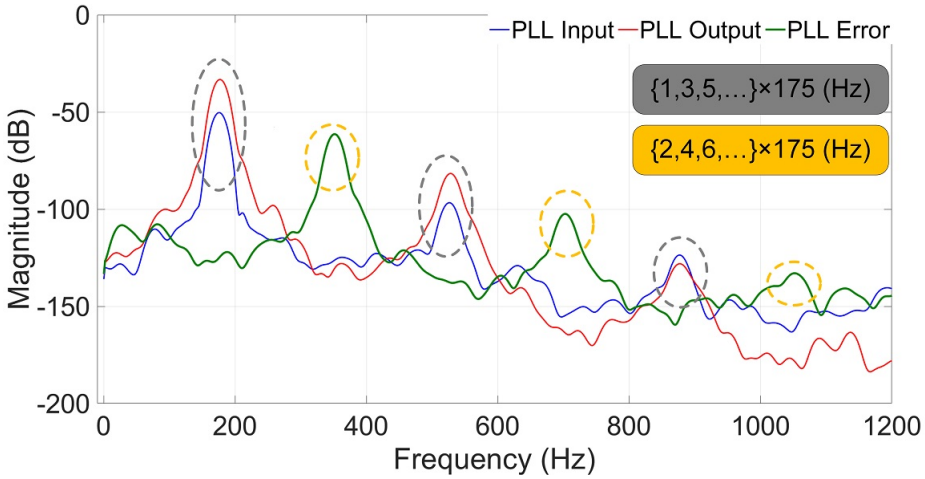

Figure 3.33: FFT analysis in experimental condition for the case of PWM with $f_e = 25Hz$ and $h = 7$.

The input has the fundamental frequency of $7*25 = 175Hz$ in addition to some odd-order harmonics ($\{1, 3, 5, ...\} \times 175Hz$). The odd multiples of the input fundamental frequency are also appeared within the output spectrum. Accordingly, the error contains even-order harmonics of the input fundamental component at $\{2, 4, 6, ...\} \times 175Hz$.

Given the provided results for both PLL and QPLL, the following conclusions could be drawn:

- All the frequency components within the input spectrum are directly reflected in the output spectrum.
- Given each frequency component in the input, corresponding odd harmonics are appeared within the output.
- Given the input-output interaction and knowing the input harmonics, the error harmonics are defined.

In conclusion, the error has the following general format comprising a DC and several AC terms (harmonics):

$$e = e_{dc} + e_{ac} \tag{3.55}$$

The DC term is eliminated by the action of the loop filter (PI regulator), yet the AC components pass through the loop filter and appear within the estimated phase and frequency as undesired extra ripple. To this end, the following section deals with modifications made in the PLL or QPLL structure, by which the undesired AC terms within the error are mitigated.

3.5 Elimination of Harmonics Within the Estimation Error

Harmonic elimination methods have been widely utilised in the literature, with eclectic applications including current harmonic suppression in electric drives, improvement of the position estimation in sensorless methods, and improving the frequency estimation in power system studies.

- **Improved Position Observers**

One of the most conspicuous weakpoints of the PI regulators is their inability in controlling the AC reference points. Therefore, resonant controllers (RC) are used, when dealing

with AC inputs [212–214]. The second-order generalized integrator (SOGI) shares a same transfer function with RC and is used for the sake of harmonic extraction. In order to reduce the torque ripple, as a solution for having smooth speed control, a SOGI-based active disturbance rejection algorithm is used [215]. An adaptive quasi-proportional-resonant observer (AQPRO) is used in order to suppress the position estimation error harmonics [216]. An optimized PLL topology, using Levenberg-Marquardt (LMOPLL) is also used for this goal [217]. A novel finite position-set PLL (FPS-PLL), using a newton iteration-based algorithm for improving the estimation performance, is proposed in [218]. For improving the estimation performance in BEMF-based sensorless controls, a reduced-order quasi resonant-based extended state observer (ROQR-ESO) is used for the estimation of EEMF, and a newton-raphson based PLL (NRM-PLL) is used as the position observer [219].

- **Compensation of Current Harmonics in PMSM Operation**

For PMSM drives operating with low switching frequency, there are large sidebands around the PWM carrier which deteriorate the overall performance. Accordingly, a method consisting a velocity controller and a sideband harmonic compensator is proposed in [220]. In high-speed zone, the current would be contaminated with numerous harmonics. A multiple synchronous frame transformation (MSRFT) coupled with a closed-loop harmonic detection algorithm are proposed to eliminate the undesired current harmonics with high precision [221].

- **Applications of Harmonic Elimination in Power Systems**

Similar to the ADALINE-based filter, RC has also been widely utilized within the power system applications. A multi-resonant current regulator with adaptive performance equipped with diturbance rejection capability is used for single-phase grid-tied inverters [222]. Grid synchronisation is an integral part within the control algorithm of grid-connected converters, which is realized by the grid voltage frequency estimation through an SRFPLL. Extra harmonics within the frequency estimation, leading to frequency deviation, is detrimental to synchronization performance, so RC-based current controllers are widely used as a solution to approach this malfunction [223–226].

Having reviewed the above-mentioned harmonic suppression methods, a novel position observer, capable of providing an enhanced estimation performance with suppression of the position estimation error harmonics, is proposed in the following part.

3.5.1 Proposed RCPLL

The underlying reason behind the occurrence of ripple in the estimated phase and frequency is the undesired AC terms in the estimation error. As the result, finding a way to eliminate or suppress the AC terms within the error term is the key in improving the estimation performance of PLL/QPLL.

Identifying the harmonics within the error, a compensating term is fed forward to the error with the responsibility to counteract the AC terms. The harmonic compensation block is based on using resonant controller (RC) tuned at a specific frequency; therefore, multiple RCs could be paralleled in case several harmonics are to be suppressed. The harmonic compensation block is integrated into the QPLL structure and the overall configuration is depicted in Fig. (3.34).

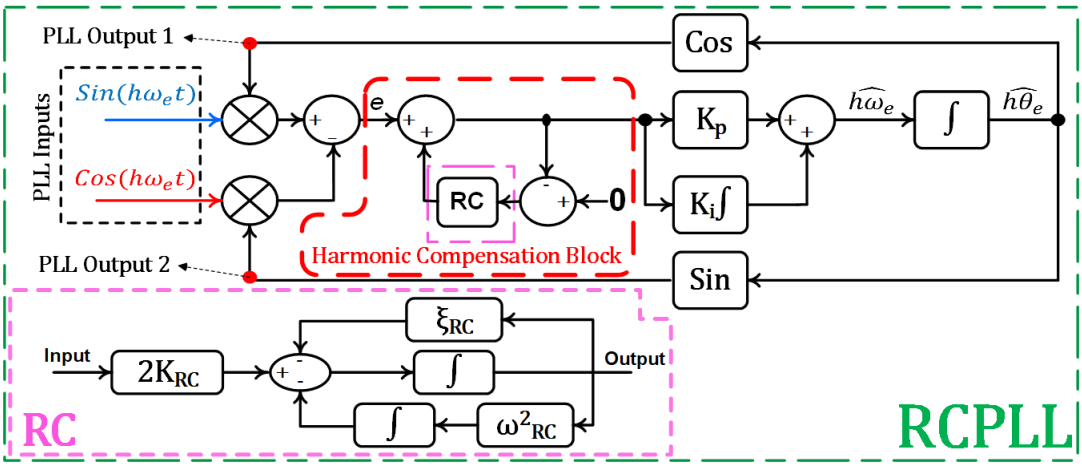

Figure 3.34: The proposed RCPLL observer structure.

Transfer function of an RC with the respective resonant frequency and damping ratio of ω_{RC} and ξ_{RC} is given as:

$$RC\,(s) = \frac{2K_{RC}\xi_{RC}s}{s^2 + 2\xi_{RC}s + \omega_{RC}^2} \tag{3.56}$$

$$\begin{cases} \omega_{RC} = \alpha.h.\omega_e \\ \xi_{RC} = \gamma.\omega_e \end{cases} \tag{3.57}$$

where $\alpha = |h_i - h_o|$ represnets the order of the harmonics within the error and $0 \leqslant \gamma < 1$ controls the damping intensity. Also, the RC parameters are tuned in such a manner to be adaptive with respect to ω_e.

The closed-loop transfer function of the compensation block is obtained as:

$$G_{RC}(s) = \frac{1}{1-(-RC(s))} = \frac{s^2 + 2\xi_{RC}s + \omega_{RC}^2}{s^2 + 2\xi_{RC}(1+K_{RC})s + \omega_{RC}^2} \tag{3.58}$$

If $K_{RC} = 0$, eq. (3.58) equals one, and the impact of the resonating compensation block is disabled (also evident from Fig. (3.34)).

In the next stage, the forward-path transfer function of the RCPLL, including both RC and QPLL, is obtained as:

$$G_{RCPLL}^{frw}(s) = \frac{a_3 s^3 + a_2 s^2 + a_1 s + a_0}{b_4 s^4 + b_3 s^3 + b_2 s^2 + b_1 s + b_0} \tag{3.59}$$

$$\begin{cases} a_3 = K_p \\ a_2 = K_i + 2\xi_{RC}K_p \\ a_1 = 2\xi_{RC}K_i + K_p\omega_{RC}^2 \\ a_0 = K_i\omega_{RC}^2 \\ b_4 = 1 \\ b_3 = 2\xi_{RC}(1+K_{RC}) \\ b_2 = \omega_{RC}^2 \\ b_1 = b_0 = 0 \end{cases} \tag{3.60}$$

Considering the case of PWM-induced acoustic noise, and for the revolution speed of $500rpm$ ($h = 7$ and $\alpha = 2$ are chosen for example), bode diagram of the system is plotted in Fig. (3.35) when $0 \leqslant K_{RC} < 20.0$.

As can be noticed, K_{RC} has a direct impact on the behaviour of the RCPLL observer in such a manner that choosing it to be zero transforms the RCPLL into a simple PLL. However, increasing the value boosts the harmonic suppression capability. It is also worth mentioning that, K_{RC} cannot have inexorable value as the phase margin is almost reached $-180°$ when the value is jumped from 5.0 to 20.0 (Fig. (3.35)).

In order to evaluate the impact of the proposed RCPLL on the overall system stability, the closed-loop transfer function of the proposed RCPLL observer is firstly obtained as follows.

$$G_{RCPLL}^{cl}(s) = \frac{a_3 s^3 + a_2 s^2 + a_1 s + a_0}{s^4 + (a_3+b_3)s^3 + (a_2+b_2)s^2 + a_1 s + a_0} \tag{3.61}$$

In the next step, the forward-path transfer function of the overall speed loop, containing the

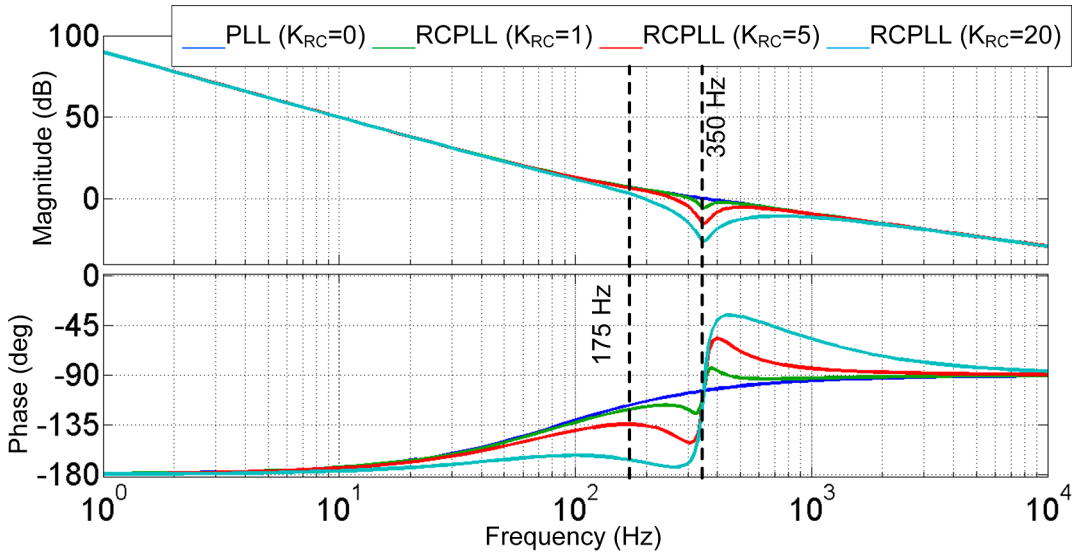

Figure 3.35: Bode diagram comparison of PLL and RCPLL, for different K_{RC} values.

RCPLL as the position observer, is:

$$G_{\omega}^{frw} = G_{RCPLL}^{cl} \cdot \frac{K_{p_\omega} s + K_{i_\omega}}{s} \cdot \frac{1}{T_{eq} s + 1} \cdot \frac{1}{Js + B} = \frac{m_4 s^4 + m_3 s^3 + m_2 s^2 + m_1 s + m_0}{n_7 s^7 + n_6 s^6 + n_5 s^5 + n_4 s^4 + n_2 s^2 + n_1 s + n_0} \tag{3.62}$$

$$\begin{cases} m_4 = a_3 K_{p_\omega} \\ m_3 = a_3 K_{i_\omega} + a_2 K_{p_\omega} \\ m_2 = a_2 K_{i_\omega} + a_1 K_{p_\omega} \\ m_1 = a_1 K_{i_\omega} + a_0 K_{p_\omega} \\ m_0 = a_0 K_{i_\omega} \\ n_7 = T_{eq} J \\ n_6 = \upsilon + T_{eq} (a_3 + b_3) \end{cases} \quad \begin{cases} n_5 = B + \upsilon (a_3 + b_3) + T_{eq} J (a_2 + b_2) \\ n_4 = a_1 T_{eq} J + \upsilon (a_2 + b_2) + B (a_3 + b_3) \\ n_3 = a_0 T_{eq} J + a_1 \upsilon + B (a_2 + b_2) \\ n_2 = a_1 B + a_0 \upsilon \\ n_1 = a_0 B \\ n_0 = 0 \\ \upsilon = T_{eq} B + J \end{cases} \tag{3.63}$$

Verifying the overall speed loop stability, the bode diagrams for three speeds of $50rpm$, $500rpm$, and $1000rpm$ with the following parameters $K_{RC} = 5$, $h = 7$, and $\alpha = 2$ are plotted in Fig. (3.36).

Given the plotted bode diagrams, the system has positive phase margin and gain margin, which indicates the stable performance. Three vertical dashed lines, at $35Hz$, $350Hz$, and $700Hz$, are correspondingly the central frequencies of the RC for the revolution speeds of $50rpm$, $500rpm$, and $1000rpm$.

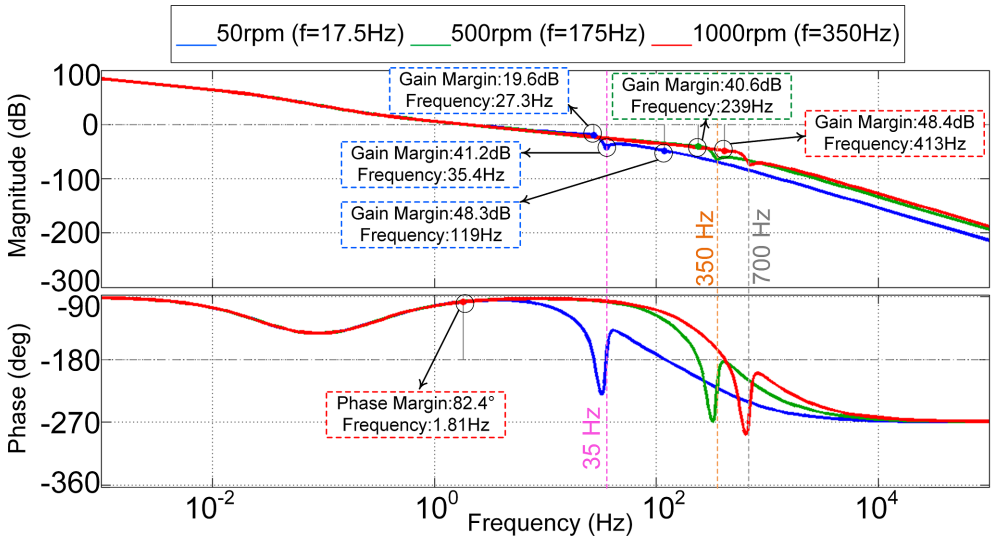

Figure 3.36: Bode diagram of the overall speed loop.

In order to assess the performance of RCPLL and compare it with that of PLL (for the case of HFI-induced acoustic noise), the revolution speed is fixed at $500rpm$ (which is equal to $f_e = 25Hz$) and $h = 6$. As the result, the fundamental input frequency is $6 * 25 = 150Hz$. Waveforms of the input and output of the QPLL are illustrated in Fig. (3.37) in which, in addition to the fundamental frequency, the input contains additional harmonics. Existence of extra harmonics within the input coupled with the interactions with the output harmonics lead to the appearance of harmonics within the error and estimated frequency. Comparing

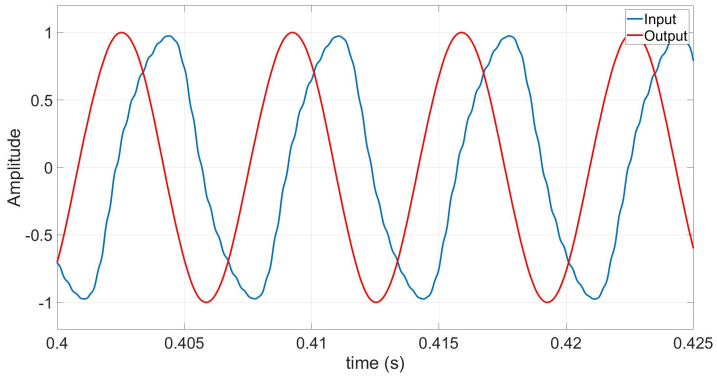

Figure 3.37: The input and output of QPLL for the processed acoustic noise signal - $f_e = 25Hz$ and $h = 6$.

the performance of RCPLL and QPLL/PLL, the value of K_{RC} is varied from zero to 20.0 and the estimation error, estimated frequency, and estimated phase waveforms are compared

as respectively illustrated in Fig. (3.38), Fig. (3.39), and Fig. (3.40).

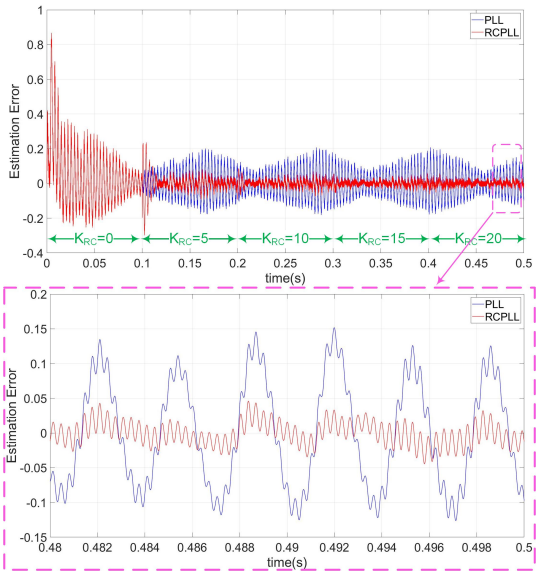

Figure 3.38: The estimation error comparison between PLL and RCPLL - $f_e = 25Hz$ and $h = 6$.

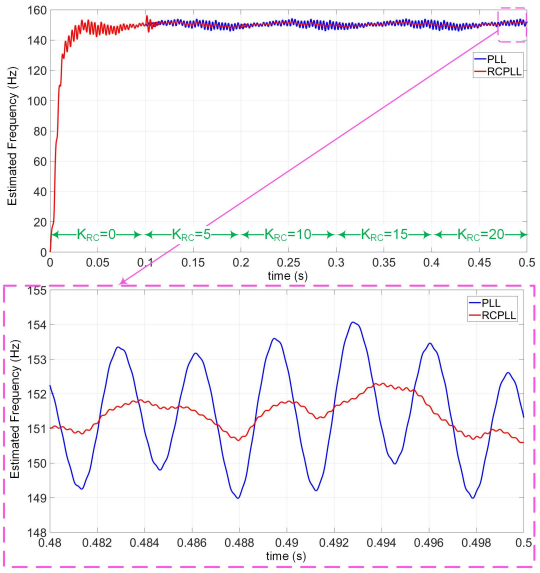

Figure 3.39: The estimated frequency comparison between PLL and RCPLL - $f_e = 25Hz$ and $h = 6$.

As the value of K_{RC} is increased, the estimation ripple is reduced; also, the enlarged portions of waveforms for the period of $0.48 - 0.50s$ while $K_{RC} = 20.0$ are provided which

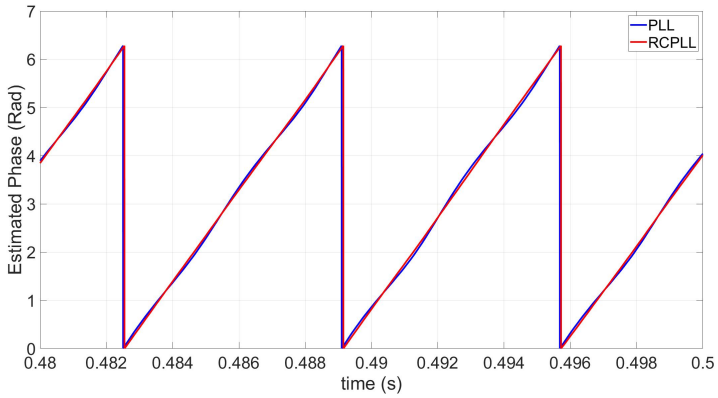

Figure 3.40: The estimated phase comparison between PLL and RCPLL - $f_e = 25Hz$ and $h = 6$.

verifies the tangible impact of RCPLL on the estimation performance. Considering the estimation error, there is a maximum peak-to-peak ripple of 0.275 observed for the PLL condition, while this value is reduced to 0.075 for the RCPLL condition (showing a 72% suppression). For the estimated frequency, utilisation of RCPLL yields 70% improvement since the peak-to-peak ripple is reduced from $5Hz$ to $1.5Hz$. It is important to note that, the estimated phase also contains a double-frequency ripple which is almost suppressed when RCPLL is used (Fig. (3.40)).

Given the prior analysis about the harmonics within the QPLL error term and as the input fundamental frequency is equal to $150Hz$, the RCPLL is tunned to compensate the double-frequency term within the error, at $2 * 150 = 300Hz$. FFT of the estimation error for the PLL and RCPLL conditions are illustrated in Fig. (3.41).

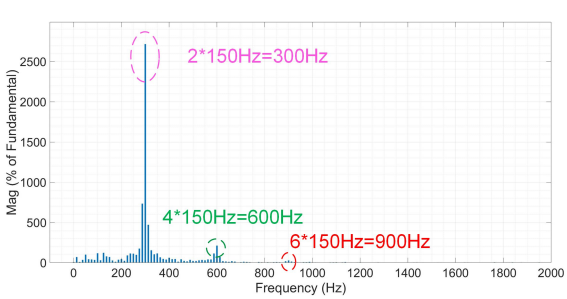

(a) Estimation error FFT in PLL condition.

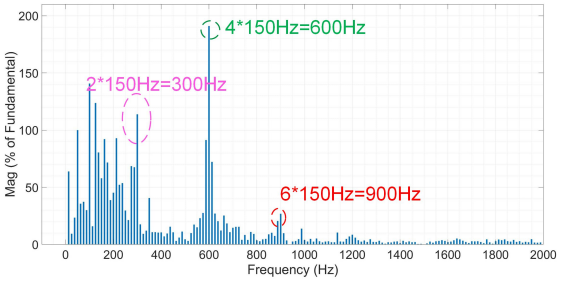

(b) Estimation error FFT in RCPLL condition.

Figure 3.41: Comparison of the estimation error FFT between PLL and RCPLL.

Looking at Fig. (3.41a), the estimation error contains even-order harmonics of the in-

put fundamental frequency (respectively at $\{300, 600, 900, ...\}Hz$). After applying RCPLL, the magnitude of the $300Hz$-component is reduced from 2500 to 120 which shows a 95% suppression. It is to be mentioned that, the magnitude of other harmonics are almost intact.

3.5.2 Proposed ADALINE-PLL

Instead of using an RC within the structure of the harmonic compensation block, an ADALINE-based filter can be used. Similar to the RCPLL case, several ADALINE-based compensation blocks could be placed in parallel in case different harmonics are to be compensated. The overall structure of the proposed observer is shown in Fig. (3.42).

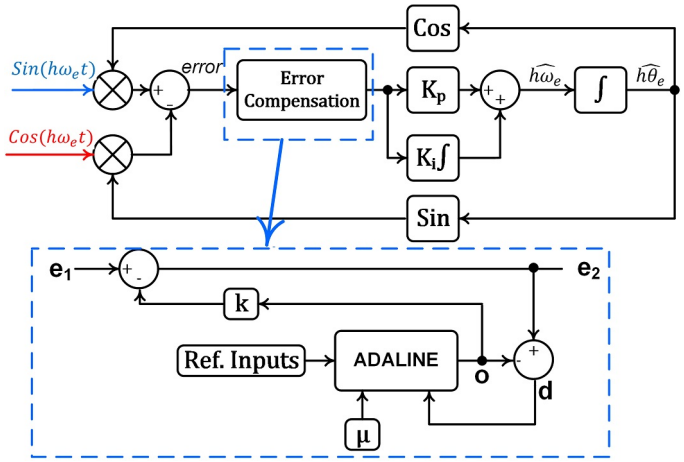

Figure 3.42: Structure of the proposed ADALINE-PLL.

Due to the nature of ADALINE, both the learning rate (μ) and the output coefficient (K which is shown in Fig. (3.42)) should be chosen with trial and error to reach a desirable performance. Similar to the previous RCPLL condition, ADALINE-PLL behaviour is compared with a simple QPLL when the actual acoustic noise of the machine is processed and fed to the observers. In order to show the positive impact of ADALINE-PLL in harmonic suppression, the BPF II is tuned with a wider passing band (compared to the case for RCPLL); therefore, the orthogonal inputs fed to the observer are not perfectly sinusoidal (as shown in Fig. (3.43)) and contain high-order harmonics in addition to the fundamental frequency at $150Hz$.

The orthogonal signals are then passed through the normalization block and fed to the QPLL. The FFT of QPLL's input, output, and error signals are shown in Fig. (3.44). Since the zone around the fundamental frequency ($150Hz$) is important in this study, the FFT is

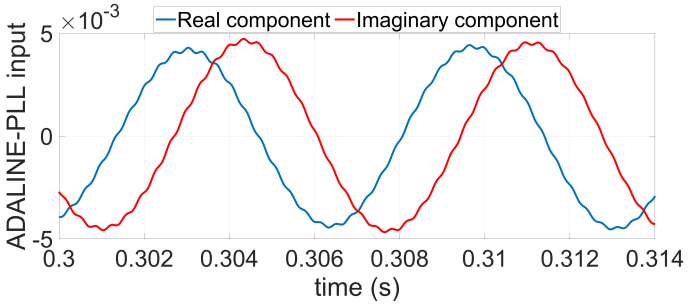

Figure 3.43: Observer inputs which contain extra harmonics.

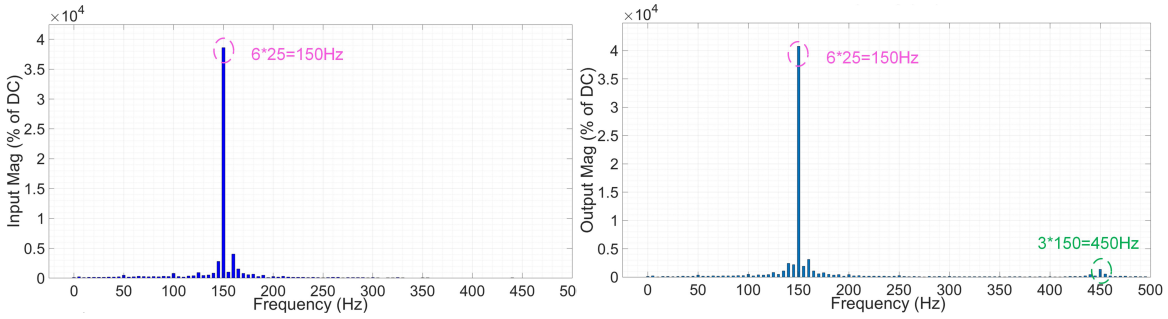

(a) Input signal FFT in PLL condition. (b) Output signal FFT in PLL condition.

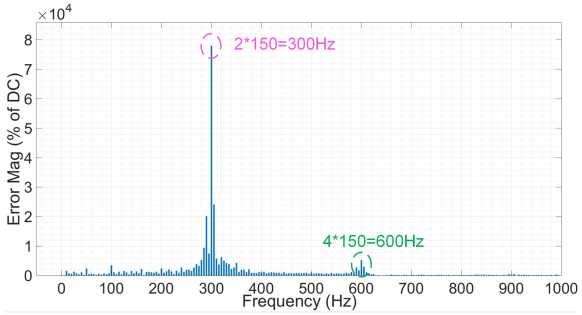

(c) Estimation error FFT in PLL condition.

Figure 3.44: FFT of PLL's input, output, and estimation error.

shown up to the frequency of $500Hz$ and other higher-order harmonics are not shown. Given the figures, the output contains the 3^{rd} multiple of the fundamental frequency; therefore, even-order multiples of the fundamental frequency are generated within the estimation error (at $\{300, 600, ...\}Hz$). Similar to the RCPLL condition, the ADALINE-based filter is tuned for the $300Hz$-component.

The performance of PLL and ADALINE-PLL with respect to the estimation error, estimated frequency, and estimated phase are compared and the waceforms are respectively illustrated in Fig. (3.45), Fig. (3.46), and Fig. (3.47). The estimation error signal has

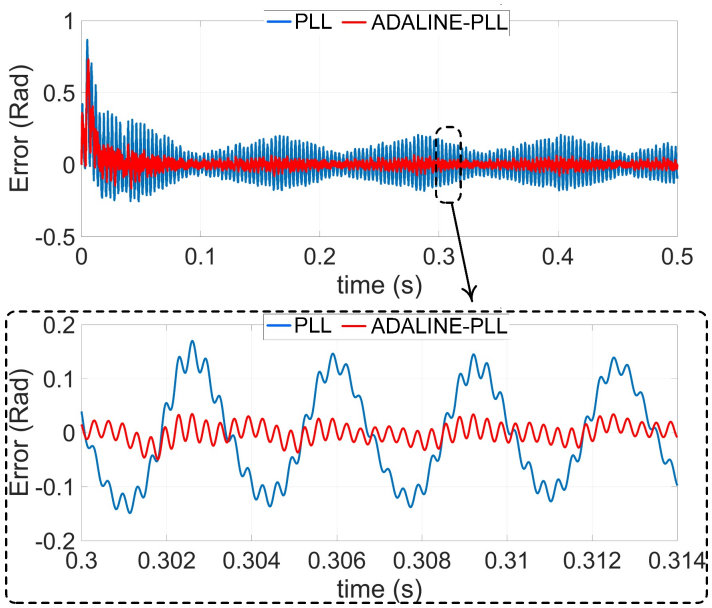

Figure 3.45: Estimation error comparison between PLL and ADALINE-PLL.

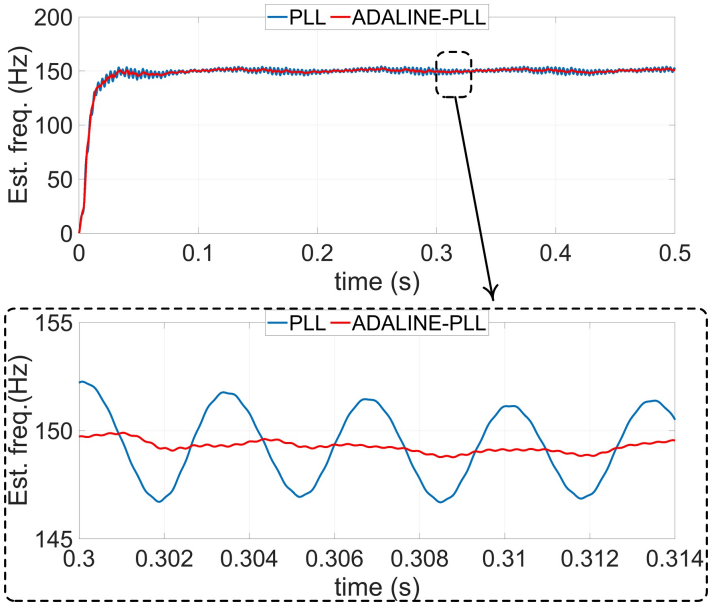

Figure 3.46: Estimated frequency comparison between PLL and ADALINE-PLL.

the maximum peak-to-peak value of 0.3 which is reduced to 0.06 when ADALINE-PLL is used, which is equal to an 80%-improvement. Similarly for the estimated fequency, the maximum peak-to-peak value is about $7Hz$ while it is reduced to $2Hz$ for the ADALINE-PLL, showing 71.43% improvement. Additionally, the estimated phase also fluctuates with

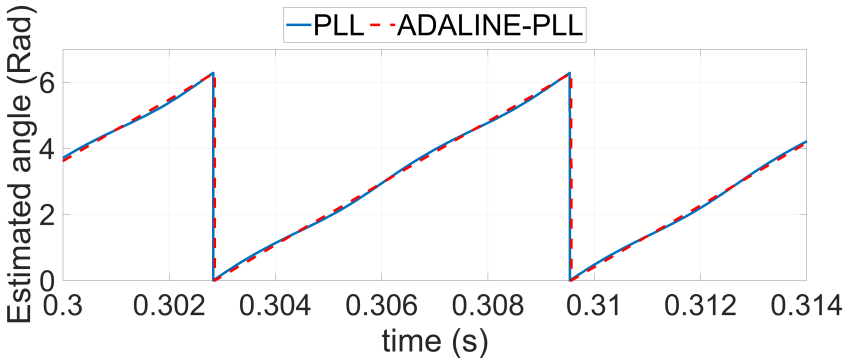

Figure 3.47: Estimated phase comparison between PLL and ADALINE-PLL.

a double-frequency term which is almost eliminated when ADALINE-PLL is used.

3.5.3 Importance of Harmonic Suppression

With respect to the analytical derivation of the harmonics within the estimated values and the topologies of QPLL, RCPLL, and ADALINE-PLL, the following important points are concluded:

- The dominant harmonics within the spectrum of estimated values are even-order multiples of the input fundamental component. Especially, the harmonic with double the input frequency is the most dominant component in the estimated values.
- The loop filter is unable to suppress the error harmonics; therefore, the estimated phase and frequency also contain these harmonics.
- As the estimated values are directly used in the coordinate transformation for the filed-oriented algorithm, existance of extra harmonics - in the form of extra ripple - deteriorates the performance. This ill-impact shows itself in the form of extra torque ripple, increased current consumption, and extra losses.
- RCPLL and ADALINE-PLL have shown to be effective solutions for suppressing the extra harmonics within the estimated values.
- Application of RCPLL and ADALINE-PLL is not limited to the sensorless control. These two novel observers can be used in power system studies where grid synchronization is of paramount importance and extra ripple within the estimated frequency can compromise the overall stability.

3.6 Conclusion

The closed loop sensorless control of PMSM based-on the machine output acoustic noise was investigated in this chapter. Signal processing algorithms, by which the speed-dependant components are extracted, were proposed and investigated. In the following section, the observer (PLL) was analytically investigated and the estimation performance was analyzed. In the third section, the overall system was modelled and the stability of the system was verified. Owing to the processed signals harmonics and the observer non-linear structure, the estimated values are contaminated with even-order harmonics. Therefore, two new observer topologies were introduced in the forth section. With the aid of these new observers, the harmonics within the estimation error were suppressed and the estimation performance was accordingly improved.

Experimental validation of the proposed acoustic noise-based PMSM sensorless controls are presented in the next chapter.

Chapter 4

Experimental Results

Throughout the previous chapter, the theoretical aspects related to the acoustic noise-based PMSM sensorless control were detailed. In this chapter, the following proposed methods are experimentally tested:

- **HFI-based acoustic noise-driven PMSM sensorless control:** in this condition, an HFI is used and the acoustic noise-based PMSM sensorless control is experimentally tested.
- **Injectionless acoustic noise-driven PMSM sensorless control:** in this method, the injectionless acoustic noise-based PMSM sensorless control (relying on the PWM harmonics) is experimentally investigated.
- **Sensorless performance when RCPLL is used**: although RCPLL is a general-purpose observer, its effectivity in improving the estimation performance (through suppression of unwanted harmonics) is experimentally verified on the injectionless acoustic noise-based sensorless control.

The experimental results are carried out on a test bench, shown in Fig. (4.1), which comprises a 1.6KW PMSM with the parameters given in Table. 4.1, a PMSG coupled to the motor, a tunable resistive load bank serving as the applied load to the generator, a Texas Instrument DRV8301-HC kit (inverter plus TMS320F28069 DSP board), and an ADC-connected microphone for acoustic noise sampling. It is worth mentioning that the proposed methods are applied on a cheap PMSM, which is for general applications without any special mechanical design characteristics.

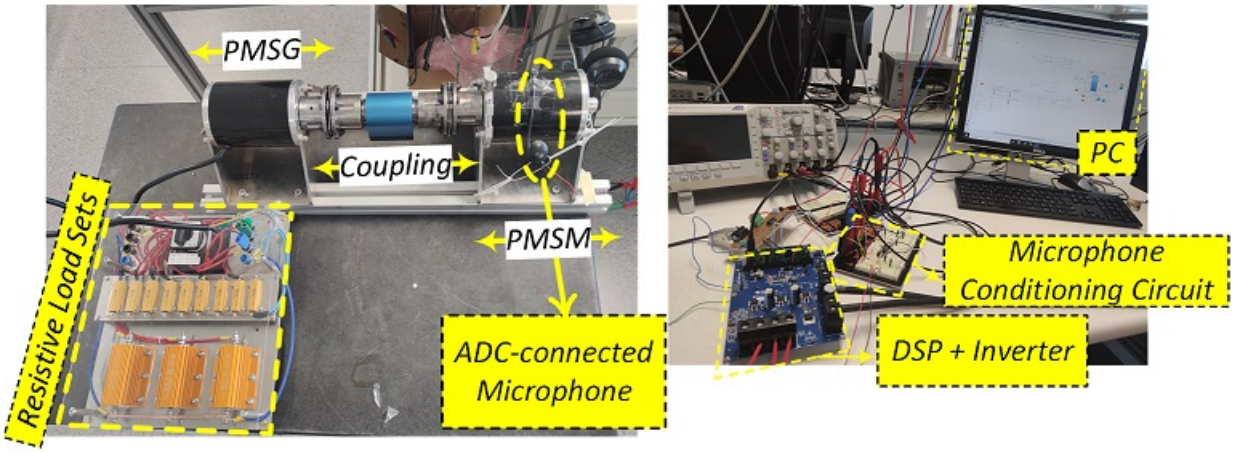

Figure 4.1: Overview of the testbench.

Table 4.1: Parameters of the PMSM drive system.

Parameter	***Value***
No. of Slots/Poles	9/6
Rated Power	$1600W$
Rated Speed	$1500rpm$
d-/q-axis Inductances	$140\mu H/178\mu H$
Phase Resistance	$97m\Omega$
PM Flux Linkage	$39.5mWb$
Rated Current	$30A$
DC-link Voltage	$55V$
Switching Frequency	$10KHz$
HFI Frequency	$1.44KHz$

Algorithm commissioning: Due to the fact that our PMSM has 6 rotor poles, there are 3 positions where the d-axis (or α-axis) can lie. Consequently, given each time the algorithm is emulated by the processor, a DC α-axis voltage is firstly injected so as to lock the rotor to any of the 3 positions. In the following step, the encoder reading is set to zero (by offsetting the value). Finally, the injected voltage is set to zero and the acoustic noise-based FOC sensorless algorithm is run.

Doing such initial commissioning reassures us that both the initial estimated and actual rotor positions are zero and there is no DC offset among them. In another word, by doing such initialisation procedure, the impact of the arbitrary integration coefficient, which can alter the initial rotor position, is counteracted.

4.1 HFI-based Acoustic Noise-Driven PMSM Sensorless Control

In this method, an HFI voltage is applied within the estimated dq-frame which is shown in eq. (4.1). Moreover, the sixth harmonic sideband around the injected frequency ($h = 6$) is used for the acoustic noise signal processing in all experiments. The tests are categorized into static and dynamic conditions in order to showcase the robustness and stability of the proposed method in different conditions.

$$V_{dqh} = 5 \cdot e^{j(2\pi * 1440)t} = 5 \begin{bmatrix} \cos(2\pi * 1440 * t) \\ \sin(2\pi * 1440 * t) \end{bmatrix} \tag{4.1}$$

It is to be mentioned that, the proposed Type I signal processing (shown in Fig. (3.2)) is used within all the experiments.

4.1.1 Static Conditions

4.1.1.1 Signal Processing

In order to verify the effectiveness of the proposed signal processing, the two orthogonal signals (the outputs of BPF II which are fed to the PLL for the position estimation), are shown at $75rpm$ and $1000rpm$. Figure (4.2) depicts the extracted orthogonal signals for the revolution speed of $75rpm$, as a low-speed zone. The fundamental frequency is theoretically $22.5Hz$, while it is experimentally acquired as $20.83Hz$ which shows a difference equal to 7.42%. This small difference is justifiable due to the existence of non-modelled nonlinearities of the system in addition to the imperfect mechanical structure of the machine.

Transitioning into the high-speed zone, the extracted orthogonal signals for the speed of $1000rpm$ are illustrated in Fig. (4.3). At this speed, the theoretical fundamental frequency is $300Hz$ and the signal processing has extracted signals with the frequency of $306.748Hz$ which shows 2.24% difference.

4.1.1.2 Steady-state Performance

Figure (4.4) shows the estimation performance at $75rpm$. The theoretical mechanical frequency is $1.25Hz$ and it is experimentally acquired as $1.28Hz$ (2.4% difference). Moreover, the peak value of the estimation error is obtained as $0.606°$.

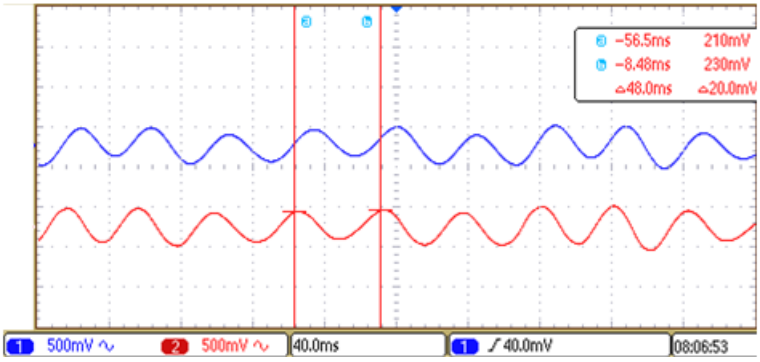

Figure 4.2: The extracted orthogonal signals at the revolution speed of $75rpm$ (the outputs of the Type I signal processing algorithm).

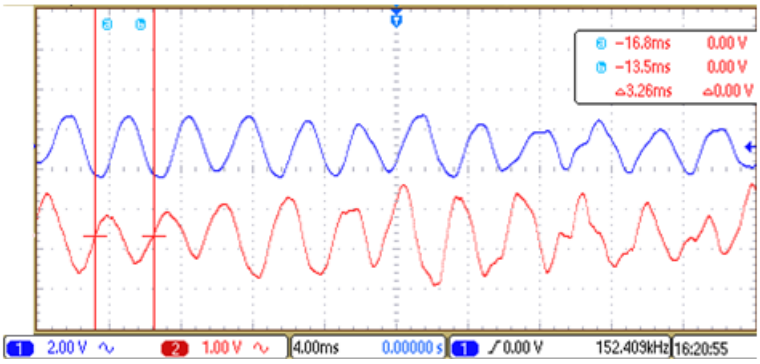

Figure 4.3: The extracted orthogonal signals at the revolution speed of $1000rpm$ (the outputs of the Type I signal processing algorithm).

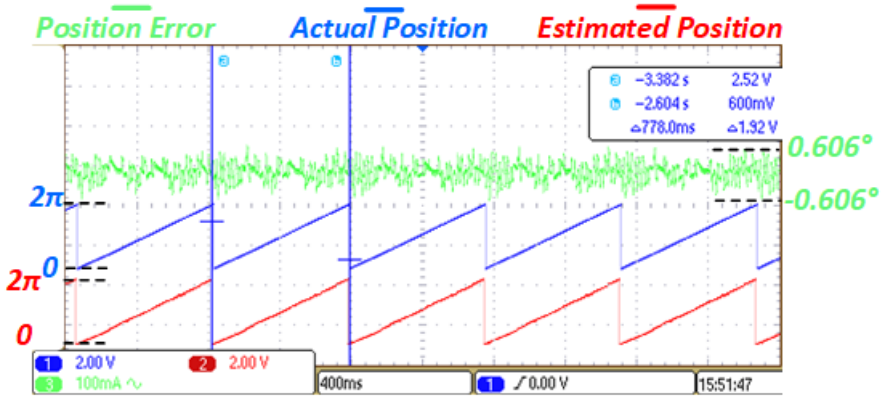

Figure 4.4: Evaluation of the estimation performance at $75rpm$.

The estimation performance at $1000rpm$ is also shown in Fig. (4.5) where the theoretical mechanical frequency is equal to $16.67Hz$ and its experimental value is obtained as $16.83Hz$, leaving 0.95% difference.

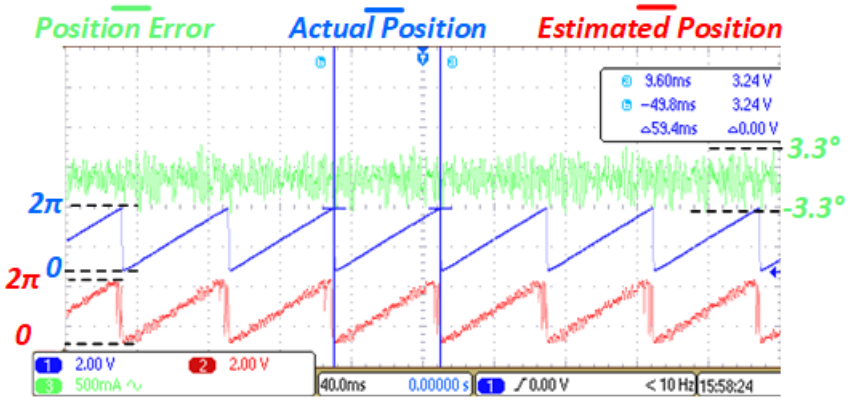

Figure 4.5: Evaluation of the estimation performance at $1000rpm$.

The maximum observed estimation error is also equal to 3.3°, where its impact is appeared within the estimated position as extra ripple.

The spectrogram of acoustic noise for the dq-frame HFI at $1440Hz$ was shown in Fig. (2.28), and is re-illustrated here for convenience in Fig. (4.6) . Given the spectrogram, as the speed increases and exceeds $1000rpm$, the components in the PM-origined zone meet those occupying the HFI zone, which results in component interference. Such interference directly affects the estimation performance and causes distortion within the estimation error and the estimated position, like what is observed in Fig. (4.5). Overcoming this, the HFI frequency can be increased so as to provide extended margin for the interference occurrence.

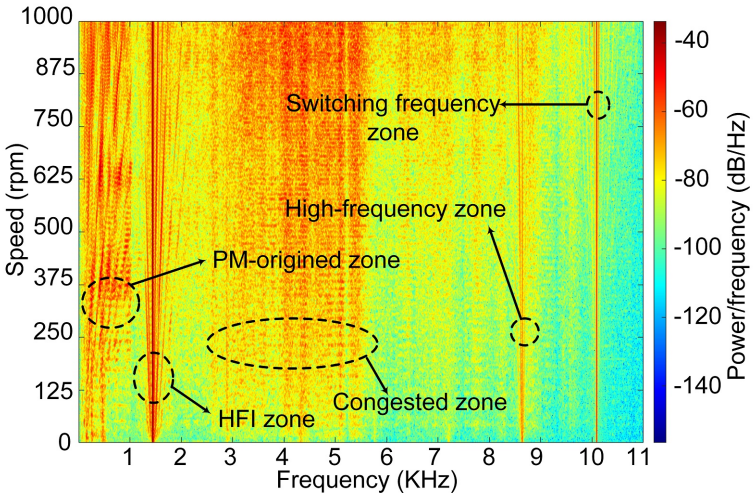

Figure 4.6: Acoustic noise spectrogram for the case of dq-frame HFI with $f_h = 1440Hz$.

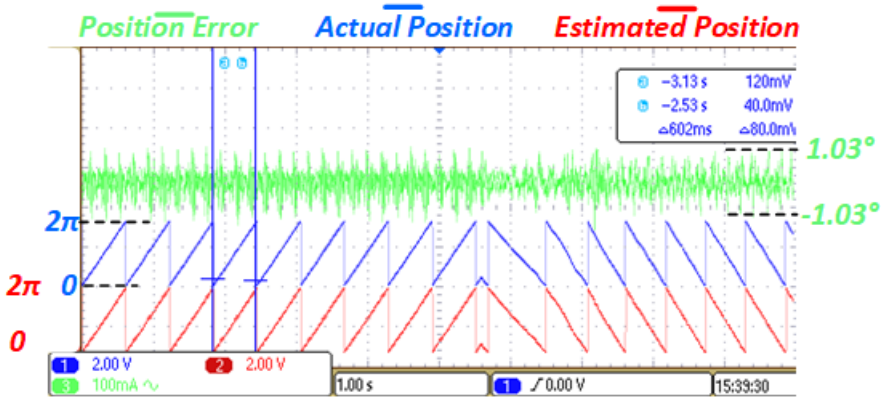

Figure 4.7: Sensorless performance in sudden speed reversal ($\pm 100 rpm$).

4.1.2 Dynamic Conditions

Robustness of the proposed sensorless algorithm is accentuated through investigation of its performance in dynamic operating points. Successful dynamic performance, per se, is an indicator of the overall stability and robustness of the proposed method.

4.1.2.1 Speed Reversal Performance

Figure (4.7) depicts the sensorless performance when the speed command is changed, in a step-wise manner, from $+100 rpm$ to $-100 rpm$. The peak-to-peak estimation error is 2.06° and the mechanical period is obtained as $602 ms$, which verifies the accurate performance of the speed loop in tracking the speed command. The performance is also inspected when the speed is changed from $100 rpm$ to standstill and then to $-100 rpm$, as shown in Fig. (4.8). Three important instances of steady-state at $100 rpm$, stop, and start-up toward $-100 rpm$ are enlarged. In all of the conditions, the estimated and actual positions are almost identical, which is an indicator of performance robustness and stability.

4.1.2.2 Start-up Performance

Given a same set of HFI voltages, PLL parameters, and PI regulators for the speed and current loops, the start-up performance of the proposed method and the conventional current-based sensorless control (rotating signal injection method) are compared in Fig. (4.9). In terms of start-up transient, both methods complete the procedure in a similar period, which is $3 s$. Such a long start-up transient is attributed to the heavy coupling used for coupling the motor to the load generator (look at Fig. (4.1)). Moreover, both the actual and esti-

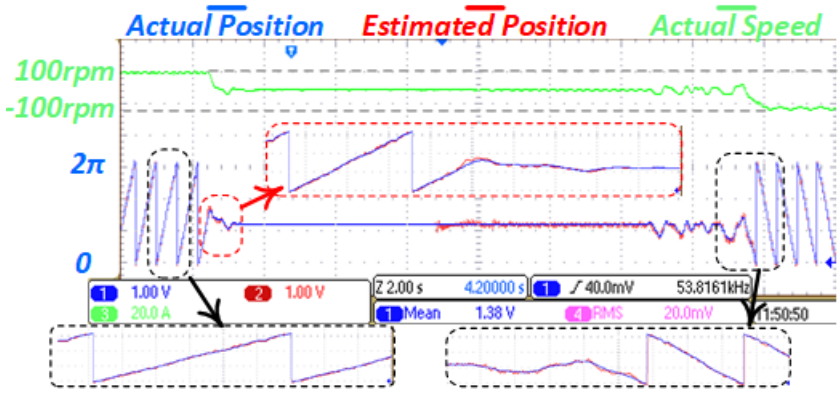

Figure 4.8: Sensorless performance when the speed is changed from $100rpm$ to zero and from zero to $-100rpm$.

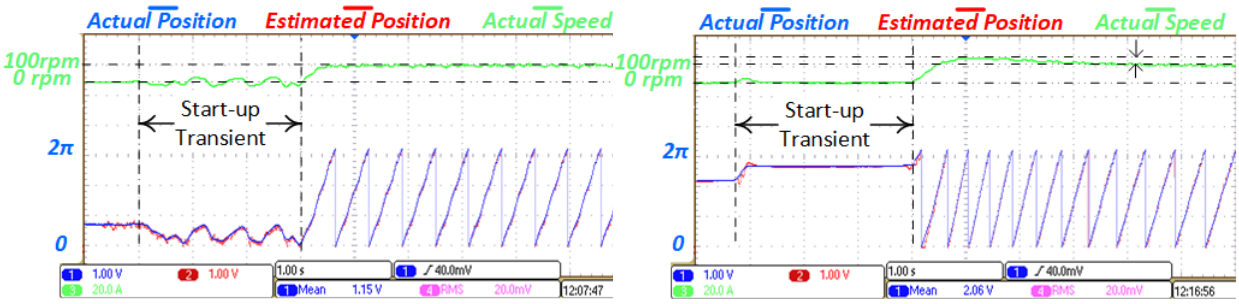

(a) The proposed method.

(b) The conventional method.

Figure 4.9: Comparison of start-up performance.

mated rotor positions are perfectly synchronised, without any DC offset, which indicates a satisfactory performance. In terms of the speed profile, the proposed method reaches the reference value, while there is an overshoot of about 50% within the conventional method (prior to reaching the final reference speed).

4.1.2.3 Sudden Switch Between the Sensorless and Sensored Operations

One of the main justifications of using sensorless algorithms, over the encoder-based methods, is the potential of sensorless control to be used in times of a sudden outage of the position sensor. Such a scenario is shown in Fig. (4.10), in which the estimated values of speed and position are suddenly replaced by their actual values for the coordinate transformation and FOC algorithm.

In this test, the actual and estimated positions are synchronised. In addition, the fundamental component of the phase current is shown, with its amplitude remaining the same

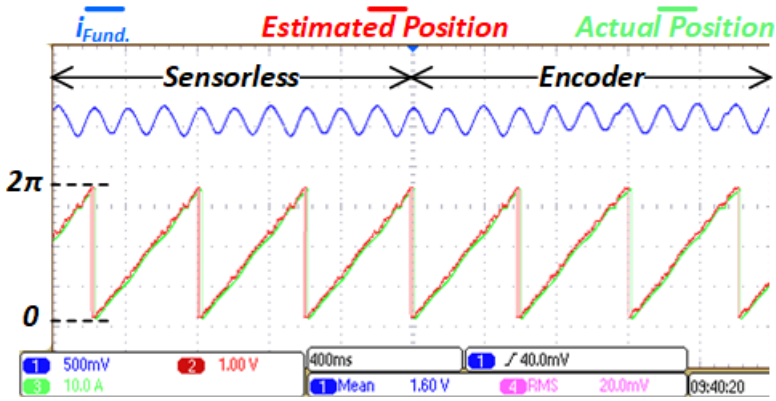

Figure 4.10: Sudden switch among the proposed method and the encoder-based method.

before and after the switching. The current profile shows that the estimation is perfectly accomplished. Otherwise, if there had been a difference among the actual and estimated d-axes, the phase current amplitude would have changed before and after the switching. Additionally, this test substantiates the stable performance of the proposed sensorless algorithm, as the positioning of the actual and estimated rotor positions has not witnessed any change before and after the sudden switch.

4.1.2.4 Dynamic Loading Performance

Sensorless performance during dynamic loading condition is of paramount importance, which is investigated in Fig. (4.11). The reference speed is fixed at $500rpm$ while different loads are applied to the machine. Given the static resistive load bank connected to the PMSG, the maximum available load is obtained at the revolution speed of $500rpm$ and the q-axis current of $22A$ which represents 78.2% nominal current. Although there are speed deviations observed at the instances of load change, the speed profile is able to track the reference value, which verifies the robust and stable performance of the whole system. In addition, in both light and heavy loads, the waveforms are enlarged and it is observed that both the estimated and actual positions are synchronised.

4.1.2.5 Dynamic Speed Change Performance

Investigation of sensorless performance during dynamic speed change is another test illustrated within Fig. (4.12). The reference speed is arbitrarily changed from $100rpm$ to $500rpm$ while the actual and estimated positions are shown. For the lowest and highest speeds, the waveforms are magnified, which show that the estimated and actual positions are completely

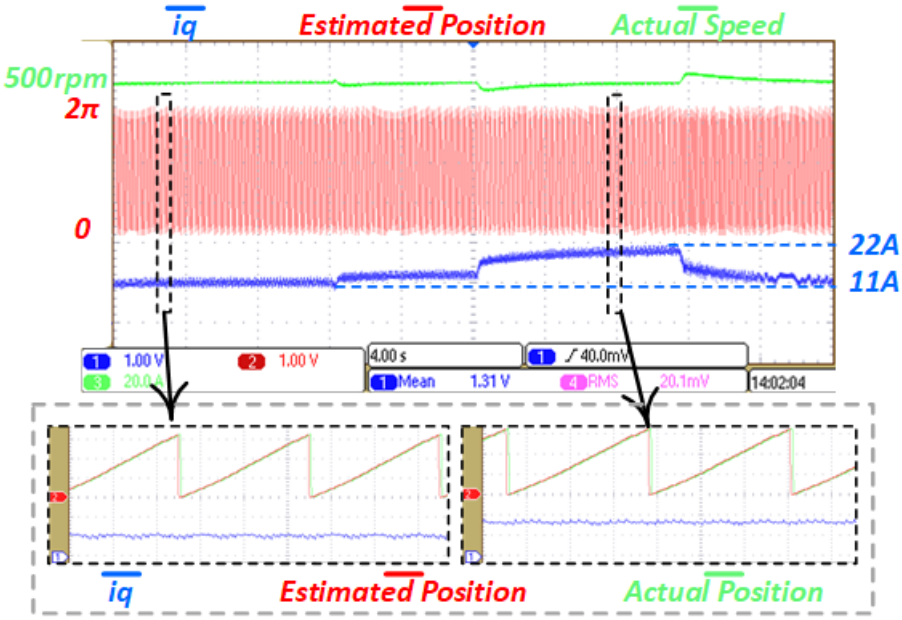

Figure 4.11: Sensorless performance at $500rpm$ in dynamic loading condition.

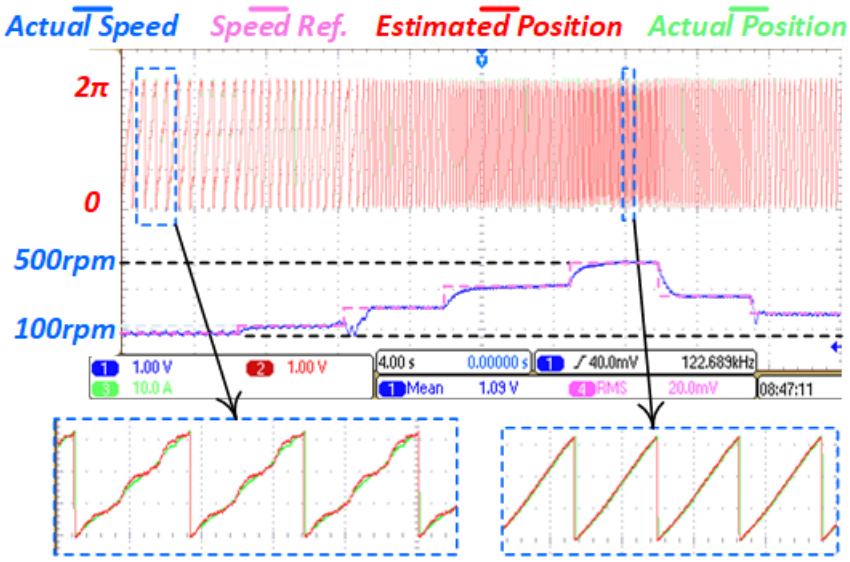

Figure 4.12: Sensorless performance in dynamic speed change.

synchronised. Although there is a low-frequency ripple on the estimated position at $100rpm$, it is diminished as the speed is increased.

In this section, the performane of the proposed HFI-based, acoustic noise-driven sensorless control was verified through static and dynamic tests performed in various conditions. In all of the conditions, the performance was stable and robust, which introduces the proposed

method as a reliable alternative to the conventional sensorless methods.

4.2 Injectionless Acoustic Noise-driven PMSM Sensorless Control

In this section, the performance of the proposed sensorless control relying on the PWM harmonics is experimentally scrutinized. As mentioned earlier in Chapter 2, Section 2.5, the proposed injectionless sensorless control has significantly lower disseminated acoustic noise and current profiles with noticeably lower distortions. Therefore, using this method is deemed a suitable improvement, over the HFI-based methods.

Similar to the previous section, the performance is inspected in static and dynamic conditions in order to prove the robustness and stability of the proposed method. In all of the tests, a simple PLL is used as the observer and it is observed that the estimated values are contaminated with specific-order harmonics. Therefore, the PLL is replaced by an RCPLL (proposed in Chapter 3, Subsection 3.5.1), in order to suppress the unwanted harmonics, and the performance is evaluated. In addition, the switching frequency is fixed at $10KHz$ and the seventh harmonic sideband ($h = 7$), amongst the possible odd-order sidebands, is used for the signal processing for all the presented results.

4.2.1 Static Conditions

Throughout this section, the steady-state performance of the proposed sensorless algorithm is investigated in different operating points. It is to be mentioned that a simple PLL, as the position observer, is used for the tests in this subsection.

4.2.1.1 Signal Processing

Figure (4.13) shows the raw sampled acoustic noise in addition to the extracted orthogonal signals (Signal I ad Signal II are the outputs of the signal processing) at $500rpm$. Even though the testbench is not isolated in an anechoic chamber and random environmental noises are present which is exactly the case in actual experimental conditions, the extracted signals are perfectly sinusoidal with the desired frequency, which validates the signal processing accuracy. The extracted signals must, theoretically, have the frequency of $175Hz$ with the period of $5.71ms$, yet the frequency is experimentally obtained as $178.57Hz$ with the period

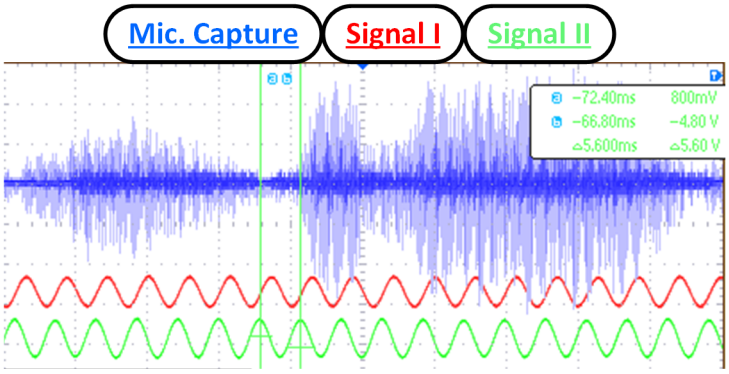

Figure 4.13: Signal processing performance.

of 5.60ms (1.92% difference).

4.2.1.2 Steady-state Performance

The steady-state performance at the low-speed of 75rpm is illustrated in Fig. (4.14). The maximum peak-to-peak estimation error is 0.085°, and both the actual and estimated positions are synchronized. The theoretical mechanical period is 800ms, while the experimental one is obtained as 797ms which shows there is a difference of 0.375%.

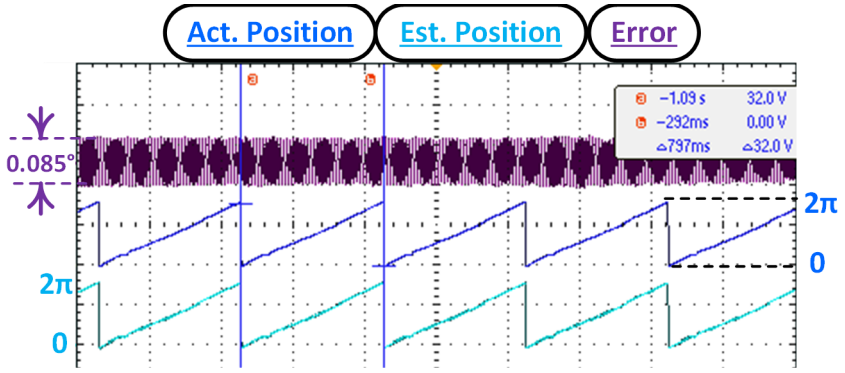

Figure 4.14: Performance at 75rpm.

The performance at 800rpm is shown in Fig. (4.15) in which the maximum estimation error is 3.42°. The theoretical mechanical period is 75ms and the experimental value is obtained with 3.54% difference at 77.66ms.

Given the presented figures and although there is zero DC offset among the actual and estimated positions, the estimation error contains unwanted harmonics which are appeared in the estimated position also. Existence of such harmonics means that the PLL's loop filter

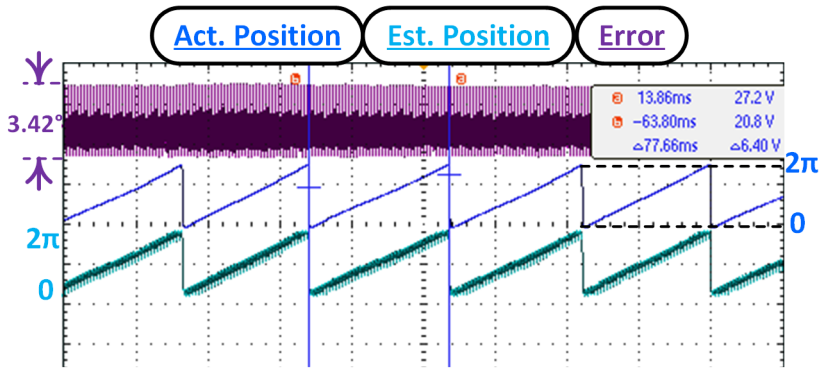

Figure 4.15: Performance at 800rpm.

is not able to suppress them effectively.

4.2.2 Dynamic Conditions

Similar to the previous section, the performance of this method is also inspected in several dynamic conditions. Again, the utilised observer is a simple PLL in order to show that the performance is robust even if there exist unwanted harmonics within the estimated values.

4.2.2.1 Speed Reversal Performance

Figure (4.16) depicts the performance during transitioning from standstill to 100rpm and standstill toward $-100rpm$. The maximum peak-to-peak estimation error is 0.2° and the estimated and actual positions are synchronised. The theoretical mechanical period at 100rpm is 598ms, and it is experimentally obtained 600ms which shows a discrepancy equal to 0.33%.

4.2.2.2 Dynamic Speed Change Performance

The dynamic performance during speed change is another test shown in Fig. (4.17). The reference speed is randomly changed from 100rpm-500rpm and the estimated and actual positions are shown. For the zones at the lowest and highest speed, the waveforms are enlarged which shows that the estimated and actual positions are perfectly synchronised.

4.2.2.3 Dynamic Loading Performance

Maintaining a robust operation at times of sudden load change is an important performance metric. In this regard, Fig. (4.18) shows the sensorless performance at the revolution speed

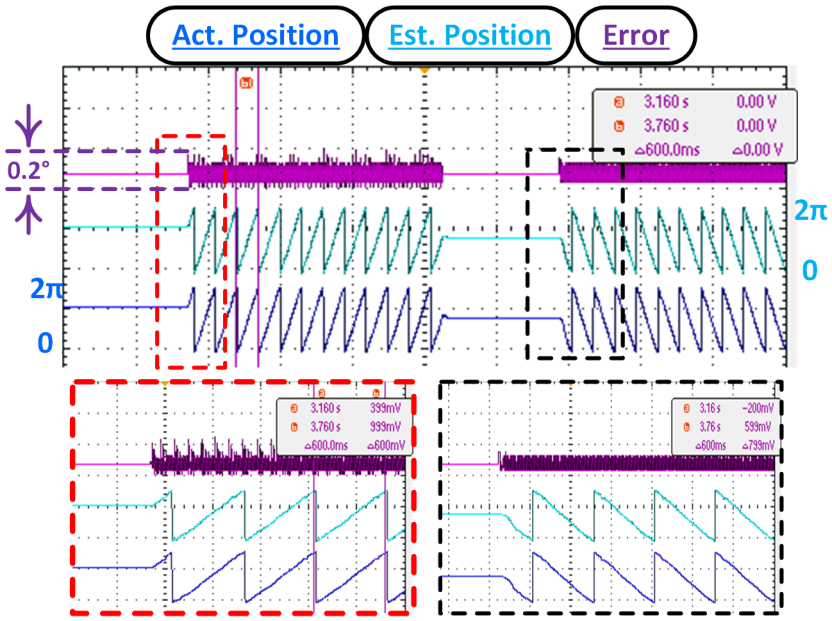

Figure 4.16: Performance at positive, zero, and negative speeds.

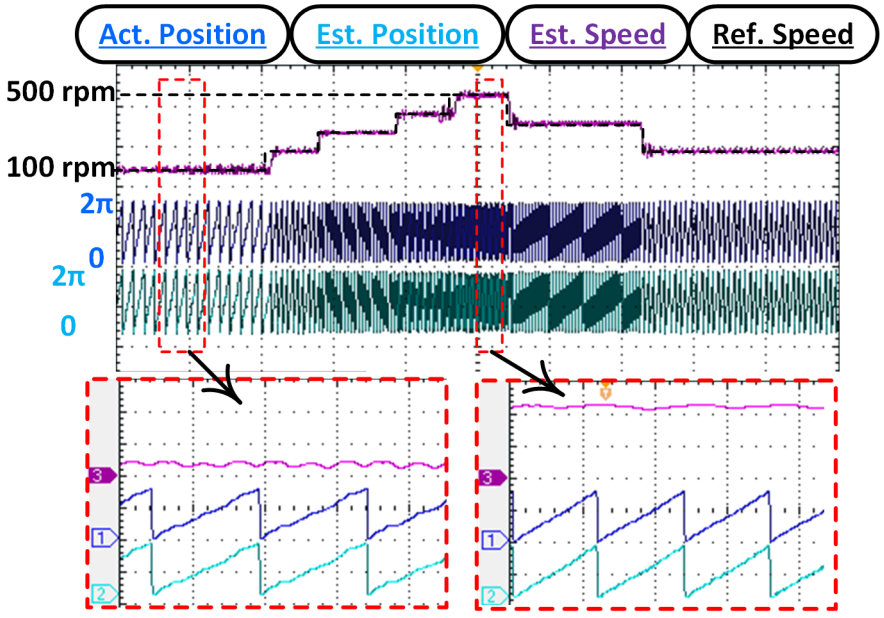

Figure 4.17: Performance at dynamic speed change.

of 500rpm while the machine undergoes several step-wise changes in the loading profile. The q-axis curent, which represents the generated torque, is shown with changes from 11A to 22A (78.2% nominal current). At the instances of load change, the speed profile experiences fluctuations within 5% of the reference speed. In addition, the waveforms for the lightest

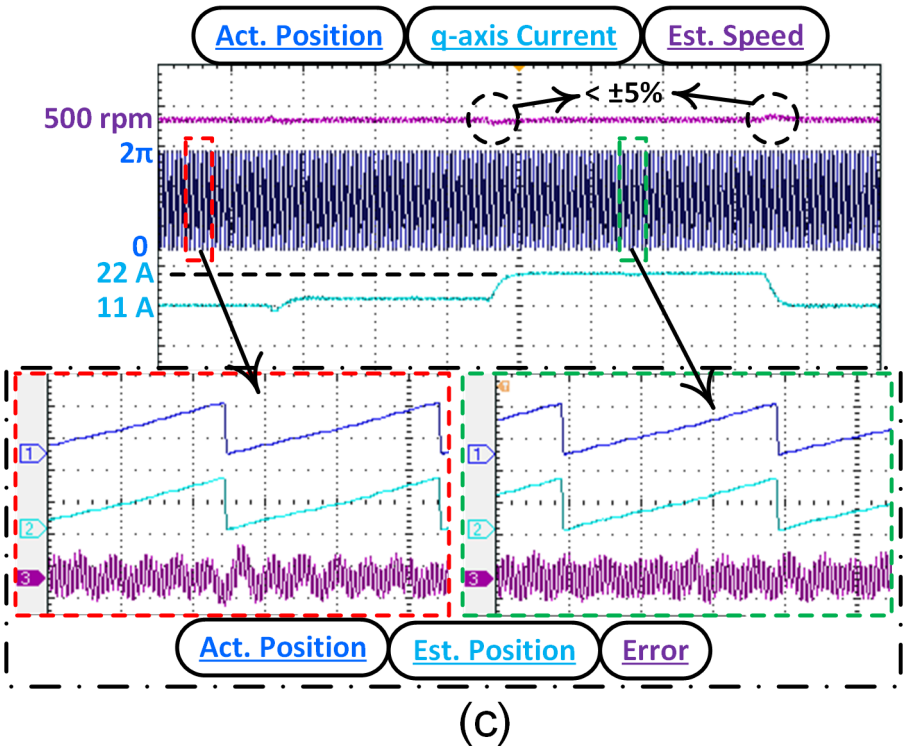

Figure 4.18: Performance at dynamic loading.

and heaviest loads are enlarged, which show that the estimated and actual positions are synchronised.

4.2.2.4 Start-up Performance

Start-up performance has always been one of the most challenging aspects for the sensorless algorithms. To this end, Fig. (4.19) draws a comparison between the start-up performance of the proposed injectionless sensorless control (relying on acoustic noise), the proposed HFI-based sensorless control (relying on acoustic noise), and the conventional HFI-based sensorless control (relying on the $\alpha\beta$-frame currents - rotating signal injection method). For all conditions, the reference speed is stepped from zero to $110rpm$. Moreover, for the HFI-based methods, a same set of HFI voltages with the magnitude of $5V$ and the frequency of $1440Hz$ is used within the estimated dq-frame (the injectionless method only relies on the PWM harmonics). Moreover, a same set of PI settings (for the speed loop, current loop, and PLL) are used for all the three compared methods.

In terms of the start-up dynamics, the injectionless method completes the procedure

in $3.75s$, while the other two methods respectively complete the procedure in $5s$ and $4s$. Regarding the estimation error, the injectionless method has the peak-to-peak value of $0.5°$, while the other two methods have respective peak-to-peak values of $1.1°$ and $1°$. Both the acoustic noise-based methods are able to reach the reference speed after the start-up dynamics, but the conventional current-based sensorless method experiences an overshoot within its speed profile (since the mechanical period for the acoustic noise-based methods is stable at $547ms$, yet it has not yet fixed for the other method).

The main goal of this start-up comparison was to showcase the potential of the two proposed methods, compared to the conventional current-based method. By changing the PI settings, for each method individually, it is possible to have very similar start-up performances.

Given the presented results in this section, the estimation error is composed of a DC term which is eliminated by the loop filter (PI within the PLL) and some AC terms (harmonics) which are passed through the loop filter and appeared in the estimated position and estimated speed profiles. Consequetly, throughout the next subsection, the performance of the proposed sensorless control is compared when the PLL and RCPLL are used as the observer.

4.2.3 RCPLL Impact on Sensorless Performance

4.2.3.1 Steady-state Performance

The effectivity of using RCPLL is verified for the speeds of $75rpm$ and $800rpm$ as shown in Fig. (4.20) and Fig. (4.21); in each figure, the sensorless performance with PLL and RCPLL is compared.

In Fig. (4.20a), the peak-to-peak estimation error is $0.171°$ for the PLL, while it is plunged to $0.057°$ when RCPLL is used. Given both observers, the synchronism between the actual and estimated positions, with the period of $802ms$, is maintained. This means that introduction of RCPLL to the system does not affect the DC offset, yet substantially reduces the estimation error harmonics. The estimated speed harmonics are also shown in Fig. (4.20b) with a $\pm 5rpm$ ripple for the case of PLL, which is alleviated to $\pm 1.67rpm$ for the case of RCPLL. The zoomed version of the waveforms are also shown which certifies the effectivity of using RCPLL is suppression of the undesired harmonics.

Looking at the waveforms in the frequency domain shown in Fig. (4.20c), the fundamental harmonic within the estimation error is double the PLL input frequency (at $75rpm$ and $h = 7$, the PLL input frequency is $26.25Hz$); the other harmonics can be neglected due to their tiny

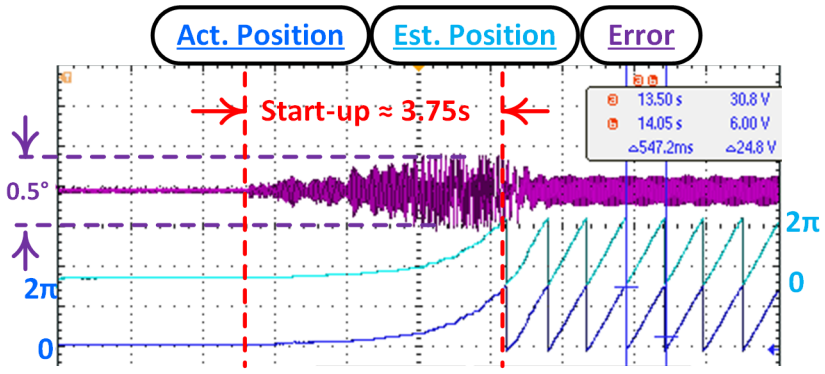

(a) Injectionless acoustic noise-based sensorless control.

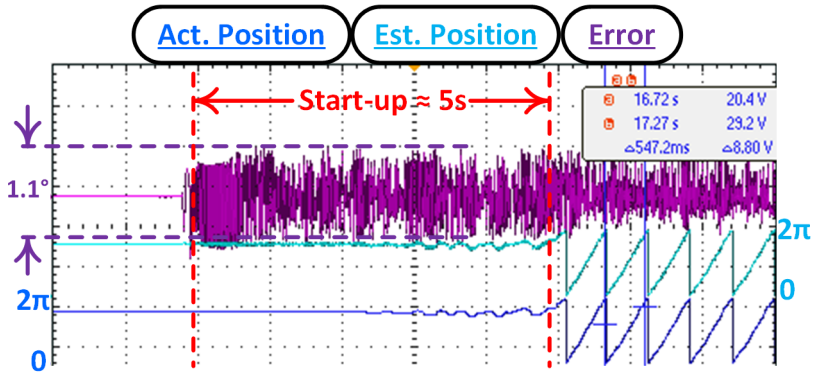

(b) Acoustic noise-based sensorless control with HFI.

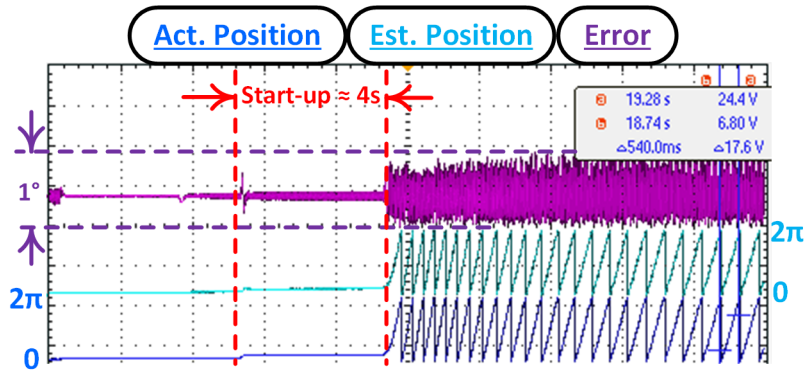

(c) Conventional current-based sensorless control.

Figure 4.19: Start-up performance comparison.

magnitudes. Accordingly, the resonating compensation block is tuned at this frequency and it is observed that there is a 68.75% reduction in the harmonic magnitude (reduction from

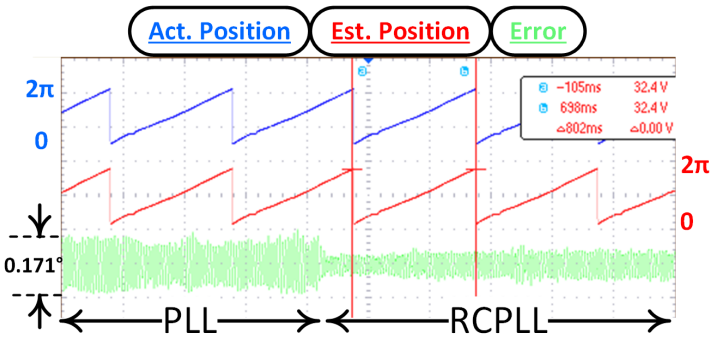

(a) The actual and estimated positions alongside the estimation error.

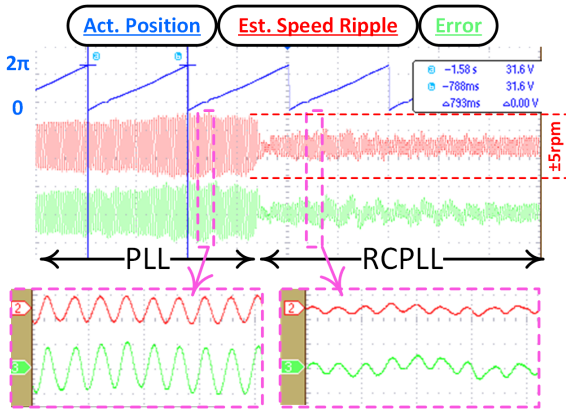

(b) Ripple of the estimated speed and estimation error.

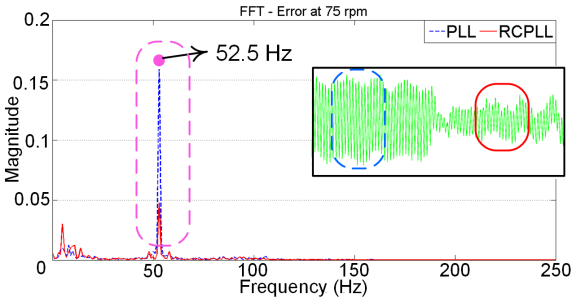

(c) FFT of the estimation error.

Figure 4.20: Comparison of PLL and RCPLL performance at $75rpm$.

0.16 to 0.05). It is worth mentioning that the similar reducing-trend governs the harmonics of the estimated speed.

Looking at the performance at $800rpm$ with the mechanical period of $72.60ms$ shown in Fig. (4.21a), there is a peak-to-peak estimation error of 2.57°. Moreover, there is a high-frequency ripple on the estimated position. As the result, RCPLL is accordingly used in order to suppress theses harmonics. Its impact is noticeable on both the estimation error and the estimated position, which is now much smoother. There is a speed ripple equal to $\pm 20rpm$ which is reduced by 66% when RCPLL is used, as shown in Fig. (4.21b). In order to further magnify the positive impact of RCPLL on the estimation performance, the zoomed versions are also provided in this figure.

Both the estimated speed and estimated positions contain harmonics of order 2 and 4 (with respect to the observer input at $280Hz$); consequently, the resonating compensation

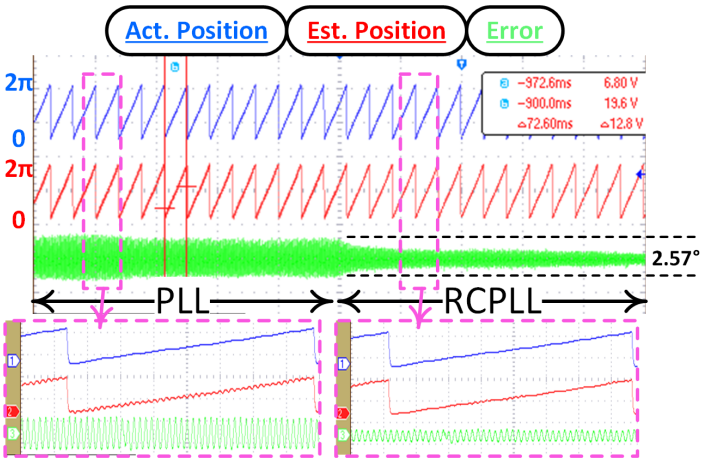

(a) The actual and estimated positions alongside the estimation error.

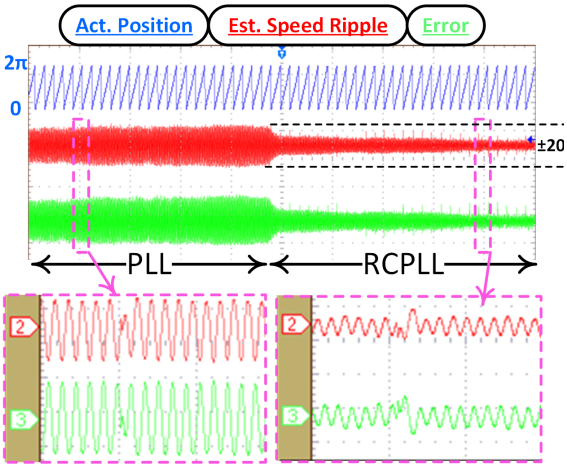

(b) Ripple of the estimated speed and estimation error.

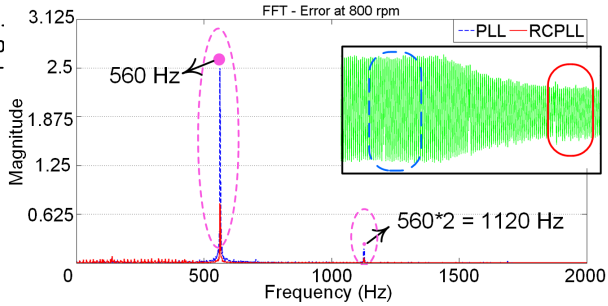

(c) FFT of the estimation error.

Figure 4.21: Comparison of PLL and RCPLL performance at 800rpm.

block is tuned for 560Hz and 1120Hz. Given the estimation error, the harmonics at 560Hz and 1120Hz are respectively reduced by 75% when the RCPLL is applied as shown in Fig. (4.21c).

4.2.3.2 Dynamic Speed Change Performance

The comparative performance of PLL and RCPLL in dynamic speed change is also provided in Fig. (4.22). The reference speed is stepped from 200rpm to 300rpm and the actual and estimated positions alongside the estimation error are illustrated. In the case of PLL and at

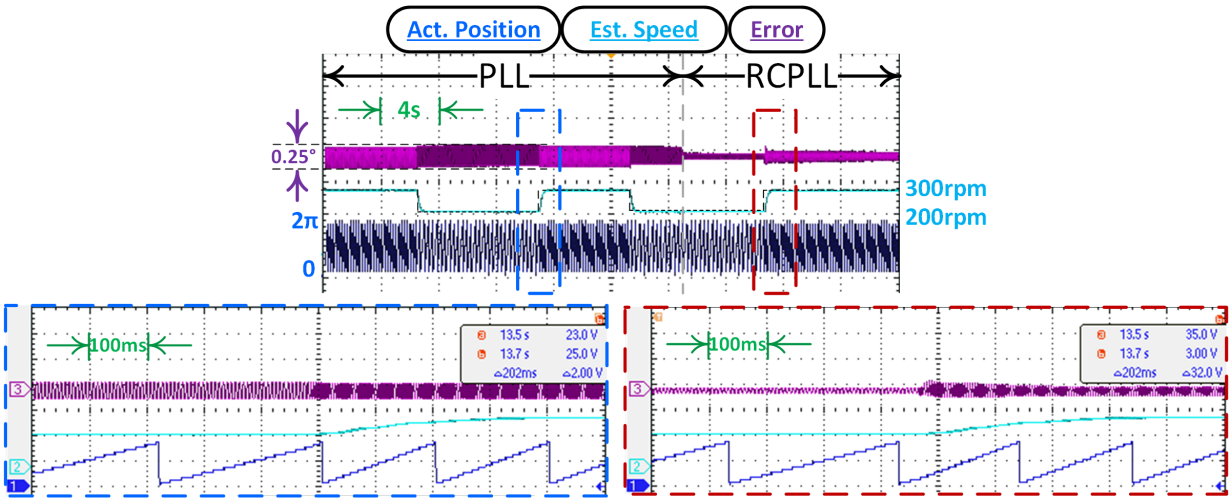

Figure 4.22: Comparison of dynamic performance between PLL and RCPLL in case of step speed change.

200rpm, the peak-to-peak estimation error is 0.25°, while using RCLL has culminated in a 75% reduction of the error magnitude. At 300rpm and for the case of PLL, the maximum value of error is around 0.22°, while it has experienced 50% reduction when RCPLL is used.

In both speeds, the value of $K_{RC} = 0$ is used for the PLL scenario and $K_{RC} = 5$ for the RCPLL scenario. Due to the adpative designs of the signal processing and RCPLL, the parameters of the resonating compensation block are autmatically adapted to the reference speed. The zoomed versions of the waveforms are also shown at the onsets of the speed change. It is observed that the RCPLL does not affect the dynamic performance (which is mainly governed by the PI regulators within the PLL and the speed loop), yet significantly improves the estimation performance (as its impact is clear on the estimation error value).

Finally, it is worth mentioning that complete suppresion of the unwanted harmonics, using RCPLL, is not practically posible. The reason behind that is the harmonic repression capability of the RCPLL is directly controlled by the value of K_{RC}, yet assigning high values to this coefficient makes the RCPLL approach its unstable region.

4.3 Conclusion

In this chapter, performances of the proposed HFI-based and HFIless acoustic noise-driven sensorless algorithms were experimentally investigated. The methods were tested under various static and dynamic conditions. During the static tests, the steady-state performances

of both low-speed and high-speed zones, including the position estimation error in addition to the actual and estimated rotor positions, were investigated. In dynamic conditions, the sudden speed reversal, dynamic speed change, dynamic load change, and the start-up performance, were inspected. In all of the tests, the proposed methods operated with robustness and stability, which introduced them as reliable alternatives to the conventional sensorless algorithms.

Suppresing the undesired harmonics within the estimated parameters, the proposed RC-PLL performance was investigated, by comparison with PLL. The comparison was made in static conditions in both low- and high-speed zones. Additionally, the comparative performance in dynamic step-wise speed change was conducted. In all conditions, RCPLL was able to provide an stable performance with improved estimation performance (compared with PLL).

Conclusion

Conclusion

A novel method for implementation of PMSM sensorless control, relying on the machine output acoustic noise was developed in this thesis. This method utilises the multi-physics aspects of the machine, in an active manner, and incorporates the extracted information within the control algorithm. Due to the multifaceted nature of this topic, electromagnetic, mechanical, and control aspects should be deeply investigated.

Chapter 1 was dedicated to the state-of-the-art about the PMSM fundamentals, sensorless control algorithms, and vibration and acoustic noise occurrence in electric machines (with a special focus on PMSM), serving as the necessary background for the upcoming topics throughout the following chapters.

Given the medium-high speed range, the model-based sensorless methods, relying on the EEMF/linear flux, in addition to the state space notation and corresponding observers were presented.

On the other hand, given the zero and low-speed range, saliency tracking-based methods which rely on the machine saliency alteration were presented. Both the HFI-based and PWM carrier-based methods alongside the initial magnet polarity detection algorithms were reviewed.

The final section was dedicated to the vibration/acoustic noise phenomena in PMSM. The electromagnetic equations describing the formation of airgap fields and radial forces were firstly provided. Following that, the origins and fundamental equations of the vibration/acoustic noise in electric machines were reviewed.

Chapter 2 investigated the vibro-acoustic response of PMSM, to the HFI and PWM voltage excitations. The investigation was firstly conducted for the case of HFI, then similar approach was adopted for the case of PWM.

Given various HFI voltages, the harmonics within the current, airgap field and radial force, and resulting vibration/acoustic noise were identified. It was shown that the specific speed-dependent harmonics within the radial force were directly reflected within the output vibration/acoustic noise, verified through simulation and experimental tests.

Eliminating the HFI, the impact of PWM voltages was also investigated. The PWM voltage generation, taking into consideration the impact of deadtime, was mathematically modelled. Although the PWM deadtime contaminated the spectrum of current, magnetic field and radial force, its impact upon the output vibration/acoustic noise was negligible (all verified through experimental tests in different conditions with various deadtime intervals and acoustic sampling rates). This important feature is a key advantage in terms of signal processing and harmonic extraction.

Given both conditions and irrespective of the revolution speed, the acoustic noise spectrograms were devided into five different zones, among which the one around the injected frequency (either HFI or PWM carrier frequency) hosted several specific speed-dependent sidebands and could be used as the source for extraction of the rotor position information.

Finally, considering the acoustic noise spectrum, the harmonics located in the proximity the PWM zone were exactly similar for both conditions, yet the HFI condition contained several additional harmonic components around the HFI frequency and in higher-frequency zones (due to the resonance phenomenon). It is to be mentioned that, the components lying in the low-frequency zone (near the fundamental electrical frequency and its low-order harmonics) were almost similar in both scenarios.

Chapter 3 implemented two novel acoustic noise-based PMSM sensorless controls, using HFI and PWM voltages. Two adaptive signal processing algorithms were proposed. The first strategy comprised four stages, including two BPF, one demodulation block, and one normalization block. The other 2-stage signal processing algorithm eliminated the BPF stages, and incorporated an ADALINE-based filtering stage instead while mantaining the demodulation block. The proposed signal processing structures in addition to the final normalization stages guarantee that the impact of environmental noise, on the extracted signals, is minimized and the extraction is realized with the utmost precision. Regardless of the adopted signal processing method, the two orthogonal speed-dependent signals were successfully extracted.

Design and stability analysis of the current loop, position observer loop, and the overall speed loop were also presented in this chapter. Detailed model of each loop, taking into

account the digital delays within the actual system implementation, was considered. Stability of each loop, was verified by the associated bode plot and step response.

It was observed that several specific-order harmonics appeared within the estimation error of the position observer (PLL), which also appeared within the estimated rotor speed and position. Given the harmonics within the acoustic noise and dynamic model of PLL, the expected harmonics within the estimation error were identified. Suppressing these harmonics, a feed-forward harmonic compensation block was integrated into the PLL. Two harmonic compensation blocks, based on an RC or an ADALINE, were proposed which respectively resulted in two novel position observers called RCPLL and ADALINE-PLL. By using these two novel observers, equipped with adaptive harmonic compenstion, the estimation performance was improved, compared to a simple PLL.

Experimental verification of the proposed acoustic noise-based sensorless algorithms was presented in **Chapter 4**. All of the methods were tested in static and dynamic conditions to verify the accuracy of the signal processing, steady-state response, and transient behaviour of the overall system. For the HFI-based case, a voltage signal was injected in the estimated dq-frame with the frequency of $1440Hz$ and the PWM carrier was fixed at $10KHz$ for both the HFI and HFIless conditions.

In all conditions, the actual and estimated rotor positions were synchronized, without any DC offset, indicating appropriate d-axis estimation and signal processing without significant delay. Also, the sensorless algorithms were capable of providing satisfactory performance in dynamic conditions, including speed reversal, start-up, speed change, and load variation. In terms of start-up dynamic performance, the proposed methods were compared with the conventional current-based sensorless algorithms, and similar performances were observed which showed the reliability of the proposed methods.

Moreover, the performances of the PLL and proposed RCPLL were compared in static and dynamic conditions. The results revealed that using RCPLL provides the sensorless performance with an improved estimation with significnatly lower harmonics.

Overall, both of the propsoed methods were able to provide estimation at standstill and self start-up while also operation at medium-high speed region. This wide operating range is a key characteristic which substantiates the reliability and robustness of the proposed methods.

Research Perspective

This dissertation introduced a novel acoustic noise-driven method for implementation of sensorless control, which is a new perspective in active utilization of cross-coupled phenomena in electric machines. Consequently, this section deals with the potential improvements and future research vistas, which can broaden the application of this new technology.

- **Application to Other Machines**

  This thesis developed the proposed sensorless algorithms for a PMSM, yet there is an essential need for further development of this method to other SM or IM topologies. In this regard, the analytical equations should be used step-by-step so as to identify the harmonics within the magnetic fields and radial forces.

  In addition, the existing FEM-based softwares are not optimized enough for delivering rapid multi-physics analyses during the theoretical stages. More specifically, performing transient mechanical analysis, providing the time-based vibration/acoustic noise (instead of just the FFT) requires a large amount of time and huge processing power which is a hindrance to the first stages of the study.

- **Active Diagnosis**

  Active fault diagnosis is a potential auxiliary application of the proposed methods in this thesis. A single (or combination of) HFI signals alongside an array of microphones can be used to perform condition monitoring or prognosis in an active manner, which reveals potential faults in their early stages (which is in direct contrast to the conventional passive diagnosis procedures where the fault is only detected after its occurrence).

  Beam forming of the disseminated acoustic noise is also a potential way of facilitating the active fault diagnosis.

- **Machine Optimization**

  The proposed methods were experimentally verified on a typical PMSM. However, the machine structure can be undergone several optimizations with the goals of having improved directive sound propagation and optimized magnetic behaviour. Performing these optimizations yields the production of purpose-built machines for the acoustic noise-based applications.

- **Improved Algorithms**

  Using improved signal processing algorithms and position observers, yielding a better sensorless performance, is a potential improvement.

  Our machine was placed in an open laboratory environment, full of natural surrounding noise, and the sensorless algorithms were able to perform satisfactorily. However, when a sudden high-pitch noise (representing a dirac-like function) was generated close to the microphone, the estimation was temporarily disrupted. Consequently, finding solution to tackle this issue - *i.e.*, improved signal processing algorithms equipped with active noise cancellation techniques or using artificial intelligence-based noise rejection - is essential. Moreover, providing physical protection against unwanted disturbances can also be considered (e.g. placing the microphone inside the stator structure to be naturally isolated from the outer environment).

- **Increased Frequency**

  Incearsing the HFI and/or PWM carier frequency is not only a direct improvement to the proposed methods but also to the conventional saliency tracking-baseed methods, providing lower acoustic noise level and better spectral separation which facilitates the signal processing algorithm. However, increasing the frequency requires significant hardware revision. Adoption of wide-bandgap semiconductors (SiC/GaN), with the rapid boom in their application, is a feasible option which enables the inverter to operate at higher frequencies. At the same time, the calculation power of the processor must also be high enough to keep up with the increased overall system frequecy.

  Besides, operation at flux-weakening region, can also be addressed in the future studies. Study of the airgap fields and radial forces at this important region is the key for evaluation of performance.

Research Outputs

Peer-reviewed Journal Publication

1. A. Malekipour, A. Corne, L. Garbuio, P. Granjon and L. Gerbaud, "A Closed-Loop PMSM Sensorless Control Based on the Machine Acoustic Noise," in *IEEE Transactions on Industrial Electronics*, vol. 70, no. 10, pp. 9859-9869, Oct. 2023, doi: 10.1109/TIE.2022.3206755.

2. A. Malekipour, A. Corne, L. Garbuio, P. Granjon and L. Gerbaud, "Injectionless Acoustic Noise Based PMSM Sensorless Control Using RCPLL for Improved Estimation Performance," in *IEEE Transactions on Power Electronics*, doi: 10.1109/TPEL.2023.3319824.

Peer-reviewed Conference Publication

1. A. Malekipour, A. Corne, L. Garbuio, P. Granjon and L. Gerbaud, "On the Sensorless PMSM Rotor Position Estimation Enhancement: Application of ADALINE-PLL," 2023 25^{th} *European Conference on Power Electronics and Applications (EPE'*23 *ECCE Europe), Aalborg, Denmark*, 2023, pp. 1-8, doi: 10.23919/EPE23ECCEEurope58414.2023.10264353.

Patent

1. A. Malekipour, L. Garbuio, A. Corne, P. Granjon, and Z. Simeu-Abazi, "Dispositif de Détermination de la Position et/ou de la vitesse d'une Partie Mobile d'une Machine Électrique et Procédé Associé," $Ref.No.: B04767FR - RT2022013 - FRANCE.$

Bibliography

[1] Peter Vas. *Sensorless vector and direct torque control*. 1998.

[2] Gonzalo Abad et al. *Power electronics and electric drives for traction applications*. Wiley Online Library, 2017.

[3] Liuping Wang, Shan Chai, Dae Yoo, Lu Gan, and Ki Ng. *PID and predictive control of electrical drives and power converters using MATLAB/Simulink*. John Wiley & Sons, 2015.

[4] Seung-Ki Sul. *Control of electric machine drive systems*. John Wiley & Sons, 2011.

[5] František Mejdr. Determination of initial commutation angle offset of permanent magnet sybchronous machine-an overview and simulation. 2014.

[6] Mario Pacas. Sensorless drives in industrial applications. *IEEE Industrial Electronics Magazine*, 5(2):16–23, 2011.

[7] Gérard-André Capolino and Andrea Cavagnino. New trends in electrical machines technology—part ii. *IEEE Transactions on Industrial Electronics*, 61(9):4931–4936, 2014.

[8] Cesar José Volpato Filho, Dianxun Xiao, Rodrigo Padilha Vieira, and Ali Emadi. Observers for high-speed sensorless pmsm drives: Design methods, tuning challenges and future trends. *IEEE Access*, 9:56397–56415, 2021.

[9] Gaolin Wang, Maria Valla, and Jorge Solsona. Position sensorless permanent magnet synchronous machine drives—a review. *IEEE Transactions on Industrial Electronics*, 67(7):5830–5842, 2019.

[10] Allan B Plunkett and Fred G Turnbull. Load-commutated inverter/synchronous motor drive without a shaft position sensor. *IEEE Transactions on Industry Applications*, (1):63–71, 1979.

[11] Kenichi Iizuka, Hideo Uzuhashi, Minoru Kano, Tsunehiro Endo, and Katsuo Mohri. Microcomputer control for sensorless brushless motor. *IEEE Transactions on Industry Applications*, (3):595–601, 1985.

[12] Jacques Davoine, Robert Perret, and Hoang Le-Huy. Operation of a self-controlled synchronous motor without a shaft position sensor. *IEEE Transactions on Industry Applications*, (2):217–222, 1983.

[13] Rusong Wu and Gordon R Slemon. A permanent magnet motor drive without a shaft sensor. *IEEE Transactions on Industry Applications*, 27(5):1005–1011, 1991.

[14] Raymond B Sepe and Jeffrey H Lang. Real-time observer-based (adaptive) control of a permanent-magnet synchronous motor without mechanical sensors. *IEEE Transactions on Industry Applications*, 28(6):1345–1352, 1992.

[15] Min-Ho Park and Hong-Hee Lee. Sensorless vector control of permanent magnet synchronous motor using adaptive identification. In *15th Annual Conference of IEEE Industrial Electronics Society*, pages 209–214. IEEE, 1989.

[16] Alfio Consoli, Salvatore Musumeci, Angelo Raciti, and Antonio Testa. Sensorless vector and speed control of brushless motor drives. *IEEE Transactions on Industrial Electronics*, 41(1):91–96, 1994.

[17] Mutuwo Tomita, Tomonobu Senjyu, Shinji Doki, and Shigeru Okuma. New sensorless control for brushless dc motors using disturbance observers and adaptive velocity estimations. *IEEE transactions on industrial electronics*, 45(2):274–282, 1998.

[18] Nobuyuki Matsui. Sensorless pm brushless dc motor drives. *IEEE Transactions on industrial Electronics*, 43(2):300–308, 1996.

[19] Zhiqian Chen. Sensorless control of interior permanent magnet synchronous motor by estimation of an extended electromotive force. In *Conference Record of the 2000 IEEE Industry Applications Conference. Thirty-Fifth IAS Annual Meeting and World Conference on Industrial Applications of Electrical Energy (Cat. No. 00CH37129)*, volume 3, pages 1814–1819. IEEE, 2000.

[20] Shigeo Morimoto, Keisuke Kawamoto, Masayuki Sanada, and Yoji Takeda. Sensorless control strategy for salient-pole pmsm based on extended emf in rotating reference frame. In *Conference Record of the 2001 IEEE Industry Applications Conference. 36th IAS Annual Meeting (Cat. No. 01CH37248)*, volume 4, pages 2637–2644. IEEE, 2001.

[21] Shigeo Morimoto, Keisuke Kawamoto, and Yoji Takeda. Position and speed sensorless control for ipmsm based on estimation of position error. *IEEJ Transactions on Industry Applications*, 122(7):722–729, 2002.

[22] M Hasegawa and K Matsui. Position sensorless control for interior permanent magnet synchronous motor using adaptive flux observer with inductance identification. *IET electric power applications*, 3(3):209–217, 2009.

[23] Mohamad Koteich, Abdelmalek Maloum, Gilles Duc, and Guillaume Sandou. Discussion on "ac drive observability analysis". *IEEE Transactions on Industrial Electronics*, 62(11):7224–7225, 2015.

[24] Mohammadreza Moradian, Jafar Soltani, Abbas Najjar-Khodabakhsh, and GR Arab Markadeh. Adaptive torque and flux control of sensorless ipmsm drive in the stator flux field oriented reference frame. *IEEE Transactions on Industrial Informatics*, 15 (1):205–212, 2018.

[25] Mohamed Darouach, Michel Zasadzinski, and Shi Jie Xu. Full-order observers for linear systems with unknown inputs. *IEEE transactions on automatic control*, 39(3): 606–609, 1994.

[26] Wen-Hua Chen, Jun Yang, Lei Guo, and Shihua Li. Disturbance-observer-based control and related methods—an overview. *IEEE Transactions on industrial electronics*, 63 (2):1083–1095, 2015.

[27] Cassio Luciano Baratieri and Humberto Pinheiro. Sensorless vector control for pm brushless motors with nonsinusoidal back-emf. In *2014 International Conference on Electrical Machines (ICEM)*, pages 915–921. IEEE, 2014.

[28] Lu Xiaoquan, Lin Heyun, and Han Junlin. Load disturbance observer-based control method for sensorless pmsm drive. *IET Electric Power Applications*, 10(8):735–743, 2016.

[29] Wenxiang Zhao, Shuai Jiao, Qian Chen, Dezhi Xu, and Jinghua Ji. Sensorless control of a linear permanent-magnet motor based on an improved disturbance observer. *IEEE Transactions on Industrial Electronics*, 65(12):9291–9300, 2018.

[30] Li Ding, Yun Wei Li, and Navid R Zargari. Discrete-time smo sensorless control of current source converter-fed pmsm drives with low switching frequency. *IEEE Transactions on Industrial Electronics*, 68(3):2120–2129, 2020.

[31] Quntao An, Jianqiu Zhang, Qi An, Xingya Liu, Alexander Shamekov, and Kaitao Bi. Frequency-adaptive complex-coefficient filter-based enhanced sliding mode observer for sensorless control of permanent magnet synchronous motor drives. *IEEE Transactions on Industry Applications*, 56(1):335–343, 2019.

[32] Song Chi, Zheng Zhang, and Longya Xu. Sliding-mode sensorless control of direct-drive pm synchronous motors for washing machine applications. *IEEE Transactions on Industry Applications*, 45(2):582–590, 2009.

[33] Zhaowei Qiao, Tingna Shi, Yindong Wang, Yan Yan, Changliang Xia, and Xiangning He. New sliding-mode observer for position sensorless control of permanent-magnet synchronous motor. *IEEE Transactions on Industrial electronics*, 60(2):710–719, 2012.

[34] Yue Zhao, Wei Qiao, and Long Wu. An adaptive quasi-sliding-mode rotor position observer-based sensorless control for interior permanent magnet synchronous machines. *IEEE Transactions on Power Electronics*, 28(12):5618–5629, 2013.

[35] Ying Zuo, Chunyan Lai, and K Lakshmi Varaha Iyer. A review of sliding mode observer based sensorless control methods for pmsm drive. *IEEE Transactions on Power Electronics*, 2023.

[36] Arie Levant. Sliding order and sliding accuracy in sliding mode control. *International journal of control*, 58(6):1247–1263, 1993.

[37] Donglai Liang, Jian Li, and Ronghai Qu. Sensorless control of permanent magnet synchronous machine based on second-order sliding-mode observer with online resistance estimation. *IEEE transactions on industry applications*, 53(4):3672–3682, 2017.

[38] Cassio Luciano Baratieri and Humberto Pinheiro. New variable gain super-twisting sliding mode observer for sensorless vector control of nonsinusoidal back-emf pmsm. *Control Engineering Practice*, 52:59–69, 2016.

[39] R Sreejith and Bhim Singh. Sensorless predictive control of spmsm-driven light ev drive using modified speed adaptive super twisting sliding mode observer with maf-pll. *IEEE Journal of Emerging and Selected Topics in Industrial Electronics*, 2(1):42–52, 2020.

[40] Donglai Liang, Jian Li, Ronghai Qu, and Wubin Kong. Adaptive second-order sliding-mode observer for pmsm sensorless control considering vsi nonlinearity. *IEEE Transactions on Power Electronics*, 33(10):8994–9004, 2017.

[41] Shaofang Wu, Jianwu Zhang, and Benben Chai. Adaptive super-twisting sliding mode observer based robust backstepping sensorless speed control for ipmsm. *ISA transactions*, 92:155–165, 2019.

[42] Cesar Jose Volpato Filho and Rodrigo Padilha Vieira. Adaptive full-order observer analysis and design for sensorless interior permanent magnet synchronous motors drives. *IEEE Transactions on Industrial Electronics*, 68(8):6527–6536, 2020.

[43] Sakorn Po-Ngam and Somboon Sangwongwanich. Stability and dynamic performance improvement of adaptive full-order observers for sensorless pmsm drive. *IEEE Transactions on power electronics*, 27(2):588–600, 2011.

[44] Toni Tuovinen, Marko Hinkkanen, Lennart Harnefors, and Jorma Luomi. Comparison of a reduced-order observer and a full-order observer for sensorless synchronous motor drives. *IEEE Transactions on Industry Applications*, 48(6):1959–1967, 2012.

[45] Marko Hinkkanen, Toni Tuovinen, Lennart Harnefors, and Jorma Luomi. A combined position and stator-resistance observer for salient pmsm drives: Design and stability analysis. *IEEE Transactions on Power Electronics*, 27(2):601–609, 2011.

[46] Antti Piippo, Marko Hinkkanen, and Jorma Luomi. Analysis of an adaptive observer for sensorless control of interior permanent magnet synchronous motors. *IEEE Transactions on Industrial Electronics*, 55(2):570–576, 2008.

[47] Parag Kshirsagar, Rolando P Burgos, Jihoon Jang, Alessandro Lidozzi, Fei Wang, Dushan Boroyevich, and Seung-Ki Sul. Implementation and sensorless vector-control design and tuning strategy for smpm machines in fan-type applications. *IEEE Transactions on Industry Applications*, 48(6):2402–2413, 2012.

[48] Silverio Bolognani, Luca Tubiana, and Mauro Zigliotto. Extended kalman filter tuning in sensorless pmsm drives. *IEEE Transactions on Industry Applications*, 39(6):1741–1747, 2003.

[49] Zheng Wang, Yang Zheng, Zhixiang Zou, and Ming Cheng. Position sensorless control of interleaved csi fed pmsm drive with extended kalman filter. *IEEE Transactions on Magnetics*, 48(11):3688–3691, 2012.

[50] Ruiwu Cao, Ning Jiang, and Minghang Lu. Sensorless control of linear flux-switching permanent magnet motor based on extended kalman filter. *IEEE Transactions on Industrial Electronics*, 67(7):5971–5979, 2019.

[51] Vaclav Smidl and Zdeněk Peroutka. Advantages of square-root extended kalman filter for sensorless control of ac drives. *IEEE Transactions on Industrial Electronics*, 59 (11):4189–4196, 2011.

[52] Silverio Bolognani, Luca Tubiana, and Mauro Zigliotto. Ekf-based sensorless ipm synchronous motor drive for flux-weakening applications. *IEEE Transactions on Industry Applications*, 39(3):768–775, 2003.

[53] Silverio Bolognani, Roberto Oboe, and Mauro Zigliotto. Sensorless full-digital pmsm drive with ekf estimation of speed and rotor position. *IEEE transactions on Industrial Electronics*, 46(1):184–191, 1999.

[54] Gilbert Hock Beng Foo, Xinan Zhang, and D Mahinda Vilathgamuwa. A sensor fault detection and isolation method in interior permanent-magnet synchronous motor drives based on an extended kalman filter. *IEEE Transactions on Industrial Electronics*, 60 (8):3485–3495, 2013.

[55] Gaolin Wang, Zhuomin Li, Guoqiang Zhang, Yong Yu, and Dianguo Xu. Quadrature pll-based high-order sliding-mode observer for ipmsm sensorless control with online mtpa control strategy. *IEEE Transactions on Energy Conversion*, 28(1):214–224, 2012.

[56] Dong Yeob Han, Yongsoo Cho, and Kyo-Beum Lee. Simple sensorless control of interior permanent magnet synchronous motor using pll based on extended emf. *Journal of Electrical Engineering & Technology*, 12(2):711–717, 2017.

[57] Matthew J Corley and Robert D Lorenz. Rotor position and velocity estimation for a salient-pole permanent magnet synchronous machine at standstill and high speeds. *IEEE transactions on industry applications*, 34(4):784–789, 1998.

[58] Fernando Briz and Michael W Degner. Rotor position estimation. *IEEE Industrial Electronics Magazine*, 5(2):24–36, 2011.

[59] Fei Peng, Jin Ye, Ali Emadi, and Yunkai Huang. Position sensorless control of switched reluctance motor drives based on numerical method. *IEEE Transactions on Industry Applications*, 53(3):2159–2168, 2017.

[60] Haoye Qin and Zhong Wu. Angle tracking observer with improved accuracy for resolver-to-digital conversion. *Symmetry*, 11(11):1347, 2019.

[61] Thiago Bernardes, Vinicius Foletto Montagner, Hilton Abilio Gründling, and Humberto Pinheiro. Discrete-time sliding mode observer for sensorless vector control of permanent magnet synchronous machine. *IEEE Transactions on industrial electronics*, 61(4):1679–1691, 2013.

[62] Yong Li, Hao Wu, Xing Xu, Xiaodong Sun, and Jindong Zhao. Rotor position estimation approaches for sensorless control of permanent magnet traction motor in electric vehicles: A review. *World Electric Vehicle Journal*, 12(1):9, 2021.

[63] Changliang Xia, D Wen, J Fan, and X Yang. Based on rbf neural network position sensorless control for brushless dc motors. *Transactions of China electrotechnical society*, 17(3):26–29, 2002.

[64] Li Hongru and Gu Shusheng. Neural-network-based adaptive observer of position and speed of pmsm. *PROCEEDINGS-CHINESE SOCIETY OF ELECTRICAL ENGINEERING*, 22(12):32–35, 2002.

[65] Xuan Wu, Dan Yang, Xu Yu, Kaiyuan Lu, Ting Wu, Shoudao Huang, and Hesong Cui. Improved position observer using adaptive training control-based filter for interior permanent magnet synchronous motor drives. *IEEE Transactions on Power Electronics*, 2023.

[66] Dario Pasqualotto, Saverio Rigon, and Mauro Zigliotto. Sensorless speed control of synchronous reluctance motor drives based on extended kalman filter and neural magnetic model. *IEEE Transactions on Industrial Electronics*, 70(2):1321–1330, 2022.

[67] Tae-Uk Jung, Jung-Hoon Jang, and Chang-Seok Park. A back-emf estimation error compensation method for accurate rotor position estimation of surface mounted permanent magnet synchronous motors. *Energies*, 10(8):1160, 2017.

[68] Linxin Yu and Dazhi Wang. A hybrid filtering stage-based rotor position estimation method of pmsm with adaptive parameter. *Sensors*, 21(14):4667, 2021.

[69] Tzu-Chi Lin, Zi-Qiang Zhu, and JM Liu. Improved rotor position estimation in sensorless-controlled permanent-magnet synchronous machines having asymmetric-emf with harmonic compensation. *IEEE Transactions on Industrial Electronics*, 62(10): 6131–6139, 2015.

[70] Marcin Morawiec, Arkadiusz Lewicki, and Charles Odeh. Rotor-flux vector based observer of interior permanent synchronous machine. *IEEE Transactions on Industrial Electronics*, 2023.

[71] Yanping Zhang, Zhonggang Yin, Cong Bai, Gaolin Wang, and Jing Liu. A rotor position and speed estimation method using an improved linear extended state observer for ipmsm sensorless drives. *IEEE Transactions on Power Electronics*, 36(12):14062–14073, 2021.

[72] Yao Xu, Cheng Lin, and Jilei Xing. Transient response characteristics improvement of permanent magnet synchronous motor based on enhanced linear active disturbance rejection sensorless control. *IEEE Transactions on Power Electronics*, 38(4):4378–4390, 2022.

[73] Younggi Lee and Seung-Ki Sul. Model-based sensorless control of an ipmsm with enhanced robustness against load disturbances based on position and speed estimator using a speed error. *IEEE Transactions on Industry Applications*, 54(2):1448–1459, 2017.

[74] G Scarcella, G Scelba, and A Testa. High performance sensorless controls based on hf excitation: A viable solution for future ac motor drives? In *2015 IEEE Workshop on Electrical Machines Design, Control and Diagnosis (WEMDCD)*, pages 178–187. IEEE, 2015.

[75] David Reigosa, Ye gu Kang, María Martínez, Daniel Fernández, Juan Manuel Guerrero, and Fernando Briz. Spmsms sensorless torque estimation using high-frequency signal injection. *IEEE Transactions on Industry Applications*, 56(3):2700–2708, 2020.

[76] Sang-Il Kim, Jun-Hyuk Im, Eui-Young Song, and Rae-Young Kim. A new rotor position estimation method of ipmsm using all-pass filter on high-frequency rotating voltage signal injection. *IEEE Transactions on Industrial Electronics*, 63(10):6499–6509, 2016.

[77] Lei Chen, Gunther Götting, Simon Dietrich, and Ingo Hahn. Self-sensing control of permanent-magnet synchronous machines with multiple saliencies using pulse-voltage-injection. *IEEE Transactions on Industry Applications*, 52(4):3480–3491, 2016.

[78] Slimane Medjmadj, Demba Diallo, Mohammed Mostefai, Claude Delpha, and Antoni Arias. Pmsm drive position estimation: Contribution to the high-frequency injection voltage selection issue. *IEEE Transactions on energy conversion*, 30(1):349–358, 2014.

[79] Fabien Gabriel, Frederik De Belie, Xavier Neyt, and Philippe Lataire. High-frequency issues using rotating voltage injections intended for position self-sensing. *IEEE Transactions on Industrial Electronics*, 60(12):5447–5457, 2012.

[80] Duro Basic, Francois Malrait, and Pierre Rouchon. Current controller for low-frequency signal injection and rotor flux position tracking at low speeds. *IEEE Transactions on Industrial Electronics*, 58(9):4010–4022, 2010.

[81] Dejan Raca, Pablo Garcia, David DÍaz Reigosa, Fernando Briz, and Robert D Lorenz. Carrier-signal selection for sensorless control of pm synchronous machines at zero and very low speeds. *IEEE Transactions on Industry Applications*, 46(1):167–178, 2009.

[82] Dejan Raca, Michael C Harke, and Robert D Lorenz. Robust magnet polarity estimation for initialization of pm synchronous machines with near-zero saliency. *IEEE Transactions on Industry Applications*, 44(4):1199–1209, 2008.

[83] Sung-Yeol Kim and In-Joong Ha. A new observer design method for hf signal injection sensorless control of ipmsms. *IEEE Transactions on Industrial Electronics*, 55(6): 2525–2529, 2008.

[84] Ludovico Ortombina, Matteo Berto, and Luigi Alberti. Sensorless drive for salient synchronous motors based on direct fitting of elliptical-shape high-frequency currents. *IEEE Transactions on Industrial Electronics*, 70(4):3394–3403, 2022.

[85] Ali Habib Almarhoon, ZQ Zhu, and Peilin Xu. Improved rotor position estimation accuracy by rotating carrier signal injection utilizing zero-sequence carrier voltage for dual three-phase pmsm. *IEEE Transactions on Industrial Electronics*, 64(6):4454–4462, 2016.

[86] PL Xu and ZQ Zhu. Novel square-wave signal injection method using zero-sequence voltage for sensorless control of pmsm drives. *IEEE Transactions on Industrial Electronics*, 63(12):7444–7454, 2016.

[87] PL Xu and ZQ Zhu. Novel carrier signal injection method using zero-sequence voltage for sensorless control of pmsm drives. *IEEE Transactions on Industrial Electronics*, 63 (4):2053–2061, 2015.

[88] Xing Zhang, Haoyuan Li, Shuying Yang, and Mingyao Ma. Improved initial rotor position estimation for pmsm drives based on hf pulsating voltage signal injection. *IEEE Transactions on Industrial Electronics*, 65(6):4702–4713, 2017.

[89] Guoqiang Zhang, Gaolin Wang, Huiying Wang, Dianxun Xiao, Liyi Li, and Dianguo Xu. Pseudorandom-frequency sinusoidal injection based sensorless ipmsm drives with tolerance for system delays. *IEEE Transactions on Power Electronics*, 34(4):3623–3632, 2018.

[90] Qipeng Tang, Anwen Shen, Xin Luo, and Jinbang Xu. Pmsm sensorless control by injecting hf pulsating carrier signal into abc frame. *IEEE Transactions on Power Electronics*, 32(5):3767–3776, 2016.

[91] PL Xu and ZQ Zhu. Carrier signal injection-based sensorless control for permanent-magnet synchronous machine drives considering machine parameter asymmetry. *IEEE Transactions on Industrial Electronics*, 63(5):2813–2824, 2015.

[92] Xin Luo, Qipeng Tang, Anwen Shen, and Qiao Zhang. Pmsm sensorless control by injecting hf pulsating carrier signal into estimated fixed-frequency rotating reference frame. *IEEE Transactions on Industrial Electronics*, 63(4):2294–2303, 2015.

[93] JM Liu and ZQ Zhu. Novel sensorless control strategy with injection of high-frequency pulsating carrier signal into stationary reference frame. *IEEE Transactions on Industry Applications*, 50(4):2574–2583, 2013.

[94] Sohji Murakami, Takayuki Shiota, Motomichi Ohto, Kozo Ide, and Masaki Hisatsune. Encoderless servo drive with adequately designed ipmsm for pulse-voltage-injection-based position detection. *IEEE Transactions on Industry Applications*, 48(6):1922–1930, 2012.

[95] Antonio Griffo, David Drury, Tadashi Sawata, and Phil H Mellor. Sensorless starting of a wound-field synchronous starter/generator for aerospace applications. *IEEE Transactions on Industrial Electronics*, 59(9):3579–3587, 2011.

[96] Joachim Holtz. Acquisition of position error and magnet polarity for sensorless control of pm synchronous machines. *IEEE Transactions on Industry Applications*, 44(4): 1172–1180, 2008.

[97] Nicola Bianchi, Silverio Bolognani, Ji-Hoon Jang, and Seung-Ki Sul. Comparison of pm motor structures and sensorless control techniques for zero-speed rotor position detection. *IEEE transactions on power Electronics*, 22(6):2466–2475, 2007.

[98] Ji-Hoon Jang, Jung-Ik Ha, Motomichi Ohto, Kozo Ide, and Seung-Ki Sul. Analysis of permanent-magnet machine for sensorless control based on high-frequency signal injection. *IEEE Transactions on Industry Applications*, 40(6):1595–1604, 2004.

[99] Jung-Ik Ha, Kozo Ide, Toshihiro Sawa, and Seung-Ki Sul. Sensorless rotor position estimation of an interior permanent-magnet motor from initial states. *IEEE Transactions on Industry Applications*, 39(3):761–767, 2003.

[100] Ji-Hoon Jang, Seung-Ki Sul, Jung-Ik Ha, Kozo Ide, and Mitsujiro Sawamura. Sensorless drive of surface-mounted permanent-magnet motor by high-frequency signal injection based on magnetic saliency. *IEEE Transactions on Industry Applications*, 39 (4):1031–1039, 2003.

[101] Daichi Hirakawa, Kichiro Yamamoto, and Atsushi Shinohara. Estimated position error compensation method considering impact of speed and load in permanent magnet synchronous motor position sensorless control based on high-frequency voltage injection. *IEEJ Journal of Industry Applications*, 10(6):624–631, 2021.

[102] Qing Lu, Yeqin Wang, Lihong Mo, and Tao Zhang. Pulsating high frequency voltage injection strategy for sensorless permanent magnet synchronous motor drives. *IEEE Transactions on Applied Superconductivity*, 31(8):1–4, 2021.

[103] Shuang Wang, Zhiwei Li, Deliang Wu, and Jianfei Zhao. Sensorless control of spmsm based on high-frequency positive-and negative-sequence current dual-demodulation. *IEEE Transactions on Industrial Electronics*, 70(5):4631–4639, 2022.

[104] Gaolin Wang, Honglei Zhou, Nannan Zhao, Chengrui Li, and Dianguo Xu. Sensorless control of ipmsm drives using a pseudo-random phase-switching fixed-frequency signal injection scheme. *IEEE Transactions on Industrial Electronics*, 65(10):7660–7671, 2018.

[105] Gaolin Wang, Dianxun Xiao, Guoqiang Zhang, Chengrui Li, Xueguang Zhang, and Dianguo Xu. Sensorless control scheme of ipmsms using hf orthogonal square-wave voltage injection into a stationary reference frame. *IEEE Transactions on Power Electronics*, 34(3):2573–2584, 2018.

[106] Chengrui Li, Gaolin Wang, Guoqiang Zhang, Dianguo Xu, and Dianxun Xiao. Saliency-based sensorless control for synrm drives with suppression of position estimation error. *IEEE Transactions on Industrial Electronics*, 66(8):5839–5849, 2018.

[107] Shih-Chin Yang, Sheng-Ming Yang, and Jing-Hui Hu. Design consideration on the square-wave voltage injection for sensorless drive of interior permanent-magnet machines. *IEEE Transactions on Industrial Electronics*, 64(1):159–168, 2016.

[108] Gaolin Wang, Lei Yang, Guoqiang Zhang, Xueguang Zhang, and Dianguo Xu. Comparative investigation of pseudorandom high-frequency signal injection schemes for sensorless ipmsm drives. *IEEE Transactions on Power Electronics*, 32(3):2123–2132, 2016.

[109] Gaolin Wang, Dianxun Xiao, Nannan Zhao, Xueguang Zhang, Wei Wang, and Dianguo Xu. Low-frequency pulse voltage injection scheme-based sensorless control of ipmsm drives for audible noise reduction. *IEEE Transactions on Industrial Electronics*, 64 (11):8415–8426, 2017.

[110] Ronggang Ni, Dianguo Xu, Frede Blaabjerg, Kaiyuan Lu, Gaolin Wang, and Guoqiang Zhang. Square-wave voltage injection algorithm for pmsm position sensorless control with high robustness to voltage errors. *IEEE Transactions on Power Electronics*, 32 (7):5425–5437, 2016.

[111] Gaolin Wang, Lei Yang, Bihe Yuan, Bowen Wang, Guoqiang Zhang, and Dianguo Xu. Pseudo-random high-frequency square-wave voltage injection based sensorless control of ipmsm drives for audible noise reduction. *IEEE Transactions on Industrial Electronics*, 63(12):7423–7433, 2016.

[112] Dongouk Kim, Yong-Cheol Kwon, Seung-Ki Sul, Jang-Hwan Kim, and Rae-Sung Yu. Suppression of injection voltage disturbance for high-frequency square-wave injection sensorless drive with regulation of induced high-frequency current ripple. *IEEE Transactions on Industry Applications*, 52(1):302–312, 2015.

[113] Young-Doo Yoon and Seung-Ki Sul. Sensorless control for induction machines based on square-wave voltage injection. *IEEE Transactions on Power Electronics*, 29(7): 3637–3645, 2013.

[114] Nae-Chun Park and Sang-Hoon Kim. Simple sensorless algorithm for interior permanent magnet synchronous motors based on high-frequency voltage injection method. *IET Electric Power Applications*, 8(2):68–75, 2014.

[115] JM Liu and ZQ Zhu. Sensorless control strategy by square-waveform high-frequency pulsating signal injection into stationary reference frame. *IEEE Journal of Emerging and Selected Topics in Power Electronics*, 2(2):171–180, 2013.

[116] Chen-Yen Yu, Jun Tamura, David Díaz Reigosa, and Robert D Lorenz. Position self-sensing evaluation of a fi-ipmsm based on high-frequency signal injection methods. *IEEE Transactions on Industry Applications*, 49(2):880–888, 2013.

[117] Sungmin Kim, Jung-Ik Ha, and Seung-Ki Sul. Pwm switching frequency signal injection sensorless method in ipmsm. *IEEE Transactions on Industry Applications*, 48(5): 1576–1587, 2012.

[118] Young-Doo Yoon, Seung-Ki Sul, Shinya Morimoto, and Kozo Ide. High-bandwidth sensorless algorithm for ac machines based on square-wave-type voltage injection. *IEEE transactions on Industry Applications*, 47(3):1361–1370, 2011.

[119] Kozo Ide, Mamoru Takaki, Shinya Morimoto, Yosuke Kawazoe, Akihiko Maemura, and Motomichi Ohto. Saliency-based sensorless drive of an adequately designed ipm motor for robot vehicle application. *IEEJ Transactions on Industry Applications*, 128 (4):379–387, 2008.

[120] Sichun Wang, Guoqiang Zhang, Song Liang, Gaolin Wang, Yihua Hu, and Dianguo Xu. Adaptive pll for high-frequency signal injection based sensorless pmsm drives. In *2021 24th International Conference on Electrical Machines and Systems (ICEMS)*, pages 850–855. IEEE, 2021.

[121] Piyush Kumar, Omar Bottesi, Sandro Calligaro, Luigi Alberti, and Roberto Petrella. Self-adaptive high-frequency injection based sensorless control for interior permanent magnet synchronous motor drives. *Energies*, 12(19):3645, 2019.

[122] Zhe Chen, Xuxuan Zhang, Shouluo Chen, Hang Zhang, Guangzhao Luo, et al. Position estimation accuracy improvement for spmsm sensorless drives by adaptive complex-coefficient filter and dpll. *IEEE Transactions on Industry Applications*, 59(1):857–865, 2022.

[123] Chan-Hee Choi and Jul-Ki Seok. Compensation of zero-current clamping effects for sensorless drives based on high-frequency signal injection. In *Conference Record of the 2006 IEEE Industry Applications Conference Forty-First IAS Annual Meeting*, volume 5, pages 2466–2471. IEEE, 2006.

[124] Dejan Raca, Pablo Garcia, David Reigosa, Fernando Briz, and Robert Lorenz. A comparative analysis of pulsating vs. rotating vector carrier signal injection-based sensorless control. In *2008 Twenty-Third Annual IEEE Applied Power Electronics Conference and Exposition*, pages 879–885. IEEE, 2008.

[125] LM Gong and ZQ Zhu. A novel method for compensating inverter nonlinearity effects in carrier signal injection-based sensorless control from positive-sequence carrier current distortion. *IEEE Transactions on Industry Applications*, 47(3):1283–1292, 2011.

[126] Karsten Wiedmann, Florian Wallrapp, and Axel Mertens. Analysis of inverter nonlinearity effects on sensorless control for permanent magnet machine drives based on high-frequency signal injection. In *2009 13th European Conference on Power Electronics and Applications*, pages 1–10. IEEE, 2009.

[127] Alessandro Benevieri, Andrea Formentini, Mario Marchesoni, Massimiliano Passalacqua, and Luis Vaccaro. Sensorless control with switching frequency square wave voltage injection for spmsm with low rotor magnetic anisotropy. *IEEE Transactions on Power Electronics*, 2023.

[128] Tetsuji Daido, Ryo Hisamatsu, Taisei Araki, and Shin-ichi Hamasaki. Novel compensation method for current distortion in ipmsm with pwm carrier-synchronized voltage injection. *IEEE Transactions on Industry Applications*, 59(2):1800–1811, 2022.

[129] Zheng Wang, Kailiang Yu, Yuqing Li, and Minrui Gu. Position sensorless control of dual three-phase ipmsm drives with high-frequency square-wave voltage injection. *IEEE Transactions on Industrial Electronics*, 70(10):9925–9934, 2022.

[130] Shuo Chen, Wen Ding, Xiang Wu, Lujie Huo, Ruiming Hu, and Shuai Shi. Sensorless control of ipmsm drives using high-frequency pulse voltage injection with random pulse sequence for audible noise reduction. *IEEE Transactions on Power Electronics*, 2023.

[131] Shuo Chen, Wen Ding, Xiang Wu, Ruiming Hu, and Shuai Shi. Novel random high-frequency square-wave and pulse voltage injection scheme-based sensorless control of ipmsm drives. *IEEE Journal of Emerging and Selected Topics in Power Electronics*, 11(2):1705–1721, 2022.

[132] Myeong-Won Kim, Junhyuk Lee, Mriganka Biswas, and Jung-Wook Park. New acoustic noise reduction method for signal-injection-based ipmsm sensorless drive. *IEEE Transactions on Power Electronics*, 38(3):3180–3190, 2022.

[133] Mengesha Mamo, Kozo Ide, Mitsujiro Sawamura, and Jun Oyama. Novel rotor position extraction based on carrier frequency component method (cfcm) using two reference frames for ipm drives. *IEEE Transactions on industrial electronics*, 52(2):508–514, 2005.

[134] Manfred Schroedl. Sensorless control of ac machines at low speed and standstill based on the" inform" method. In *IAS'96. Conference Record of the 1996 IEEE Industry Applications Conference Thirty-First IAS Annual Meeting*, volume 1, pages 270–277. IEEE, 1996.

[135] Florian Demmelmayr, Markus Troyer, and Manfred Schroedl. Advantages of pm-machines compared to induction machines in terms of efficiency and sensorless control in traction applications. In *IECON 2011-37th Annual Conference of the IEEE Industrial Electronics Society*, pages 2762–2768. IEEE, 2011.

[136] Matthias Hofer, Mario Nikowitz, and Manfred Schroedl. Sensorless control of a reluctance synchronous machine in the whole speed range without voltage pulse injections. In *2017 IEEE 3rd International Future Energy Electronics Conference and ECCE Asia (IFEEC 2017-ECCE Asia)*, pages 1194–1198. IEEE, 2017.

[137] Ewald Robeischl and Manfred Schrödl. Optimized inform-measurement sequence for sensorless pm synchronous motor drives with respect to minimum current distortion. In *Conference Record of the 2002 IEEE Industry Applications Conference. 37th IAS Annual Meeting (Cat. No. 02CH37344)*, volume 1, pages 92–98. IEEE, 2002.

[138] U-H Rieder, Manfred Schrödl, and Arno Ebner. Sensorless control of an external rotor pmsm in the whole speed range including standstill using dc-link measurements only. In *2004 IEEE 35th Annual Power Electronics Specialists Conference (IEEE Cat. No. 04CH37551)*, volume 2, pages 1280–1285. IEEE, 2004.

[139] Cyril Spiteri Staines, Cedric Caruana, Greg M Asher, and Mark Sumner. Sensorless control of induction machines at zero and low frequency using zero sequence currents. *IEEE Transactions on Industrial Electronics*, 53(1):195–206, 2006.

[140] Cyril Spiteri Staines, Greg M Asher, and Mark Sumner. Rotor position estimation for induction machines at zero and low frequency utilising zero sequence currents. In

Conference Record of the 2004 IEEE Industry Applications Conference, 2004. 39th IAS Annual Meeting., volume 2, pages 1313–1320. IEEE, 2004.

[141] Gao Qiang, GM Asher, M Sumner, and P Makys. Position estimation of ac machines at all frequencies using only space vector pwm based excitation. 2006.

[142] Q Gao, GM Asher, M Sumner, and P Makys. Sensorless control of induction machines, including zero frequency using only fundamental pwm excitation. In *IECON 2006-32nd Annual Conference on IEEE Industrial Electronics*, pages 793–798. IEEE, 2006.

[143] Chen Zhao, Marko Tanaskovic, Federico Percacci, Sébastien Mariéthoz, and Patrik Gnos. Sensorless position estimation for slotless surface mounted permanent magnet synchronous motors in full speed range. *IEEE Transactions on Power Electronics*, 34 (12):11566–11579, 2019.

[144] David Hind, Chen Li, Mark Sumner, and Chris Gerada. Realising robust low speed sensorless pmsm control using current derivatives obtained from standard current sensors. In *2017 IEEE International Electric Machines and Drives Conference (IEMDC)*, pages 1–6. IEEE, 2017.

[145] DQ Guan, MX Bui, D Xiao, and MF Rahman. Performance comparison of two fpe sensorless control methods on a direct torque controlled interior permanent magnet synchronous motor drive. In *2016 19th International Conference on Electrical Machines and Systems (ICEMS)*, pages 1–6. IEEE, 2016.

[146] Yoshitaka Iwaji, Ryoichi Takahata, Takahiro Suzuki, and Shigehisa Aoyagi. Position sensorless control method at zero-speed region for permanent magnet synchronous motors using the neutral point voltage of stator windings. *IEEE Transactions on Industry Applications*, 52(5):4020–4028, 2016.

[147] Gaolin Wang, Junyao Kuang, Nannan Zhao, Guoqiang Zhang, and Dianguo Xu. Rotor position estimation of pmsm in low-speed region and standstill using zero-voltage vector injection. *IEEE Transactions on Power Electronics*, 33(9):7948–7958, 2017.

[148] Ge Xie, Kaiyuan Lu, Sanjeet Kumar Dwivedi, Rosholm Jesper Riber, and Weimin Wu. Permanent magnet flux online estimation based on zero-voltage vector injection method. *IEEE Transactions on Power Electronics*, 30(12):6506–6509, 2015.

[149] DQ Guan, MX Bui, D Xiao, and MF Rahman. Evaluation of an fpga current derivative measurement system for the fundamental pwm excitation sensorless method for ipmsm. In *2016 IEEE 2nd Annual Southern Power Electronics Conference (SPEC)*, pages 1–6. IEEE, 2016.

[150] Yuji Hosogaya and Hisao Kubota. Flux position estimation method of ipmsm by controlling current derivative at zero voltage vector. In *2010 International Conference on Electrical Machines and Systems*, pages 894–899. IEEE, 2010.

[151] Ge Xie, Kaiyuan Lu, Dwivedi Sanjeet Kumar, and Rosholm Jesper Riber. High bandwidth zero voltage injection method for sensorless control of pmsm. In *2014 17th International Conference on Electrical Machines and Systems (ICEMS)*, pages 3546–3552. IEEE, 2014.

[152] Shin Nakashima, Yuya Inagaki, and Ichiro Miki. Sensorless initial rotor position estimation of surface permanent-magnet synchronous motor. *IEEE Transactions on Industry Applications*, 36(6):1598–1603, 2000.

[153] Hyunbae Kim, Kum-Kang Huh, Robert D Lorenz, and Thomas M Jahns. A novel method for initial rotor position estimation for ipm synchronous machine drives. *IEEE Transactions on Industry Applications*, 40(5):1369–1378, 2004.

[154] Xuan Wu, Yaojing Feng, Xiao Liu, Shouddao Huang, Xiaofang Yuan, Jian Gao, and Jian Zheng. Initial rotor position detection for sensorless interior pmsm with square-wave voltage injection. *IEEE transactions on magnetics*, 53(11):1–4, 2017.

[155] Sohji Murakami, Takayuki Shiota, Motomichi Ohto, Kozo Ide, and Masaki Hisatsune. Encoderless servo drive with adequately designed ipmsm for pulse-voltage-injection-based position detection. *IEEE Transactions on Industry Applications*, 48(6):1922–1930, 2012.

[156] Xinghe Fu, Yutian Xu, Hang He, and Xiangda Fu. Initial rotor position estimation by detecting vibration of permanent magnet synchronous machine. *IEEE Transactions on Industrial Electronics*, 68(8):6595–6606, 2020.

[157] Hyunbae Kim and Robert D Lorenz. Carrier signal injection based sensorless control methods for ipm synchronous machine drives. In *Conference Record of the 2004 IEEE Industry Applications Conference, 2004. 39th IAS Annual Meeting.*, volume 2, pages 977–984. IEEE, 2004.

[158] W Zine. Hf signal injection and machine learning for the sensorless control of ipmsm-based ev drives. *Ph. D. thesis*, 2017.

[159] Damiano Mingardi, Mattia Morandin, Silverio Bolognani, and Nicola Bianchi. On the proprieties of the differential cross-saturation inductance in synchronous machines. *IEEE Transactions on Industry Applications*, 53(2):991–1000, 2016.

[160] ZQ Zhu, Y Li, D Howe, and CM Bingham. Compensation for rotor position estimation error due to cross-coupling magnetic saturation in signal injection based sensorless control of pm brushless ac motors. In *2007 IEEE International Electric Machines & Drives Conference*, volume 1, pages 208–213. IEEE, 2007.

[161] Michael W Degner and Robert D Lorenz. Using multiple saliencies for the estimation of flux, position, and velocity in ac machines. *IEEE Transactions on Industry Applications*, 34(5):1097–1104, 1998.

[162] Matteo Berto, Luigi Alberti, and Silverio Bolognani. Measurement of the self-sensing capability of synchronous machines for high frequency signal injection sensorless drives. *IEEE Transactions on Industry Applications*, 2023.

[163] Inhwi Hwang, Yong-Cheol Kwon, and Seung-Ki Sul. Enhanced dynamic operation of heavily saturated ipmsm in signal-injection sensorless control with ancillary reference frame. *IEEE Transactions on Power Electronics*, 38(5):5726–5741, 2022.

[164] Guangdong Bi, Guoqiang Zhang, Qiwei Wang, Dawei Ding, Binxing Li, Gaolin Wang, and Dianguo Xu. High-frequency injection angle self-adjustment based online position error suppression method for sensorless pmsm drives. *IEEE Transactions on Power Electronics*, 38(2):1412–1417, 2022.

[165] Anian Brosch, Fabio Tinazzi, Oliver Wallscheid, Mauro Zigliotto, and Joachim Böcker. Finite set sensorless control with minimum a priori knowledge and tuning effort for interior permanent magnet synchronous motors. 2023.

[166] Jiabao Kou, Gaoxiang Liu, Fengrui Yang, and Fengyi Guo. Lci control strategy of sensorless eesm based on minimum remainder commutation angle. *IEEE Transactions on Power Electronics*, 2023.

[167] Zhuoyi Chen, Wentai Qu, and Jianqi Qiu. Ripple excitation-based adaptive sensorless control of ipmsm in full speed range. *IEEE Access*, 11:33160–33177, 2023.

[168] Sari Maekawa, Mariko Sugimoto, Keiichi Ishida, Masaya Nogi, and Masaki Kanamori. Stability analysis of sensorless speed control for pmsm considered current control system. *IEEJ Journal of Industry Applications*, 8(4):736–744, 2019.

[169] Virginia Manzolini, Mattia Morandin, and Silverio Bolognani. The crowded axis of the frequency: Optimal pole/zero allocation for a full speed sensorless synchronous motor drives. In *2016 IEEE Energy Conversion Congress and Exposition (ECCE)*, pages 1–8. IEEE, 2016.

[170] Xinmin Li, Chuang Dai, Wei Chen, Qiang Geng, and Huimin Wang. Position detection and speed recording method for power-off ipmsm in full-speed range based on ultrahigh frequency signal injection. *IEEE Transactions on Power Electronics*, 2023.

[171] João Pedro A Bastos and Nelson Sadowski. *Electromagnetic modeling by finite element methods*. CRC press, 2003.

[172] ZQ Zhu, David Howe, Ekkehard Bolte, and Bernd Ackermann. Instantaneous magnetic field distribution in brushless permanent magnet dc motors. i. open-circuit field. *IEEE transactions on magnetics*, 29(1):124–135, 1993.

[173] ZQ Zhu and David Howe. Instantaneous magnetic field distribution in brushless permanent magnet dc motors. ii. armature-reaction field. *IEEE transactions on magnetics*, 29(1):136–142, 1993.

[174] ZQ Zhu and David Howe. Instantaneous magnetic field distribution in brushless permanent magnet dc motors. iii. effect of stator slotting. *IEEE transactions on magnetics*, 29(1):143–151, 1993.

[175] ZQ Zhu and David Howe. Instantaneous magnetic field distribution in permanent magnet brushless dc motors. iv. magnetic field on load. *IEEE Transactions on Magnetics*, 29(1):152–158, 1993.

[176] ZQ Zhu, Zh P Xia, LJ Wu, and Geraint W Jewell. Analytical modeling and finite-element computation of radial vibration force in fractional-slot permanent-magnet brushless machines. *IEEE Transactions on Industry Applications*, 46(5):1908–1918, 2010.

[177] ZQ Zhu, David Howe, and CC Chan. Improved analytical model for predicting the magnetic field distribution in brushless permanent-magnet machines. *IEEE Transactions on Magnetics*, 38(1):229–238, 2002.

[178] Damir Zarko, Drago Ban, and Thomas A Lipo. Analytical calculation of magnetic field distribution in the slotted air gap of a surface permanent-magnet motor using complex relative air-gap permeance. *IEEE Transactions on Magnetics*, 42(7):1828–1837, 2006.

[179] Ungtae Kim and Dennis K Lieu. Magnetic field calculation in permanent magnet motors with rotor eccentricity: Without slotting effect. *IEEE Transactions on Magnetics*, 34(4):2243–2252, 1998.

[180] Ungtae Kim and Dennis K Lieu. Magnetic field calculation in permanent magnet motors with rotor eccentricity: With slotting effect considered. *IEEE Transactions on Magnetics*, 34(4):2253–2266, 1998.

[181] Jacek F Gieras, Chong Wang, and Joseph Cho Lai. *Noise of polyphase electric motors*. CRC press, 2018.

[182] Z.Q. Zhu, Z.P. Xia, L.J. Wu, and G.W. Jewell. Influence of slot and pole number combination on radial force and vibration modes in fractional slot pm brushless machines having single- and double-layer windings. pages 3443–3450, 2009.

[183] Fu Lin, Shuguang Zuo, Wenzhe Deng, and Shuanglong Wu. Modelling and analysis of electromagnetic force, vibration, and noise in permanent magnet synchronous motor considering current harmonics. *IEEE Transactions on Industrial Electronics*, 63(12): 7455–7466, 2016.

[184] Ramu Krishnan. *Switched reluctance motor drives: modeling, simulation, analysis, design, and applications*. CRC press, 2017.

[185] Wenzhe Deng and Shuguang Zuo. Analysis of the sideband electromagnetic noise in permanent magnet synchronous motors generated by rotor position error. *IEEE Transactions on Industrial Electronics*, 69(5):4460–4471, 2021.

[186] Dimitri Torregrossa, Babak Fahimi, François Peyraut, and Abdellatif Miraoui. Fast computation of electromagnetic vibrations in electrical machines via field reconstruction method and knowledge of mechanical impulse response. *IEEE Transactions on Industrial Electronics*, 59(2):839–847, 2011.

[187] Dimitri Torregrossa, Francois Peyraut, Babak Fahimi, Jérémie M'Boua, and Abdellatif Miraoui. Multiphysics finite-element modeling for vibration and acoustic analysis of permanent magnet synchronous machine. *IEEE Transactions on Energy Conversion*, 26(2):490–500, 2010.

[188] Rajesh M Pindoriya, Rishi Kant Thakur, Bharat Singh Rajpurohit, and Rajeev Kumar. Numerical and experimental analysis of torsional vibration and acoustic noise of pmsm coupled with dc generator. *IEEE Transactions on Industrial Electronics*, 69(4): 3345–3356, 2021.

[189] Rajesh M Pindoriya, Bharat Singh Rajpurohit, and Rajeev Kumar. A novel application of harmonics spread spectrum technique for acoustic noise and vibration reduction of pmsm drive. *IEEE Access*, 8:103273–103284, 2020.

[190] Rajesh M Pindoriya, Gaurav Gautam, and Bharat Singh Rajpurohit. A novel application of pseudorandom-based technique for acoustic noise and vibration reduction of pmsm drive. *IEEE Transactions on Industry Applications*, 56(5):5511–5522, 2020.

[191] Michael Møller Bech. *Analysis of random pulse-width modulation techniques for power electronic converters*. Aalborg Universitetsforlag, 2000.

[192] Jui-Yuan Chai, Yeh-Hsiang Ho, Yu-Choung Chang, and Chang-Ming Liaw. On acoustic-noise-reduction control using random switching technique for switch-mode rectifiers in pmsm drive. *IEEE Transactions on Industrial Electronics*, 55(3):1295–1309, 2008.

[193] Le Kang, Jiakuan Xia, Han Su, Zexing Li, and Siqi Liu. Online control strategy for radial vibration suppression of pmsm by multiharmonic current injection method. *IEEE Transactions on Industrial Electronics*, 69(9):8692–8704, 2021.

[194] Fu Lin, Shuguang Zuo, Wenzhe Deng, and Shuanglong Wu. Noise prediction and sound quality analysis of variable-speed permanent magnet synchronous motor. *IEEE Transactions on Energy Conversion*, 32(2):698–706, 2017.

[195] Vasilios C Ilioudis. *Sensorless control of permanent magnet synchronous machine with magnetic saliency tracking based on voltage signal injection*, volume 8. MDPI, 2020.

[196] Yi Ji, Yong Yang, Jiale Zhou, Hao Ding, Xiaoqiang Guo, and Sanjeevikumar Padmanaban. Control strategies of mitigating dead-time effect on power converters: An overview. *Electronics*, 8(2):196, 2019.

[197] Gregory R Ainslie-Malik. *Mathematical analysis of PWM processes*. PhD thesis, University of Nottingham, 2013.

[198] Bernard Widrow and Michael A Lehr. 30 years of adaptive neural networks: perceptron, madaline, and backpropagation. *Proceedings of the IEEE*, 78(9):1415–1442, 1990.

[199] Rong-Jong Wai and Chun-Yu Lin. Active low-frequency ripple control for clean-energy power-conditioning mechanism. *IEEE Transactions on Industrial Electronics*, 57(11): 3780–3792, 2010.

[200] L Merabet, S Saad, A Omeiri, and D Ould Abdeslam. A comparative study of harmonic current identification for active power filter. In *2012 First International Conference on Renewable Energies and Vehicular Technology*, pages 366–371. IEEE, 2012.

[201] Djaffar Ould Abdeslam, Patrice Wira, Jean Mercklé, Damien Flieller, and Yves-Andr Chapuis. A unified artificial neural network architecture for active power filters. *IEEE transactions on industrial electronics*, 54(1):61–76, 2007.

[202] PK Dash, DP Swain, AC Liew, and Saifur Rahman. An adaptive linear combiner for on-line tracking of power system harmonics. *IEEE transactions on power systems*, 11 (4):1730–1735, 1996.

[203] PK Dash, DP Swain, A Routray, and AC Liew. An adaptive neural network approach for the estimation of power system frequency. *Electric power systems research*, 41(3): 203–210, 1997.

[204] MI Marei, EF El-Saadany, and MMA Salama. An intelligent control for the dg interface to mitigate voltage flicker. In *Eighteenth Annual IEEE Applied Power Electronics Conference and Exposition, 2003. APEC'03.*, volume 1, pages 179–183. IEEE, 2003.

[205] Damien Flieller, D Ould Abdeslam, Patrice Wira, and Jean Merckle. Distortions identification and compensation based on artificial neural networks using symmetrical components of the voltages and the currents. *Electric Power Systems Research*, 79(7): 1145–1154, 2009.

[206] Ngac Ky Nguyen, Damien Flieller, Patrice Wira, and Djaffar Ould Abdeslam. Neural networks for phase and symmetrical components estimation in power systems. In *2009 35th Annual Conference of IEEE Industrial Electronics*, pages 3252–3257. IEEE, 2009.

[207] Yang Han. On using adaline algorithm for harmonic estimation and phase-synchronization for the grid-connected converters in smart grid applications. In *Adaptive Filtering-Theories and Applications*. IntechOpen, 2013.

[208] Guoqiang Zhang, Gaolin Wang, Dianguo Xu, and Nannan Zhao. Adaline-network-based pll for position sensorless interior permanent magnet synchronous motor drives. *IEEE Transactions on Power Electronics*, 31(2):1450–1460, 2015.

[209] Ngac Ky Nguyen, Eric Semail, Frederic De Belie, and Xavier Kestelyn. Adaline neural networks-based sensorless control of five-phase pmsm drives. In *IECON 2016-42nd Annual Conference of the IEEE Industrial Electronics Society*, pages 5741–5746. IEEE, 2016.

[210] Lu Wang, Zi-Qiang Zhu, Hong Bin, and LM Gong. Current harmonics suppression strategy for pmsm with nonsinusoidal back-emf based on adaptive linear neuron method. *IEEE Transactions on Industrial Electronics*, 67(11):9164–9173, 2019.

[211] Masoud Karimi Ghartemani, Sayed Ali Khajehoddin, Praveen K Jain, and Alireza Bakhshai. Problems of startup and phase jumps in pll systems. *IEEE Transactions on Power Electronics*, 27(4):1830–1838, 2011.

[212] Yukihiko Sato, Tomotsugu Ishizuka, Kazuyoshi Nezu, and Teruo Kataoka. A new control strategy for voltage-type pwm rectifiers to realize zero steady-state control error in input current. *IEEE Transactions on Industry Applications*, 34(3):480–486, 1998.

[213] Shoji Fukuda and Takehito Yoda. A novel current-tracking method for active filters based on a sinusoidal internal model [for pwm invertors]. *IEEE transactions on industry applications*, 37(3):888–895, 2001.

[214] Mohammad Parvez, Mohamad Fathi Mohamad Elias, Nasrudin Abd Rahim, Frede Blaabjerg, Derek Abbott, and Said F Al-Sarawi. Comparative study of discrete pi and pr controls for single-phase ups inverter. *IEEE Access*, 8:45584–45595, 2020.

[215] Yuefei Zuo, Jingwei Zhu, Wenhao Jiang, Shuangchun Xie, Xiaoyong Zhu, Wen-Hua Chen, and Christopher HT Lee. Active disturbance rejection controller for smooth speed control of electric drives using adaptive generalized integrator extended state observer. *IEEE Transactions on Power Electronics*, 38(4):4323–4334, 2022.

[216] Guangdong Bi, Dawei Ding, Guoqiang Zhang, Qiwei Wang, Runze Jing, Gaolin Wang, and Dianguo Xu. Adaptive quasi-proportional-resonant observer-based rotor position estimation for sensorless pmsm drives. *IEEE Transactions on Power Electronics*, 37 (12):15221–15233, 2022.

[217] Ting Wu, Xuan Wu, Shoudao Huang, Kaiyuan Lu, and Hesong Cui. An optimized pll with time delay and harmonic suppression for improved position estimation accuracy of pmsm based on levenberg–marquardt. *IEEE Transactions on Industrial Electronics*, 70(10):9847–9858, 2022.

[218] Shuo Chen, Wen Ding, Xiang Wu, Ruiming Hu, and Shuai Shi. Finite position set-phase-locked loop with low computational burden for sensorless control of pmsm drives. *IEEE Transactions on Industrial Electronics*, 70(9):9672–9676, 2022.

[219] Shuo Chen, Wen Ding, Ruiming Hu, Xiang Wu, and Shuai Shi. Sensorless control of pmsm drives using reduced order quasi resonant-based eso and newton–raphson method-based pll. *IEEE Transactions on Power Electronics*, 38(1):229–244, 2022.

[220] Youngwoo Lee, Jeonghwan Gil, and Wonhee Kim. Velocity control for sideband harmonics compensation in permanent magnet synchronous motors with low switching frequency inverter. *IEEE Transactions on Industrial Electronics*, 68(4):3434–3444, 2020.

[221] Gang Liu, Baodong Chen, Kun Wang, and Xinda Song. Selective current harmonic suppression for high-speed pmsm based on high-precision harmonic detection method. *IEEE Transactions on Industrial Informatics*, 15(6):3457–3468, 2018.

[222] Anup Kumar, Mohan V Aware, Bhimrao S Umre, and Manoj A Waghmare. An adaptive multi-resonant current controller for a single-phase grid-tied converter with grid disturbance rejection capability. *IEEE Access*, 10:28053–28065, 2022.

[223] Yongheng Yang, Keliang Zhou, and Frede Blaabjerg. Enhancing the frequency adaptability of periodic current controllers with a fixed sampling rate for grid-connected power converters. *IEEE Transactions on Power Electronics*, 31(10):7273–7285, 2015.

[224] Sakda Somkun. High performance current control of single-phase grid-connected converter with harmonic mitigation, power extraction and frequency adaptation capabilities. *IET Power Electronics*, 14(2):352–372, 2021.

[225] Alessandro Lidozzi, Marco Di Benedetto, Stefano Bifaretti, Luca Solero, and Fabio Crescimbini. Resonant controllers with three degrees of freedom for ac power electronic converters. *IEEE Transactions on Industry Applications*, 51(6):4595–4604, 2015.

[226] Daniel Nahum Zmood and Donald Grahame Holmes. Stationary frame current regulation of pwm inverters with zero steady-state error. *IEEE Transactions on power electronics*, 18(3):814–822, 2003.

[227] C Captain. *Torque control in field weakening mode. Aalborg University M. Sc.* PhD thesis, thesis, PED4-1038, 2009.

[228] Bojan Stumberger, Gorazd Stumberger, Drago Dolinar, Anton Hamler, and Mladen Trlep. Evaluation of saturation and cross-magnetization effects in interior permanent-magnet synchronous motor. *IEEE Transactions on Industry Applications*, 39(5):1264–1271, 2003.

[229] Tatsuki Inoue, Yukinori Inoue, Shigeo Morimoto, and Masayuki Sanada. Maximum torque per ampere control of a direct torque-controlled pmsm in a stator flux linkage synchronous frame. *IEEE Transactions on Industry Applications*, 52(3):2360–2367, 2016.

[230] Nicola Bianchi and Sliverio Bolognani. Magnetic models of saturated interior permanent magnet motors based on finite element analysis. In *Conference Record of 1998 IEEE Industry Applications Conference. Thirty-Third IAS Annual Meeting (Cat. No. 98CH36242)*, volume 1, pages 27–34. IEEE, 1998.

[231] Koen J Meessen, Peter Thelin, Juliette Soulard, and EA Lomonova. Inductance calculations of permanent-magnet synchronous machines including flux change and self-and cross-saturations. *IEEE Transactions on Magnetics*, 44(10):2324–2331, 2008.

[232] Thorsten Frenzke. Impacts of cross-saturation on sensorless control of surface permanent magnet synchronous motors. In *2005 European Conference on Power Electronics and Applications*, pages 10–pp. IEEE, 2005.

[233] Roberto Morales-Caporal and Mario Pacas. Impact of the magnetic cross-saturation in a sensorless direct torque controlled synchronous reluctance machine based on test voltage signal injections. In *2008 34th Annual Conference of IEEE Industrial Electronics*, pages 1234–1239. IEEE, 2008.

[234] Muhammed Fazlur Rahman, L Zhong, and Khiang Wee Lim. A direct torque-controlled interior permanent magnet synchronous motor drive incorporating field weakening. *IEEE Transactions on Industry Applications*, 34(6):1246–1253, 1998.

[235] Isao Takahashi and Toshihiko Noguchi. A new quick-response and high-efficiency control strategy of an induction motor. *IEEE Transactions on Industry applications*, (5): 820–827, 1986.

[236] Gianmario Pellegrino, Radu Iustin Bojoi, and Paolo Guglielmi. Unified direct-flux vector control for ac motor drives. *IEEE Transactions on Industry Applications*, 47 (5):2093–2102, 2011.

[237] Tatsuki Inoue, Yukinori Inoue, Shigeo Morimoto, and Masayuki Sanada. Maximum torque per ampere control of a direct torque-controlled pmsm in a stator flux linkage synchronous frame. *IEEE Transactions on Industry Applications*, 52(3):2360–2367, 2016.

[238] Guodong Feng, Chunyan Lai, Xiaojun Tan, and Narayan C Kar. Maximum-torque-per-square-ampere control for interior pmsms considering cross-saturation inductances. *IEEE Transactions on Transportation Electrification*, 7(3):1482–1492, 2021.

[239] SD Sudhoff, KA Corzine, and HJ Hegner. A flux-weakening strategy for current-regulated surface-mounted permanent-magnet machine drives. *IEEE Transactions on Energy Conversion*, 10(3):431–437, 1995.

[240] Jong-Hwan Song, Jang-Mok Kim, and Seung-Ki Sul. A new robust spmsm control to parameter variations in flux weakening region. In *Proceedings of the 1996 IEEE*

IECON. 22nd international conference on industrial electronics, control, and instrumentation, volume 2, pages 1193–1198. IEEE, 1996.

[241] Bimal K Bose. A high-performance inverter-fed drive system of an interior permanent magnet synchronous machine. *IEEE Transactions on Industry Applications*, 24(6): 987–997, 1988.

[242] Jang-Mok Kim and Seung-Ki Sul. Speed control of interior permanent magnet synchronous motor drive for the flux weakening operation. *IEEE Transactions on Industry Applications*, 33(1):43–48, 1997.

[243] Muhammed Fazlur Rahman, L Zhong, and Khiang Wee Lim. A direct torque-controlled interior permanent magnet synchronous motor drive incorporating field weakening. *IEEE Transactions on Industry Applications*, 34(6):1246–1253, 1998.

[244] Muhammed Fazlur Rahman, Li Zhong, Md E Haque, and MA Rahman. A direct torque-controlled interior permanent-magnet synchronous motor drive without a speed sensor. *IEEE Transactions on Energy Conversion*, 18(1):17–22, 2003.

[245] Ali Sarikhani and Osama A Mohammed. Demagnetization control for reliable flux weakening control in pm synchronous machine. *IEEE Transactions on Energy Conversion*, 27(4):1046–1055, 2012.

[246] Jun Li, Qinruo Wang, Jiajun Yu, and Jianbin Xiong. Field-weakening control algorithm for interior permanent magnet synchronous motor based on space-vector modulation technique. *Journal of Convergence Information Technology*, 8(3):1–9, 2013.

[247] Wei Xu, Moustafa Magdi Ismail, Yi Liu, and Md Rabiul Islam. Parameter optimization of adaptive flux-weakening strategy for permanent-magnet synchronous motor drives based on particle swarm algorithm. *IEEE Transactions on Power Electronics*, 34(12): 12128–12140, 2019.

[248] Kai Zhou, Min Ai, Dongyang Sun, Ningzhi Jin, and Xiaogang Wu. Field weakening operation control strategies of pmsm based on feedback linearization. *Energies*, 12(23): 4526, 2019.

[249] Zhihao Zheng, Dan Sun, Mingze Wang, and Heng Nian. A dual two-vector-based model predictive flux control with field-weakening operation for ow-pmsm drives. *IEEE Transactions on Power Electronics*, 36(2):2191–2200, 2020.

Appendix A

Dynamic Three-phase Model of PMSM

As mentioned earlier, the stator of SM has three-phase windings (which can be of distributed or concentrated type depending on the the number of stator slots and pole/slot ratio) which are excited by a three-phase symmetrical voltage. The stator voltage equation is defined in eq. (A.1).

$$\begin{bmatrix} V_a \\ V_b \\ V_c \end{bmatrix} = R_s \begin{bmatrix} i_a \\ i_b \\ i_c \end{bmatrix} + \frac{d}{dt} \begin{bmatrix} \psi_a \\ \psi_b \\ \psi_c \end{bmatrix} \tag{A.1}$$

$$\begin{bmatrix} \psi_a \\ \psi_b \\ \psi_c \end{bmatrix} = \begin{bmatrix} L_s & L_m & L_m \\ L_m & L_s & L_m \\ L_m & L_m & L_s \end{bmatrix} \begin{bmatrix} i_a \\ i_b \\ i_c \end{bmatrix} + \underbrace{\psi_m \cdot \begin{bmatrix} cos\left(\theta_e\right) \\ cos\left(\theta_e - 2\pi/3\right) \\ cos\left(\theta_e + 2\pi/3\right) \end{bmatrix}}_{\psi_{rotor}} \tag{A.2}$$

In the above equations:

- V denotes the phase voltage.
- i denotes the phase current.
- ψ represents the stator flux.
- R_s represents the phase resistance.
- $L_s = L_{sl} + L_{sm}$ is the self inductance obtained as the sum of the stator leakage inductance (L_{ls}) and the stator magnetizing inductance (L_{sm}).

- $L_m = L_{sm}.\cos(\pm 2\pi/3) = -0.5L_{sm}$ is the mutual inductance. For the case of non-salient structure, the values of inductances are, ideally, considered as constants.
- ψ_m is the permanent magnet flux and ψ_{rotor} is the rotor flux generated via either the permanent magnets or rotor field winding.
- $\theta_e = p.\theta_m$ is the electrical position of the rotor with respect to the reference frame fixed to the stator windings (for instance, direct-axis of phase A). The number of pole pairs is denoted by p and the mechanical rotor position is represented by θ_m.

Considering that sum of the stator currents adds up to zero ($i_a + i_b + i_c = 0$), and defining $L_{ss} = L_s - L_m$, the stator flux and voltage equations are respectively revised as [2]:

$$\begin{bmatrix} \psi_a \\ \psi_b \\ \psi_c \end{bmatrix} = \underbrace{(L_s - L_m)}_{L_{ss}} \begin{bmatrix} i_a \\ i_b \\ i_c \end{bmatrix} + \psi_m \begin{bmatrix} \cos(\theta_e) \\ \cos\left(\theta_e - 2\pi/3\right) \\ \cos\left(\theta_e + 2\pi/3\right) \end{bmatrix} \tag{A.3}$$

$$\begin{bmatrix} V_a \\ V_b \\ V_c \end{bmatrix} = R_s \begin{bmatrix} i_a \\ i_b \\ i_c \end{bmatrix} + \begin{bmatrix} L_{ss} & 0 & 0 \\ 0 & L_{ss} & 0 \\ 0 & 0 & L_{ss} \end{bmatrix} \cdot \frac{d}{dt} \begin{bmatrix} i_a \\ i_b \\ i_c \end{bmatrix} - \omega_e \cdot \psi_m \begin{bmatrix} \sin(\theta_e) \\ \sin\left(\theta_e - 2\pi/3\right) \\ \sin\left(\theta_e + 2\pi/3\right) \end{bmatrix} \tag{A.4}$$

Appendix B

Maximum Torque-per-Ampere Control

As discussed, in salient SM, the torque comprises two terms: an electromagnetic term, which is directly controlled by the q-axis current, and a reluctance term, which is controlled by both the d-axis and q-axis components of the current. As the result, by proper control of the values of the dq-frame current components, the amount of generated torque could be optimized in such a manner that the current drawn is minimised.

Given the maximum deliverable current magnitude, considering the converter limits, to be:

$$I_s = \sqrt{i_d^2 + i_q^2} \Rightarrow i_q = \sqrt{I_s^2 - i_d^2} \tag{B.1}$$

the torque equation, using eq. (B.1), is derived as [227]:

$$T_e = \frac{3}{2} p \left[\psi_m \sqrt{I_s^2 - i_d^2} + (L_d - L_q)\, i_d \sqrt{I_s^2 - i_d^2} \right] \tag{B.2}$$

In order to find the minimum value of i_d corresponding to a given value of torque, eq. (B.2) should be derived with respect to i_d and made equal to zero, which gives:

$$\frac{dT_e}{di_d} = \frac{3}{2} p \cdot \frac{-i_d \psi_m + (L_d + L_q)\,(I_s - 2i_d^2)}{\sqrt{I_s^2 - i_d^2}} = 0 \tag{B.3}$$

$$i_d = \frac{\sqrt{\psi_m^2 + 8(L_d + L_q)^2 I_s^2} - \psi_m}{4\,(L_d - L_q)} \tag{B.4}$$

Equation (B.4) is the minimum value of the d-axis current component corresponding to a given torque. The value of the corresponding q-axis current is therefore easily obtained by using eq. (B.1). As the result, the obtained electromagnetic torque equation is obtained as [2]:

$$T_e = \frac{3}{2}p\left[\frac{\psi_m i_q}{2} + (L_d - L_q)\, i_q \sqrt{i_q^2 + \frac{\psi_m^2}{4\,(L_q - L_d)}}\right] \tag{B.5}$$

In normal conditions, the MTPA algorithm realized in the dq-frame is known as a highly-efficient control method. However, cross-coupling and magnetic saturation are two of the undesirable phenomena that occur in high-power and high-torque working points, which result in the variation of the machine's parameters (mainly the dq-frame inductances). The parameter variation directly affects the control precision especially in sensorless applications, which are highly dependent upon the machine inductances [228, 229]. The ill-impact of cross-coupling and magnetic saturation upon the machine performance and parameters are deeply investigated in [228, 230, 231]. As the result of cross-coupling and magnetic saturation, the dq-frame inductances become functions of the armature current and the rotor position; the inductance models are derived for IPMSM, SPMSM, SynRM, and IM in [232, 233].

Direct torque control (DTC) is a simple algorithm used for both PMSM and IM, which directly uses the estimated magnetic flux and torque in its feedback loops (instead of speed and currents used in FOC algorithm). This control algorithm does not depend on the position sensor all the time (except for acquiring the initial rotor position) since the rotor position is abtained through the estimated dq-frame fluxes [234],[235].

Instead of using dq-frame for FOC implementation, the stator flux linkage frame (MT-frame) is used which is applicable to both SM and IM [236]. The mathematical model of the machine in the dq-frame becomes complicated when cross-coupling and magnetic saturation are taken into consideration. Therefore, the machine model in the MT-frame is alternatively used which offers significant simplification in the modeling process. DTC algorithm using the MT-frame is proposed in [237] which merely needs three parameters that can be measured from three different operating points.

An efficient maximum torque-per-square-ampere (MTPSA) control for IPMSM is proposed in [238]. This method utilizes a parameter called MTPSA angle to maximize the ratio of the generated torque to the square of the current. This method does not depend on the machine parameters; therefore, the impact of parameter variation on the performance is eliminated.

Appendix C

Field-Weakening Control

The machine and power converter limitations are vital to the appropriate design of current controllers. The thermal restrictions of both the machine and power converter impose a limit upon the current as follows. Exceeding the overall stator current limit (I_{s_Max}) exposes the machine to saturation, which easily alters the machine parameters.

$$i_d^2 + i_q^2 \leqslant I_{s\_Max}^2 \tag{C.1}$$

On the other hand, there is a voltage limit (V_{s_Max}) which must be strictly upheld, which origins from the maximum DC link voltage of the converter or the machine isolation aspects.

$$V_d^2 + V_q^2 \leqslant V_{s\_Max}^2 \tag{C.2}$$

At low speed range, the voltage provided by the inverter is large enough to suppress the impact of BEMF voltages; therefore, the current can be easily controlled and only the current limit given in eq. (C.1) must be taken into condideration. As the speed increases, especially for the speeds near or above the nominal speed, the BEMF value approaches that of the V_{s_Max}. Consequently, the machine does no longer have enough voltage to control the current and the machine losses its torque generation capability and the speed cannot be increased any further, as the result.

At the speed zone near or above the nominal speed and within the steady-state regime, the resistive voltage drop can be neglected which results in the following simplified voltage equations [2], [227].

$$V_d \approx -\omega_e L_q i_q \tag{C.3}$$

$$V_q \approx \omega_e \left(\psi_m + L_d i_d\right) \tag{C.4}$$

At this condition, it is possible to inject a negative d-axis current in order to reduce the direct-axis stator flux and quadrature-axis stator voltage; this method is well known as the flux-weakening or field-weakening method. By doing so, the overall torque generation capability of the machine is reduced, yet the machine is able to operate at high speeds.

A flux-weakening control algorithm applicable to SPMSM, which is not dependent upon the machine parameters, is proposed in [239]. Another method for the flux-weakening control of SPMSM, based on the output of the synchronous PI current regulator, is proposed in [240]. In this method, the saturation of the current regulator at the onset of the flux-weakening regime is avoided by control of the d-axis current through the outer voltage loop. Four-quadrant operation of IMPSM, in both constant torque region and flux-weakening region, is investigated in [241]. The output of the synchronous PI current controller is used to generate the reference PWM voltages as a required asset for implementation of the speed control of an IPMSM in flux-weakening region, which smoothly transits into or out of this operating region [242]. The flux level and starting point of the flux-weakening region are regulated by using an outer voltage loop which acts as an impediment to the current loop saturation. Direct torque control of an IMPSM, operating in both constant torque and flux-weakening regions, is proposed in [243],[244]. In this method, the current controllers which are followed by PWM and coordinate transformations are eliminated, which removes the associated digital delay and also dispenses with the position sensor since an estimated initial rotor position suffices for the algorithm commencement.

As stated earlier, flux-weakening algorithm relies upon injecting a negative d-axis current in order to weaken the stator flux. To this end, a physics-based finite element model of the magnet flux which takes into account the impact of temperature and armature field is proposed in [245]. This method is verified on a V-shape PMSM and has substantiated itself as a reliable algorithm. In flux-weakening algorithm, the DC link voltage is not completely exploited; consequently, a new algorithm based on the space vector PWM (SVPWM) technique is proposed [246]. The period of zero-voltage vector is used as the feedback signal to determine the switching instances and in order to avoid the q-axis current regulation lag, a lead angle control strategy is incorporated. In the flux-weakening region, due to the increased BEMF value, the inverter approaches its voltage limit. To alleviate this problem, the parameters of the anti-windup proportional and integral (AWPI) controller are undergone an optimization using an adaptive particle swarm algorithm (AVPSO) [247]. The state feedback of the nonlinear PMSM control system is obtained, and the dynamic characteristics of the

system are transformed into linear dynamic characteristics [248]. To this end, a new topology for the current controllers, relying on the input-output feedback linearisation algorithm, is proposed for the flux-weakening algorithm implementation. A field-weakening algorithm for open-winding PMSM using dual-vector-based model predictive flux control (DVT-MPFC) is proposed [249]. In this proposal, two isolated voltage source inverters are utilised and the reference stator flux vector is compensated by controlling a cost function value so as to facilitate the flux-weakening algorithm commissioning.

Appendix D

Digital Implementation

In this appendix, important aspects related to the digital implementation of the control algorithms are presented. The overall schematic of the dq-injected HFI-based sensorless control is illustrated in Fig. (D.1), as an example.

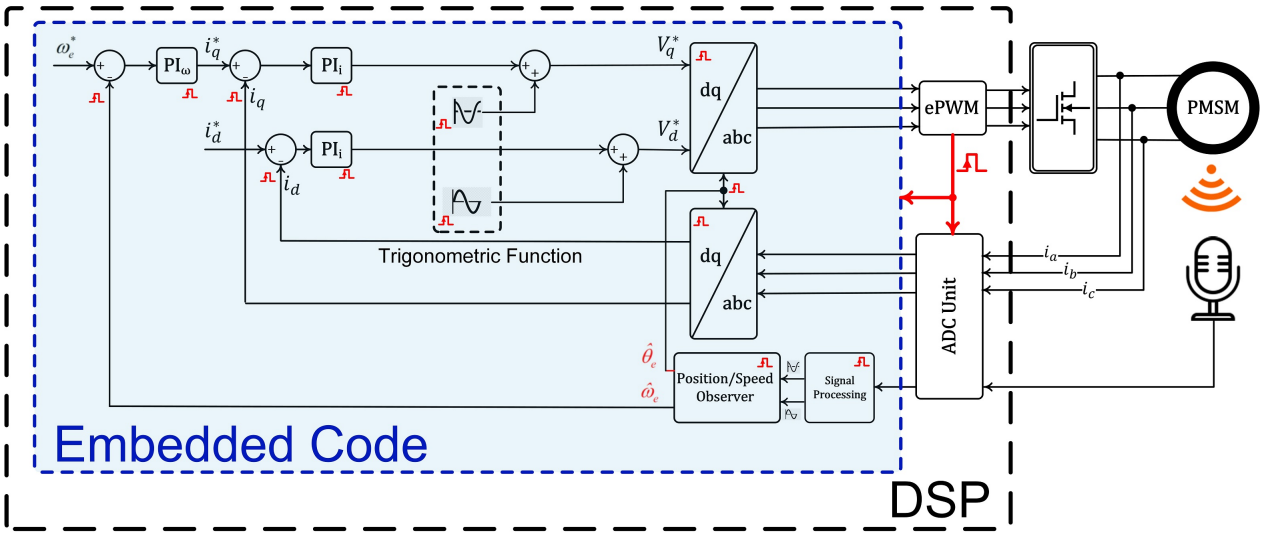

Figure D.1: Overall schematic of the proposed sensorless algorithm, taking into account both hardware and control algorithm.

In order for the sensorless FOC algorithm to work accurately, maintaining synchronism among the ADC readings, feedback loops, and PWM pulses is critically important. To this end, one of the PWM blocks (called ePWM in the DSP used in this thesis) is used as a reference, by which synchronization pulses are generated serving as a global interrupt service routine for the whole control algorithm. At the instance of zero-crossing of the

carrier waveform of the chosen master ePWM block (which can be of triangular or sawtooth waveform), a synchronizing pulse will be generated as shown in Fig. (D.2). Rising edge of the generated pulse is then used to generate a global interrup, trigerring all of the blocks within the embedded C code. Only in this way, can the user make sure of the seamless syncronization between all the ePWM blocks, ADC readings, feedback loops, PI regulators, unit delays, and counters. The generated synchronizing pulse in addition to the synchronized blocks are depicted with a red pulse icon in Fig. (D.1).

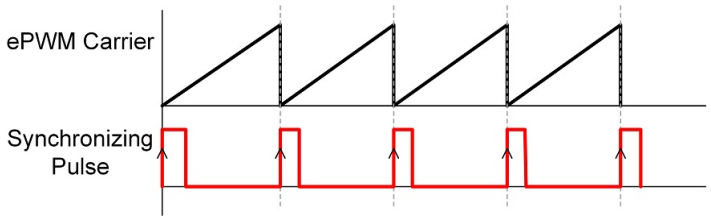

Figure D.2: Synchronizing pulse generation.

Apart from the importance of synchronization and in order to implement the embedded C code for the DSP, all of the S-domain transfer functions must be transformed into their equivalent Z-domain version. Therefore, all the integrators, unit delays, zero-order holds, filters, and resonant controllers - which are all mathematically modelled in S-domain - must be transformed. Adopting appropriate transformation algorithm, per transfer function, is of paramount importance as it guarantees having system stability and equalled performance in the discrete domain.

Assuming that the sampling rate of the discrete system is defined by T_s, which is the sampling period of the highest-frequency global interrupt of the embedded C code. The following table summarizes the three most common s2z transformation methods, namely *Forward*, *Backward-Euler*, and *Trapezoid*.

Table D.1: Different transformation methods

Method	**Transformation**	**Inverse Transformation**
Forward	$s = \frac{1}{T_s}(z-1)$	$z = 1 + T_s s$
Backward-Euler	$s = \frac{1}{T_s}\frac{z-1}{z}$	$z = \frac{1}{1-T_s s}$
Trapezoid	$s = \frac{2}{T_s}\frac{z-1}{z+1}$	$z = \frac{1+(T_s/2)s}{1-(T_s/2)s}$

Considering a general format for a transfer function in the s-domain given in eq. (D.1)

with the respective input and output denoted by X and Y,

$$H(s) = \frac{Y(s)}{X(s)} = \frac{B_0 + B_1 s + B_2 s^2 + \cdots + B_n s^n}{A_0 + A_1 s + A_2 s^2 + \cdots + A_n s^n} \tag{D.1}$$

the equivalent z-domain transfer function, with the standardized notation, is derived as shown in eq. (D.2) through using either of the transformation methods mentioned in Table. D.1.

$$H_d(z) = \frac{Y_d(z)}{X_d(z)} = \frac{b_0 + b_1 z^{-1} + b_2 z^{-1} + \cdots + b_n z^{-n}}{a_0 + a_1 z^{-1} + a_2 z^{-2} + \cdots + a_n z^{-n}} \tag{D.2}$$

It is worth mentioning that the author has always used *Backward-Euler* or *Trapezoid* method for DSP implmentation of the utilized BPFs and RCs in this thesis.

Using *Trapezoid* method and defining a constant $K = \frac{2}{T_s}$, z-domain equivalent transfer functions are obtained for general transfer functions of orders 1 to 3 as examples.

- **First-order Transfer Function**

$$H(s) = \frac{B_1 s + B_0}{A_1 s + A_0} \tag{D.3}$$

$$H_d(z) = \frac{b_0 + b_1 z^{-1}}{a_0 + a_1 z^{-1}} \tag{D.4}$$

$$\begin{aligned} b_0 &= \frac{B_0 + B_1 \frac{2}{T_s}}{A_0 + A_1 \frac{2}{T_s}} & b_1 &= \frac{B_0 - B_1 \frac{2}{T_s}}{A_0 + A_1 \frac{2}{T_s}} \\ a_0 &= 1 & a_1 &= \frac{A_0 - A_1 \frac{2}{T_s}}{A_0 + A_1 \frac{2}{T_s}} \end{aligned} \tag{D.5}$$

- **Second-order Transfer Function**

$$H(s) = \frac{B_2 s^2 + B_1 S + B_0}{A_2 s^2 + A_1 S + A_0} \tag{D.6}$$

$$H_d(z) = \frac{b_0 + b_1 z^{-1} + b_2 z^{-2}}{a_0 + a_1 z^{-1} + a_2 z^{-2}} \tag{D.7}$$

$$\begin{aligned} b_0 &= \frac{B_0 + B_1 K + B_2 K^2}{A_0 + A_1 K + A_2 K^2} & a_0 &= 1 \\ b_1 &= \frac{2B_0 - 2B_2 K^2}{A_0 + A_1 K + A_2 K^2} & a_1 &= \frac{2A_0 - 2A_2 K^2}{A_0 + A_1 K + A_2 K^2} \\ b_2 &= \frac{B_0 - B_1 K + B_2 K^2}{A_0 + A_1 K + A_2 K^2} & a_2 &= \frac{A_0 - A_1 K + A_2 K^2}{A_0 + A_1 K + A_2 K^2} \end{aligned} \tag{D.8}$$

- **Third-order Transfer Function**

$$H(s) = \frac{B_3 s^3 + B_2 S^2 + B_1 S + B_0}{A_3 s^3 + A_3 S^2 + A_1 S + A_0} \tag{D.9}$$

$$H_d(z) = \frac{b_0 + b_1 z^{-1} + b_2 z^{-2} + b_3 z^{-3}}{a_0 + a_1 z^{-1} + a_2 z^{-2} + a_3 z^{-3}} \tag{D.10}$$

$$\begin{array}{ll} b_0 = \frac{B_0+B_1K+B_2K^2+B_3K^3}{A_0+A_1K+A_2K^2+A_3K^3} & a_0 = 1 \\ b_1 = \frac{3B_0+B_1K-B_2K^2-3B_3K^3}{A_0+A_1K+A_2K^2+A_3K^3} & a_1 = \frac{3A_0+A_1K-A_2K^2-3A_3K^3}{A_0+A_1K+A_2K^2+A_3K^3} \\ b_2 = \frac{3B_0-B_1K-B_2K^2+3B_3K^3}{A_0+A_1K+A_2K^2+A_3K^3} & a_2 = \frac{3A_0-A_1K-A_2K^2+3A_3K^3}{A_0+A_1K+A_2K^2+A_3K^3} \\ b_3 = \frac{B_0-B_1K+B_2K^2-B_3K^3}{A_0+A_1K+A_2K^2+A_3K^3} & a_3 = \frac{A_0-A_1K+A_2K^2-A_3K^3}{A_0+A_1K+A_2K^2+A_3K^3} \end{array} \tag{D.11}$$

Contrôle Sans Capteur Basé sur le Bruit Acoustique d'une Machine Synchrone à Aimants Permanents

Un nouveau système de contrôle sans capteur pour les machines synchrones à aimants permanents (MSAP), qui repose sur l'extraction de l'information de position du rotor à partir du bruit acoustique généré lors du fonctionnement, est présenté dans cette thèse. La thèse examine en détail la nature des champs d'entrefer électromagnétiques, des forces radiales d'entrefer, ainsi que des vibrations et du bruit acoustique d'origine électromagnétique qui en résultent. Cette thèse propose deux nouveaux algorithmes sans capteur sont utilisant soit l'injection sinusoïdale à haute fréquence (HFI) habituelle, soit des impulsions de tension PWM intégrées. Pour extraire l'information de position du rotor, la thèse introduit des algorithmes de traitement du signal appropriés. Bien que les signaux souhaités soient correctement extraits lors de l'étape de traitement du signal, des harmoniques supplémentaires apparaissent dans la vitesse et la position estimées. Pour résoudre les problèmes qui en découle, la thèse propose deux observateurs novateurs, appelés RCPLL et ADALINE-PLL. En conclusion, la stabilité, la robustesse et la fiabilité des algorithmes sans capteur proposés sont étayées par des tests expérimentaux réalisés à travers divers points de fonctionnement statiques et dynamiques. De plus, la performance au démarrage est comparée à celle des algorithmes sans capteur conventionnels, révélant des réponses similaires et satisfaisantes en régime permanent et en transitoire. Ces résultats indiquent fortement la fiabilité et l'efficacité des méthodes sans capteur proposées.

Mot clés: Contrôle sans capteur, machine synchrone à aimants permanents (MSAP), bruit acoustique, traitement du signal, estimation de la position, banc d'essai expérimental

Acoustic Noise Based Sensorless Control of Permanent Magnet Synchronous Machine

A new sensorless control system for Permanent Magnet Synchronous Machines (PMSM) is presented in this thesis, which relies on extracting rotor position information from the acoustic noise generated during operation. The thesis thoroughly examines the nature of electromagnetic air gap fields, radial air gap forces, as well as resulting electromagnetically-origined vibrations and acoustic noise. This thesis proposes two new sensorless algorithms using either the conventional high-frequency sinusoidal injection (HFI) or integrated PWM voltage pulses. To extract rotor position information, appropriate signal processing algorithms are introduced in the thesis. Although the desired signals are correctly extracted during the signal processing step, additional harmonics appear in the estimated speed and position. To address the issues arising from this, the thesis proposes two innovative observers, named RCPLL and ADALINE-PLL. In conclusion, the stability, robustness, and reliability of the proposed sensorless algorithms are supported by experimental tests conducted across various static and dynamic operating points. Furthermore, the startup performance is compared to that of conventional sensorless algorithms, revealing similar and satisfactory responses in both steady-state and transient conditions. These results strongly indicate the reliability and effectiveness of the proposed sensorless methods.

Keywords: Sensorless control, permanent magnet synchronous machine (PMSM), acoustic noise, signal processing, position estimation, experimental benchmark